# Gravitational Wave Exotica – Advancing the Search for Signatures of Exotic Compact Objects and Gravitational Lensing from Data-Analysis and Theoretical Perspectives

Thesis by
Ka Lok (Rico) Lo

In Partial Fulfillment of the Requirements for the
Degree of
Doctor of Philosophy


CALIFORNIA INSTITUTE OF TECHNOLOGY
Pasadena, California

2024
Defended August 1, 2023

Ka Lok (Rico) Lo
ORCID: 0000-0003-1561-6716

# ACKNOWLEDGEMENTS

I would first like to thank my thesis advisor Alan Weinstein for his unwavering support throughout my doctoral study and giving me the academic freedom to pursue various research topics. I am also very grateful to Yanbei Chen for his invaluable insights and allowing me to tag along with his group, as well as my undergraduate thesis advisor Tjonnie G. F. Li for giving me the first research opportunity that kickstarted everything.

I am fortunate to have had the opportunity to collaborate with many amazing people and I would like to especially thank Jose María Ezquiaga, Wayne Hu, Alvin K. Y. Li, Masamune Oguri, Manu Srivastava, Yijun Wang and Shuo Xin. I would also like to thank past and current members of the LIGO Laboratory and the TAPIR group whom I had the honor to interact with. I am also grateful to Ignacio Magaña Hernandez, Ken K. Y. Ng, Peter T. H. Pang and Isaac C. F. Wong for being there when I needed someone to talk to. Finally, I owe much to my parents. This thesis would be literally and figuratively impossible without them.

I am a member of the LIGO Laboratory. LIGO was constructed by the California Institute of Technology and the Massachusetts Institute of Technology with funding from the National Science Foundation and operates under cooperative agreement PHY-0757058. I would like to acknowledge the support from the Croucher Foundation through the Croucher Scholarships for Doctoral Study, and the National Science Foundation through awards PHY-1912594 and PHY-2207758. I carried out most of the work presented here as a member of the LIGO-Virgo-KAGRA (LVK) Collaboration and benefited from interaction with many of its members. However, except where otherwise indicated, the descriptions and results presented in this thesis are my own and not necessarily those of the Collaboration.

This material is based upon work supported by NSF's LIGO Laboratory which is a major facility fully funded by the National Science Foundation.

# ABSTRACT

In this thesis, I explore two new arenas of gravitational-wave physics and advance them from both data-analysis and theoretical perspectives. I probe the nature of the remnant of a compact binary merger and study the strong gravitational lensing of gravitational waves. For probing the nature of a merger remnant, I first describe recipes of computing radiation emitted by a perturbed Kerr black hole, and in particular using the Generalized Sasaki-Nakamura formalism. Using a modified Kerr black hole spacetime as a model of a generic compact object, I then describe a prescription to compute waveforms of the repeating bursts of gravitational waves, referred to as gravitational-wave echoes, that are theorized to be emitted when a compact object with a reflective surface is formed as the remnant of a merger. Equipped with a waveform model for these echoes, I present a Bayesian model selection approach to look for echoes in data while inferring properties of the potential exotic compact object. I apply this approach to search for echoes in the data covering the first, the second, and the first half of the third observing run of the LIGO-Virgo-KAGRA network. For the strong lensing of gravitational waves, I first develop a Bayesian statistical framework that is capable of computing the probability of a given set of gravitational-wave events being the strongly-lensed counterparts of the same source or simply coming from distinct sources. If they are truly lensed, the framework can also infer the properties of the lensed source in a way unaffected by lensing. I apply this framework to search for signatures of strongly-lensed binary black hole systems in the data covering the third observing run. While we did not find any statistically significant evidence in the search for gravitational-wave echoes and strongly-lensed binary black holes, we can still place limits using the null results. Admittedly the existence of exotic compact objects is speculative and the observing rate of strongly-lensed gravitational waves is rare; however, the scientific impacts that they can bring are profound if they are proven to exist.

# PUBLISHED CONTENT AND CONTRIBUTIONS

*Notes:*

Chapter 4 is an adaptation of Ref. [1].

Chapter 5 is an adaptation of Ref. [7].

Chapter 6 is an adaptation of Ref. [13].

Chapter 8 is an adaptation of Ref. [11].

Chapter 11 is an adaptation of Ref. [9].

Chapter 12 is an adaptation of Ref. [8].

Chapter 13 is an adaptation of Ref. [4].

Chapter 14 is an adaptation of Ref. [3] and Ref. [2].


[1] R. K. L. Lo. "Recipes for computing radiation from a Kerr black hole using Generalized Sasaki-Nakamura formalism: I. Homogeneous solutions". *Submitted to Phys. Rev. D*. arXiv: 2306.16469 [gr-qc].

[2] J. Janquart et al. "Follow-up Analyses to the O3 LIGO-Virgo-KAGRA Lensing Searches". *Submitted to Mon. Not. Roy. Astron. Soc.* arXiv: 2306.03827 [gr-qc].
R. K. L. L performed the follow-up analyses on the two pairs of binary black hole merger signals highlighted in this paper using the code `hanabi` and wrote part of the manuscript.

[3] R. K. L. Lo. "denmarf: a Python package for density estimation using masked autoregressive flow". *Submitted to J. Open Source Softw.* DOI: 10.48550/arXiv.2305.14379. arXiv: 2305.14379 [astro-ph.IM].

[4] LIGO Scientific, VIRGO, KAGRA Collaboration. "Search for gravitational-lensing signatures in the full third observing run of the LIGO-Virgo network". *Submitted to Astrophys. J.* arXiv: 2304.08393 [gr-qc].
R. K. L. L performed the analyses for identifying strongly lensed binary black hole signals using the code `hanabi` and wrote part of the manuscript.

[5] H. W. Y. Wong, L. W. L. Chan, I. C. F. Wong, et al. “Using overlap of sky localization probability maps for filtering potentially lensed pairs of gravitational-wave signals”. In: *arXiv e-prints* (Dec. 2021). arXiv: 2112.05932 [gr-qc].
R. K. L. L conceived the project and wrote the code that was used to perform the overlap calculation. R. K. L. L co-mentored the two lead authors to perform the analysis and write the manuscript.

[6] J. Y. L. Kwok, R. K. L. Lo, A. J. Weinstein, et al. “Investigation of the effects of non-Gaussian noise transients and their mitigation in parameterized gravitational-wave tests of general relativity”. In: *Phys. Rev. D* 105.2 (2022), p. 024066. DOI: 10.1103/PhysRevD.105.024066. arXiv: 2109.07642 [gr-qc].
R. K. L. L conceived the project and mentored the lead author to complete the project and write the manuscript.

[7] S. Xin, B. Chen, R. K. L. Lo, et al. “Gravitational-wave echoes from spinning exotic compact objects: Numerical waveforms from the Teukolsky equation”. In: *Phys. Rev. D* 104.10 (2021), p. 104005. DOI: 10.1103/PhysRevD.104.104005. arXiv: 2105.12313 [gr-qc].
R. K. L. L performed the detectability analysis of echoes in current and future generation gravitational-wave detectors and wrote part of the manuscript.

[8] LIGO Scientific, VIRGO Collaboration. “Search for Lensing Signatures in the Gravitational-Wave Observations from the First Half of LIGO–Virgo’s Third Observing Run”. In: *Astrophys. J.* 923.1 (2021), p. 14. DOI: 10.3847/1538-4357/ac23db. arXiv: 2105.06384 [gr-qc].
R. K. L. L performed the analyses for identifying strongly lensed binary black hole signals using the code `hanabi` and wrote part of the manuscript.

[9] R. K. L. Lo and I. Magana Hernandez. “Bayesian statistical framework for identifying strongly lensed gravitational-wave signals”. In: *Phys. Rev. D* 107.12 (2023), p. 123015. DOI: 10.1103/PhysRevD.107.123015. arXiv: 2104.09339 [gr-qc].
R. K. L. L conceived the project, wrote a `python` implementation of the framework (i.e., `hanabi`), performed the analyses and wrote the manuscript.

[10] Y. Wang, R. K. L. Lo, A. K. Y. Li, et al. “Identifying Type II Strongly Lensed Gravitational-Wave Images in Third-Generation Gravitational-Wave Detectors”. In: *Phys. Rev. D* 103.10 (2021), p. 104055. DOI: 10.1103/PhysRevD.103.104055. arXiv: 2101.08264 [gr-qc].
R. K. L. L performed the analysis that established the scaling between the Bayes factor and the mis-match of a type-I lensed/un-lensed signal and a type-II lensed signal, and wrote part of the manuscript.

[11] LIGO Scientific, Virgo Collaboration. “Tests of general relativity with binary black holes from the second LIGO-Virgo gravitational-wave transient catalog”. In: *Phys. Rev. D* 103.12 (2021), p. 122002. DOI: 10.1103/PhysRevD.103.122002. arXiv: 2010.14529 [gr-qc].
R. K. L. L performed the analyses featured in this paper that search for echoes from binary black hole events in the second LIGO-Virgo gravitational-wave transient catalog. R. K. L. L was the internal editor/writer for the remnant properties section of the paper.

[12] A. K. Y. Li, R. K. L. Lo, S. Sachdev, et al. “Targeted subthreshold search for strongly lensed gravitational-wave events”. In: *Phys. Rev. D* 107.12 (2023), p. 123014. DOI: 10.1103/PhysRevD.107.123014. arXiv: 1904.06020 [gr-qc].
R. K. L. L was involved in the inception of this work and wrote part of the manuscript.

[13] R. K. L. Lo, T. G. F. Li, and A. J. Weinstein. “Template-based Gravitational-Wave Echoes Search Using Bayesian Model Selection”. In: *Phys. Rev. D* 99.8 (2019), p. 084052. DOI: 10.1103/PhysRevD.99.084052. arXiv: 1811.07431 [gr-qc].
R. K. L. L performed the analyses and wrote the manuscript.

# TABLE OF CONTENTS

# LIST OF ILLUSTRATIONS

# LIST OF TABLES

# LIST OF ACRONYMS

**AD** automatic differentiation.

**aLIGO** Advanced LIGO.

**BBH** binary black hole.

**BH** black hole.

**BHPT** black hole perturbation theory.

**BNS** binary neutron star.

**CBC** compact binary coalescence.

**CCDF** complementary cumulative distribution function.

**CE** Cosmic Explorer.

**DECIGO** Deci-hertz Interferometer Gravitational wave Observatory.

**ECO** exotic compact object.

**EM** electromagnetic.

**EMRI** extreme mass-ratio inspiral.

**ET** Einstein Telescope.

**FAR** false-alarm rate.

**GR** general relativity.

**GSN** Generalized Sasaki-Nakamura.

**GW** gravitational wave.

**HL** Hanford-Livingston.

**HLV** Hanford-Livingston-Virgo.

**HST** Hubble Space Telescope.

**IMR** inspiral-merger-ringdown.

**IMRE** inspiral-merger-ringdown-echo.

**JWST** James Webb Space Telescope.

**KAGRA** Kamioka Gravitational Wave Detector.

**KDE** kernel density estimation.

**LIGO** Laser Interferometer Gravitational-Wave Observatory.

**LISA** Laser Interferometer Space Antenna.

**LSST** Legacy Survey of Space and Time.

**MAP** maximum a posteriori estimator.

**ML** machine learning.

**MLE** maximum likelihood estimator.

**MST** Mano-Suzuki-Takasugi.

**NF** normalizing flow.

**NS** neutron star.

**O1** the first observing run.

**O2** the second observing run.

**O3** the third observing run.

**O3a** the first half of the third observing run.

**O3b** the second half of the third observing run.

**O4** the fourth observing run.

**ODE** ordinary differential equation.

**PE** parameter estimation.

**QNM** quasi-normal mode.

**ROC** receiver operating characteristic.

**SDSS** Sloan Digital Sky Survey.

**SIE** singular isothermal ellipsoid.

**SIS** singular isothermal sphere.

**skymap** sky localization probability map.

**SL** strong gravitational lensing.

**SN** Sasaki-Nakamura.

**SNR** signal-to-noise ratio.

# Prologue

*Chapter 1*

# INTRODUCTION: THE PAST, THE PRESENT AND THE FUTURE OF GRAVITATIONAL-WAVE PHYSICS

With the gravitational-wave (GW) detector network formed by the interferometers at Hanford and Livingston from Laser Interferometer Gravitational-Wave Observatory (LIGO) in the United States [1], the Virgo interferometer in Italy [2], the GEO600 interferometer in Germany [3, 4, 5] and the Kamioka Gravitational Wave Detector (KAGRA) interferometer in Japan [6, 7, 8], we are now routinely observing GW signals coming from collisions of compact objects such as black holes (BHs) and neutron stars (NSs) that occurred more than gigalight-years away from us. As two compact objects coalesce with each other, the binary system emits gravitational radiation with a characteristic chirping waveform where the frequency increases with time. As of the time of this writing, the GW detector network has registered over a hundred of those cataclysmic collisions [9, 10, 11, 12].

Those GWs not only carry the news about an occurrence of a compact binary coalescence (CBC), we can also learn a great deal of physics and astrophysics from them. By comparing detected GW signals with theoretical waveforms that CBCs should emit, we can infer the properties such as the masses and the spins of the GW sources. Once we have collected enough such measurements, we can also infer the mass distribution and the spin distribution of these compact objects on the population level, which will tell us more about the astrophysics of their formation mechanisms [13, 14].

Furthermore, we can also learn about the composition and the structure of compact objects through their tidal interaction signatures imprinted in the GWs they emit when they merge with each other. For example, we can probe the equation of state of nuclear matter that NSs are made up of when they smash into each other,

at the densities that are impossible to create in laboratory settings [15]. This is exactly what happened in the binary neutron star (BNS) collision GW170817 [16], which was observed in both the GW and the electromagnetic (EM) spectrum [17]. The coincident detection in both spectra allows us to constrain, in a way that is independent to previous measurements, the Hubble constant $H_0$ which is an important quantity in cosmology that indicates the expansion rate of the Universe [18].

Last but not least, GWs can be used to study fundamental physics, such as gravity itself. Since we use general relativity (GR) to compute expected gravitational waveforms coming from those CBCs, therefore by measuring deviations of what we have actually observed in data with the GR predictions, we can test for the correctness of GR, which is currently the best theory of gravity we have, in the strong-gravity limit that was not accessible to other weak-field tests of GR such as the perihelion precession of Mercury [19, 20, 21, 22, 23].

Indeed, the existence of GWs was predicted by Einstein with his GR for a little over a hundred years. While we now celebrate the success of GR and use GWs to achieve many scientific breakthroughs, the field of GW science is not without controversies at the beginning. From the theoretical perspective, scientists were not sure at first whether GWs are physical and real in the sense that they carry energy with them as they propagate or they are simply artifacts from choosing a particular coordinate system where the apparent GWs can be removed by choosing different coordinate systems. The doubt concerning the reality of GWs largely went away after the monumental Chapel Hill conference in 1957 where Feynman presented his "sticky bead" argument [24] to show that when a GW passes through a rod with two beads that are free to slide across the rod with a small amount of friction, the incoming GW will cause the beads to move even in the presence of friction and thus the GW is physical and does work on the beads.

From the experimental side, Weber invented the first GW detector in 1960 based on resonance of a solid triggered by a passing GW and began to observe GWs

the new instrument, now referred to as the Weber bar, throughout the 1960s. His claims of detecting GWs were later discredited after many groups failed to reproduce his results. Another approach to measure GWs is to use a Michelson interferometer to measure the very minute stretching and squeezing of the space-time due to GWs. In a Michelson interferometer, a light beam is directed towards the center of the interferometer where there is an optical device called a beam splitter that divides the incident beam into two and sends the split beams onto two different paths along the $x$ and the $y$ arm of the interferometer, respectively. At the end of each arm, there is a mirror that reflects the light beam back towards the center where the reflected beams from the two arms are recombined. When the length of the $x$ and the $y$ arm are equal, no special pattern should emerge from the interferometer. However, when there is a GW passing through the interferometer causing the length of the $x$ and the $y$ arm to differ, a fringe pattern will appear. This is the technical basis of the GW detectors that we use today [25], which also led to the discovery of the first direct detection of GW coming from a binary black hole (BBH) merger, now referred to as GW150914 [26]. The Nobel Prize in Physics 2017 was awarded to Weiss, Thorne and Barish for their contributions to the LIGO detectors and observations of GWs.

Fast-forwarding to the present and looking ahead, it is projected that the fourth observing run (O4) will see well over a hundred of GW signals coming from CBCs [27]. With the new GW detector, LIGO India, currently under construction and other planned upgrades to existing GW detectors and constructions of new detectors [28, 29, 30, 31, 32], we will be able to observe even more GW signals which were emitted from even greater distances with louder amplitudes, and consequently be able to study rarer and more exotic phenomena with GW observations, which are the main subjects of this thesis.

*Chapter 2*

# OVERVIEW OF THE THESIS

In this thesis, I will explore new arenas of gravitational-wave (GW) physics and will advance them from both data-analysis and theoretical perspectives. In particular, I will focus on two topics — probing the nature of a merger remnant using a unique waveform signature theorized when the remnant is of an *exotic* type of compact object in Part I, and the strong gravitational lensing of GWs in Part II.

In the first part of the thesis, I will first give a brief introduction in Chapter 3 to the notion of exotic compact objects (ECOs) and the physics of their repetitive emissions of GW bursts, which are referred to as GW echoes, after they are formed as the remnants of mergers. Developments in the theoretical and the data-analysis aspect have to come together in unison in order to maximize the science we can do. Considering that, in Chapter 4, I first describe a way to compute radiation emitted by a spinning black hole (BH) under the framework of black hole perturbation theory (BHPT) in general relativity (GR). Then in Chapter 5, I present a prescription to compute waveforms of the aforementioned GW echoes using BHPT with a slightly modified BH spacetime as a model of an ECO and the recipes to compute gravitational waveforms in Chapter 4. Equipped with theoretical predictions of what GW echoes should look like, in Chapter 6 I take the data-analysis perspective and present a Bayesian model selection approach to look for these GW echoes in data. In Chapter 7, I describe the search results of GW echoes in the data covering the first observing run (O1) and the second observing run (O2) using the technique in Chapter 6 and demonstrate things that we can learn/limits that we can place with GW echoes. The search is extended to cover also the data in the first half of the third observing run (O3a) and the results are presented in Chapter 8. Lastly, I give concluding

remarks to Part I of my thesis in Chapter 9.

In the second part of the thesis, I will start with a brief introduction to the phenomenon of strong gravitational lensing of GWs in Chapter 10. Then in Chapter 11, I will develop a Bayesian statistical framework that simultaneously identifies strongly-lensed GWs and characterizes the properties of their source. In Chapter 12 and Chapter 13, I present the analysis results for finding strongly-lensed binary black hole (BBH) mergers in the data covering O3a and the third observing run (O3) entirely, respectively. Then in Chapter 14, I describe an extension to the framework introduced in Chapter 11 that incorporates realistic simulations of strongly-lensed background objects by galaxy-scale foreground lenses into strong lensing analysis of GWs, which is applied to two interesting candidates of strongly-lensed BBH pairs found in O3 as a demonstration. At last in Chapter 15 I will give concluding remarks to Part II of my thesis.

Finally, I will summarize the thesis and discuss future work in Chapter 16.

# Part I

# Exotic Compact Objects as Remnants of Binary Black Hole Mergers

*Chapter 3*

# OVERVIEW OF PART I

In the first part of the thesis, let us focus on using gravitational waves (GWs) to probe the nature of the remnant of a compact binary merger. In general relativity (GR), after the merger of two black holes (BHs), a new BH should be formed as the remnant. The new-born BH is highly excited by the merger but it will relax to a stationary state by the emission of "ringing" gravitational radiation (commonly referred to as the *ringdown*). This is akin to the excitation and the subsequent relaxation of a damped harmonic oscillator.

The GWs generated by the merger will propagate *both* outwards to infinity (and be seen by GW detectors) and inwards to the BH itself (see Figure 3.1). However, we will not observe the wave packet that fell into the BH as the hole will absorb all the incoming radiation (hence the name black hole). If one instead relaxes the perfect absorption assumption of the hole (not black anymore), perhaps due to a reflective structure near the would-be event horizon as motivated by some quantum gravity considerations, the falling wave packet will be partially reflected off the hole. The now-reflected wave packet will travel outwards and encounter the potential barrier (roughly) at the light ring. The wave packet will again be partially reflected towards the hole and partially transmitted towards infinity. This effectively forms a GW cavity trapping GWs (see Figure 3.2). The GWs escaped from the cavity will be seen by the detectors as bursts of waves time-shifted and modulated with respect to each other, referred to as GW *echoes*. The observation of GW echoes in the post-merger part of a signal will indicate that the merger remnant is a hole that is not a BH in GR. These new class of remnants are collectively referred to as *exotic compact objects (ECOs)*. This can also be interpreted as testing the "blackness" of the remnant compact object.

This thesis will be covering both the theoretical and the data-analysis perspective

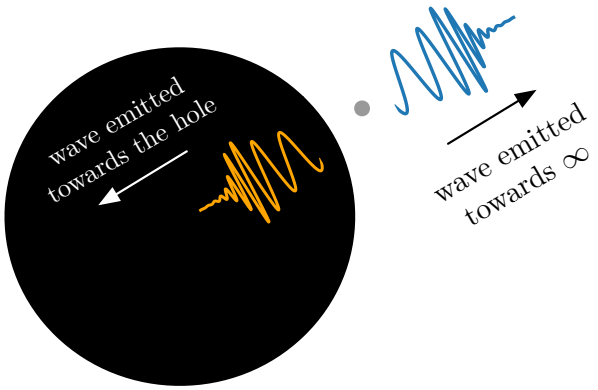


Figure 3.1: An illustration of the GW emission during a merger of two holes (represented by the black and grey circles). The black circle represents the much heavier hole of the two and the grey circle represents the lighter hole. As they merge, GWs are emitted both towards infinity (shown in blue) and towards the heavier hole (shown in orange). If they are indeed BHs in GR, the wave falling towards the heavier hole will be absorbed completely.

of GW echoes from ECOs. In Chapter 4, I will present the Generalized Sasaki-Nakamura (GSN) formalism that allows us to compute radiation from Kerr BHs by solving the Teukolsky equation, the master equation governing the generation and propagation of waves emitted by BHs. Next in Chapter 5, I will briefly describe a prescription to compute waveforms of GW echoes from spinning compact objects, based on Ref. [33] that I co-authored. The prescription uses the Teukolsky equation for Kerr BHs in GR as the foundation where an ECO is modeled as a Kerr-BH-like object that satisfies a reflective boundary condition at its surface instead of a purely in-going boundary condition at the horizon of a BH. The source term to the Teukolsky equation that drives the radiation is modeled as a test particle plunging towards the ECO surface.

In particular, two sets of solutions to the Teukolsky equation, namely $\psi_0$ that encodes gravitational radiation falling into the compact object and $\psi_4$ that encodes radiation emitted towards infinity (to GW detectors). Typically, at the location

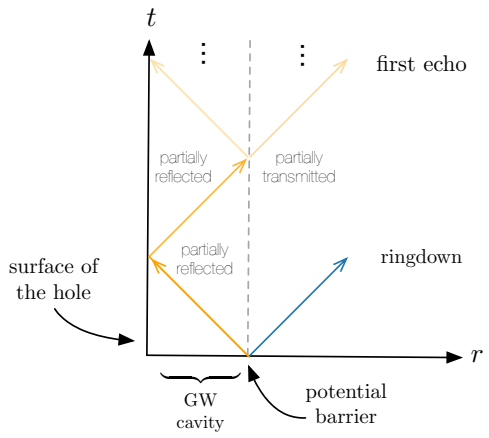


Figure 3.2: A spacetime diagram illustrating the generation mechanism of GW echoes. The GW generated by a merger will propagate both outwards to infinity and inwards to the remnant of the merger. The in-going wave packet will be partially reflected off the remnant. The now-reflected wave packet will travel outwards and encounter the potential barrier. The wave packet will again be partially reflected towards the remnant and partially transmitted towards infinity. This effectively forms a GW cavity, and the repeated burst of GWs are referred to as GW echoes.

where the source term that drives the radiation vanishes, the $\psi_0$ and $\psi_4$ solutions are related to each other via the Teukolsky-Starobinsky identities and thus one only needs to solve one of the two solutions numerically. However in our prescription, these identities do not apply since the source term evidently does not vanish at the ECO surface. This is a major caveat of Ref. [33] where we blatantly misused the Teukolsky-Starobinsky identities to convert $\psi_4$ solutions to $\psi_0$ solutions. Indeed, a follow-up work [34] showed that the waveform from a direct calculation of $\psi_0$ for a non-spinning BH differs from that obtained by converting $\psi_4$ using the identities. While the simple regularization procedure that enables the calculation in Ref. [34] can be easily generalized to spinning BHs, the resulting expression for the regularized source term is too complicated to be used in any practical calculation. The GSN formalism in Chapter 4 provides an alternative approach to computing gravitational radiation. The source term in the

GSN formalism is naturally regularized and numerically better-behaved than in the Teukolsky formalism. While only the source-free case is being discussed in Chapter 4, it can be extended to work in a generic setting where the source is non-vanishing everywhere and the manuscript for the extension is in preparation [35]. With the complete GSN formalism, we would be able to compute theoretical waveforms for GW echoes in a consistent manner.

The theoretical waveforms can then be fed into data-analysis pipelines that search for GW echoes in data. In Chapter 6, I will describe one such pipeline that uses a Bayes factor as the detection statistic to determine if echoes are present in a given GW data, while simultaneously characterizing properties of the would-be ECO remnant from the echoes. In particular, the behavior of the detection statistic under different noise characteristics when there is no echoes in the data was studied by performing numerous mock analyses, which allows us to compute the probability (commonly referred to as the $p$-value) of having the detection statistic greater than a certain value when there is actually no echoes and also gives us the statistical significance of a detection of GW echoes in data.

In Chapter 7, I will present a search for GW echoes in the data near the binary black hole (BBH) merger signals found during the first observing run (O1) and the second observing run (O2). While no statistical evidence evidence of echoes were found, constraints can still be placed with the null detections, both on population level and individual level. For instance, an upper limit on the formation of ECO from BBH mergers can be obtained. With the null discovery of echoes for a BBH merger, limits on the location and the reflectivity of the surface of the would-be ECO remnant formed after the merger can be constructed. In Chapter 8, I will report the result of a search for GW echoes in the data near selected statistically-confident BBH mergers in the first half of the third observing run (O3a).

*Chapter 4*

# RECIPES FOR COMPUTING RADIATION FROM A KERR BLACK HOLE USING GENERALIZED SASAKI-NAKAMURA FORMALISM

This chapter contains work from

> R. K. L. Lo. "Recipes for computing radiation from a Kerr black hole using Generalized Sasaki-Nakamura formalism: I. Homogeneous solutions". *Submitted to Phys. Rev. D*. arXiv: 2306.16469 [gr-qc].

## 4.1 Introduction

The first detection of a binary black hole merger by the two detectors of the Laser Interferometer Gravitational-Wave Observatory (LIGO) in 2015 [26] marked the beginning of a new era in physics where scientists can directly observe gravitational radiation emitted from collisions of compact objects such as black holes (BHs), allowing the strong field regime of gravity to be probed. Subsequent observing runs of the Advanced LIGO [1], Advanced Virgo [2], and KAGRA [6, 7, 8] detectors have unveiled about a hundred more such gravitational waves (GWs) coming from the collisions of compact objects [36, 9, 10, 12]. With planned updates to the current detectors [27] and constructions of new detectors [29, 30], some targeting different frequency ranges such as the Laser Interferometer Space Antenna (LISA) [31] and the Deci-hertz Interferometer Gravitational wave Observatory (DECIGO) [32], we will be observing GWs coming from various kind of sources on a regular basis.

In order to identify GW signals from noisy data and characterize properties of their sources, it is imperative to have theoretical understanding of what those waveforms look like so that we can compare them with observations. Gravitational waveforms can be computed using a number of approaches, such as

numerically solving the full non-linear Einstein field equation, or solving a linearized field equation as an approximation. BH perturbation theory is one such approximation scheme where the dynamical spacetime is decomposed into a stationary background spacetime and a small radiative perturbation on top of it. The metric of the background spacetime is known exactly, and we only need to solve, usually numerically, for the metric perturbation. See for example Refs. [37, 38, 39, 40] for a comprehensive review on BH perturbation theory.

At the core of BH perturbation theory is the Teukolsky formalism [41, 42, 43, 44] where a rotating (and uncharged) BH of mass $M$ and angular momentum per unit mass $a$ is used as the background spacetime. The metric for such a spacetime is known as the Kerr metric [45], and in the Boyer-Lindquist coordinates $(t, r, \theta, \phi)$ the exact line element $ds$ is given by [46, 47]

$$ds^2 = -\left(1 - \frac{2Mr}{\Sigma}\right) dt^2 - \frac{4Mar\sin^2\theta}{\Sigma} dt d\phi + \frac{\Sigma}{\Delta} dr^2 + \Sigma d\theta^2 + \sin^2\theta \left(r^2 + a^2 + \frac{2Ma^2 r \sin^2\theta}{\Sigma}\right) d\phi^2, \quad (4.1)$$

where $\Sigma \equiv r^2 + a^2\cos^2\theta$ and $\Delta \equiv r^2 - 2Mr + a^2 = (r - r_+)(r - r_-)$ with $r_+ = M + \sqrt{M^2 - a^2}$ as the outer event horizon and $r_- = M - \sqrt{M^2 - a^2}$ as the inner Cauchy horizon. In the Teukolsky formalism, instead of solving directly the perturbed radiative field (e.g., the metric for gravitational radiation, and the electromagnetic field tensor for electromagnetic radiation), we solve for its (gauge-invariant) *scalar* projections onto a tetrad. For instance, the (Weyl) scalar $\psi_0$ and $\psi_4$ contain information about the in-going and the out-going gravitational radiation, respectively [41]. Teukolsky showed that these scalar quantities all follow the same form of the master equation (aptly named the Teukolsky equation), and it

is given by [41]

$$\left[\frac{\left(r^2+a^2\right)^2}{\Delta}-a^2\sin^2\theta\right]\frac{\partial^2\psi}{\partial t^2}+\frac{4Mar}{\Delta}\frac{\partial^2\psi}{\partial t\partial\phi}$$
$$+\left[\frac{a^2}{\Delta}-\frac{1}{\sin^2\theta}\right]\frac{\partial^2\psi}{\partial\phi^2}-\Delta^{-s}\frac{\partial}{\partial r}\left(\Delta^{s+1}\frac{\partial\psi}{\partial r}\right)$$
$$-\frac{1}{\sin\theta}\frac{\partial}{\partial\theta}\left(\sin\theta\frac{\partial\psi}{\partial\theta}\right)-2s\left[\frac{a\left(r-M\right)}{\Delta}+\frac{i\cos\theta}{\sin^2\theta}\right]\frac{\partial\psi}{\partial\phi}$$
$$-2s\left[\frac{M\left(r^2-a^2\right)}{\Delta}-r-ia\cos\theta\right]\frac{\partial\psi}{\partial t}$$
$$+\left(s^2\cot^2\theta-s\right)\psi=4\pi\Sigma T, \quad (4.2)$$

where $T$ is a source term for the Teukolsky equation, and $\psi$ can correspond to different scalar projections with different spin weights $s$. In particular, $s=0$ for scalar radiation, $s=\pm1$ for in-going and out-going electromagnetic radiation, respectively, and $s=\pm2$ for in-going and out-going gravitational radiation, respectively. For example, $\psi_0$ satisfies Eq. (4.2) by setting $\psi\equiv\psi_0$ and $s=2$, whereas $\psi_4$ satisfies the equation by setting $\psi\equiv(r-ia\cos\theta)^4\psi_4$ and $s=-2$.

Despite its fearsome look, Eq. (4.2) is actually separable by writing $\psi(t,r,\theta,\phi)=R(r)S(\theta,\phi)e^{-i\omega t}$. The separation of variables gives one ordinary differential equation (ODE) for the angular part in $\theta$ (since the $\phi$ dependence must be $\psi\sim e^{im\phi}$ with $m$ being an integer due to the azimuthal symmetry of a Kerr BH), and another ODE for the radial part in $r$. We discuss the angular part of the Teukolsky equation and the recipes for solving the equation numerically more in depth in App. 4.5. Limiting ourselves to consider the source-free ($T=0$) case for now[1], the ODE for the radial part is given by [41]

$$\Delta^{-s}\frac{d}{dr}\left(\Delta^{s+1}\frac{dR}{dr}\right)-V_{\rm T}(r)R=0, \quad (4.3)$$

with

$$V_{\rm T}(r)=\lambda-4is\omega r-\frac{K^2-2is(r-M)K}{\Delta}, \quad (4.4)$$

[1]We consider the $T\neq0$ case in a subsequent paper (see Sec. 4.4.1).

where $K \equiv (r^2 + a^2)\omega - ma$, and $\lambda$ is a separation constant related to the angular Teukolsky equation (see App. 4.5, and in particular Eq. (4.73)). The general solution of $\psi(t, r, \theta, \phi)$ can then be written as

$$\psi(t, r, \theta, \phi) = \sum_{\ell m \omega} {}_sR_{\ell m\omega}(r)\,{}_sS_{\ell m\omega}(\theta, \phi)e^{-i\omega t}, \tag{4.5}$$

where $\ell$ labels an eigenfunction of the angular Teukolsky equation (c.f. App. 4.5).

While the radial Teukolsky equation in Eq. (4.3) looks benign, it is challenging to solve it numerically in that form because the potential associated with the ODE is long-ranged. To see this, we can re-cast Eq. (4.3) into the Schrödinger equation form that is schematically given by

$$\frac{d^2Y}{dr_*^2} + \Big(\omega^2 - V_Y\Big)\,Y = 0, \tag{4.6}$$

with $r_*$ being the tortoise coordinate for Kerr BHs defined by

$$\frac{dr_*}{dr} = \frac{r^2 + a^2}{\Delta}, \tag{4.7}$$

where $Y$ is some function transformed from the Teukolsky function $R$, and $V_Y$ is the potential associated with the ODE [42]. For the radial Teukolsky equation, the potential $V_Y$ is long-ranged[2] in the sense that $V_Y \sim -2is\omega/r$ as $r \to \infty$, as opposed to a short-ranged potential that falls at $1/r^n$ with $n \geq 2$ (for an illustration, see Fig. 4.3). The long-ranged-ness of the potential $V_{\rm T}$ implies that the two wave-like "left-going" and "right-going" solutions of Eq. (4.3) will have different power-law dependences of $r$ in their wave amplitudes as $r \to \infty$ [42, 48]. A direct numerical integration of Eq. (4.3) will suffer from the problem where the solution with a higher power of $r$ in its asymptotic amplitude will overwhelm the other solution and eventually take over the entire numerical solution due to finite precision in computation when $r$ becomes large [42, 48]. In fact, the same problem arises when $r \to r_+$ (equivalently when $\Delta \to 0$) where the left- and the

[2] A prime example of a long-ranged potential is the Coulomb potential in electrostatics.

right-going waves have again different power-law dependences of $\Delta$ in their wave amplitudes and the solution with a smaller power of $\Delta$ in its asymptotic amplitude will overwhelm the other one numerically as $\Delta \to 0$ [42, 48].[3] Therefore, a direct numerical integration, at least with the Boyer-Lindquist coordinates, is not suitable for solving the radial Teukolsky equation accurately.

Fortunately, there are other techniques that can get around this issue and allow us to solve for $R(r)$ accurately. One such technique is the Mano-Suzuki-Takasugi (MST) method [49], originally as a low frequency expansion and later extended by Fujita and Tagoshi [50, 51] as a numerical method for solving the homogeneous radial Teukolsky equation at arbitrary frequency. The Sasaki-Nakamura (SN) formalism [52, 53, 54], which is the main topic of this paper (and subsequent papers), also enables accurate and efficient numerical computations of homogeneous solutions to the radial Teukolsky equation. In short, Sasaki and Nakamura devised a class of transformations, originally only for $s = -2$, that convert the radial Teukolsky equation with the long-ranged potential $V_{\rm T}$ into another ODE with a short-ranged potential. One can then solve the numerically better-behaved ODE instead. The transformations were later generalized by Hughes [48] to work for arbitrary integer spin-weight $s$.

Comparing to the MST method, the Generalized Sasaki-Nakamura (GSN) formalism is conceptually simpler and thus easier to implement. Practically speaking, the MST method expresses a homogeneous solution to the radial Teukolsky solution $R(r)$ in terms of special functions, which makes it ideal for analytical work. However, for numerical work there are no closed-form expressions for these special functions and oftentimes the evaluations of these special functions involve solving some ODEs numerically [55]! Thus, efficiency-wise the GSN formalism is not inferior, at the very least, to the MST method even at low frequencies. On the other hand, while the extension of the MST method by Fujita and Tagoshi [50, 51] allows the method to in principle compute homogeneous

[3] Refer to Sec. 4.2.2 for more details and the explicit dependence in $r$ and $\Delta$ for the asymptotic wave amplitudes of $R$ approaching infinity and the horizon, respectively.

solutions at arbitrary frequency, practically the authors of Refs. [50, 51] reported that it was numerically challenging to find solutions when wave frequencies become somewhat large. The GSN formalism, as we will show later, becomes *even more efficient* in those cases at high frequencies.

Another appealing capability of the SN formalism has to do with computing solutions to the inhomogeneous radial Teukolsky equation. The solutions encode the physical information about the radiation emitted by a perturbed BH, say for example the GW emitted when a test particle plunges towards a BH. Based on the SN transformation (for the source-free case), the SN formalism has a prescription to convert a Teukolsky source term that could be divergent, near infinity or the horizon (or both), into a well-behaved source term.[4]

In this paper, we revamp the GSN formalism for the source-free case to take full advantages of the formalism for computing radiation from a Kerr BH. We explicitly show the GSN transformations for physically relevant radiation fields ($s = 0, \pm 1, \pm 2$) that transform the radial Teukolsky equation with a long-ranged potential into a new ODE, referred to as the GSN equation, which has a short-ranged potential instead. To aid numerical computations using the GSN formalism, we derive expressions for the higher-order corrections to the asymptotic solutions of the GSN equation, improving the accuracy of numerical solutions. We also derive expressions for the frequency-dependent conversion factors that convert asymptotic amplitudes of GSN solutions to that of their corresponding Teukolsky solutions, which are needed in wave scattering problems and computations of inhomogeneous solutions.

Furthermore, we describe an open-source implementation of the aforementioned GSN formalism that is written in `julia` [56], a modern programming language designed with numerical analysis and scientific computing in mind. The numerical implementation leverages the re-formulation of the GSN equation, which is a second-order linear ODE, into a form of first-order non-linear ODE known as

[4] For more discussions on solving the inhomogeneous radial Teukolsky equation using the SN formalism, see Sec. 4.4.1.

a Riccati equation to gain additional performance. Our new code is validated by comparing results with an established code `Teukolsky` [57] that implements the MST method.

The paper is structured as follows: In Sec. 4.2, we first review the GSN formalism for the source-free case. We then derive the asymptotic behaviors and the appropriate boundary conditions for solving the GSN equation. In Sec. 4.3, we describe our numerical implementation of the GSN formalism and compare it with the MST method. Finally, in Sec. 4.4 we summarize our results and briefly discuss two applications of the GSN formalism developed in this paper, namely laying the foundation for an efficient procedure to compute gravitational radiation from BHs near *both* infinity and the horizon, and as an alternative method for determining quasi-normal modes (QNMs). For busy readers, in App. 4.9 we give "ready-to-use" expressions for both the GSN transformations, the asymptotic solutions to the corresponding GSN equation, as well as the conversion factors to convert between the Teukolsky and the GSN formalism.

Throughout this paper, we use geometric units $c = G = M = 1$, and a prime to denote differentiation with respect to $r$.

### 4.2 Generalized Sasaki-Nakamura formalism

In this section, we first review, following Ref. [48] closely, the core idea behind the Generalized Sasaki-Nakamura (GSN) formalism, i.e., performing a transformation, which is different for each spin weight $s$, from the Teukolsky function $R(r)$ into a new function $X(r_*)$. This new function $X(r_*)$ is referred to as the GSN function, expressed in the tortoise coordinate $r_*$ (for Kerr BHs) instead of the Boyer-Lindquist $r$-coordinate. A defining feature of the $r_*$-coordinate is that it maps the horizon to $r_* \to -\infty$ and infinity to $r_* \to \infty$. The GSN transformations were chosen such that the new ODE that $X(r_*)$ satisfies, which is referred to as the GSN equation, is more suitable for numerical computations than the original radial Teukolsky equation in Eq. (4.3). We then study the leading asymptotic behaviors, approaching the horizon $r \to r_+$ ($r_* \to -\infty$) and approaching infinity

$r \to \infty\,(r_* \to \infty)$, of both the GSN equation and the GSN transformations to establish the boundary conditions to be imposed, as well as the conversion factors for converting the *complex* amplitude of a GSN function to that of the corresponding Teukolsky function at the two boundaries. To aid numerical computations when using numerically-*finite* inner and outer boundaries (in place of negative and positive infinity, respectively, in the $r_*$ coordinate), we also derive the higher-order corrections to the asymptotic boundary conditions.

### 4.2.1 Generalized Sasaki-Nakamura transformation

The GSN transformation can be broken down into two parts. The first part transforms the Teukolsky function $R(r)$ and its derivative $R'(r)$ into a new set of functions $(\chi(r), \chi'(r))$ as an intermediate step. In general, we write such a transformation as

$$\chi(r) = \tilde{\alpha}(r)R(r) + \tilde{\beta}(r)R'(r), \tag{4.8}$$

where $\tilde{\alpha}(r)$ and $\beta(r)$ are weighting functions that generate the transformation. This kind of transformation is also known as a Generalized Darboux transformation [58], but differs from a "conventional" Darboux transformation in that the weighting function $\tilde{\beta}(r)$ for a conventional Darboux transformation is a constant instead of a function of $r$. For later convenience, we rescale $\tilde{\beta}$ by $\Delta^{s+1}$ and write $\alpha(r) = \tilde{\alpha}(r)$ and $\beta(r) = \tilde{\beta}(r)\Delta^{-(s+1)}$. Differentiating Eq. (4.8) with respect to $r$ and packaging them into a matrix equation, we have [48]

$$\begin{pmatrix} \chi \\ \chi' \end{pmatrix} = \begin{pmatrix} \alpha & \beta\Delta^{s+1} \\ \alpha' + \beta V_{\mathrm{T}}\Delta^{s} & \alpha + \beta'\Delta^{s+1} \end{pmatrix} \begin{pmatrix} R \\ R' \end{pmatrix}, \tag{4.9}$$

where we have used Eq. (4.3) to write $R''$ in terms of $R, R'$ as

$$R''(r) = \frac{V_{\mathrm{T}}}{\Delta}R(r) - \frac{2(s+1)(r-1)}{\Delta}R'(r). \tag{4.10}$$

The inverse transformation going from $(\chi(r), \chi'(r))$ to $(R(r), R'(r))$ is obtained by inverting Eq. (4.9) and is given by [48]

$$\begin{pmatrix} R \\ R' \end{pmatrix} = \frac{1}{\eta}\begin{pmatrix} \alpha + \beta'\Delta^{s+1} & -\beta\Delta^{s+1} \\ -(\alpha' + \beta V_{\mathrm{T}}\Delta^{s}) & \alpha \end{pmatrix} \begin{pmatrix} \chi \\ \chi' \end{pmatrix}, \tag{4.11}$$

where $\eta(r)$ is the determinant of the above matrix, which is given by [48]

$$\eta = \alpha\left(\alpha + \beta'\Delta^{s+1}\right) - \beta\Delta^{s+1}\left(\alpha' + \beta V_{\rm T}\Delta^{s}\right). \tag{4.12}$$

In the second step of the GSN transformation, we further rescale $\chi(r)$ to $X(r_*)$ (the motivation of doing so can be found in Ref. [48]) by

$$X(r_*(r)) = \chi(r)\sqrt{(r^2+a^2)\Delta^s}, \tag{4.13}$$

where an analytical expression of $r_*(r)$ can be obtained by integrating Eq. (4.7) (with a particular choice of the integration constant) such that the transformation from $r$ to $r_*$ is given by

$$r_*(r) = r + \frac{2r_+}{r_+ - r_-}\ln\left(\frac{r-r_+}{2}\right) - \frac{2r_-}{r_+ - r_-}\ln\left(\frac{r-r_-}{2}\right). \tag{4.14}$$

It should be noted that there is no simple analytical expression for the inverse transformation $r = r(r_*)$ and one has to invert $r_*$ numerically, typically using root-finding algorithms (for example see App. 4.6).

In short, the GSN transformation amounts to acting a linear differential operator ${}_s\Lambda$ on the Teukolsky radial function $R(r)$ that transforms it into the GSN function $X(r_*)$.[5] Schematically this means

$$X(r_*(r)) = {}_s\Lambda\left[R(r)\right]. \tag{4.15}$$

Using Eq. (4.9) and Eq. (4.13) we see that the ${}_s\Lambda$ operator is given by

$${}_s\Lambda\left[R(r)\right] = \sqrt{\left(r^2+a^2\right)\Delta^s}\left[\left(\alpha + \beta\Delta^{s+1}\frac{d}{dr}\right)R(r)\right]. \tag{4.16}$$

While the inverse GSN transformation amounts to acting the inverse operator ${}_s\Lambda^{-1}$ on the GSN function that gives back the Teukolsky function. Again, schematically this can be written as

$$R(r(r_*)) = {}_s\Lambda^{-1}\left[X(r_*)\right]. \tag{4.17}$$

[5] This is a generalization of the $\Lambda$ operator introduced in Ref. [40] for $s = -2$ to any integer $s$.

Using Eq. (4.11) and Eq. (4.13), we see that ${}_s\Lambda^{-1}$ is given by

$$
{}_s\Lambda^{-1}\left[X(r_*)\right] = \frac{1}{\eta}\left\{\left[\left(\alpha+\beta'\Delta^{s+1}\right)-\beta\Delta^{s+1}\frac{d}{dr}\right]\frac{X(r_*)}{\sqrt{\left(r^2+a^2\right)\Delta^s}}\right\}. \tag{4.18}
$$

Equipped with the transformation, one can show that by substituting $R(r), R'(r)$ given by Eq. (4.11) into Eq. (4.3), the intermediate function $\chi(r)$ satisfies the following ODE, which is given by [48]

$$
\Delta^{-s}\left(\Delta^{s+1}\chi'\right)' - \Delta F_1\chi' - U_1\chi = 0, \tag{4.19}
$$

with

$$
F_1(r) = \frac{\eta'}{\eta}, \tag{4.20}
$$

$$
U_1(r) = V_{\mathrm{T}} + \frac{1}{\beta\Delta^s}\left[\left(2\alpha+\beta'\Delta^{s+1}\right)' - F_1\left(\alpha+\beta'\Delta^{s+1}\right)\right]. \tag{4.21}
$$

Further rewriting Eq. (4.19) in terms of $X$ and its first and second derivatives with respect to $r_*$ using Eq. (4.13) and (4.7), one can show that $X(r_*)$ satisfies the GSN equation, which is given by [48]

$$
\frac{d^2X}{dr_*^2} - \mathcal{F}(r)\frac{dX}{dr_*} - \mathcal{U}(r)X = 0, \tag{4.22}
$$

with the GSN potentials $\mathcal{F}(r)$ and $\mathcal{U}(r)$ given by [48]

$$
\mathcal{F}(r) = \frac{\Delta F_1}{r^2+a^2}, \tag{4.23}
$$

$$
\mathcal{U}(r) = \frac{\Delta U_1}{\left(r^2+a^2\right)^2} + G^2 + \frac{\Delta G'}{r^2+a^2} - \frac{\Delta G F_1}{r^2+a^2}, \tag{4.24}
$$

where

$$
G = \frac{r\Delta}{\left(r^2+a^2\right)^2} + \frac{s(r-1)}{r^2+a^2}.
$$

While the GSN equation given by Eq. (4.22) looks significantly more complicated than the original radial Teukolsky equation given by Eq. (4.3), Eq. (4.22) actually represents *a collection of ODEs* equivalent to Eq. (4.3) that we can engineer so that the resulting ODE has a short-ranged potential and thus can be solved more easily and efficiently with numerical algorithms.

Up to this point, the weighting functions $\alpha(r)$ and $\beta(r)$ are arbitrary, apart from being continuous and differentiable (so that Eq. (4.9) and Eq. (4.11) make sense). However, in order to generate useful transformations, these functions have to satisfy certain criteria. For example, they can be constrained by requiring that when $a \to 0$, the function $X(r_*)$ satisfies the Regge-Wheeler equation [52, 53, 54, 48]. Transformations for fields with different spin-weight $s$ that satisfy such a constraint were first given in Ref. [48] and can be written in the form of

$$\chi = \begin{cases} \left(\sqrt{(r^2+a^2)\Delta}\right)^{|s|} g_0(r) J_- \left[ g_1(r) J_- \left[ g_2(r) \dots J_- \left[ g_{|s|}(r) \left( \dfrac{1}{\sqrt{r^2+a^2}} \right)^{|s|} R \right] \right] \right], & s < 0 \\ g_0(r) R, & s = 0 \ , \\ \left( \sqrt{\dfrac{r^2+a^2}{\Delta}} \right)^{s} g_0(r) J_+ \left[ g_1(r) J_+ \left[ g_2(r) \dots J_+ \left[ g_s(r) \left( \dfrac{\Delta}{\sqrt{r^2+a^2}} \right)^{s} R \right] \right] \right], & s > 0 \end{cases} \tag{4.25}$$

where $J_\pm$ are two linear differential operators defined by

$$J_\pm = \frac{d}{dr} \pm i \frac{K}{\Delta}. \tag{4.26}$$

Inspecting Eq. (4.25), we see that for a spin-$|s|$ field, the operator $J_\pm$ will act on $R(r)$ $|s|$-many times, leading to an expression relating $\chi(r)$ *linearly* to $R(r), R'(r), \dots, R^{(|s|)}(r)$. Higher-order derivatives $R^{(n)}(r)$ can be evaluated in terms of $R(r), R'(r)$ by using Eq. (4.10) successively for $n \geq 2$. Therefore, by comparing Eq. (4.9) and Eq. (4.25), one can extract the appropriate $\alpha(r)$ and $\beta(r)$ for different $s$ modulo some functions $g_i(r)$ that remain unspecified.

These functions $g_i(r)$ should reduce to non-vanishing constants when $a \to 0$ such that Eq. (4.22) is exactly the Regge-Wheeler equation for Schwarzschild BHs. In practice it was found that choosing $g_i(r)$ as simple rational functions of $r$ leads

to desirable short-ranged GSN potentials. With some particular choices of $g_i(r)$, which we explicitly show in App. 4.9 for fields with spin-weight $s = 0, \pm 1, \pm 2$, the expressions for $\alpha(r)$ and $\beta(r)$ can be quite concise, and we can write $\eta(r)$ in a compact form as

$$\eta(r) = c_0 + c_1/r + c_2/r^2 + c_3/r^3 + c_4/r^4. \tag{4.27}$$

It should be noted that if one chooses instead $g_i(r) = 1$, while the associated GSN potentials are still short-ranged, the corresponding expression for $\eta(r)$ *cannot* be written in the form of Eq. (4.27) and the weighting functions $\alpha(r)$ and $\beta(r)$ are long (except for $s = 0$).

### 4.2.2 Asymptotic behaviors and boundary conditions of the Generalized Sasaki-Nakamura equation

#### 4.2.2.1 Teukolsky equation

Before studying the asymptotic behaviors of the GSN equation, it is educational to first revisit the asymptotic behaviors of the radial Teukolsky equation so that we can compare the behaviors of the two equations and understand the reasons why it is preferred to use the GSN equation instead of the Teukolsky equation when performing numerical computations.

It can be shown that (for example see Refs. [42, 40]) when $r \to \infty$ ($r_* \to \infty$) the radial Teukolsky equation admits two (linearly-independent) asymptotic solutions that go like $R \sim r^{-1}e^{-i\omega r_*}$ or $R \sim r^{-(2s+1)}e^{i\omega r_*}$. Similarly, when $r \to r_+$ ($r_* \to -\infty$) the equation admits two (linearly-independent) asymptotic solutions $R \sim \Delta^{-s}e^{-ipr_*}$ or $R \sim e^{ipr_*}$, where we define a new wave frequency

$$p \equiv \omega - m\Omega_{\rm H}, \tag{4.28}$$

with $\Omega_{\rm H} \equiv a/(2r_+)$ being the angular velocity of the horizon (therefore intuitively speaking $p$ is the "effective" wave frequency near the horizon).

Using these asymptotic solutions at the two boundaries, we can construct pairs of linearly independent solutions. A pair that is commonly used in literature

(and is physically motivated) is $\left\{R^{\rm in}, R^{\rm up}\right\}$ with $R^{\rm in}$ satisfying a purely-ingoing boundary condition at the horizon and $R^{\rm up}$ satisfying a purely out-going boundary condition at infinity.[6] Mathematically,

$$R^{\rm in}(r) = \begin{cases} B^{\rm trans}_{\rm T}\Delta^{-s}e^{-ipr_*}, & r \to r_+ \\ B^{\rm inc}_{\rm T}\dfrac{e^{-i\omega r_*}}{r} + B^{\rm ref}_{\rm T}\dfrac{e^{i\omega r_*}}{r^{2s+1}}, & r \to \infty \end{cases}, \tag{4.29}$$

$$R^{\rm up}(r) = \begin{cases} C^{\rm ref}_{\rm T}\Delta^{-s}e^{-ipr_*} + C^{\rm inc}_{\rm T}e^{ipr_*}, & r \to r_+ \\ C^{\rm trans}_{\rm T}\dfrac{e^{i\omega r_*}}{r^{2s+1}}, & r \to \infty \end{cases}. \tag{4.30}$$

Here we follow mostly Ref. [38] in naming the coefficients/amplitudes in front of each of the asymptotic solutions (except renaming $C^{\rm up}$ in Ref. [38] to $C^{\rm inc}$ for a more symmetric form and adding a subscript T for Teukolsky formalism). These amplitudes carry physical interpretations. Conceptually for the $R^{\rm in}$ ($R^{\rm up}$) solution, imagine sending a "left-going" wave from infinity towards the horizon (a "right-going" wave from the horizon towards infinity)[7] with an amplitude $B^{\rm inc}_{\rm T}$ ($C^{\rm inc}_{\rm T}$). As the wave propagates through the potential barrier (see Fig. 4.1), part of the *inc*ident wave is *trans*mitted through the barrier and continues to travel with an amplitude $B^{\rm trans}_{\rm T}$ ($C^{\rm trans}_{\rm T}$), while part of the incident wave is *ref*lected by the barrier and travels in the opposite direction with an amplitude $B^{\rm ref}_{\rm T}$ ($C^{\rm ref}_{\rm T}$). This setup is reminiscent to a potential well problem in quantum mechanics.[8]

In numerical computations, however, instead of starting with an incident wave, it is easier to start with a transmitted wave, and then integrate outward (inward) for $R^{\rm in}$ ($R^{\rm up}$) to extract the corresponding incidence and reflection amplitude at

[6] In some literature, for example Ref. [48], $R^{\rm in}$ is also denoted by $R^{\rm H}$ and $R^{\rm up}$ also being denoted by $R^{\infty}$.

[7] As we have assumed a harmonic time dependence of $\exp(-i\omega t)$, radial functions of the form $\exp(i\omega r_*)$ are said to be traveling to the right since the waves would depend on the combination $t - r_*$. Similarly, for radial functions of the form $\exp(-i\omega r_*)$ they are said to be traveling to the left since the waves would depend on the combination $t + r_*$.

[8] However, unlike a potential well problem in quantum mechanics, the square of the reflection amplitude and the square of the transmission amplitude (each normalized by the incidence amplitude) does not have to add up to unity. This is known as super-radiance where energy is being extracted from the black hole.

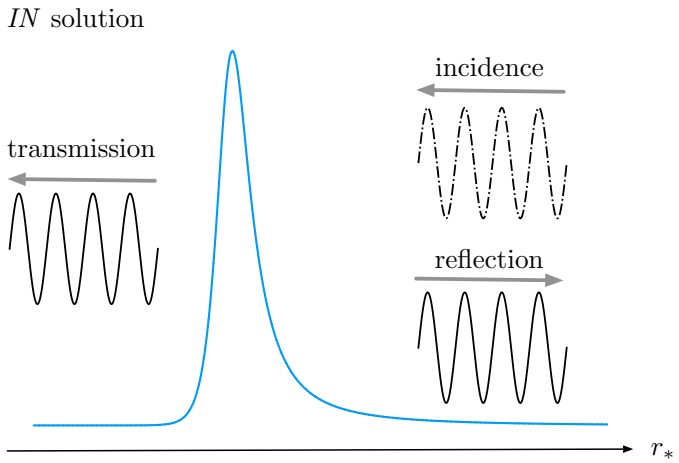


(a) IN solution

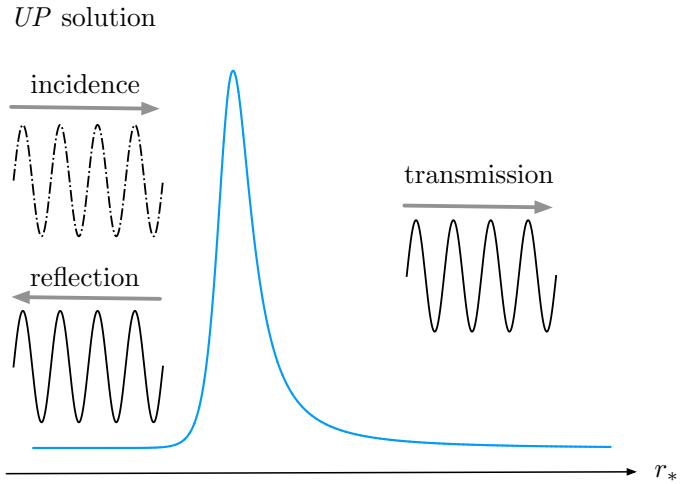


(b) UP solution

Figure 4.1: Physical interpretations of the amplitudes in front of each of the asymptotic solutions, for the *IN* solution (upper panel) and for the *UP* solution (lower panel).

infinity (at the horizon). Inspecting Eq. (4.29) and (4.30), we can see why it is challenging to accurately read off those amplitudes if one solves the Teukolsky equation numerically using Eq. (4.3) directly as the amplitude of the incident and the reflected wave are of different orders of magnitude. For the $R^{\text{in}}$ solution as

$r \to \infty$, the ratio of the amplitude of the right-going wave to that of the left-going wave is $\sim 1/r^{2s}$ (which becomes infinitely-large for $s < 0$ and infinitely-small for $s > 0$). While for the $R^{\rm up}$ solution as $r \to r_+$, that ratio is $\sim \Delta^s$ (which again becomes infinitely-large for $s < 0$ and infinitely-small for $s > 0$ as $\Delta \to 0$ when $r \to r_+$). This implies that when solving Eq. (4.3) numerically with a finite precision, the numerical solution will be completely dominated by the right-going wave and thus impossible to extract the amplitude for the left-going wave.

To see that $R^{\rm in}$ and $R^{\rm up}$ are indeed linearly independent, we can calculate the scaled Wronskian $\mathcal{W}_R$ of the two solutions, which is given by

$$\mathcal{W}_R = \Delta^{s+1}\left(R^{\rm in}R^{\rm up\prime} - R^{\rm up}R^{\rm in\prime}\right). \tag{4.31}$$

Substituting the asymptotic forms of the two solutions $R^{\rm in,up}$ in Eq. (4.29) and (4.30), respectively, when $r \to \infty$ gives the relation

$$\mathcal{W}_R = 2i\omega C_{\rm T}^{\rm trans} B_{\rm T}^{\rm inc}, \tag{4.32}$$

which is a non-zero constant[9] (when $\omega \neq 0$) and thus they are indeed linearly independent. If instead we substitute the asymptotic forms of $R^{\rm in,up}$ when $r \to r_+$ into Eq. (4.31), we obtain another relation for $\mathcal{W}_R$, which is

$$\mathcal{W}_R = \left[2ip(r_+^2 + a^2) + 2s(r_+ - 1)\right] B_{\rm T}^{\rm trans} C_{\rm T}^{\rm inc}. \tag{4.33}$$

By equating Eq. (4.32) and Eq. (4.33), we get an *identity* relating $(B_{\rm T}^{\rm inc}/B_{\rm T}^{\rm trans})$ with $(C_{\rm T}^{\rm inc}/C_{\rm T}^{\rm trans})$. From a numerical standpoint, we can use this identity as a sanity check of numerical solutions. More explicitly, the identity is given by

$$\frac{B_{\rm T}^{\rm inc}}{B_{\rm T}^{\rm trans}} = \frac{p(r_+^2 + a^2) - is(r_+ - 1)}{\omega}\frac{C_{\rm T}^{\rm inc}}{C_{\rm T}^{\rm trans}}. \tag{4.34}$$

It also means that we technically only need to read off $\left\{B_{\rm T}^{\rm ref}, B_{\rm T}^{\rm inc}, C_{\rm T}^{\rm ref}\right\}$ or $\left\{B_{\rm T}^{\rm ref}, C_{\rm T}^{\rm ref}, C_{\rm T}^{\rm inc}\right\}$ from numerical solutions since the rest of the amplitudes are

[9] Scaled Wronskians are by construction constants and are not functions of the independent variable. For more details, see App. 4.7.

either fixed by the normalization convention (which will be covered shortly below), or by the constant scaled Wronskian which can be computed at an arbitrary location within the domain of the numerical solutions.

#### 4.2.2.2 Generalized Sasaki-Nakamura equation

Now we turn to the GSN equation. Suppose the GSN transformation is of the form of Eq. (4.25) and satisfies Eq. (4.27), the GSN potentials $\mathcal{F}(r)$ and $\mathcal{U}(r)$ then have the following asymptotic behaviors (see Fig. 4.2 for a visualization)

$$\mathcal{F}(r) \sim \begin{cases} 0 + O(r - r_+) & r \to r_+ \\ \dfrac{-c_1/c_0}{r^2} + O(r^{-3}) & r \to \infty \end{cases}, \tag{4.35}$$

$$\mathcal{U}(r) \sim \begin{cases} -p^2 + O(r - r_+) & r \to r_+ \\ -\omega^2 + O(r^{-2}) & r \to \infty \end{cases}. \tag{4.36}$$

To see more clearly that the GSN potentials are indeed short-ranged, we recast the GSN equation into the same form as Eq. (4.6) by writing $Y \equiv X/\sqrt{\eta}$. Fig. 4.3 shows the magnitude of the potential $V_Y(r)$ associated with the Teukolsky equation (blue) and the GSN equation (orange), respectively. Specifically we are showing the potentials of the $s = -2, \ell = 2, m = 2$ mode with $a = 0.7$ and $\omega = 1$ as examples. We can see that the potential for the Teukolsky equation decays only at $1/r$ when $r \to \infty$ (and hence long-ranged) while the potential for the GSN equation decays at $1/r^2$ when $r \to \infty$ (and hence short-ranged).

The asymptotic behaviors of the GSN potentials imply that as $r \to r_+$, the GSN equation behaves like a simple wave equation $d^2X/dr_*^2 + p^2X = 0$, admitting simple plane-wave solutions $e^{\pm ipr_*}$. Similarly when $r \to \infty$, the GSN equation behaves like $d^2X/dr_*^2 + \omega^2X = 0$, again admitting plane-wave solutions $e^{\pm i\omega r_*}$. Therefore, we can similarly construct the pair of linearly-independent solutions $\{X^{\text{in}}, X^{\text{up}}\}$ that satisfies the purely-ingoing boundary condition at the horizon and the purely-outgoing boundary condition at infinity, respectively, using these

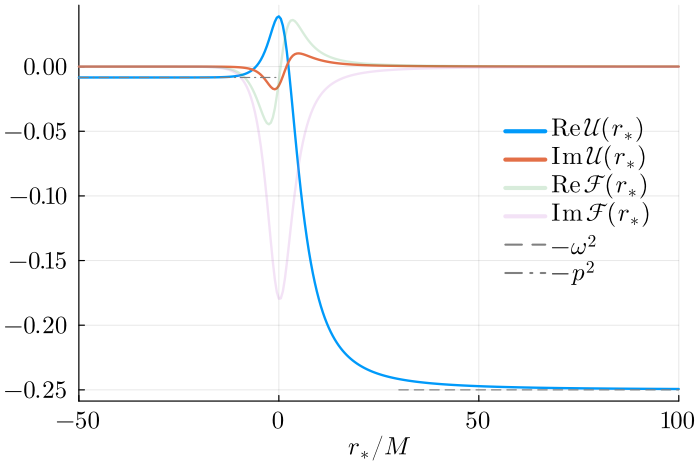


Figure 4.2: Asymptotic behaviors of the GSN potentials $\mathcal{F}(r)$ and $\mathcal{U}(r)$. Both potentials quickly approach to their corresponding asymptotic values. In particular, $\mathcal{U}(r)$ approaches to $-p^2$ near the horizon and $-\omega^2$ near infinity, respectively.

asymptotic solutions. Mathematically,

$$X^{\mathrm{in}}(r_*) = \begin{cases} B^{\mathrm{trans}}_{\mathrm{SN}} e^{-ipr_*} & r_* \to -\infty \\ B^{\mathrm{inc}}_{\mathrm{SN}} e^{-i\omega r_*} + B^{\mathrm{ref}}_{\mathrm{SN}} e^{i\omega r_*} & r_* \to \infty \end{cases}, \tag{4.37}$$

$$X^{\mathrm{up}}(r_*) = \begin{cases} C^{\mathrm{ref}}_{\mathrm{SN}} e^{-ipr_*} + C^{\mathrm{inc}}_{\mathrm{SN}} e^{ipr_*} & r_* \to -\infty \\ C^{\mathrm{trans}}_{\mathrm{SN}} e^{i\omega r_*} & r_* \to \infty \end{cases}. \tag{4.38}$$

Here the amplitudes in front of each of the asymptotic solutions have the same physical interpretations as in Eq. (4.29) and (4.30) (c.f. Fig. 4.1). Again by inspecting Eq. (4.37) and (4.38), we can see that it is easy to accurately read off those amplitudes as the ratio of the asymptotic amplitude of the incident wave to that of the reflected wave at both boundaries is $\sim \mathcal{O}(1)$, instead of being infinitely-large or infinitely-small in the Teukolsky formalism.

Similar to the case of Teukolsky functions, we can also define a scaled Wronskian

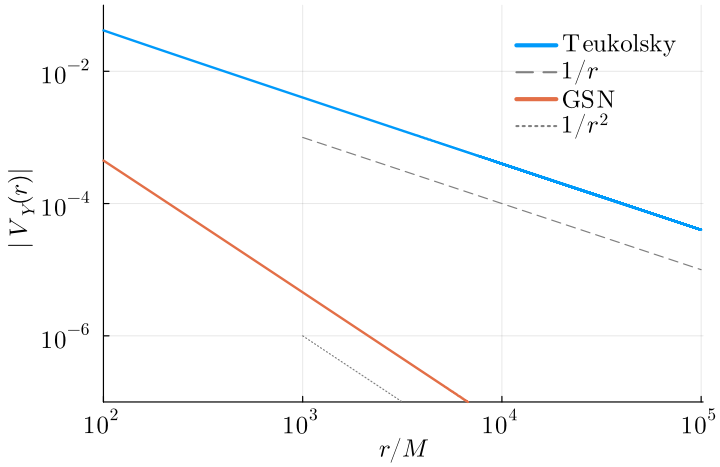


Figure 4.3: Potential $V_Y(r)$ associated with the Teukolsky equation and the GSN equation. As $r \to \infty$, the potential for the Teukolsky equation decays at $1/r$ and thus it is long-ranged, while the potential for the GSN equation decays at a steeper $1/r^2$ and hence it is short-ranged.

$\mathcal{W}_X$ for the GSN functions, namely

$$\mathcal{W}_X = \frac{1}{\eta}\left[X^{\rm in}(dX^{\rm up}/dr_*) - (dX^{\rm in}/dr_*)X^{\rm up}\right], \tag{4.39}$$

which is also a constant. Substituting the asymptotic forms of $X^{\rm in,up}$ in Eq. (4.37) and (4.38), respectively, as $r_* \to \infty$, and the fact that $\eta(r) \to c_0$ as $r \to \infty$, it can be shown that

$$\mathcal{W}_X = \frac{2i\omega C^{\rm trans}_{\rm SN} B^{\rm inc}_{\rm SN}}{c_0}. \tag{4.40}$$

Equivalently, we can also use the asymptotic forms of $X^{\rm in,up}$ as $r_* \to -\infty$, and the fact that $\eta(r \to r_+) \sim \mathcal{O}(1)$ to show that

$$\mathcal{W}_X = \frac{2ipB^{\rm trans}_{\rm SN} C^{\rm inc}_{\rm SN}}{\eta(r_+)}, \tag{4.41}$$

We can again equate Eq. (4.40) and Eq. (4.41) to get an *identity* relating $B^{\rm inc}_{\rm SN}/B^{\rm trans}_{\rm SN}$ with $C^{\rm inc}_{\rm SN}/C^{\rm trans}_{\rm SN}$ to check the sanity of numerical solutions. Explicitly, the identity

is given by

$$\frac{B_{\rm SN}^{\rm inc}}{B_{\rm SN}^{\rm trans}} = \frac{pc_0}{\omega\eta(r_+)}\frac{C_{\rm SN}^{\rm inc}}{C_{\rm SN}^{\rm trans}}. \tag{4.42}$$

An interesting and useful relation between the scaled Wronskians for GSN functions $\mathcal{W}_X$ and that for Teukolsky functions $\mathcal{W}_R$ (with the same $s, \ell, m, a, \omega$) is that despite having different definitions (see Eq. (4.31) for $\mathcal{W}_R$ and Eq. (4.39) for $\mathcal{W}_X$), they are actually *identical*, i.e.,

$$\mathcal{W}_X = \mathcal{W}_R, \tag{4.43}$$

where we give a derivation in App. 4.7. This means that GSN transformations (not limited only to our particular choices of $g_i$) are scaled-Wronskian-preserving. This also means that one can compute the QNM spectra of Kerr BHs using either the Teukolsky formalism or the GSN formalism (see Sec. 4.4.2).

Since one can freely rescale a homogeneous solution by a constant factor, we use this freedom to set $B_{\rm SN}^{\rm trans} = C_{\rm SN}^{\rm trans} = 1$, i.e., we *normalize* our solutions to the GSN equation to have a unit SN transmission amplitude. However, the common normalization convention in literature is to normalize $R^{\rm in}(r)$ and $R^{\rm up}(r)$ to each have a unit transmission amplitude, i.e., $B_{\rm T}^{\rm trans} = C_{\rm T}^{\rm trans} = 1$. In fact, one can relate incidence/reflection/transmission amplitudes in the GSN formalism to that in the Teukolsky formalism and vice versa by frequency-dependent conversion factors. To see why this is the case and to obtain the conversion factors, note that when going from a Teukolsky function to the corresponding GSN function, we have the ${}_s\Lambda$ operator that satisfies

$${}_s\Lambda\left[f(r)e^{\pm ikr_*}\right] \propto e^{\pm ikr_*}, \tag{4.44}$$

and vice versa with the inverse operator ${}_s\Lambda^{-1}$ that satisfies

$${}_s\Lambda^{-1}\left[f(r)e^{\pm ikr_*}\right] \propto e^{\pm ikr_*}, \tag{4.45}$$

for any differentiable function $f(r)$ and $k$ is any non-zero constant, since both ${}_s\Lambda$ and ${}_s\Lambda^{-1}$ are linear differential operators. This means that we can simply match

the asymptotic solution in one formalism with the corresponding asymptotic solution with the *same* exponential dependence in another formalism transformed by either ${}_s\Lambda$ or ${}_s\Lambda^{-1}$ at the appropriate boundary.

For example, to get the conversion factor $C_{\rm T}^{\rm trans}/C_{\rm SN}^{\rm trans}$, we match the asymptotic solution as $r \to \infty$ for the Teukolsky and the GSN formalism like

$$C_{\rm SN}^{\rm trans}\left[1+\mathcal{O}\left(\frac{1}{r}\right)\right]e^{i\omega r_*} \quad = \quad C_{\rm T}^{\rm trans}\,{}_s\Lambda\left\{\frac{1}{r^{2s+1}}\left[1+\mathcal{O}\left(\frac{1}{r}\right)\right]e^{i\omega r_*}\right\}, \quad (4.46)$$

where the expression on the RHS, to the leading order, should be $\sim \mathcal{O}\,(1)\,e^{i\omega r_*}$. We can then obtain the desired conversion factor by taking the limit as

$$\frac{C_{\rm SN}^{\rm trans}}{C_{\rm T}^{\rm trans}} = \lim_{r\to\infty}{}_s\Lambda\left\{\frac{1}{r^{2s+1}}\left[1+\mathcal{O}\left(\frac{1}{r}\right)\right]e^{i\omega r_*}\right\}e^{-i\omega r_*}, \quad (4.47)$$

and we know that the expression on the RHS does not depend on $e^{\pm i\omega r_*}$ using Eq. (4.44) so that the limit could be determinate. Equivalently, we can also match the asymptotic solution as $r \to \infty$ in the two formalism like this instead

$$C_{\rm T}^{\rm trans}\frac{1}{r^{2s+1}}\left[1+\mathcal{O}\left(\frac{1}{r}\right)\right]e^{i\omega r_*} \quad = \quad C_{\rm SN}^{\rm trans}\,{}_s\Lambda^{-1}\left\{\left[1+\mathcal{O}\left(\frac{1}{r}\right)\right]e^{i\omega r_*}\right\}, \quad (4.48)$$

where the expression on the RHS, to the leading order, should be $\sim \mathcal{O}\,(1)\,r^{-(2s+1)}e^{i\omega r_*}$. Similarly we can obtain

$$\frac{C_{\rm T}^{\rm trans}}{C_{\rm SN}^{\rm trans}} = \lim_{r\to\infty}{}_s\Lambda^{-1}\left\{\left[1+\mathcal{O}\left(\frac{1}{r}\right)\right]e^{i\omega r_*}\right\}r^{2s+1}e^{-i\omega r_*}, \quad (4.49)$$

and again we know that the RHS of the expression does not depend on $e^{\pm i\omega r_*}$ using Eq. (4.45) so that the limit could be determinate.

We find that sometimes it is more convenient to compute the limit in the form of Eq. (4.47) than to use the limit in the form of Eq. (4.49) in order to find the same conversion factor, and in some cases the reverse is true even though formally both expressions should give the same answer. In fact, using the identity between the

scaled Wronskian of the GSN functions $\mathcal{W}_X$ and that of the Teukolsky functions $\mathcal{W}_R$, we can simplify expressions for these conversion factors by equating expressions of $\mathcal{W}_X$ in terms of the incidence and transmission amplitudes in the GSN formalism with expressions of $\mathcal{W}_R$ in terms of those amplitudes in the Teukolsky formalism. In particular, we get identities relating these conversion factors as

$$\frac{C_{\rm T}^{\rm trans}}{C_{\rm SN}^{\rm trans}}\frac{B_{\rm T}^{\rm inc}}{B_{\rm SN}^{\rm inc}} = \frac{1}{c_0}, \tag{4.50}$$

$$\frac{B_{\rm T}^{\rm trans}}{B_{\rm SN}^{\rm trans}}\frac{C_{\rm T}^{\rm inc}}{C_{\rm SN}^{\rm inc}} = \frac{2ip}{\eta(r_+)\left[2ip(r_+^2+a^2)+2s(r_+-1)\right]}. \tag{4.51}$$

These identities imply that we only need to derive either $\dfrac{C_{\rm T}^{\rm trans}}{C_{\rm SN}^{\rm trans}}$ or $\dfrac{B_{\rm T}^{\rm inc}}{B_{\rm SN}^{\rm inc}}$ and either $\dfrac{B_{\rm T}^{\rm trans}}{B_{\rm SN}^{\rm trans}}$ or $\dfrac{C_{\rm T}^{\rm inc}}{C_{\rm SN}^{\rm inc}}$.

#### 4.2.2.3 Higher-order corrections to asymptotic behaviors

In Eq. (4.37) and (4.38), we use the asymptotic solutions of the GSN equation only to their leading order (i.e., $O(r^0)$). However, in order to obtain accurate numerical solutions solved on a numerically-finite interval (e.g., $\left[r_*^{\rm in}, r_*^{\rm out}\right]$), it is more efficient to include higher-order corrections to the asymptotic solutions than to simply set $r_*^{\rm in}$ as a small number and $r_*^{\rm out}$ as a large number. To find such higher-order corrections, we use an ansatz of the form

$$X(r_*) \sim \begin{cases} f_\pm^\infty(r)e^{\pm i\omega r_*}, & r_* \to \infty \\ g_\pm^{\rm H}(r)e^{\pm ipr_*}, & r_* \to -\infty \end{cases}, \tag{4.52}$$

where the plus (minus) sign corresponds to the out/right-going (in/left-going) mode, and the superscript $\infty$ (H) corresponds to the outer (inner) boundary at infinity (the horizon). Substituting Eq. (4.52) back to the GSN equation in Eq. (4.22), we get *four* second-order ODEs for each of the functions $f_\pm^\infty(r)$ and

$g^{\rm H}_{\pm}(r)$ (c.f. Eq. (4.89)). We look for their *formal series expansions* of the form

$$f^{\infty}_{\pm}(r) = \sum_{j=0}^{\infty} \frac{C^{\infty}_{\pm,j}}{(\omega r)^j}, \tag{4.53}$$

$$g^{\rm H}_{\pm}(r) = \sum_{j=0}^{\infty} C^{\rm H}_{\pm,j} \left[\omega(r - r_+)\right]^j , \tag{4.54}$$

where $C^{\infty/{\rm H}}_{\pm,j}$ are the expansion coefficients. In App. 4.8, we show how one can compute these coefficients using recurrence relations. Such recurrence relations for some of the spin weights ($s = 0$ and $s = -2$) can also be found in literature (e.g., Refs. [59, 60, 61]).[10] In App. 4.9, we show explicitly the expressions of the expansion coefficients $C^{\infty}_{\pm,j}$ for $j = 0, 1, 2, 3$.

With the explicit GSN transformation and hence the GSN potentials and the GSN equation as discussed in Sec. 4.2.1, as well as the asymptotic solutions to the GSN equation and the conversion factors for converting asymptotic amplitudes between the Teukolsky and the GSN formalism as discussed in Sec. 4.2.2, we now have all the necessary ingredients to use the GSN formalism to perform numerical computations. In the next section, we describe the recipes to use those ingredients to get homogenous solutions to both the Teukolsky and the GSN equation.

## 4.3 Numerical implementation

In principle, a frequency-domain Teukolsky/GSN equation solver can be implemented in any programming language with the help of the ingredients in Sec. 4.2 and App. 4.9. Here we describe an open-source implementation of the GSN formalism that is written in `julia` [56], namely `GeneralizedSasakiNakamura.jl`.[11] Instead of fixing a particular choice of an numerical integrator for

[10] Unfortunately the expansion coefficients given in Refs. [48] are incorrect except for the case with $s = 0$ because the author made an incorrect assumption that the GSN potentials are purely real, which is not true in general.

[11] `https://github.com/ricokaloklo/GeneralizedSasakiNakamura.jl`

solving Eq. (4.22), the code can be used in conjunction with other `julia` packages, such as `DifferentialEquations.jl` [62], which implements a suite of ODE solvers. The GSN potentials $\mathcal{F}(r), \mathcal{U}(r)$ for $s = 0, \pm 1, \pm 2$ are implemented as pure functions in `julia`, and can be evaluated to arbitrary precision. This also allows us to use automatic differentiation (AD) to compute corrections to the asymptotic boundary conditions at arbitrary order (see App. 4.8).[12]

### 4.3.1 Numerical solutions to the Generalized Sasaki-Nakamura equation

#### 4.3.1.1 Rewriting Generalized Sasaki-Nakamura functions as complex phase functions

Instead of solving directly for the GSN function $X(r_*)$, we follow Ref. [65] and introduce a complex phase function $\Phi(r_*)$ such that

$$X(r_*) \equiv \exp\left[i\Phi\left(r_*\right)\right] . \tag{4.55}$$

Substituting Eq. (4.55) into Eq. (4.22), we obtain a *first-order non-linear* differential equation[13] as

$$\frac{d}{dr_*}\left(\frac{d\Phi}{dr_*}\right) = -i\,\mathcal{U} + \mathcal{F}\left(\frac{d\Phi}{dr_*}\right) - i\left(\frac{d\Phi}{dr_*}\right)^2 . \tag{4.56}$$

[12] In particular, we use two variants of AD. The first type is referred to as the forward-mode AD as implemented in `ForwardDiff.jl` [63]. However, the computational cost of using the forward-mode AD to compute higher-order derivatives scales exponentially with the order. Therefore, for computing corrections to the asymptotic boundary conditions we switch to the second type, which is based on Taylor expansion as implemented in `TaylorSeries.jl` [64], where the cost only scales linearly with the order of the derivatives.

[13] Unlike what was claimed in App. 3 of Ref. [65], we find that the ODE for *both* the real and the imaginary part of $\Phi$ can be integrated immediately to first-order (non-linear) differential equations in $(d\Phi_{\rm Re}/dr_*, d\Phi_{\rm Im}/dr_*)$, which is expected since solutions to a homogeneous ODE are determined only up to a multiplicative factor. Combining the differential equations for $d\Phi_{\rm Re}/dr_*$ and $d\Phi_{\rm Im}/dr_*$ such that $d\Phi/dr_* = (d\Phi_{\rm Re}/dr_* + i d\Phi_{\rm Im}/dr_*)$ will give Eq. (4.56).

Such a differential equation is also known as a Riccati equation. Furthermore, the conversion between $(X, dX/dr_*)$ and $(\Phi, d\Phi/dr_*)$ is given by

$$\Phi = -i \log(X), \tag{4.57}$$

$$\frac{d\Phi}{dr_*} = -i\frac{dX/dr_*}{X}. \tag{4.58}$$

While at first glance it may seem unwise to turn a linear problem into a non-linear problem, solving Eq. (4.56) numerically presents no additional challenge compared to solving directly Eq. (4.22). In fact, there are advantages in writing the GSN function in the form of Eq. (4.55), especially when $|\omega|$ is large. Recall that asymptotically (both near infinity and near the horizon) GSN functions behave like plane waves, i.e., $X$ oscillates like $\exp(\pm ikr_*)$ where $|k|$ is the oscillation frequency (assuming $k$ is real, and recall that $|k| \to |\omega|$ when $r_* \to \infty$ and $|k| \to |p|$ when $r_* \to -\infty$). Therefore, in order to properly resolve the oscillations, the step size $\delta r_*$ for the numerical integrator needs to be much less than the wavelength, i.e., $\delta r_* \ll 1/|k|$. This can get quite small for large $|k|$, which results in taking a longer time to integrate Eq. (4.22) for a fixed accuracy.

Fortunately this is not the case when solving for the complex phase function $\Phi(r_*)$ since it is varying much slower (spatially) than the GSN function $X(r_*)$. Intuitively this is because the complex exponential in Eq. (4.55) accounts for most of the oscillatory behaviors. This is especially true if we consider the asymptotic plane-wave-like solutions of the GSN equation, where the real part of the phase function $\Phi_{\mathrm{Re}}(r_*) \sim kr_*$ is linear in $r_*$, and the imaginary part of the phase function $\Phi_{\mathrm{Im}}(r_*)$ is constant in $r_*$.

However, this might not be the case when we consider general solutions to the GSN equation where the left-going and the right-going modes are superimposed, for example the $X^{\mathrm{in,up}}$ pair as shown in Eq. (4.37) and Eq. (4.38). That being said, the variation of the complex phase function due to the beating or interference between the left-/right-going modes depends on their relative amplitude (which is in general a complex number and hence introduces a phase shift). In particular,

physically Kerr BHs are *much more* permeable to waves at high frequencies (see Fig. 4.6). This means that at those high frequencies, the relative amplitudes of the left-/right-going modes are going to be extreme and hence the beating will be suppressed.

#### 4.3.1.2 Solving $X^{\rm in,up}$ as initial value problems

Recall that there is a pair of linearly-independent solutions to the GSN equation that is of particular interest, namely $\left\{X^{\rm in}, X^{\rm up}\right\}$, where $X^{\rm in}$ satisfies the boundary condition that it is purely in-going at the horizon as given by Eq. (4.37), and $X^{\rm up}$ satisfies the boundary condition that it is purely out-going at infinity as given by Eq. (4.38), respectively.

Despite the usage of the term "boundary condition", what we are really enforcing is *the asymptotic form of a solution at one of the two boundaries*, $X^{\rm in}$ at the horizon and $X^{\rm up}$ at infinity, respectively. This can be formulated as an initial value problem. Explicitly for $\hat{X}^{\rm in}$, where a hat denotes a numerical solution hereafter, we integrate Eq. (4.56) outwards from the (finite) inner boundary $r_*^{\rm in}$ to the (finite) outer boundary $r_*^{\rm out}$ with

$$\hat{X}(r_*^{\rm in}) = g_-^{\rm H}\left(r(r_*^{\rm in})\right) e^{-ipr_*^{\rm in}}, \tag{4.59}$$

$$\frac{d\hat{X}(r_*^{\rm in})}{dr_*} = -ip\hat{X}(r_*^{\rm in}) + \frac{dr}{dr_*}\frac{dg_-^{\rm H}(r)}{dr}\bigg|_{r=r(r_*^{\rm in})} e^{-ipr_*^{\rm in}}, \tag{4.60}$$

as the initial values at $r_* = r_*^{\rm in}$ after converting them to $\hat{\Phi}^{\rm in}$ and $d\hat{\Phi}^{\rm in}/dr_*$ using Eq. (4.57) and Eq. (4.58), respectively. Similarly for $\hat{X}^{\rm up}$, we integrate Eq. (4.56) inwards from the outer boundary $r_*^{\rm out}$ to the inner boundary $r_*^{\rm in}$ with

$$\hat{X}(r_*^{\rm out}) = f_+^{\infty}\left(r(r_*^{\rm out})\right) e^{i\omega r_*^{\rm out}}, \tag{4.61}$$

$$\frac{d\hat{X}(r_*^{\rm out})}{dr_*} = i\omega\hat{X}(r_*^{\rm out}) + \frac{dr}{dr_*}\frac{df_+^{\infty}(r)}{dr}\bigg|_{r=r(r_*^{\rm out})} e^{i\omega r_*^{\rm out}}, \tag{4.62}$$

as the initial values at $r_* = r_*^{\rm out}$ after converting them to $\hat{\Phi}^{\rm up}$ and $d\hat{\Phi}^{\rm up}/dr_*$ using again Eq. (4.57) and Eq. (4.58) respectively. Note that for both $\hat{X}^{\rm in}$ and $\hat{X}^{\rm up}$, we

have chosen the normalization convention of a unit transmission amplitude, i.e., $B_{\rm SN}^{\rm trans} = C_{\rm SN}^{\rm trans} = 1$. After solving Eq. (4.56) numerically for a complex phase function $\hat{\Phi}(r_*)$ and its derivative $d\hat{\Phi}/dr_*$ on a grid of $r_* \in [r_*^{\rm in}, r_*^{\rm out}]$, we first convert them back to $\hat{X}$ and $d\hat{X}/dr_*$ using Eq. (4.55) and Eq. (4.58), respectively.

#### 4.3.1.3 Transforming Generalized Sasaki-Nakamura functions to Teukolsky functions

In principle, if we want to transform a GSN function $\hat{X}$ back to a Teukolsky function, we simply need to apply the inverse operator ${}_s\Lambda^{-1}$ on the numerical GSN function. Since we have the numerical solutions to both $\hat{X}$ and $d\hat{X}/dr_*$, the inverse operator can actually be written as a matrix multiplication to the column vector $\left(\hat{X}, d\hat{X}/dr_*\right)^T$.

First, consider the conversion from $\left(\hat{X}, d\hat{X}/dr_*\right)^T$ to $\left(\hat{X}, \hat{X}'\right)^T$. This can be done by left-multiplying the column vector with the matrix

$$M_1 = \begin{pmatrix} 1 & 0 \\ 0 & \dfrac{r^2+a^2}{\Delta} \end{pmatrix}. \tag{4.63}$$

Next, consider the transformation from $\left(\hat{X}, \hat{X}'\right)^T$ to $(\hat{\chi}, \hat{\chi}')^T$ using Eq. (4.13). Again this can be done by left-multiplying the column vector $\left(\hat{X}, \hat{X}'\right)^T$ by the matrix

$$M_2 = \begin{pmatrix} \dfrac{1}{\sqrt{\left(r^2+a^2\right)\Delta^s}} & 0 \\ \left(\dfrac{1}{\sqrt{\left(r^2+a^2\right)\Delta^s}}\right)' & \dfrac{1}{\sqrt{\left(r^2+a^2\right)\Delta^s}} \end{pmatrix}. \tag{4.64}$$

At last, the transformation from $(\hat{\chi}, \hat{\chi}')^T$ to $(R, R')^T$ is given by the matrix equation as shown in Eq. (4.11), where we now explicitly define the matrix as

$$M_3 = \frac{1}{\eta} \begin{pmatrix} \alpha + \beta' \Delta^{s+1} & -\beta \Delta^{s+1} \\ -(\alpha' + \beta V_{\rm T} \Delta^s) & \alpha \end{pmatrix}. \tag{4.65}$$

The overall transformation from $\hat{X}$ and $d\hat{X}/dr_*$ to $R$ and $R'$ is thus given by the matrix equation

$$\begin{pmatrix} \hat{R} \\ \hat{R}' \end{pmatrix} = M_3 M_2 M_1 \begin{pmatrix} \hat{X} \\ \dfrac{d\hat{X}}{dr_*} \end{pmatrix}. \tag{4.66}$$

By multiplying $\left(\hat{X}, d\hat{X}/dr_*\right)^T$ with the overall transformation matrix $M_3 M_2 M_1$ that we explicitly simplified in order to facilitate cancellations between terms. This allows us to accurately convert numerical GSN functions to Teukolsky functions close to the horizon ($\Delta \to 0$) when some of the terms, such as $\alpha(r)$, diverge near the horizon.

### 4.3.2 Extracting incidence and reflection amplitudes from numerical solutions

Apart from evaluating a GSN or a Teukolsky function numerically on a grid of $r$- or $r_*$-coordinates, it is also useful to be able to determine the incidence and the reflection amplitude at a particular frequency $\omega$ (see Sec. 4.2.2 for a theoretical discussion) from a numerical solution accurately. This is essential for constructing inhomogeneous solutions using the Green's function method (e.g., calculating gravitational waveforms observed at infinity) and for scattering problems (e.g., calculating the greybody factor of a BH as a function of the wave frequency $\omega$).

Since we only have numerical solutions on a finite grid of $r_* \in [r_*^{\rm in}, r_*^{\rm out}]$, in order to determine the reflection amplitude $\hat{B}^{\rm ref}_{\rm SN}$ and the incidence amplitude $\hat{B}^{\rm inc}_{\rm SN}$ of a $\hat{X}^{\rm in}$ solution in the GSN formalism we solve the system of linear equations at the outer boundary $r_*^{\rm out}$ that

$$\begin{pmatrix} f_+^\infty(r)e^{i\omega r_*} & f_-^\infty(r)e^{-i\omega r_*} \\ (df_+^\infty/dr_* + i\omega f_+^\infty)e^{i\omega r_*} & (df_-^\infty/dr_* - i\omega f_-^\infty)e^{-i\omega r_*} \end{pmatrix}\Bigg|_{r_*^{\rm out}} \begin{pmatrix} \hat{B}^{\rm ref}_{\rm SN} \\ \hat{B}^{\rm inc}_{\rm SN} \end{pmatrix} = \begin{pmatrix} \hat{X}^{\rm in} \\ \dfrac{d\hat{X}^{\rm in}}{dr_*} \end{pmatrix}\Bigg|_{r_*^{\rm out}}, \tag{4.67}$$

where we impose continuity of the numerical solution $(\hat{X}^{\rm in}, d\hat{X}^{\rm in}/dr_*)$ with the analytical asymptotic solution near infinity at $r_* = r_*^{\rm out}$. Similarly, we use the same scheme to determine the reflection amplitude $\hat{C}^{\rm ref}_{\rm SN}$ and the incidence amplitude $\hat{C}^{\rm inc}_{\rm SN}$ of a $\hat{X}^{\rm up}$ solution in the GSN formalism at the inner boundary $r_*^{\rm in}$ by solving

$$\begin{pmatrix} g_+^{\rm H}(r)e^{ipr_*} & g_-^{\rm H}(r)e^{-ipr_*} \\ (dg_+^{\rm H}/dr_* + ipg_+^{\rm H})e^{ipr_*} & (dg_-^{\rm H}/dr_* - ipg_-^{\rm H})e^{-ipr_*} \end{pmatrix}\Bigg|_{r_*^{\rm in}} \begin{pmatrix} \hat{C}^{\rm inc}_{\rm SN} \\ \hat{C}^{\rm ref}_{\rm SN} \end{pmatrix} = \begin{pmatrix} \hat{X}^{\rm up} \\ \dfrac{d\hat{X}^{\rm up}}{dr_*} \end{pmatrix}\Bigg|_{r_*^{\rm in}}, \tag{4.68}$$

where again we impose continuity of the numerical solution $(\hat{X}^{\rm up}, d\hat{X}^{\rm up}/dr_*)$ to the asymptotic solution near the horizon at $r_* = r_*^{\rm in}$.[14]

Indeed, the inclusion of the higher-order corrections $f_\pm^\infty$ at the outer boundary and $g_\pm^{\rm H}$ at the inner boundary, respectively, allow us to get very good agreements on the incidence and the reflection amplitudes over a range of frequencies with the MST method, which we will show in the next sub-section.

### 4.3.3 Numerical results

Here we showcase some numerical results obtained using our `GeneralizedSasakiNakamura.jl` implementation. Unless otherwise specified, we use the ODE solver `Vern9` [66] as implemented in `DifferentialEquations.jl` [62], and we include corrections to the asymptotic solutions at infinity up to the third order (i.e., truncating the sum in Eq. (4.53) at $j = 3$) and that at the horizon only to the zeroth order (i.e., taking only the leading term $j = 0$ in the sum in

[14] This matching procedure at the two numerical boundaries actually allows us to obtain "semi-analytical" GSN functions (and by extension Teukolsky functions) that are *accurate everywhere*, even outside the grid $[r_*^{\rm in}, r_*^{\rm out}]$. Using $X^{\rm in}$ as an example, for $r_* < r_*^{\rm in}$ the analytical ansatz $g_-^{\rm H}(r(r_*))e^{-ipr_*}$ can be used. This is because the numerical solution $\hat{X}^{\rm in}$ was constructed by using that ansatz to compute the appropriate initial conditions. While for $r_* > r_*^{\rm out}$, the linear combination of the analytical ansatzes $\hat{B}^{\rm ref}_{\rm SN} f_+^\infty(r(r_*))e^{i\omega r_*} + \hat{B}^{\rm inc}_{\rm SN} f_-^\infty(r(r_*))e^{-i\omega r_*}$ can be used, where the reflection and the incidence coefficient were constructed to ensure continuity with the numerical solution.

Eq. (4.54)). We set the numerical inner boundary at $r_*^{\rm in} = -50M$[15] and the outer boundary at $r_*^{\rm out} = 1000M$. We use double-precision floating-point numbers throughout, and both the "absolute tolerance" `abstol` (roughly the error around the zero point) and the "relative tolerance" `reltol` (roughly the local error) passed to the numerical ODE solver are set to $10^{-12}$.

#### 4.3.3.1 Numerical solutions

Fig. 4.4 shows the IN solution in the GSN formalism of the $s = -2, \ell = 2, m = 2$ mode for a BH with $a/M = 0.7$ and two different values of $\omega$, in terms of the GSN function $X$ and the complex frequency function $d\Phi/dr_*$. Recall that for an IN solution, it is purely in-going at the horizon. We see from the figure that for both $M\omega = 0.5$ (upper panel) and $M\omega = 1$ (lower panel), near the horizon, $d\hat{\Phi}/dr_*$ is flat and approaches to the imposed asymptotic value $-p^2$, while $\hat{X}$ is oscillating with the frequency $p$. On the other hand when $r_* \to \infty$, the IN solution is an admixture of the left- and the right-going modes where their relative amplitude, $B^{\rm ref}_{\rm SN}/B^{\rm inc}_{\rm SN}$, is $\omega$-dependent. We see from Fig. 4.4a that both $\hat{X}$ and $d\hat{\Phi}/dr_*$ exhibit oscillatory behaviors, and that the oscillation frequency for $d\hat{\Phi}/dr_*$ from beating is twice of that for $\hat{X}$. While we see from Fig. 4.4b that $\hat{X}$ is oscillatory but $d\hat{\Phi}/dr_*$ is flat as the ratio of the left- and right-going mode is extreme and hence beating is heavily suppressed.

This can be more easily seen in Fig. 4.5 where it shows the first derivative of the numerical IN solutions $d\hat{\Phi}/dr_*$, i.e., $d^2\hat{\Phi}/dr_*^2$, as indicators of how much they change locally as functions of $r_*$, for both the $M\omega = 0.5$ and the $M\omega = 1$ case. We compute the numerical derivatives using AD on the interpolant of the numerical solutions of $d\hat{\Phi}/dr_*$ to avoid issues with using a finite difference method. We see from the upper panel (Fig. 4.5a) that for $M\omega = 0.5$ the oscillation in $d\hat{\Phi}/dr_*$ is significant, while for $M\omega = 1$ we can see from the lower panel (Fig. 4.5b) that

[15] More concretely, this corresponds to $\left(r^{\rm in} - r_+\right)/M \approx 8 \times 10^{-10}$ when $a/M = 0.7$. This difference is a monotonically increasing function in $|a|/M$ (for a similar discussion but for $r_*/M = 0$, see Fig. 4.12).

the oscillation is much more minute. Note that the two panels have very different scales for their $y$-axes.

Physically this boils down to the fact that the potential barriers of a Kerr BH for different types of radiation are all very permeable to waves at high frequencies. Fig. 4.6 shows the reflectivity of the potential barriers (for $s = 0, \pm 1, \pm 2$ with $a/M = 0.7$) as defined by $B^{\rm ref}_{\rm SN}/B^{\rm inc}_{\rm SN}$. This ratio compares the wave amplitude $B^{\rm ref}_{\rm SN}$ that is reflected off the potential barrier when a wave with an asymptotic amplitude $B^{\rm inc}_{\rm SN}$ is approaching the barrier from infinity. We see from Fig. 4.6 that the reflectivities become zero when the wave frequency gets large (while we only show for the $a/M = 0.7$ case, the same is true for other values of $a/M$ as well). A low reflectivity means that the ratio of the left- and the right-going mode is going to be extreme. Explicitly for the case in Fig. 4.6, the right-going mode has an amplitude $|B^{\rm ref}_{\rm SN}|$ that is much smaller than the left-going mode $|B^{\rm inc}_{\rm SN}|$ when $M\omega \gtrsim 1$. The lack of beating in Fig. 4.4b is a manifestation of this fact.

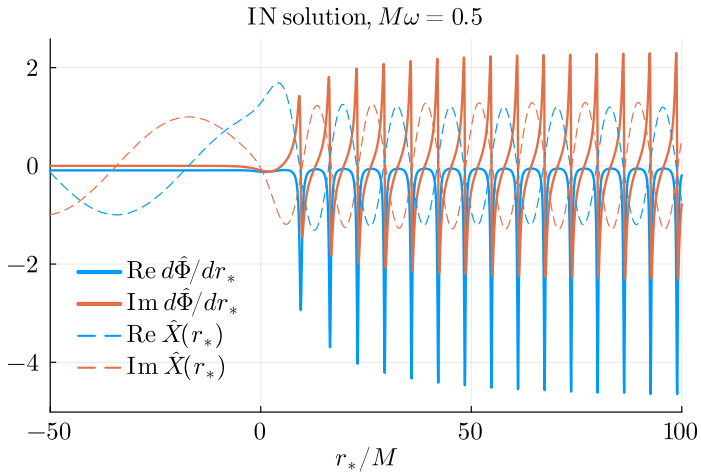


(a)

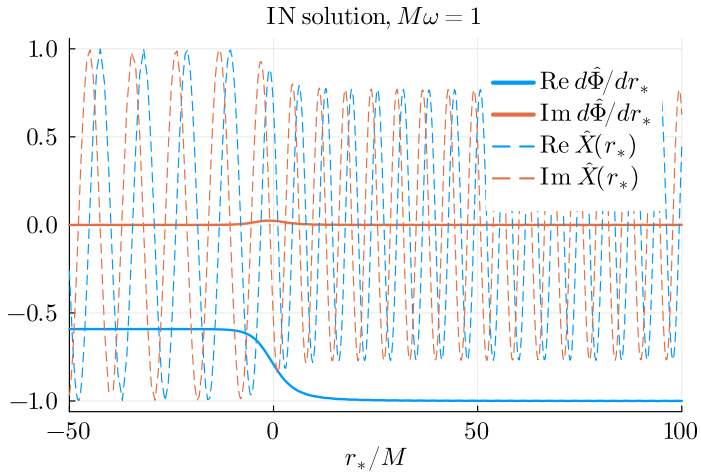


(b)

Figure 4.4: GSN IN solution of the $s = -2, \ell = 2, m = 2$ mode of a BH with $a/M = 0.7$ and two different values of $\omega$ (upper panel: $M\omega = 0.5$; lower panel: $M\omega = 1$), in terms of the GSN function $X$ and the complex frequency function $d\Phi/dr_*$.

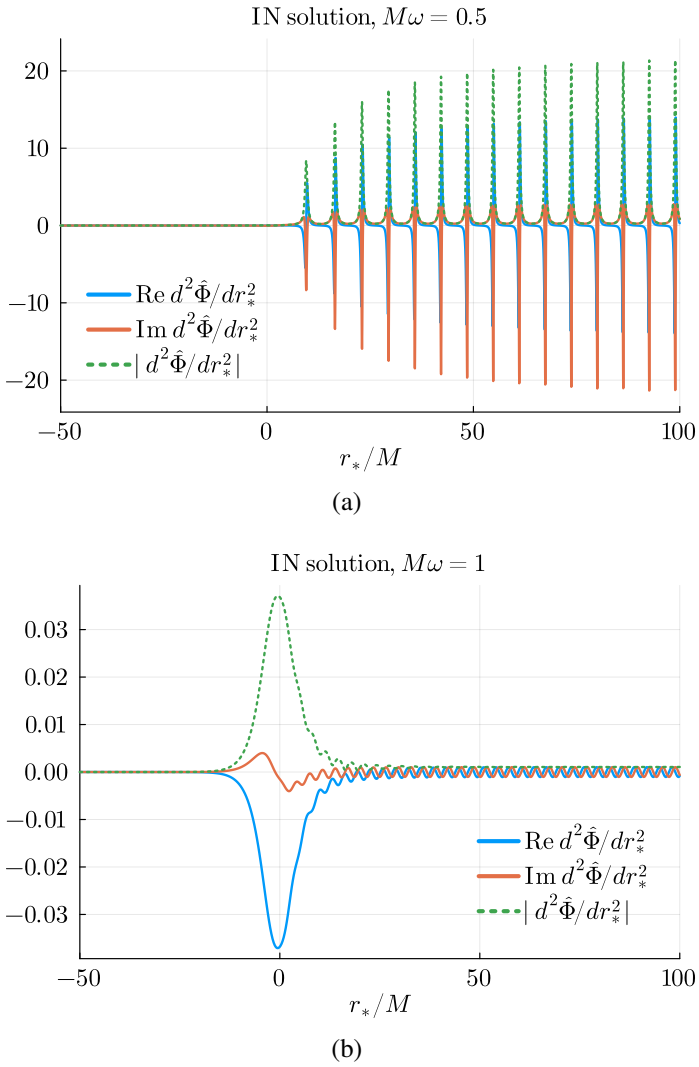


Figure 4.5: First derivative of the numerical solutions to the complex frequency function in Fig. 4.4 (i.e., $d/dr_*(d\hat{\Phi}/dr_*)$), computed using AD, as indicators of how much the numerical solutions are changed locally as functions of $r_*$ (upper panel: $M\omega = 0.5$; lower panel: $M\omega = 1$).

Fig. 4.7 is similar to Fig. 4.4 but showing the UP solution instead. Recall that for an UP solution, it is purely out-going at infinity. Again, we see from the figure that for both $M\omega = 0.5$ and $M\omega = 1$ (upper and lower panel, respectively),

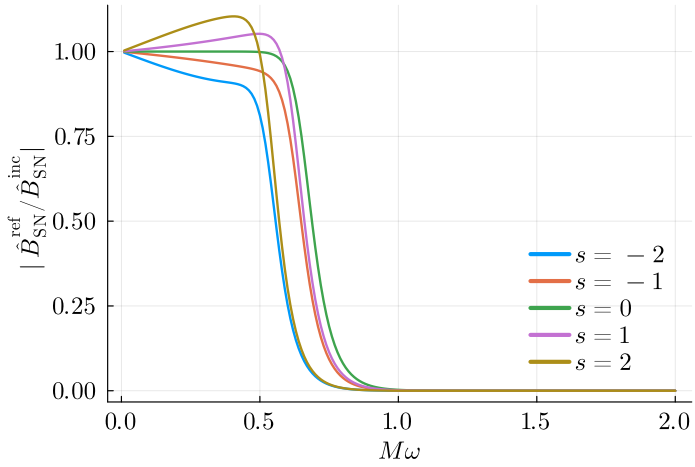


Figure 4.6: Reflectivity $B^{\rm ref}_{\rm SN}/B^{\rm inc}_{\rm SN}$ of a Kerr BH potential barrier in the GSN formalism. We see that for all the spin weights $s$ considered in this paper, the corresponding potential barriers are very permeable to high-frequency ($M\omega \gtrsim 1$) waves, meaning that the potentials will not reflect off the incidence waves and instead allow them to pass right through. In this figure, the BH angular momentum was set to $a/M = 0.7$ but the same is true for other values of $a/M$ as well.

$d\hat{\Phi}/dr_*$ is flat and approaches to the imposed asymptotic value $\omega^2$ as $r_* \to \infty$, while $\hat{X}$ is oscillating with the frequency $\omega$. Similar to the IN solutions shown in Fig. 4.4, since an UP solution is an admixture of the left- and the right-going modes near the horizon, depending on their relative amplitude $C^{\rm ref}_{\rm SN}/C^{\rm inc}_{\rm SN}$, both $\hat{X}$ and $d\hat{\Phi}/dr_*$ can be oscillatory near the horizon as shown in Fig. 4.7a. When the frequency $\omega$ is sufficiently high, the beating in $d\hat{\Phi}/dr_*$ is suppressed while $\hat{X}$ remains oscillatory as shown in Fig. 4.7b.

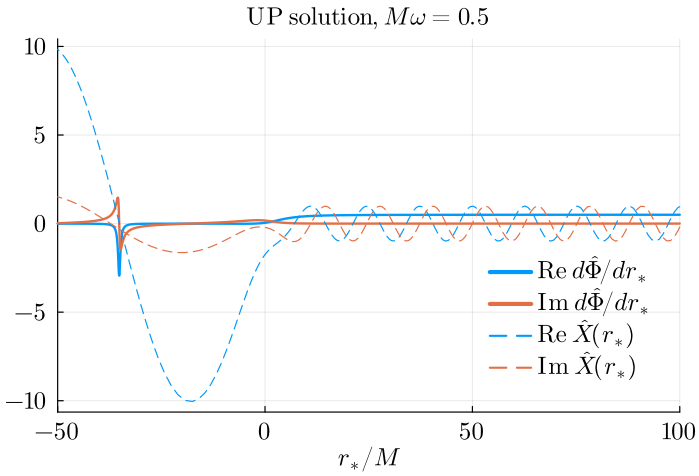


(a)

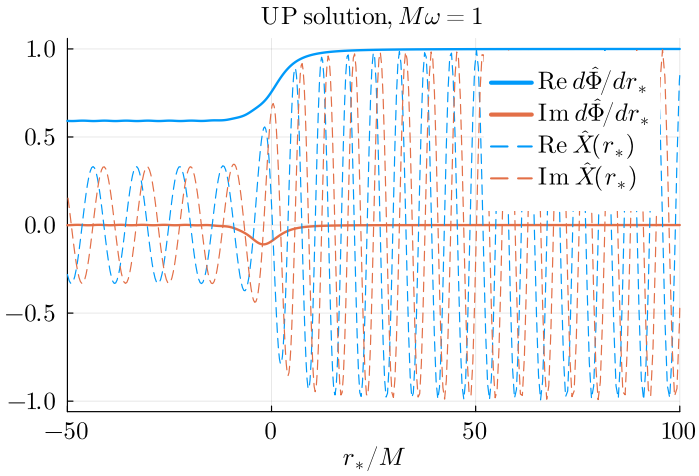


(b)

Figure 4.7: GSN UP solution of the $s = -2, \ell = 2, m = 2$ mode of a BH with $a/M = 0.7$ and two different values of $\omega$ (upper panel: $M\omega = 0.5$; lower panel: $M\omega = 1$), in terms of the GSN function $X$ and the complex frequency function $d\Phi/dr_*$.

#### 4.3.3.2 Numerical accuracy

As numerical solutions are only approximations to the true solutions, it is necessary to verify their accuracies. First, we need to show that the initial conditions $\hat{X}$ and $d\hat{X}/dr_*$ that we use are sufficiently accurate such that when solving for $\hat{X}^{\rm in,up}$ the corresponding asymptotic boundary forms are satisfied. Next, we need to show that the numerical solutions actually satisfy the GSN equation inside the integration domain. In both cases, we can evaluate the residual $\varepsilon$, which is defined as

$$\varepsilon = \left| \frac{d^2\hat{X}}{dr_*^2} - \mathcal{F}(r)\frac{d\hat{X}}{dr_*} - \mathcal{U}(r)\hat{X} \right|, \tag{4.69}$$

where a smaller value (ideally zero) means a better agreement of a numerical solution $\hat{X}$ with the GSN equation.

Fig. 4.8 shows the residual $\varepsilon$ of the ansatz, $f_\pm^\infty$ near infinity (upper panel) and $g_\pm^{\rm H}$ near the horizon (lower panel) as functions of $r_*$. For both panels, solid lines correspond to the out-going ansatzes and dash lines correspond to the in-going ansatzes truncated to different orders $N = 0, 1, 2, 3$, i.e., keeping the first $N + 1$ terms in Eq. (4.53) and Eq. (4.54) respectively. Recall that for all the numerical results we have shown previously, we set the numerical outer boundary $r_*^{\rm out} = 1000M$ and truncate $f_\pm^\infty$ at $N = 3$ (i.e., including the first four terms). From Fig. 4.8a we see that this corresponds to $\varepsilon \approx 10^{-13}$. As expected, for a fixed $r_* \gg 1$, the residual $\varepsilon$ decreases as one keeps more terms (i.e., higher $N$) in the summation in Eq. (4.53). Alternatively, for a fixed $N$, the residual $\varepsilon$ goes down as one has an numerical outer boundary $r_*^{\rm out}$ further away from the BH.

As for the numerical inner boundary $r_*^{\rm in}$, recall that we set $r_*^{\rm in} = -50M$ and truncate $g_\pm^{\rm H}$ such that only the leading term is kept (i.e., $N = 0$). From Fig. 4.8b we see that this corresponds to $\varepsilon \approx 10^{-10}$. Similar to $f_\pm^\infty$, the residual decreases with a higher $N$ in the summation of Eq. (4.54) for a fixed $r_*$ until the precision of a double-precision floating-point number (around $10^{-15}$) is reached and $\varepsilon$ plateaus. Again, for a fixed $N$, as one sets the inner boundary closer to the horizon, the residual drops until around $10^{-15}$.

Fig. 4.9 shows the residual $\varepsilon$ for the numerical GSN UP solutions in Fig. 4.7 (with $s = -2, \ell = 2, m = 2$, and $a/M = 0.7$), for both $M\omega = 0.5$ and $M\omega = 1$. We see that the residuals are indeed very small, and stay roughly at $\varepsilon \approx 10^{-12}$, which is the absolute and relative tolerance given to the ODE solver. As for the numerical GSN IN solutions, the residuals are similar to that for the UP solutions.

The scaled Wronskian $\mathcal{W}_X$ (c.f. Eq. (4.39)) can be used as a sanity check. Using again the numerical solutions in Fig. 4.7 for the UP solution and Fig. 4.4 for the IN solution with $M\omega = 0.5$ and $M\omega = 1$, we evaluate the magnitude of the complex scaled Wronskian $|\mathcal{W}_X|$, which should be constant, at four different values of $r_*/M = -50, 0, 50, 1000$, respectively. The scaled Wronskian can also be computed using the asymptotic amplitudes at infinity (c.f. Eq. (4.40)) and at the horizon (c.f. Eq. (4.41)), respectively. The values are tabulated in Tab. 4.1. We see that the scaled Wronskians computed from the numerical solutions for the two values of $M\omega$ are indeed constant, at least up to the eleventh digit, across the integration domain $r_* \in [-50M, 1000M]$. This means that our method for solving GSN functions are numerically stable. The agreement of the scaled Wronskian evaluated at different locations in the integration domain and that evaluated using the asymptotic amplitudes at both boundaries also implies that our procedure of extracting incidence and reflection amplitudes from numerical solutions works.

#### 4.3.3.3 Comparisons with the Mano-Suzuki-Takasugi method

As mentioned in Sec. 4.1, there are other ways of computing homogeneous solutions to the radial Teukolsky equation, and one of which is the MST method. Using the MST method, asymptotic amplitudes of Teukolsky functions (i.e., incidence and reflection amplitudes normalized by transmission amplitudes) can be determined accurately, together with the homogenous solutions themselves. Here we compare our numerical solutions and asymptotic amplitudes using the GSN formalism with that using the MST method. In particular, we use the implementation in the `Teukolsky` [67] MATHEMATICA package from the Black

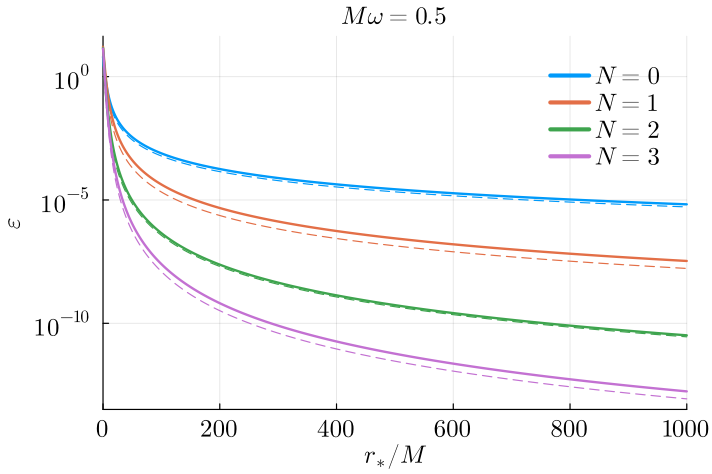


(a) for ansatz near infinity, $f_{\pm}^{\infty}$

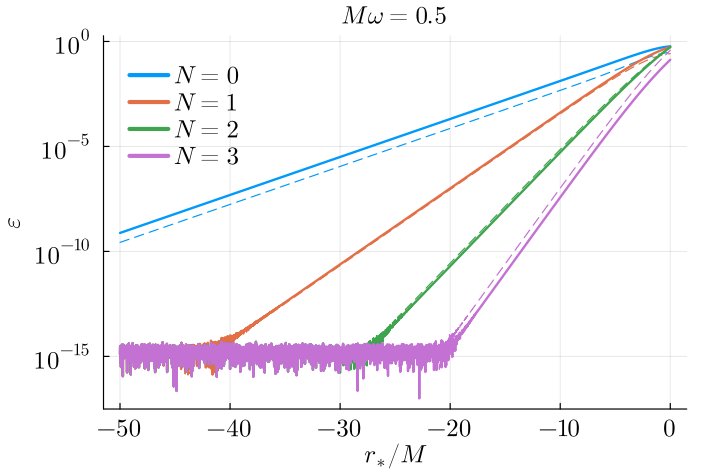


(b) for ansatz near the horizon, $g_{\pm}^{\mathrm{H}}$

Figure 4.8: Residual $\varepsilon$ of the ansatz (c.f. Eq. (4.52)) $f_{\pm}^{\infty}$ (upper panel) and $g_{\pm}^{\mathrm{H}}$ (lower panel) that we use in evaluating the initial conditions when solving for $X^{\mathrm{in,up}}$ and extracting the incidence and reflection amplitudes from the numerical solutions. In particular, we set $s = -2, \ell = 2, m = 2, a/M = 0.7$ for the purpose of demonstration. For both plots, solid lines correspond to the *out-going* ansatzes and dash lines correspond to the *in-going* ansatzes truncated to different orders $N = 0, 1, 2, 3$, respectively.

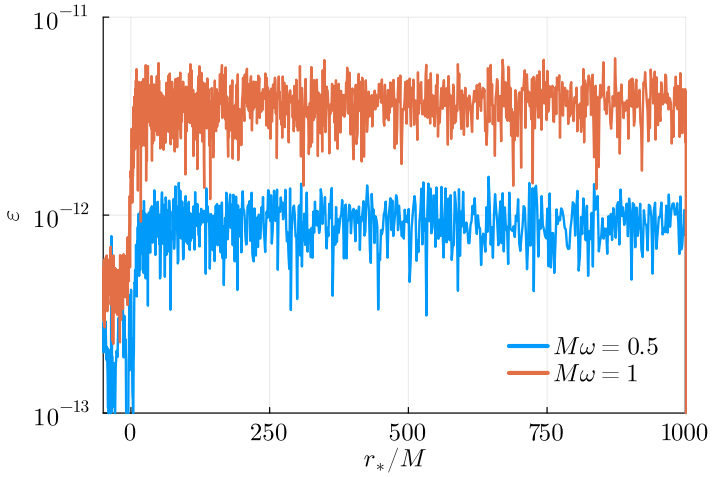


Figure 4.9: Residual $\varepsilon$ of the numerical GSN UP solutions shown in Fig. 4.7 for $M\omega = 0.5$ and $M\omega = 1$, respectively. Recall that both the absolute tolerance and the relative tolerance passed to the numerical ODE solver are set to $10^{-12}$.

| $r_*/M$ | $M\omega = 0.5$ | $M\omega = 1$ |
|---|---|---|
| $-\infty$ | 0.06686918718(132409) | 0.09801150092(211632) |
| $-50$ | 0.06686918718(132406) | 0.09801150092(220787) |
| 0 | 0.06686918718(135844) | 0.09801150092(220655) |
| 50 | 0.06686918718(137257) | 0.09801150092(220637) |
| 1000 | 0.06686918718(173902) | 0.09801150092(220587) |
| $\infty$ | 0.06686918718(244163) | 0.09801150092(220785) |

Table 4.1: Magnitude of the (complex) scaled Wronskian $|\mathcal{W}_X|$ of two frequencies, $M\omega = 0.5$ and $M\omega = 1$, evaluated at four different positions, $r_*/M = -50, 0, 50, 1000$, respectively, and evaluated using the asymptotic amplitudes, with the `GeneralizedSasakiNakamura.jl` code. Digits beyond the eleventh digit are shown in brackets.

Hole Perturbation Toolkit [57].

We compute the scaled Wronskian $\mathcal{W}_R$ of the numerical solutions for $s = -2, \ell = 2, m = 2, a/M = 0.7$ mode for both $M\omega = 0.5$ and $M\omega = 1$ (the same setup as in Tab. 4.1), using the MST method. Similar to the case for GSN functions, we

can compute $\mathcal{W}_R$ either from the numerical solutions $R^{\rm in,up}$ using Eq. (4.31), or from the asymptotic amplitudes using Eq. (4.32) or Eq. (4.33), and they should agree. In addition, the values for $\mathcal{W}_R$ should be the same as $\mathcal{W}_X$.[16] The results are tabulated in Tab. 4.2. We see that the numbers shown in Tab. 4.1, which were computed using the GSN formalism, agree with the numbers in Tab. 4.2 at least up to the eleventh digit, testifying the numerical accuracy and correctness of the solutions and the asymptotic amplitudes computed using `GeneralizedSasakiNakamura.jl`. It should also be remarked that the implementation of the MST method in the `Teukolsky` package seems to be struggling either very close (e.g., $r_* = -50M$) or very far away (e.g., $r_* = 1000M$) from the BH, and in general the MST method struggles more as $M\omega$ becomes larger[17] while the GSN formalism becomes more efficient instead.[18]

### 4.4 Conclusion and future work

In this paper, we have revamped the Generalized Sasaki-Nakamura (GSN) formalism for computing homogeneous solutions to both the GSN equation and the radial Teukolsky equation for scalar, electromagnetic and gravitational perturbations. Specifically, we have provided explicit expressions for the transformations between the Teukolsky formalism and the GSN formalism. We have also derived expressions for higher-order corrections to asymptotic solutions of the GSN equation, as well as frequency-dependent conversion factors between asymptotic solutions in the Teukolsky and the GSN formalism. Both are essential for using the GSN formalism to perform numerical work. We have also described an open-source implementation of the now-complete GSN formalism for solv-

[16] Note that the `Teukolsky` package uses a normalization convention that $B_{\rm T}^{\rm trans} = C_{\rm T}^{\rm trans} = 1$, which is different from our `GeneralizedSasakiNakamura.jl` implementation. To account for the difference in the normalization convention, a factor of $\left(C_{\rm T}^{\rm trans}/C_{\rm SN}^{\rm trans}\right)\left(B_{\rm T}^{\rm trans}/B_{\rm SN}^{\rm trans}\right)$ is multiplied to $\mathcal{W}_R$ computed from the `Teukolsky` code.

[17] We performed the same set of calculations in Sec. 4.3.3.3 using another MST-based `Fortran` code described in Ref. [68] that uses machine-precision numbers. The same conclusion is reached.

[18] More concretely, the authors of Ref. [51] gave explicit examples ($s = -2, \ell = 2, a/M = 0, M\omega > 5$) where they found their MST code were struggling to compute, while the GSN formalism, for example using our code, can handle these cases with ease.

| $r_*/M$ | $M\omega = 0.5$ | $M\omega = 1$ |
|---|---|---|
| $-\infty$ | 0.06686918718(210336) | 0.09801150092(219980) |
| $-50$ | Aborted | Aborted |
| 0 | 0.06686918718(210336) | 0.09801150092(219978) |
| 50 | 0.06686918718(210336) | Error |
| 1000 | Error | Error |
| $\infty$ | 0.06686918718(210336) | 0.09801150092(219980) |

Table 4.2: Magnitude of the (complex) scaled Wronskian $|\mathcal{W}_R|$ of two frequencies, $M\omega = 0.5$ and $M\omega = 1$, evaluated at four different positions, $r_*/M = -50, 0, 50, 1000$, respectively, and evaluated using the asymptotic amplitudes, with the MST method implemented in the `Teukolsky` code. Note that in the computations we use the arbitrary-precision arithmetic in MATHEMATICA (specifically 64-digit accurate). Digits beyond the eleventh digit are shown in brackets and truncated to the seventeenth digit to match Tab. 4.1. The computations at $r_* = -50M$ for both cases were aborted after running for an hour.

ing homogeneous solutions, where the implementation re-formulated the GSN equation further into a Riccati equation so as to gain extra efficiency at high frequencies.

In the following we discuss two potential applications of the GSN formalism in BH perturbation theory, namely as an efficient procedure for computing gravitational radiation from BHs, and as an alternative method for QNM determination.

### 4.4.1 An efficient procedure for computing gravitational radiation from Kerr black holes

As we have demonstrated in Sec. 4.3.3, the GSN formalism is capable of producing accurate and stable numerical solutions to the homogenous GSN equation, which can then be converted to numerical Teukolsky functions, across a wide range of $r_*/M$ when the MST method tends to struggle when $r_*/M \ll 1$ and $r_*/M \gg 1$ as shown in Sec. 4.3.3.3. While we have only shown the numerical results for $M\omega = 0.5$ and $M\omega = 1$ explicitly, it is reasonable to expect the formalism to also work for other frequencies, if not even better at high frequencies

when we gain extra efficiency by further transforming a GSN function $X(r_*)$ into a complex frequency function $d\Phi/dr_*$, while the MST method requires a much higher working precision for computation. This can occur, for example, when computing a higher harmonic of an extreme mass-ratio inspiral (EMRI) waveform. For a generic orbit, the harmonic has a frequency $\omega$ given by [69]

$$\omega = m\Omega_\phi + k\Omega_\theta + n\Omega_r, \tag{4.70}$$

where $\Omega_\phi, \Omega_\theta, \Omega_r$ are the fundamental orbital frequency for the $\phi$-, $\theta$- and $r$-motion, respectively.

Indeed, we see from Sec. 4.3.3.1 that in some regions of the parameter space, it is more efficient to solve for the complex frequency function $d\Phi/dr_*$ than to solve for the GSN function $X$ itself. There are, however, cases where the reverse is true instead, especially at a lower wave frequency when the BH potential barrier is less transmissive, since it is numerically more efficient (requiring fewer nodes) to track a less oscillatory function than a more oscillatory function (c.f. Fig. 4.4). This means that a better numerical scheme solving for $X^{\text{in,up}}$ (and by extension $R^{\text{in,up}}$) can be formulated by first solving the first-order non-linear ODE for $d\Phi/dr_*$, and then "intelligently" switching to solving the second-order linear ODE for $X$ when it is more efficient, for example, when $d/dr_*(d\hat{\Phi}/dr_*)$ is above some pre-defined threshold. This hybrid approach is similar in sprit to some of the state-of-the-art solvers for oscillatory second order linear ODEs [70].[19]

While the GSN formalism is a great alternative to the MST method for computing homogeneous solutions (i.e., $T = 0$) to the radial Teukolsky equation, the real strength of the GSN formalism is the ability to also compute inhomogeneous solutions (i.e., $T \neq 0$). Given an extended Teukolsky source term, such as a plunging test particle from infinity, the convolution integral with the Teukolsky functions can be divergent when using the Green's function method to compute

[19] As mentioned in both Ref. [65] and Ref. [70], pseudo-spectral methods can be adopted instead of finite-difference methods (like the `Vern9` algorithm that this paper uses) to achieve exponential convergence. We leave this as a future improvement to this work.

the inhomogeneous solution and regularization of the integral is needed [71, 72]. In Ref. [54], Sasaki and Nakamura had worked out a formalism, which was developed upon their SN transformation, to compute the inhomogeneous solution for $s = -2$ where the new source term, constructed from the Teukolsky source term, is short-ranged such that the convolution integral with the SN functions is convergent when using the Green's function method.

In a forthcoming paper, we show that their construction can also be extended to work for $s = 2$, and the corresponding GSN transformation, in a similar fashion, serves as the foundation of the method. This will be important for studying near-horizon physics [73, 74, 33], such as computing gravitational radiation from a point particle plunging towards a BH as observed near the horizon, where the polarization contents are encoded in $\psi_0$ (with $s = 2$) instead of $\psi_4$ (with $s = -2$). In particular, the Teukolsky-Starobinsky identities [75, 44] are not valid in this case (since the source term does not vanish near the horizon) and we cannot use them to convert the asymptotic amplitude for $\psi_4$ to that for $\psi_0$.[20]

### 4.4.2 An alternative method for quasi-normal mode determination

The re-formulation of a Schrödinger-like equation into a Riccati equation introduced in Sec. 4.3.1.1 is not new and had actually been used previously, for instance, in the seminal work by Chandrasekhar and Detweiler on QNMs of Schwarzschild BHs [76]. It was used (c.f. Eq. (5) of Ref. [76]) to alleviate the numerical instability associated with directly integrating the Zerilli equation, and equivalently also the Regge-Wheeler equation to which the GSN equation reduces in the non-spinning limit. Therefore, it is reasonable to expect that the re-formulation to be useful for determining QNM frequencies and their associated radial solutions.

Recall that a QNM solution is both purely-ingoing at the horizon and purely-

[20]Note that it is still possible to compute the asymptotic amplitude for $\psi_0$ using the Green's function method constructed from the Teukolsky functions, but regularization is needed as the convolution integral is again divergent [34].

outgoing at infinity. In terms of the asymptotic amplitudes of the corresponding Teukolsky function (c.f. Eq. (4.29) and Eq. (4.30)) at a particular frequency $\omega_{\rm QNM}$, we have

$$\begin{aligned} &B_{\rm T}^{\rm inc}(\omega_{\rm QNM}) = C_{\rm T}^{\rm inc}(\omega_{\rm QNM}) = 0 \\ &\Rightarrow \mathcal{W}_R(\omega_{\rm QNM}) = 0, \end{aligned} \tag{4.71}$$

where the second line uses Eq. (4.32). This means that searching for QNM frequencies is the same as searching for zeros of $\mathcal{W}_R$, the scaled Wronskian for Teukolsky functions. Also recall that in App. 4.7, we proved that the scaled Wronskian for Teukolsky functions $\mathcal{W}_R$ and that for the corresponding GSN functions $\mathcal{W}_X$ are the same, implying that the QNM spectra for Teukolsky functions coincide with the QNM spectra for GSN functions.[21] Thus, we can use the GSN equation, which has a short-ranged potential, instead of the Teukolsky equation for determining the QNM frequencies and the corresponding excitation factors (after applying the conversion factors shown in App. 4.9).

Indeed, Glampedakis and Andersson proposed methods to calculate QNM frequencies and excitation factors given a short-ranged potential [77], alternative to the Leaver's method [78]. They demonstrated their methods by computing a few of the QNM frequencies for scalar perturbations ($s = 0$) and gravitational perturbations ($|s| = 2$), as well as the QNM excitation factors for scalar perturbations of Kerr BHs. Together with the GSN transformations and the asymptotic solutions from this paper, it is straightforward to compute the QNM frequencies and their excitation factors for scalar, electromagnetic, and gravitational perturbations using the GSN formalism.[22] We leave this for future work.

[21] The two equations, the radial Teukolsky equation and the GSN equation, are therefore said to be iso-spectral.

[22] The excitation factors for gravitational perturbations of Kerr BHs have been calculated using a different method [79, 80, 81], by explicitly computing the gravitational waveform from an infalling test particle and then extracting the amplitudes for each of the excited QNMs.

**Acknowledgments**

The author would like to thank Yanbei Chen, Manu Srivastava, Shuo Xin, Emanuele Berti, Scott Hughes, Aaron Johnson, Jonathan Thompson and Alan Weinstein for the valuable discussions and insights when preparing this work. The author would like to especially thank Manu Srivastava for a read of an early draft of this manuscript, and Shuo Xin for performing the scaled Wronskian calculations using the `Fortran` code in Ref. [68]. R. K. L. L. acknowledges support from the National Science Foundation Awards No. PHY-1912594 and No. PHY-2207758.

## 4.5 Appendix: Angular Teukolsky equation

After performing the separation of variables to the Teukolsky equation in Eq. (4.2) using an ansatz of the form $\psi(t, r, \theta, \phi) = R(r)S(\theta, \phi)e^{-i\omega t}$, the equation is separated into two parts: the angular part and the radial part. In this appendix, we focus only on solving the angular part (aptly named the angular Teukolsky equation) numerically, and the radial part is treated in the main text.

Let us define ${}_sS_{\ell m\omega}(\theta, \phi) \equiv {}_sS_{\ell m}(x \equiv \cos\theta; c \equiv a\omega)e^{im\phi}$, where the integer $m$ labels the (trivial) eigenfunctions that satisfy the azimuthal symmetry. The angular Teukolsky equation then reads

$$\frac{d}{dx}\left[(1-x^2)\frac{d}{dx}{}_sS_{\ell m}(x;c)\right] + \left[(cx)^2 - 2csx + s + {}_s\mathcal{A}_{\ell m}(c) - \frac{(m+sx)^2}{1-x^2}\right]{}_sS_{\ell m}(x;c) = 0, \quad (4.72)$$

where ${}_s\mathcal{A}_{\ell m}$ is the angular separation constant and it is related to $\lambda$ (c.f. Eq. (4.4)) by

$$\lambda = {}_s\mathcal{A}_{\ell m} + c^2 - 2mc. \quad (4.73)$$

The angular Teukolsky equation is solved under the boundary conditions that the solutions at $x = \pm 1$ (or equivalently at $\theta = 0, \pi$) are finite, and the solutions are also known as the spin-weighted spheroidal harmonics, denoted by ${}_sS_{\ell m\omega}(\theta, \phi)$.

There are multiple methods for solving the angular Teukolsky equation numerically, such as Leaver's continued fraction method [78]. A spectral decomposition method for solving the angular Teukolsky equation can be formulated [82, 83] by writing a spin-weighted spheroidal harmonic ${}_sS_{\ell m\omega}(\theta,\phi)$ as a sum of spin-weighted *spherical* harmonics ${}_sY_{\ell m}(\theta,\phi)$. The details for such a formulation can be found in, for example, Ref. [82] and Ref. [83]. We briefly summarize the method here, mostly following and using the notations in Ref. [83], for the sake of completeness.

### 4.5.1 Spectral decomposition method

A spin-weighted spheroidal harmonic ${}_sS_{\ell m}(x;c)$ is expanded using spin-weighted spherical harmonics ${}_sY_{\ell m}(\theta)$, or equivalently ${}_sS_{\ell m}(x;0)$ as [83]

$$\begin{aligned} {}_sS_{\ell m}(x;c) &= \sum_{\ell'=\ell_{\min}}^{\infty} {}_sC_{\ell'\ell m}(c)\ {}_sS_{\ell' m}(x;0) \\ &= \left(\vec{C}_\ell\right)^T \vec{S}_\ell, \end{aligned} \tag{4.74}$$

where $\ell_{\min} = \max(|m|,|s|)$ and ${}_sC_{\ell'\ell m}(c)$ is the expansion coefficient of the $\ell$-th spheroidal harmonic with the $\ell'$-th spherical harmonic (of the same value of $s$ and $m$ and we drop them in the subscripts hereafter), as a function of $c \equiv a\omega$. Equivalently, we can define two column vectors $\vec{C}_\ell$ and $\vec{S}_\ell$, where the rows are labelled by the index $\ell'$. For example, the first row of the vectors (of index $\ell' = \ell_{\min}$) are ${}_sC_{\ell_{\min}\ell m}$ and ${}_sS_{\ell_{\min} m}(x;0)$, respectively. The index for the rows goes up to $\ell' = \ell_{\max} \to \infty$, and the vectors have a size of $\ell_{\max} - \ell_{\min} + 1$. Then the spin-weighted spheroidal harmonic $S_\ell(x;c)$ is the dot product of the two vectors.

Substituting Eq. (4.74) into Eq. (4.72), we get an eigenvalue equation [83]

$$\mathbb{M}\vec{C}_\ell = \mathcal{A}_\ell \vec{C}_\ell, \tag{4.75}$$

where $\mathbb{M}$ is a $(\ell_{\max} - \ell_{\min} + 1) \times (\ell_{\max} - \ell_{\min} + 1)$ matrix, and recall that $\mathcal{A}_\ell \equiv {}_s\mathcal{A}_{\ell m}(c \equiv a\omega)$ is the angular separation constant (after writing back all the

subscripts). The matrix elements $\mathbb{M}_{\ell\ell'}$ are given by [83]

$$\mathbb{M}_{\ell\ell'} = \begin{cases} -c^2\mathbb{A}_{\ell' m} & \text{if } \ell' = \ell - 2, \\ -c^2\mathbb{D}_{\ell' m} + 2cs\mathbb{F}_{\ell' m} & \text{if } \ell' = \ell - 1, \\ \mathcal{A}_{\ell'}(0) - c^2\mathbb{B}_{\ell' m} + 2cs\mathbb{H}_{\ell' m} & \text{if } \ell' = \ell, \\ -c^2\mathbb{E}_{\ell' m} + 2cs\mathbb{G}_{\ell' m} & \text{if } \ell' = \ell + 1, \\ -c^2\mathbb{C}_{\ell' m} & \text{if } \ell' = \ell + 2, \\ 0 & \text{otherwise} \end{cases}, \tag{4.76}$$

where

$$\mathbb{A}_{\ell m} = \mathbb{F}_{\ell m}\mathbb{F}_{(\ell+1)m}, \tag{4.77a}$$

$$\mathbb{B}_{\ell m} = \mathbb{F}_{\ell m}\mathbb{G}_{(\ell+1)m} + \mathbb{G}_{\ell m}\mathbb{F}_{(\ell-1)m} + \mathbb{H}^2_{\ell m}, \tag{4.77b}$$

$$\mathbb{C}_{\ell m} = \mathbb{G}_{\ell m}\mathbb{G}_{(\ell-1)m}, \tag{4.77c}$$

$$\mathbb{D}_{\ell m} = \mathbb{F}_{\ell m}\mathbb{H}_{(\ell+1)m} + \mathbb{F}_{\ell m}\mathbb{H}_{\ell m}, \tag{4.77d}$$

$$\mathbb{E}_{\ell m} = \mathbb{G}_{\ell m}\mathbb{H}_{(\ell-1)m} + \mathbb{G}_{\ell m}\mathbb{H}_{\ell m}, \tag{4.77e}$$

$$\mathbb{F}_{\ell m} = \sqrt{\frac{(\ell+1)^2 - m^2}{(2\ell+3)(2\ell+1)}\frac{(\ell+1)^2 - s^2}{(\ell+1)^2}}, \tag{4.77f}$$

$$\mathbb{G}_{\ell m} = \begin{cases} \sqrt{\dfrac{\ell^2 - m^2}{4\ell^2 - 1}\dfrac{\ell^2 - s^2}{\ell^2}} & \text{if } \ell \neq 0 \\ 0 & \text{if } \ell = 0 \end{cases}, \tag{4.77g}$$

$$\mathbb{H}_{\ell m} = \begin{cases} -\dfrac{ms}{\ell(\ell+1)} & \text{if } \ell \neq 0 \text{ and } s \neq 0 \\ 0 & \text{if } \ell = 0 \text{ or } s = 0 \end{cases}, \tag{4.77h}$$

$$\mathcal{A}_\ell(0) = \ell(\ell+1) - s(s+1). \tag{4.77i}$$

Solving the angular Teukolsky equation now amounts to solving the eigenvalue problem in Eq. (4.75) for the eigenvalue $\mathcal{A}_\ell$ and the eigenvector $\vec{C}_\ell$. The spin-weighted spheroidal harmonic can then be constructed using the eigenvector $\vec{C}_\ell$ and the corresponding spin-weight spherical harmonics with Eq. (4.74). In

practice, we cannot solve a matrix eigenvalue problem of infinite size and we truncate the column vector $\vec{C}_\ell$ to have a finite value of $\ell_{\rm max}$. The accuracy of the numerical eigenvalue and eigenvector solution depends on the size of the truncated matrix.

`SpinWeightedSpheroidalHarmonics.jl`[23] is our open-source implementation of the abovementioned spectral decomposition method for solving spin-weighted spheroidal harmonics in `julia`. The code solves the truncated[24] version of Eq. (4.75) to obtain the angular separation constant ${}_s\mathcal{A}_{\ell m}$ and the eigenvector ${}_s\vec{C}_{\ell m}$. Apart from the angular separation constant, the code can also compute the separation constant $\lambda$ (c.f. Eq. (4.4)), and evaluate numerical values of spin-weight spheroidal harmonics and their derivatives.[25] In particular, the code adopts the normalization convention for ${}_sS_{\ell m\omega}(\theta,\phi)$ that

$$\int_0^\pi \left[{}_sS_{\ell m}(\theta;c)\right]^2 \sin(\theta)\, d\theta = \frac{1}{2\pi}. \tag{4.78}$$

To evaluate numerical values of the spin-weighted spheroidal harmonics ${}_sS_{\ell m\omega}(\theta,\phi)$ and their derivatives, it is necessary to also be able to numerically (and possibly efficiently) evaluate the spin-weighted spheroidal harmonics ${}_sY_{\ell m}(\theta,\phi)$.

### 4.5.2 Evaluation of ${}_sS_{\ell m\omega}(\theta,\phi)$

Recall from Eq. (4.74) that the spin-weighted spheroidal harmonic ${}_sS_{\ell m\omega}(\theta,\phi)$ is expanded in terms of the spin-weighted spherical harmonics, i.e.,

$${}_sS_{\ell m}(\theta,\phi;a\omega) = \sum_{\ell'=\ell_{\rm min}}^{\infty} {}_sC_{\ell'\ell m}(a\omega)\ {}_sY_{\ell m}(\theta,\phi),$$

and the spectral decomposition method solves for the expansion coefficients ${}_sC_{\ell'\ell m}(a\omega)$, which is only part of the ingredients. It is possible to evaluate

[23] `https://github.com/ricokaloklo/SpinWeightedSpheroidalHarmonics.jl`

[24] By default the truncated matrix $\mathbb{M}$ is $10\times 10$, but the size is adjustable by setting a different $\ell_{\rm max}$ if a higher accuracy or a faster run time is needed.

[25] It should be noted that our code is also capable of handling complex $\omega$, which is necessary for carrying out quasi-normal mode related computations.

${}_sY_{\ell m}(\theta,\phi)$ exactly, and the expression is given by [84]

$$\begin{aligned} {}_sY_{\ell m}(\theta,\phi) = (-1)^m e^{im\phi}\sqrt{\frac{(\ell+m)!(\ell-m)!(2\ell+1)}{4\pi(\ell+s)!(\ell-s)!}} \\ \times\sum_{r=0}^{\ell-s}\left[\binom{\ell-s}{r}\binom{\ell+s}{r+s-m}(-1)^{\ell-r-s}\right. \\ \left.\times\cos^{2r+s-m}\left(\frac{\theta}{2}\right)\sin^{2\ell-2r-s+m}\left(\frac{\theta}{2}\right)\right] \end{aligned} \quad . \tag{4.79}$$

In principle, obtaining the value of a spin-weighted spherical harmonic ${}_sY_{\ell m}(\theta,\phi)$ is as simple as evaluating the sum as shown in Eq. (4.79). Oftentimes, however, when we solve the eigenvalue problem in Eq. (4.75), the index $\ell$ can be big enough so that a direct evaluation of the pre-factor

$$\sqrt{\frac{(\ell+m)!(\ell-m)!}{(\ell+s)!(\ell-s)!}}$$

in Eq. (4.79) on a machine can cause an overflow error because of the large factorials involved in the computation. Fortunately, the expression for the pre-factor can be simplified. In fact,

$$\begin{aligned} &\sqrt{\frac{(\ell+m)!(\ell-m)!}{(\ell+s)!(\ell-s)!}} \\ &= \begin{cases} \sqrt{\dfrac{(\ell-m)\,(\ell-m-1)\ldots(\ell-m-(s-m)+1)}{(\ell+m+(s-m))\,(\ell+m+(s-m)-1)\ldots(\ell+m+1)}} & \text{if } s>m, \\ \sqrt{\dfrac{(\ell+s+(m-s))\,(\ell+s+(m-s)-1)\ldots(\ell+s+1)}{(\ell-s)\,(\ell-s-1)\ldots(\ell-s-(m-s)+1)}} & \text{if } s<m, \\ 1 & \text{if } |s|=|m|. \end{cases} \end{aligned} \quad , \tag{4.80}$$

and now evaluations of ${}_sS_{\ell m\omega}(\theta,\phi)$ using Eq. (4.74) are free from overflow.

### 4.5.3 Evaluation of $\partial^n_{\theta,\phi}\ {}_sS_{\ell m\omega}(\theta,\phi)$

In order to evaluate partial derivatives of spin-weighted spheroidal harmonics, $\partial^n_{\theta,\phi}\ {}_sS_{\ell m\omega}(\theta,\phi)$, which are needed for evaluating source terms $T$ of the Teukolsky

equation (c.f. Eq. (4.2)), we can use the fact that the expansion coefficients ${}_sC_{\ell'\ell m}(c \equiv a\omega)$ in Eq. (4.74) are independent of $\theta$ and $\phi$. This means that the partial derivatives $\partial^n_{\theta,\phi}\ {}_sS_{\ell m\omega}(\theta,\phi)$ are given by the sum of the partial derivatives of ${}_sY_{\ell m}(\theta,\phi)$ with the same set of the expansion coefficients, i.e.,

$$\left(\frac{\partial}{\partial\{\theta,\phi\}}\right)^n\ {}_sS_{\ell m\omega}(\theta,\phi) \;=\; \sum_{\ell'=\ell_{\min}}^{\infty}\left[{}_sC_{\ell'\ell m}(a\omega)\ \left(\frac{\partial}{\partial\{\theta,\phi\}}\right)^n\ {}_sY_{\ell m}(\theta,\phi)\right]. \tag{4.81}$$

In principle, we can evaluate the partial derivatives using AD. However, the evaluation can be more performant by noticing that the exact evaluation of the partial derivative with respect to $\phi$ is trivial because of the $e^{im\phi}$ dependence. Each partial differentiation with respect to $\phi$ gives a factor of $im$. As for the partial derivative of a spin-weighted spherical harmonic with respect to $\theta$, the computation scheme is less trivial. Note that each term in Eq. (4.79) is of the form $c_r \cos^{\alpha_r}(\theta/2)\sin^{\beta_r}(\theta/2)$, where $r$ is the summation index and $c_r$ is the pre-factor with $\alpha_r$ and $\beta_r$ being the exponent for the $\cos(\theta/2)$ and $\sin(\theta/2)$ factor, respectively. Each partial differentiation with respect to $\theta$ splits the term into two terms, one with $(c_r/2)\beta_r \cos^{\alpha_r+1}(\theta/2)\sin^{\beta_r-1}(\theta/2)$, and one with $(-c_r/2)\alpha_r \cos^{\alpha_r-1}(\theta/2)\sin^{\beta_r+1}(\theta/2)$.

We can keep track of the coefficients and the exponents for the cosine and the sine factor with the help of a binary tree. We represent each term in the summation with index $r$ in Eq. (4.79) as the root node of a tree (for an illustration, see Fig. 4.10) with an entry of three numbers $(c_r, \alpha_r, \beta_r)$. Each partial differentiation with respect to $\theta$ corresponds to adding two child nodes with the entry $(c_r\beta_r/2, \alpha_r+1, \beta_r-1)$ and $(-c_r\alpha_r/2, \alpha_r-1, \beta_r+1)$, respectively. Therefore, the $n$-th order partial derivative of $\theta$ can be evaluated exactly by traversing all the nodes of depth $n$ and then summing over their contributions.

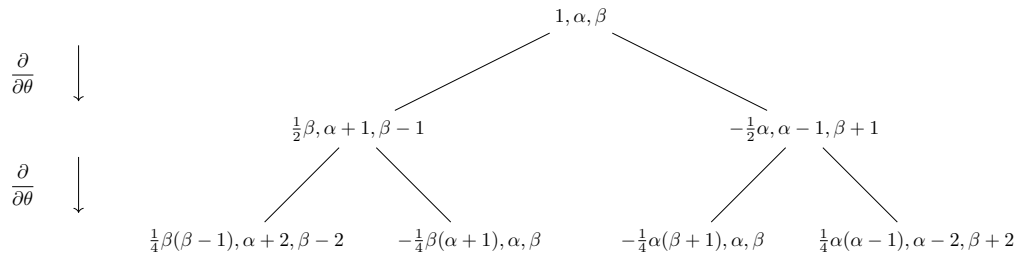


Figure 4.10: Binary tree representation of a term and its partial derivatives with respect to $\theta$ in the summation of Eq. (4.79). In each node, the three numbers correspond to the pre-factor, the exponent for the $\cos(\theta/2)$ and the $\sin(\theta/2)$ factor, respectively. A partial differentiation with respect to $\theta$ creates two leaf nodes with the pre-factor and the exponents computed according to rules of partial differentiation. The $n$-th partial derivative with respect to $\theta$ of the term in the root node can be evaluated by simply summing over all the nodes of depth $n$.

## 4.6 Appendix: Fast inversion from the tortoise coordinate $r_*$ to the Boyer-Lindquist coordinate $r$

The tortoise coordinate $r_*$ (for Kerr BHs) is defined by

$$\frac{dr_*}{dr} = \frac{r^2+a^2}{\Delta} = \frac{r^2+a^2}{(r-r_+)\,(r-r_-)}. \tag{4.7}$$

Using Eq. (4.7) one can generate different "tortoise coordinate" which differ to each other only by an integration constant. Here, and in most of the literature, we choose the integration constant such that

$$r_*(r) = r + \frac{2r_+}{r_+-r_-}\ln\left(\frac{r-r_+}{2}\right) - \frac{2r_-}{r_+-r_-}\ln\left(\frac{r-r_-}{2}\right). \tag{4.14}$$

However, there is no simple analytical expression that gives $r = r(r_*)$, and one will have to instead numerically invert Eq. (4.14). Such an inversion scheme that is both fast and accurate is needed for our numerical implementation of the GSN formalism because we numerically solve the GSN equation in the $r_*$-coordinate instead of the Boyer-Lindquist $r$-coordinate, and yet the GSN potentials, which

will be evaluated at many different values of $r_*$ during the numerical integration, are written in terms of $r$.

This coordinate inversion is equivalent to a root-finding problem. Given a value of the tortoise coordinate $r_*^0$, we solve for $h^0 \equiv \left(r^0 - r_+\right) > 0$ that satisfies

$$r_*^0 - r_*(r_+ + h^0) = 0, \tag{4.82}$$

in order to find the corresponding Boyer-Lindquist coordinate $r^0 \equiv r_+ + h^0$ that is *outside* the horizon [26].

Fig. 4.11 shows a plot of $r$ as a function of $r_*$ for $a/M = 0.7$. As the value of $r_*$ becomes larger, the simple approximation $r(r_*) \approx r_*$ works better. In fact, the slope $dr/dr_* \to 1$ as $r_* \gg 0$. Therefore, derivative-based methods such as the Newton-Raphson method and secant methods [55] are efficient in performing the coordinate inversion (since we can evaluate the derivatives exactly and cheaply). However, these methods are going to be inefficient for negative values of $r_*$ near the horizon since the slope tends to zero.

In our numerical implementation, we use a *hybrid* of root-finding algorithms. For $r_*^0 > 0$, we use the Newton-Raphson method [55] with an initial guess of $h = r_*^0$, and switch to using the bisection method [55] for $r_*^0 \leq 0$. To use the bisection method, an interval of $h$ that contains the root of Eq. (4.82) is given to the algorithm as an initial guess. Since $r = r_+$ maps to $r_* \to -\infty$, a natural choice for the lower bound of the bracketing interval would be $h = 0$. For the upper bracketing bound, from Fig. 4.12 we see that the value of $h$ that corresponds to $r_* = 0$ is a monotonically-increasing function of the spin magnitude $|a|$. Therefore, we can simply choose the upper bound value to be (equal to or greater than) the limiting value of $h$ that corresponds to $r_* = 0$ when $|a| \to 1$. Explicitly, the numerical implementation in `GeneralizedSasakiNakamura.jl` uses the bracketing interval $0 < h < 1.4$.

[26] A similar construction (i.e., enforcing $h^0 < 0$) can be used to find the Boyer-Lindquist coordinate $r \in (r_-, r_+)$ that gives the same $r_*^0$.

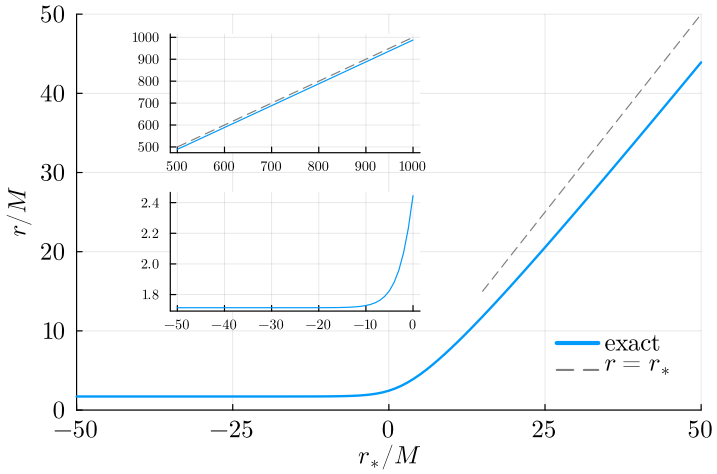


Figure 4.11: The Boyer-Lindquist $r$-coordinate as a function of the tortoise $r_*$ coordinate for $a/M = 0.7$. As the value of $r_*$ becomes larger (upper inset), the approximation $r(r_*) \approx r_*$ (dashed) gets increasingly better as $dr/dr_* \to 1$. Meanwhile as the value of $r_*$ becomes more negative (lower inset), $r(r_*)$ approaches $r = r_+$ as constructed and $dr/dr_* \to 0$.

## 4.7 Appendix: Deriving the identity between the scaled Wronskians for Teukolsky functions and Generalized Sasaki-Nakamura functions

Recall that the scaled Wronskian $\mathcal{W}_R$ for the Teukolsky functions $R^{\text{in,up}}$ is defined by

$$\mathcal{W}_R = \Delta^{s+1}\left(R^{\text{in}}R^{\text{up}\prime} - R^{\text{up}}R^{\text{in}\prime}\right), \tag{4.31}$$

whereas the scaled Wronskian $\mathcal{W}_X$ for the GSN functions $X^{\text{in,up}}$ is defined by

$$\mathcal{W}_X = \frac{1}{\eta}\left[X^{\text{in}}(dX^{\text{up}}/dr_*) - (dX^{\text{in}}/dr_*)X^{\text{up}}\right]. \tag{4.39}$$

They are called *scaled* Wronskians because they are not the same as "ordinary" Wronskians. For a generic second-order linear ODE

$$\frac{d^2y(x)}{dx^2} + p(x)\frac{dy(x)}{dx} + q(x)y(x) = 0, \tag{4.83}$$

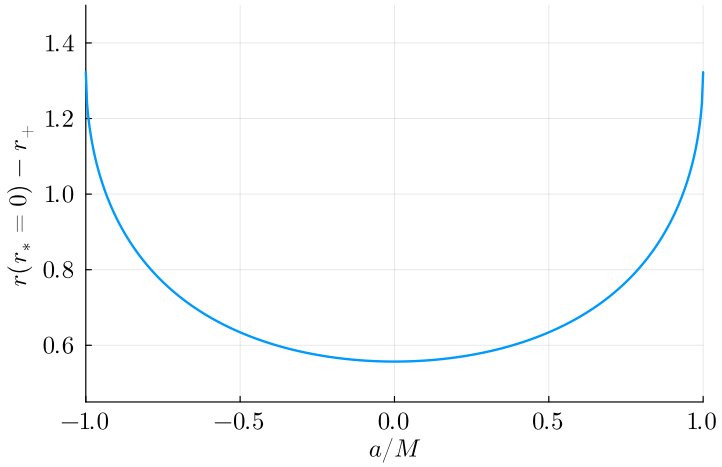


Figure 4.12: The difference between $r_* = 0$ and the horizon in the Boyer-Lindquist $r$-coordinate, $r(r_* = 0) - r_+$, as a function of the spin $a$ of the BH. We see that the difference is monotonically increasing with $|a|$, and it is the smallest when $a = 0$, and the largest ($\approx 1.3$) when $|a| \to 1$. We can use this to construct an interval of $r$ that must contain $r = r(r_*)$ for $r_* \leq 0$ when using the bisection method.

suppose it admits two linearly-independent solutions $y_1(x)$ and $y_2(x)$, then the Wronskian $W(x)$ is defined by

$$W(x) = y_1 \frac{dy_2}{dx} - y_2 \frac{dy_1}{dx}, \tag{4.84}$$

which is a function of $x$ in general. It can be shown that $W(x)$ satisfies the ODE [85]

$$\frac{dW}{dx} + p(x)W = 0. \tag{4.85}$$

Let us define the scaled Wronskian $\mathcal{W}$ such that

$$\mathcal{W} \equiv \exp\left(\int^x p(x')\, dx'\right) W(x), \tag{4.86}$$

we see that $d\mathcal{W}/dx = 0$, i.e., $\mathcal{W}$ is a constant.

It is not immediately obvious that $\mathcal{W}_X$, evaluated using Eq. (4.39), is the same as $\mathcal{W}_R$, evaluated using Eq. (4.31). From Eq. (4.39) and using Eq. (4.7), we have

$$\mathcal{W}_X = \frac{\Delta}{(r^2+a^2)\eta}\left(X^{\rm in}X^{\rm up\prime} - X^{\rm up}X^{\rm in\prime}\right). \tag{4.87}$$

Recall that the GSN function $X$ is transformed from a Teukolsky function $R$ using the ${}_s\Lambda$ operator that

$$\begin{aligned} X(r) &= {}_s\Lambda\left[R(r)\right] \\ &= \sqrt{\left(r^2+a^2\right)\Delta^s}\left[\left(\alpha+\beta\Delta^{s+1}\frac{d}{dr}\right)R(r)\right]. \end{aligned} \tag{4.16}$$

One can show that

$$\begin{aligned} &X^{\rm in}X^{\rm up\prime} - X^{\rm up}X^{\rm in\prime} \\ =&\left(r^2+a^2\right)\Delta^s\left\{\eta-(s+1)\alpha\beta\Delta^s\left[2\left(r-1\right)-\Delta'\right]\right\} \\ &\times\left(R^{\rm in}R^{\rm up\prime} - R^{\rm up}R^{\rm in\prime}\right) \\ =&\frac{\left(r^2+a^2\right)\eta}{\Delta}\Delta^{s+1}\left(R^{\rm in}R^{\rm up\prime} - R^{\rm up}R^{\rm in\prime}\right) \\ =&\frac{\left(r^2+a^2\right)\eta}{\Delta}\mathcal{W}_R, \end{aligned} \tag{4.88}$$

using Eq. (4.10) and the fact that $\Delta' = 2(r-1)$. From here, we see that indeed

$$\mathcal{W}_X = \mathcal{W}_R. \tag{4.43}$$

## 4.8 Appendix: Recurrence relations for the higher order corrections to the asymptotic boundary conditions of the Generalized Sasaki-Nakamura equation

In addition to the asymptotic boundary conditions to the leading order as shown in Eq. (4.37) and (4.38), it is useful to also compute these boundary conditions to higher orders. To start off, we assume the following ansatz for the GSN function

$$X(r_*) \sim \begin{cases} f_\pm^\infty(r)e^{\pm i\omega r_*}, & r_* \to \infty \\ g_\pm^{\rm H}(r)e^{\pm ipr_*}, & r_* \to -\infty \end{cases}. \tag{4.52}$$

By substituting the ansatz in Eq. (4.52) into the GSN equation in Eq. (4.22), it can be shown that as $r \to \infty$, the functions $f_\pm^\infty$ satisfy the following second-order ODE

$$f_\pm^{\infty\prime\prime} + P_\pm^\infty(r) f_\pm^{\infty\prime} + Q_\pm^\infty(r) f_\pm^\infty = 0, \tag{4.89}$$

where we define the functions

$$P_\pm^\infty(r) = \left(\frac{r^2+a^2}{\Delta}\right)\left[\left(\frac{\Delta}{r^2+a^2}\right)' \pm 2i\omega - \mathcal{F}\right], \tag{4.90}$$

$$Q_\pm^\infty(r) = \left(\frac{r^2+a^2}{\Delta}\right)^2\left(-\omega^2 \mp i\omega\mathcal{F} - \mathcal{U}\right). \tag{4.91}$$

As $r \to r_+$, the functions $g_\pm^{\mathrm{H}}$ satisfy the following second-order ODE

$$g_\pm^{\mathrm{H}\prime\prime} + P_\pm^{\mathrm{H}}(r) g_\pm^{\mathrm{H}\prime} + Q_\pm^{\mathrm{H}}(r) g_\pm^{\mathrm{H}} = 0, \tag{4.92}$$

where we define the functions

$$P_\pm^{\mathrm{H}}(r) = \left(\frac{r^2+a^2}{\Delta}\right)\left[\left(\frac{\Delta}{r^2+a^2}\right)' \pm 2ip - \mathcal{F}\right], \tag{4.93}$$

$$Q_\pm^{\mathrm{H}}(r) = \left(\frac{r^2+a^2}{\Delta}\right)^2\left(-p^2 \mp ip\mathcal{F} - \mathcal{U}\right). \tag{4.94}$$

We look for formal series expansions of the solutions $f_\pm^\infty$ at infinity and $g_\pm^{\mathrm{H}}$ at the horizon, respectively. We then truncate these expansions at an arbitrary order and use them to set the boundary conditions when solving the GSN equation on a numerically-finite interval.

### 4.8.1 Formal series expansion about infinity

Inspecting Eq. (4.89) with $P_\pm^\infty(r)$ and $Q_\pm^\infty(r)$ defined in Eq. (4.90) and (4.91), respectively and performing the standard change of variable $z \equiv 1/r$, we see that infinity (i.e., $z = 0$) is an irregular singularity of rank 1. We expand $P_\pm^\infty(r)$ and

$Q_{\pm}^{\infty}(r)$ as $r \to \infty$ with

$$P_{\pm}^{\infty}(r) = \sum_{j=0}^{\infty} \frac{P_{\pm,j}^{\infty}}{r^j}, \tag{4.95}$$

$$Q_{\pm}^{\infty}(r) = \sum_{j=0}^{\infty} \frac{Q_{\pm,j}^{\infty}}{r^j}. \tag{4.96}$$

In particular, we find that $Q_{\pm,0}^{\infty}$ and $Q_{\pm,1}^{\infty}$ are zero. Using these facts, the functions $f_{\pm}^{\infty}$ have the following formal series expansions near infinity as [86]

$$f_{\pm}^{\infty}(r) = e^{\nu_{\pm} r} r^{\kappa_{\pm}} \sum_{j=0}^{\infty} \frac{a_{\pm,j}}{r^j}, \tag{4.97}$$

(note that we suppress the $\infty$ superscript on the RHS since the context is clear) where $\kappa_{\pm}$ is given by

$$\kappa_{\pm} = -\frac{P_{\pm,1}\nu_{\pm} + Q_{\pm,1}}{P_{\pm,0} + 2\nu_{\pm}}, \tag{4.98}$$

and $\nu_{\pm}$ is a solution to the characteristic equation

$$\nu_{\pm}^2 - P_{\pm,0}\nu_{\pm} = 0. \tag{4.99}$$

There are two solutions to the characteristic equation: $\nu_{\pm} = 0$ or $\nu_{\pm} = P_{\pm,0}$. We pick $\nu_{+} = \nu_{-} = 0$ as this gives the desired form for the series expansions and as a result we have both $\kappa_{+} = \kappa_{-} = 0$ (recall that $Q_{\pm,1} = 0$). The expansion coefficients $a_{\pm,j}$ can be evaluated using the recurrence relation [86]

$$P_0 j a_j = j(j-1)a_{j-1} + \sum_{k=1}^{j} \left[Q_{k+1} - (j-k)\, P_k\right] a_{j-k}, \tag{4.100}$$

where we further suppress the $\pm$ subscript (both the out-going and the in-going mode have the same form above for the recurrence relations), and we set $a_0 = 1$. As an example, the coefficient $a_1$ is given by $a_1 = Q_2/P_0$. Comparing Eq. (4.53) with Eq. (4.97), we have

$$C_{\pm,j}^{\infty} = \omega^j a_{\pm,j}^{\infty}. \tag{4.101}$$

### 4.8.2 Formal series expansion about the horizon

Inspecting Eq. (4.92) with $P^{\mathrm{H}}_{\pm}(r)$ and $Q^{\mathrm{H}}_{\pm}(r)$ defined in Eq. (4.93) and Eq. (4.94), respectively, we see that $r = r_+$ is a regular singularity. In particular, $P^{\mathrm{H}}_{\pm}(r)\ (r - r_+)$ and $Q^{\mathrm{H}}_{\pm}(r)\ (r - r_+)^2$ are analytic at $r = r_+$ since

$$P^{\mathrm{H}}_{\pm}(r)\ (r - r_+) = \left(\frac{r^2 + a^2}{r - r_-}\right)\left[\left(\frac{\Delta}{r^2 + a^2}\right)' \pm 2ip - \mathcal{F}\right],$$
$$Q^{\mathrm{H}}_{\pm}(r)\ (r - r_+)^2 = \left(\frac{r^2 + a^2}{r - r_-}\right)^2 \left(-p^2 \mp ip\mathcal{F} - \mathcal{U}\right).$$

A formal series expansion near the horizon can be obtained using the Frobenius method. We expand $P^{\mathrm{H}}_{\pm}(r)$ and $Q^{\mathrm{H}}_{\pm}(r)$ near $r = r_+$ as

$$P^{\mathrm{H}}_{\pm}(r) = \sum_{j=0}^{\infty} P^{\mathrm{H}}_{\pm,j}(r - r_+)^{j-1}, \tag{4.102}$$

$$Q^{\mathrm{H}}_{\pm}(r) = \sum_{j=0}^{\infty} Q^{\mathrm{H}}_{\pm,j}(r - r_+)^{j-2}. \tag{4.103}$$

The functions $g^{\mathrm{H}}_{\pm}(r)$ again have the formal series expansions near the horizon as [86]

$$g^{\mathrm{H}}_{\pm}(r) = (r - r_+)^{\nu_\pm} \sum_{j=0}^{\infty} a_{\pm,j}(r - r_+)^j, \tag{4.104}$$

(note that we again suppress the H superscript on the RHS since the context is clear) where $\nu_\pm$ is a root to the indicial polynomial $I(\nu_\pm)$, which is given by [86]

$$I(\nu_\pm) = \nu_\pm(\nu_\pm - 1) + P_{\pm,0}\nu_\pm + Q_{\pm,0}. \tag{4.105}$$

Note that we have $Q_{\pm,0} = 0$, therefore the indicial equation $I(\nu_\pm) = 0$ has two solutions: $\nu_\pm = 0$ or $\nu_\pm = \left(1 - P_{\pm,0}\right)$. Again we pick $\nu_+ = \nu_- = 0$ as this gives the desired expansions. The expansion coefficients $a_{\pm,j}$ can be evaluated again using a recurrence relation as [86]

$$I(j)a_j = -\sum_{k=0}^{j-1}\left(kP_{j-k} + Q_{j-k}\right)a_k, \tag{4.106}$$

where we again further suppress the ± subscript (both the out-going and the in-going mode have the same form above for the recurrence relations), and we set $a_0 = 1$. For example, explicitly $a_1 = -Q_1/P_0$. Comparing Eq. (4.54) with Eq. (4.104), we have

$$C^{\rm H}_{\pm,j} = \omega^{-j} a^{\rm H}_{\pm,j}. \tag{4.107}$$

## 4.9 Appendix: Explicit Generalized Sasaki-Nakamura transformations for physically relevant radiation fields

Here in this appendix we explicitly show our choices of $g_i(r)$ for radiation fields with spin weight $s = 0, \pm 1, \pm 2$ that we use to construct the GSN transformation. For each transformation, we give *explicit expressions* for the weighting functions $\alpha(r), \beta(r)$, the determinant of the transformation matrix $\eta(r)$, the asymptotic solutions to the GSN equation at infinity and at the horizon for both the in-going and the out-going mode, and the conversion factors for transforming the asymptotic amplitudes between the Teukolsky function $R$ and the SN function $X$. Together with Sec. 4.2 and this appendix, one should have all the necessary ingredients to use the GSN formalism to numerically solve the *homogenous* radial Teukolsky equation for physically relevant radiation fields ($s = 0$ for scalar radiation, $s = \pm 1$ for electromagnetic radiation, and $s = \pm 2$ for gravitational radiation).

Despite being long-winded, we opt to show the expressions explicitly for the sake of completeness. Accompanying this paper are MATHEMATICA notebooks deriving and storing all the expressions shown here, and they can be found on Zenodo.[27] While the GSN formalism was proposed to facilitate numerical computations, all the expressions in this appendix and Sec. 4.2 are exact. In particular, we *do not assume* that $\omega$ is real when deriving expressions shown here and they can be used in QNM calculations with the GSN formalism (such as Ref. [87] using the parametrized BH quasi-normal ringdown formalism [88, 89, 90] to compute semi-analytical corrections from QNM frequencies for a

[27] https://doi.org/10.5281/zenodo.8080242

non-rotating BH, and Sec. 4.4.2). We also do not use the identities shown in Eq. (4.50) and Eq. (4.51) to simplify the expressions for the conversion factors below.

### 4.9.1 Scalar radiation $s = 0$

By choosing $g_0(r) = 1$, we have the weighting functions

$$\alpha(r) = 1, \tag{4.108a}$$

$$\beta(r) = 0. \tag{4.108b}$$

The determinant of the transformation matrix $\eta(r)$ can be written as

$$\eta = c_0 + c_1/r + c_2/r^2 + c_3/r^3 + c_4/r^4$$

with the coefficients

$$c_0 = 1, \tag{4.109a}$$

$$c_{1,2,3,4} = 0. \tag{4.109b}$$

The asymptotic out-going mode of $X$ when $r_* \to \infty$ is given by

$$X(r_* \to \infty) \propto f_+^\infty(r) e^{i\omega r_*} = e^{i\omega r_*}\left(1 + \sum_{j=1}^{\infty} \frac{C_{+,j}^\infty}{r^j}\right)$$

with the first three expansion coefficients

$$C_{+,1}^\infty = \frac{1}{2} i \left(\lambda + 2am\omega\right), \tag{4.110a}$$

$$\begin{aligned} C_{+,2}^\infty = \frac{1}{8}\{&-\lambda^2 + \lambda\left(2 - 4am\omega\right) \\ &+4\omega\left[i - a^2m^2\omega + a\left(m + 2im\omega\right)\right]\}, \end{aligned} \tag{4.110b}$$

$$\begin{aligned} C_{+,3}^\infty = -\frac{1}{48} i \{&\lambda^3 + \lambda^2(-8 + 6am\omega) \\ &+4\lambda\left[3 - (9i + 8am)\,\omega + a\left(2a - 6im + 3am^2\right)\omega^2\right] \\ &+8\omega\left[3i + a^2\left(-1 + m^2(-3 - 6i\omega)\right)\omega\right. \\ &\left.+a^3 m\left(2 + m^2\right)\omega^2 + am\left(3 - 3i\omega - 8\omega^2\right)\right]\}. \end{aligned} \tag{4.110c}$$

The asymptotic in-going mode of $X$ when $r_* \to \infty$ is given by

$$X(r_* \to \infty) \propto f_-^\infty(r) e^{-i\omega r_*} = e^{-i\omega r_*}\left(1 + \sum_{j=1}^{\infty} \frac{C_{-,j}^\infty}{r^j}\right)$$

with the first three expansion coefficients

$$\begin{aligned}
C_{-,1}^\infty &= -\frac{1}{2} i \left(\lambda + 2am\omega\right), && \text{(4.111a)}\\
C_{-,2}^\infty &= \frac{1}{8}\left\{-\lambda^2 + \lambda\left(2 - 4am\omega\right)\right. && \text{(4.111b)}\\
&\quad \left. -4\omega\left[i + am\left(-1 + 2i\omega\right) + a^2 m^2 \omega\right]\right\}, \\
C_{-,3}^\infty &= \frac{1}{48} i \left\{\lambda^3 + \lambda^2\left(-8 + 6am\omega\right)\right. && \text{(4.111c)}\\
&\quad +4\lambda\left[3 + \left(9i - 8am\right)\omega + a\left(2a + 6im + 3am^2\right)\omega^2\right] \\
&\quad +8\omega\left[-3i + a^2\left(-1 + m^2(-3 + 6i\omega)\right)\omega\right. \\
&\quad \left. \left. +a^3 m\left(2 + m^2\right)\omega^2 + am\left(3 + 3i\omega - 8\omega^2\right)\right]\right\}.
\end{aligned}$$

These expressions (except for $C_{+,j}^\infty$) match with those found in Ref. [48]. Note that $C_{+,j}^\infty = \left(C_{-,j}^\infty\right)^*$ as claimed in Ref. [48] is true only for real $\omega$ since the GSN potentials $\mathcal{F}, \mathcal{U}$ are real-valued in this case.

The conversion factors between the GSN and the Teukolsky formalism are found to be

$$\begin{aligned}
\frac{B_{\rm T}^{\rm ref}}{B_{\rm SN}^{\rm ref}} = \frac{C_{\rm T}^{\rm trans}}{C_{\rm SN}^{\rm trans}} &= 1, && \text{(4.112a)}\\
\frac{B_{\rm T}^{\rm inc}}{B_{\rm SN}^{\rm inc}} &= 1, && \text{(4.112b)}\\
\frac{C_{\rm T}^{\rm inc}}{C_{\rm SN}^{\rm inc}} &= \frac{1}{\sqrt{2r_+}}, && \text{(4.112c)}\\
\frac{B_{\rm T}^{\rm trans}}{B_{\rm SN}^{\rm trans}} = \frac{C_{\rm T}^{\rm ref}}{C_{\rm SN}^{\rm ref}} &= \frac{1}{\sqrt{2r_+}}. && \text{(4.112d)}
\end{aligned}$$

Note that these conversion factors are frequency-independent.

### 4.9.2 Electromagnetic radiation

#### 4.9.2.1 $s = +1$

By choosing $g_0(r) = \dfrac{r^2 + a^2}{r^2}$ and $g_1(r) = 1$, we have the weighting functions

$$\begin{aligned} \alpha(r) &= \frac{1}{r^2\sqrt{\Delta}}\left[-ia^3m - iamr^2 + ia^4\omega \right. \\ &\quad \left. + r^3\left(1 + ir\omega\right) + a^2\left(-2 + r + 2ir^2\omega\right)\right], \end{aligned} \tag{4.113a}$$

$$\beta(r) = \frac{\left(r^2 + a^2\right)}{r^2\Delta^{3/2}}. \tag{4.113b}$$

The determinant of the transformation matrix $\eta(r)$ can be written as

$$\eta = c_0 + c_1/r + c_2/r^2 + c_3/r^3 + c_4/r^4$$

with the coefficients

$$c_0 = -\left(2 + \lambda\right), \tag{4.114a}$$

$$c_1 = 2iam, \tag{4.114b}$$

$$c_2 = -a^2\left(3 + 2\lambda\right), \tag{4.114c}$$

$$c_3 = -2a^2\left(1 - iam\right), \tag{4.114d}$$

$$c_4 = -a^4\left(1 + \lambda\right). \tag{4.114e}$$

The asymptotic out-going mode of $X$ when $r_* \to \infty$ is given by

$$X(r_* \to \infty) \propto f_+^\infty(r) e^{i\omega r_*} = e^{i\omega r_*}\left(1 + \sum_{j=1}^{\infty} \frac{C_{+,j}^\infty}{r^j}\right)$$

with the first three expansion coefficients

$$C_{+,1}^\infty = \frac{1}{2} i \left(2 + \lambda + 2am\omega\right), \tag{4.115a}$$

$$C_{+,2}^\infty = \frac{1}{8}\left[-\lambda^2 - 2\lambda\left(1 + 2am\omega\right) - 4a\omega\left(m - 2a\omega - 2im\omega + am^2\omega\right)\right], \tag{4.115b}$$

$$\begin{aligned} C_{+,3}^\infty = -\frac{1}{48} i \Big\{ & \lambda^3 + \lambda^2\left(-2 + 6am\omega\right) \\ & + 4\lambda\left[-2 - 2\left(3i + am\right)\omega \right. \\ & \left. + a\left(-4a - 6im + 3am^2\right)\omega^2\right] \\ & + 8\omega\left[-6i + a^3 m\left(-4 + m^2\right)\omega^2 \right. \\ & \left. + 3a^2\omega\left(-1 - 2im^2\omega\right) - am\left(3 + 6i\omega + 8\omega^2\right)\right]\Big\}. \end{aligned} \tag{4.115c}$$

The asymptotic in-going mode of $X$ when $r_* \to \infty$ is given by

$$X(r_* \to \infty) \propto f_-^\infty(r) e^{-i\omega r_*} = e^{-i\omega r_*}\left(1 + \sum_{j=1}^{\infty} \frac{C_{-,j}^\infty}{r^j}\right)$$

with the first three expansion coefficients

$$\begin{aligned}
C_{-,1}^\infty &= \frac{1}{2c_0} i \left[4 + \lambda^2 + 8am\omega + 2\lambda\left(2 + am\omega\right)\right], && \text{(4.116a)}\\
C_{-,2}^\infty &= \frac{1}{8c_0}\left\{\lambda^3 + 4\lambda^2(1 + am\omega)\right. && \text{(4.116b)}\\
&\quad +8a\omega\left[m\left(2 + 2i\omega\right) - a\omega + 3am^2\omega\right]\\
&\quad \left.+4\lambda\left[1 + am\left(5 + 2i\omega\right)\omega + a^2\left(-2 + m^2\right)\omega^2\right]\right\},\\
C_{-,3}^\infty &= -\frac{1}{48c_0} i \left\{\lambda^4 + 6am\lambda^3\omega\right. && \text{(4.116c)}\\
&\quad +4\lambda^2\left[-3 + \left(6i + 4am\right)\omega\right. && \text{(4.116d)}\\
&\quad \left.+a\left(-4a + 6im + 3am^2\right)\omega^2\right]\\
&\quad +8\lambda\left[-2 + \left(12i - 5am\right)\omega\right.\\
&\quad +a\left(12im + a(-4 + 9m^2)\right)\omega^2\\
&\quad \left.+am\left(-8 + 6iam + a^2(-4 + m^2)\right)\omega^3\right]\\
&\quad +16\omega\left[6i + a^3 m\left(-1 + 4m^2\right)\omega^2\right.\\
&\quad +3ia^2\omega\left(i - 2\omega + 4m^2\omega\right)\\
&\quad \left.\left.+am\left(-3 + 12i\omega - 8\omega^2\right)\right]\right\}.
\end{aligned}$$

The conversion factors between the GSN and the Teukolsky formalism are found to be

$$\frac{B_{\rm T}^{\rm ref}}{B_{\rm SN}^{\rm ref}} = \frac{C_{\rm T}^{\rm trans}}{C_{\rm SN}^{\rm trans}} = \frac{1}{2i\omega}, \tag{4.117a}$$

$$\frac{B_{\rm T}^{\rm inc}}{B_{\rm SN}^{\rm inc}} = \frac{2i\omega}{c_0}, \tag{4.117b}$$

$$\frac{C_{\rm T}^{\rm inc}}{C_{\rm SN}^{\rm inc}} = \frac{r_+^{3/2}}{4\sqrt{2}}, \times \left[r_+(1+4i\omega - iam) - a^2(1+2i\omega)\right]^{-1} \tag{4.117c}$$

$$\frac{B_{\rm T}^{\rm trans}}{B_{\rm SN}^{\rm trans}} = \frac{C_{\rm T}^{\rm ref}}{C_{\rm SN}^{\rm ref}} = \sqrt{2r_+}\frac{2r_+\omega - am}{2am + 2i(2+\lambda)}. \tag{4.117d}$$

#### 4.9.2.2 $s = -1$

By choosing $g_0(r) = \dfrac{r^2+a^2}{r^2}$ and $g_1(r) = 1$, we have the weighting functions

$$\alpha(r) = -\frac{\sqrt{\Delta}}{r^2}\left[r + i\frac{\left(r^2+a^2\right)K}{\Delta}\right], \tag{4.118a}$$

$$\beta(r) = \frac{\sqrt{\Delta}\left(r^2+a^2\right)}{r^2}. \tag{4.118b}$$

The determinant of the transformation matrix $\eta(r)$ can be written as

$$\eta = c_0 + c_1/r + c_2/r^2 + c_3/r^3 + c_4/r^4$$

with the coefficients

$$c_0 = -\lambda, \tag{4.119a}$$

$$c_1 = -2iam, \tag{4.119b}$$

$$c_2 = a^2\left(1-2\lambda\right), \tag{4.119c}$$

$$c_3 = -2a^2\left(1+iam\right), \tag{4.119d}$$

$$c_4 = a^4\left(1-\lambda\right). \tag{4.119e}$$

The asymptotic out-going mode of $X$ when $r_* \to \infty$ is given by

$$X(r_* \to \infty) \propto f_+^\infty(r) e^{i\omega r_*} = e^{i\omega r_*}\left(1 + \sum_{j=1}^{\infty} \frac{C_{+,j}^\infty}{r^j}\right)$$

with the first three expansion coefficients

$$C_{+,1}^\infty = -\frac{1}{2c_0} i \left(\lambda^2 + 4am\omega + 2am\lambda\omega\right), \tag{4.120a}$$

$$\begin{aligned} C_{+,2}^\infty = \frac{1}{8c_0} \big[&\lambda^3 - \lambda^2 (2 - 4am\omega) - \\ &8a\omega \left(m - a\omega - 2am^2\omega\right) \\ &+4a\omega\lambda \left(m - 2a\omega - 2im\omega + am^2\omega\right)\big], \end{aligned} \tag{4.120b}$$

$$\begin{aligned} C_{+,3}^\infty = \frac{1}{48c_0} i \big\{&\lambda^4 + \lambda^3(-8 + 6am\omega) \\ &+4\lambda^2 \left[3 - (6i + 5am)\,\omega \right. \\ &\left. +a\left(-4a - 6im + 3am^2\right)\omega^2\right] \\ &+48a\omega \left[a(-1 + 2i\omega)\omega + a^2m^3\omega^2 \right. \\ &\left. -2iam^2\omega(-i + \omega) + m\left(1 - 2i\omega + a^2\omega^2\right)\right] \\ &+8a\lambda\omega \left[4a\omega + 3am^2(1 - 2i\omega)\omega + a^2m^3\omega^2 \right. \\ &\left. -4m\left(1 + (2 + a^2)\omega^2\right)\right]\big\}. \end{aligned} \tag{4.120c}$$

The asymptotic in-going mode of $X$ when $r_* \to \infty$ is given by

$$X(r_* \to \infty) \propto f_-^\infty(r) e^{-i\omega r_*} = e^{-i\omega r_*}\left(1 + \sum_{j=1}^{\infty} \frac{C_{-,j}^\infty}{r^j}\right)$$

with the first three expansion coefficients

$$\begin{aligned}
C_{-,1}^\infty &= -\frac{1}{2} i \left(\lambda + 2am\omega\right), && \text{(4.121a)}\\
C_{-,2}^\infty &= \frac{1}{8}\left[-\lambda^2 + \lambda\left(2 - 4am\omega\right)\right. && \text{(4.121b)}\\
&\quad \left. +4a\omega\left(m + 2a\omega - 2im\omega - am^2\omega\right)\right],\\
C_{-,3}^\infty &= \frac{1}{48} i \left\{\lambda^3 + \lambda^2(-8 + 6am\omega)\right. && \text{(4.121c)}\\
&\quad +4\lambda\left[3 + (6i - 8am)\omega + a\left(-4a + 6im + 3am^2\right)\omega^2\right]\\
&\quad +8a\omega\left[a\omega + 3am^2\left(-1 + 2i\omega\right)\omega + a^2m^3\omega^2\right.\\
&\quad \left.\left. +m\left(2 - 4\left(2 + a^2\right)\omega^2\right)\right]\right\}.
\end{aligned}$$

These expressions (except for $C_{+,j}^\infty$) match with those found in Ref. [48]. Note that $C_{+,j}^\infty = \left(C_{-,j}^\infty\right)^*$ as claimed in Ref. [48] is *not true* even for real $\omega$ since the GSN potentials $\mathcal{F}, \mathcal{U}$ are in general complex-valued.

The conversion factors between the GSN and the Teukolsky formalism are found to be

$$\begin{aligned}
\frac{B_{\rm T}^{\rm ref}}{B_{\rm SN}^{\rm ref}} = \frac{C_{\rm T}^{\rm trans}}{C_{\rm SN}^{\rm trans}} &= -\frac{2i\omega}{c_0}, && \text{(4.122a)}\\
\frac{B_{\rm T}^{\rm inc}}{B_{\rm SN}^{\rm inc}} &= -\frac{1}{2i\omega}, && \text{(4.122b)}\\
\frac{C_{\rm T}^{\rm inc}}{C_{\rm SN}^{\rm inc}} &= -\frac{\sqrt{r_+}\left[\left(am - 4\omega\right)r_+ + 2a^2\omega\right]}{\sqrt{2}\left(am - i\lambda\right)}, && \text{(4.122c)}\\
\frac{B_{\rm T}^{\rm trans}}{B_{\rm SN}^{\rm trans}} = \frac{C_{\rm T}^{\rm ref}}{C_{\rm SN}^{\rm ref}} &= \frac{r_+^{3/2}}{4\sqrt{2}} && \text{(4.122d)}\\
&\quad \times\left[\left(1 + iam - 4i\omega\right)r_+ - a^2\left(1 - 2i\omega\right)\right]^{-1}.
\end{aligned}$$

### 4.9.3 Gravitational radiation

#### 4.9.3.1 $s = +2$

By choosing $g_0(r) = \dfrac{r^2}{r^2+a^2}$, $g_1(r) = 1$, and $g_2(r) = \dfrac{r^2+a^2}{r^2}$ , we have the weighting functions

$$\begin{aligned}
\alpha(r) &= \frac{1}{r^2\Delta}\left\{4a^3mr\left(i+r\omega\right)\right. \qquad (4.123a)\\
&\quad +2amr^2\left(i-3ir+2r^2\omega\right)-2a^4\left(-3+2ir\omega+r^2\omega^2\right)\\
&\quad +r^3\left[-2\lambda+r\left(2+\lambda+10i\omega\right)-2r^3\omega^2\right]\\
&\quad \left.-a^2r\left(8+2m^2r-r\lambda+2ir\omega+4ir^2\omega+4r^3\omega^2\right)\right\},\\
\beta(r) &= \frac{1}{r\Delta^3}\left[-2iamr+a^2\left(-4+2ir\omega\right)+2r\left(3-r+ir^2\omega\right)\right] \qquad (4.123b)
\end{aligned}$$

The determinant of the transformation matrix $\eta(r)$ can be written as

$$\eta = c_0 + c_1/r + c_2/r^2 + c_3/r^3 + c_4/r^4$$

with the coefficients

$$\begin{aligned}
c_0 &= 24+12i\omega+\lambda(10+\lambda)-12a\omega\left(a\omega-m\right), \qquad (4.124a)\\
c_1 &= -32iam-8iam\lambda+8ia^2\omega(1+\lambda), \qquad (4.124b)\\
c_2 &= 12a^2-24iam-24a^2m^2+24ia^2\omega+48a^3m\omega-24a^4\omega^2 \qquad (4.124c)\\
c_3 &= -24ia^3\left(a\omega-m\right)-24a^2, \qquad (4.124d)\\
c_4 &= 12a^4. \qquad (4.124e)
\end{aligned}$$

The asymptotic out-going mode of $X$ when $r_* \to \infty$

$$X(r_* \to \infty) \propto f_+^\infty(r) e^{i\omega r_*} = e^{i\omega r_*}\left(1 + \sum_{j=1}^{\infty} \frac{C_{+,j}^\infty}{r^j}\right)$$

with the first three expansion coefficients

$$\begin{aligned}
C_{+,1}^\infty &= \frac{1}{2} i \left(6 + \lambda + 2am\omega\right), && \text{(4.125a)}\\
C_{+,2}^\infty &= -\frac{1}{8}\left\{\lambda^2 + 2\lambda\left(5 + 2am\omega\right)\right. && \text{(4.125b)}\\
&\quad \left. +4\left[6 + (3i + 5am)\,\omega + am\,(-2i + am)\,\omega^2\right]\right\}, \\
C_{+,3}^\infty &= -\frac{1}{48} i \left\{\lambda^3 + 2\lambda^2\left(5 + 3am\omega\right)\right. && \text{(4.125c)}\\
&\quad +4\lambda\left[6 + (3i + 10am)\,\omega + a\left(2a - 6im + 3am^2\right)\omega^2\right] \\
&\quad +8a\omega\left[a\omega + 6am^2\,(1 - i\omega)\,\omega + a^2 m^3 \omega^2\right. \\
&\quad \left.\left. +m\left(2 - 9i\omega + 2(-4 + a^2)\omega^2\right)\right]\right\}.
\end{aligned}$$

The asymptotic in-going mode of $X$ when $r_* \to \infty$

$$X(r_* \to \infty) \propto f_-^\infty(r) e^{-i\omega r_*} = e^{-i\omega r_*}\left(1 + \sum_{j=1}^{\infty} \frac{C_{-,j}^\infty}{r^j}\right)$$

with the first three expansion coefficients

$$
\begin{aligned}
C^{\infty}_{-,1} &= \frac{1}{2c_0} i \left\{ -\lambda^3 - 2\lambda^2(8 + am\omega) + 4\lambda \left[ -21 - 3\left(i + 4am\right)\omega + 7a^2\omega^2 \right] \right. && (4.126a)\\
&\quad \left. +8\left[ -18 - \left(9i + 23am\right)\omega + a\left(11a - 3im - 3am^2\right)\omega^2 + 3a^3 m\omega^3 \right] \right\},\\
C^{\infty}_{-,2} &= -\frac{1}{8c_0} \left\{ \lambda^4 + 4\lambda^3 \left(5 + am\omega\right) \right. && (4.126b)\\
&\quad +4\lambda^2 \left[ 37 + 2am\left(13 + i\omega\right)\omega + a^2\left(-11 + m^2\right)\omega^2 \right]\\
&\quad -8\lambda \left[ -60 + 8am\left(-11 - 2i\omega\right)\omega + a^2\left(39 - 19m^2\right)\omega^2 + 14a^3 m\omega^3 \right]\\
&\quad -16 \left[ a^2\left(34 + m^2(-49 - 9i\omega) + 3i\omega\right)\omega^2 \right.\\
&\quad +a^3 m\left(43 - 3m^2 + 6i\omega\right)\omega^3 + 3a^4\left(-4 + m^2\right)\omega^4\\
&\quad \left. \left. -9\left(4 + \omega^2\right) + 2am\omega\left(-44 - 15i\omega + 3\omega^2\right) \right] \right\},\\
C^{\infty}_{-,3} &= -\frac{1}{48c_0} i \left\{ -\lambda^5 - 2\lambda^4(10 + 3am\omega) \right. && (4.126c)\\
&\quad -4\lambda^3 \left[ 37 + 2am\left(20 + 3i\omega\right)\omega + a^2\left(-13 + 3m^2\right)\omega^2 \right]\\
&\quad -8\lambda^2 \left[ 60 + 2a^2\left(-29 + 3m^2(9 + i\omega)\right)\omega^2 \right.\\
&\quad \left. +a^3 m\left(-31 + m^2\right)\omega^3 + am\omega\left(157 + 48i\omega - 8\omega^2\right) \right]\\
&\quad +16\lambda \left[ a^2\left(91 + m^2(-210 - 81i\omega) + 9i\omega\right)\omega^2 \right.\\
&\quad +2a^3 m\left(73 - 13m^2 + 21i\omega\right)\omega^3 + 3a^4\left(-10 + 7m^2\right)\omega^4\\
&\quad \left. -9\left(4 + \omega^2\right) + 2am\omega\left(-116 - 63i\omega + 29\omega^2\right) \right]\\
&\quad +96a\omega \left[ -a^3 m^4\omega^3 + a\omega\left(18 + 9i\omega - 11a^2\omega^2\right) \right.\\
&\quad +a^2 m^3\omega^2\left(-28 - 7i\omega + a^2\omega^2\right)\\
&\quad +am^2\omega\left(-70 - 55i\omega + 2(7 + 15a^2)\omega^2 + 6ia^2\omega^3\right)\\
&\quad \left. \left. +m\left(-36 - 36i\omega + (25 + 47a^2)\omega^2 + i(8 + 23a^2)\omega^3 - 2a^2(4 + 5a^2)\omega^4\right) \right] \right\}.
\end{aligned}
$$

The conversion factors

$$\frac{B_{\rm T}^{\rm ref}}{B_{\rm SN}^{\rm ref}} = \frac{C_{\rm T}^{\rm trans}}{C_{\rm SN}^{\rm trans}} = -\frac{1}{4\omega^2}, \tag{4.127a}$$

$$\frac{B_{\rm T}^{\rm inc}}{B_{\rm SN}^{\rm inc}} = -\frac{4\omega^2}{c_0}, \tag{4.127b}$$

$$\begin{aligned}\frac{C_{\rm T}^{\rm inc}}{C_{\rm SN}^{\rm inc}} = & -\frac{r_+^{3/2}}{4\sqrt{2}}\left\{\left[2\left(-1-6i\omega+8\omega^2\right)\right.\right. \\ & \left.+a^2\left(2+m^2+9i\omega-8\omega^2\right)+am\left(3i-8\omega\right)\right]r_+^2 \\ & \left.+a^3\left(-3i+4\omega\right)\left(mr_+-a\omega\right)\right\}^{-1},\end{aligned} \tag{4.127c}$$

$$\begin{aligned}\frac{B_{\rm T}^{\rm trans}}{B_{\rm SN}^{\rm trans}} = \frac{C_{\rm T}^{\rm ref}}{C_{\rm SN}^{\rm ref}} = & \ 2\sqrt{2}r_+^{3/2} \\ & \times\left\{\left[4\omega\left(i-4\omega\right)-am\left(i-8\omega\right)\right.\right. \\ & \left.-a^2\left(m^2+2i\omega-4\omega^2\right)\right]r_+^2+a^2\left(i-4\omega\right)\left(am-2\omega\right)r_+\Big\} \\ & \times\left\{2r_+^3\left(24+10\lambda+\lambda^2+12i\omega\right)-r_+^2\left[8iam\left(11+2\lambda+6i\omega\right)\right.\right. \\ & \left.+a^2\left(24+24m^2+10\lambda+\lambda^2-28i\omega-16i\lambda\omega+48\omega^2\right)\right] \\ & \left.+8ia^3r_+\left[m\left(7+\lambda-6i\omega\right)-a\omega\left(4+\lambda\right)\right]+12a^5\omega\left(a\omega-3m\right)\right\}^{-1}.\end{aligned} \tag{4.127d}$$

#### 4.9.3.2 $s = -2$

By choosing $g_0(r) = \dfrac{r^2}{r^2+a^2}$, $g_1(r) = 1$, and $g_2(r) = \dfrac{r^2+a^2}{r^2}$ [28], we have the weighting functions

$$\begin{aligned}
\alpha(r) &= \frac{1}{r^2\Delta}\left\{4a^3mr\left(-i+r\omega\right)\right. \qquad (4.128a)\\
&\quad +2amr^2\left(3i-ir+2r^2\omega\right)+a^4\left(6+4ir\omega-2r^2\omega^2\right)\\
&\quad +a^2r\left[-24+r\left(12-2m^2+\lambda-6i\omega\right)+12ir^2\omega-4r^3\omega^2\right]\\
&\quad \left.+r^2\left[24-2r\left(12+\lambda\right)+r^2\left(6+\lambda-18i\omega\right)+8ir^3\omega-2r^4\omega^2\right]\right\},\\
\beta(r) &= \frac{2\Delta}{r}\left[iamr+a^2\left(-2-ir\omega\right)+r\left(3-r-ir^2\omega\right)\right]. \qquad (4.128b)
\end{aligned}$$

The determinant of the transformation matrix $\eta(r)$ can be written as

$$\eta = c_0 + c_1/r + c_2/r^2 + c_3/r^3 + c_4/r^4$$

with the coefficients

$$\begin{aligned}
c_0 &= -12i\omega+\lambda(2+\lambda)-12a\omega\left(a\omega-m\right), \qquad (4.129a)\\
c_1 &= 8iam\lambda+8ia^2\omega(3-\lambda), \qquad (4.129b)\\
c_2 &= -24ia\left(a\omega-m\right)+12a^2\left[1-2\left(a\omega-m\right)^2\right], \qquad (4.129c)\\
c_3 &= 24ia^3\left(a\omega-m\right)-24a^2, \qquad (4.129d)\\
c_4 &= 12a^4. \qquad (4.129e)
\end{aligned}$$

[28] Note that $g_0, g_1, g_2$ here are not the same as the $f, g, h$ in Ref. [54]. In fact, we see that $g = g_1 = 1$ and $h = g_2 = \dfrac{r^2+a^2}{r^2}$ but $f = g_0g_1g_2 = 1$.

The asymptotic out-going mode of $X$ when $r_* \to \infty$

$$X(r_* \to \infty) \propto f_+^\infty(r) e^{i\omega r_*} = e^{i\omega r_*}\left(1 + \sum_{j=1}^{\infty} \frac{C_{+,j}^\infty}{r^j}\right)$$

with the first three expansion coefficients

$$\begin{aligned}
C_{+,1}^\infty &= -\frac{1}{2c_0} i \left\{-\lambda^3 - 2\lambda^2(2 + am\omega)\right. && \text{(4.130a)}\\
&\quad +4\lambda\left[-1 + (3i - 8am)\,\omega + 7a^2\omega^2\right]\\
&\quad \left.+24\omega\left[i - a^2\left(1 + m^2\right)\omega + a^3 m\omega^2 + iam(i + \omega)\right]\right\},\\
C_{+,2}^\infty &= -\frac{1}{8c_0}\left\{\lambda^4 + 4\lambda^3(1 + am\omega)\right. && \text{(4.130b)}\\
&\quad +4\lambda^2\left[1 + 2am\,(7 - i\omega)\,\omega + a^2\left(-11 + m^2\right)\omega^2\right]\\
&\quad -8a\lambda\omega\left[-5a\omega - 15am^2\omega + 2m\left(-4 + 4i\omega + 7a^2\omega^2\right)\right]\\
&\quad -48\omega^2\left[-3 - a^3 m\left(-5 + m^2 + 2i\omega\right)\omega + a^4\left(-4 + m^2\right)\omega^2\right.\\
&\quad \left.\left.+2am\,(i + \omega) + ia^2\left(-\omega + 5im^2 + 3m^2\omega\right)\right]\right\},\\
C_{+,3}^\infty &= \frac{1}{48c_0} i \left\{-\lambda^5 - 6am\lambda^4\omega\right. && \text{(4.130c)}\\
&\quad -4\lambda^3\left[-3 + 2am\,(8 - 3i\omega)\,\omega + a^2\left(-13 + 3m^2\right)\omega^2\right]\\
&\quad -8\lambda^2\left[-2 + 2a^2\left(10 + 3m^2(6 - i\omega)\right)\omega^2\right.\\
&\quad \left.+a^3 m\left(-31 + m^2\right)\omega^3 - am\omega\left(11 + 12i\omega + 8\omega^2\right)\right]\\
&\quad +16\lambda\omega\left[-9\omega + 3a^2\left(5 + m^2(-10 + 19i\omega) - 3i\omega\right)\omega\right.\\
&\quad -2a^3 m\left(-11 + 11m^2 + 21i\omega\right)\omega^2 + 3a^4\left(-10 + 7m^2\right)\omega^3\\
&\quad \left.+2am\left(6 + 3i\omega + 13\omega^2\right)\right] + 96\omega^2\left[6 + am(-3 - 8i\omega)\omega\right.\\
&\quad +a^4\left(9 - m^4 + 2m^2(8 - 3i\omega)\right)\omega^2 + a^5 m\left(-10 + m^2\right)\omega^3\\
&\quad +a^3 m\omega\left(-9 + m^2(-12 + 7i\omega) + 5i\omega - 8\omega^2\right)\\
&\quad \left.\left.+a^2\left(-3i\omega + m^2\left(6 + 9i\omega + 14\omega^2\right)\right)\right]\right\}.
\end{aligned}$$

The asymptotic in-going mode of $X$ when $r_* \to \infty$

$$X(r_* \to \infty) \propto f_-^\infty(r) e^{-i\omega r_*} = e^{-i\omega r_*}\left(1 + \sum_{j=1}^{\infty} \frac{C_{-,j}^\infty}{r^j}\right)$$

with the first three expansion coefficients

$$C_{-,1}^\infty = -\frac{1}{2} i \left(2 + \lambda + 2am\omega\right), \tag{4.131a}$$

$$C_{-,2}^\infty = \frac{1}{8}\left\{-\lambda^2 - 2\lambda(1 + 2am\omega) - 4\omega\left[-3i + a^2m^2\omega + a\left(m + 2im\omega\right)\right]\right\}, \tag{4.131b}$$

$$\begin{aligned} C_{-,3}^\infty = \frac{1}{48} i \Big\{ & \lambda^3 + \lambda^2\left(-2 + 6am\omega\right) \\ & + 4\lambda\left[-2 - (3i + 2am)\,\omega + a\left(2a + 6im + 3am^2\right)\omega^2\right] \\ & + 8\omega\left[6i + a^3 m\left(2 + m^2\right)\omega^2 + 3a^2\omega\left(-1 + 2im^2\omega\right) - am\left(6 + 3i\omega + 8\omega^2\right)\right]\Big\}. \end{aligned} \tag{4.131c}$$

The conversion factors

$$\frac{B_{\mathrm{T}}^{\mathrm{ref}}}{B_{\mathrm{SN}}^{\mathrm{ref}}} = \frac{C_{\mathrm{T}}^{\mathrm{trans}}}{C_{\mathrm{SN}}^{\mathrm{trans}}} = -\frac{4\omega^2}{c_0}, \tag{4.132a}$$

$$\frac{B_{\mathrm{T}}^{\mathrm{inc}}}{B_{\mathrm{SN}}^{\mathrm{inc}}} = -\frac{1}{4\omega^2}, \tag{4.132b}$$

$$\frac{C_{\mathrm{T}}^{\mathrm{inc}}}{C_{\mathrm{SN}}^{\mathrm{inc}}} = -\frac{4p\sqrt{2r_+}}{\eta\left(r_+\right)}\left[2pr_+ + i\left(r_+ - 1\right)\right], \tag{4.132c}$$

$$\begin{aligned} \frac{B_{\mathrm{T}}^{\mathrm{trans}}}{B_{\mathrm{SN}}^{\mathrm{trans}}} = \frac{C_{\mathrm{T}}^{\mathrm{ref}}}{C_{\mathrm{SN}}^{\mathrm{ref}}} = & \frac{1}{\sqrt{2r_+}}\Big[\left(8 - 24i\omega - 16\omega^2\right) r_+^2 \\ & + \left(12iam - 16 + 16am\omega + 24i\omega\right) r_+ + \left(-4a^2m^2 - 12iam + 8\right)\Big]^{-1}. \end{aligned} \tag{4.132d}$$

These expressions match those found in literature, for example Refs. [82, 91, 61]. Note again that $C_{+,j}^\infty \neq \left(C_{-,j}^\infty\right)^*$ even for real $\omega$ since the GSN potentials $\mathcal{F}, \mathcal{U}$ are in general complex-valued.[29]

[29] This was corrected in the erratum [92] for Ref. [82]. In both Refs. [91, 92], expressions for

$C^{\infty}_{+,j}$ written in a form much more concise than that in Eq. (4.130) were shown by relating them with the complex conjugate of $C^{\infty}_{-,j}$. Those expressions are valid only for real $\omega$. We opt to not make such an assumption when deriving the expressions and hence not many simplifications can be made.

*Chapter 5*

# GRAVITATIONAL-WAVE ECHOES FROM SPINNING EXOTIC COMPACT OBJECTS: NUMERICAL WAVEFORMS FROM THE TEUKOLSKY EQUATION

This chapter contains work from

> S. Xin, B. Chen, R. K. L. Lo, et al. "Gravitational-wave echoes from spinning exotic compact objects: Numerical waveforms from the Teukolsky equation". In: *Phys. Rev. D* 104.10 (2021), p. 104005. DOI: 10.1103/PhysRevD.104.104005. arXiv: 2105.12313 [gr-qc].
> R. K. L. L performed the detectability analysis of echoes in current and future generation gravitational-wave detectors and wrote part of the manuscript.

## 5.1 Introduction

As discussed in Chapter 3, the presence of repeating bursts of gravitational waves (GWs), which are also referred to as GW echoes, after the merger of two compact objects can be used to test the nature of the merger remnant. If the remnant is not a black hole (BH) as predicted by general relativity (GR) but a novel compact object, referred to as an exotic compact object (ECO), the surface of the ECO could reflect some of the incident gravitational radiation, while the BH horizon would simply absorb all the incident radiation. In order to confidently detect these GW echoes and to also infer properties of the ECO from the echoes, we need to have a theoretical modeling of ECOs and the ability to predict gravitational waveforms of echoes being emitted by those ECO remnant.

Here we model the *exterior* spacetime of an ECO with a mass $M$ and a dimensionless spin parameter $\chi \equiv a/M$ where $a$ is the angular momentum per unit mass of the object with a Kerr BH spacetime of the same mass and dimensionless spin parameter, except when very close to the would-be event horizon of

the BH, the ECO has a surface at the Boyer-Lindquist coordinate $r^{\rm ECO}$ in place of the horizon. Since we only measure GWs reflected off of the surface, the physics of the ECO *interior* is entirely encoded in the response of the surface to incident waves, which is the surface's reflectivity. Later in this chapter, we will be using two ECO reflectivity models, namely the Lorentzian reflectivity and the Boltzmann reflectivity, in order to compute gravitational waveforms of echoes.

In this chapter, we first review the theory of computing gravitational waveforms using the Teukolsky equation in Sec. 5.2. In particular, we use a test particle falling into a Kerr BH as an example. This example also serves as a simplified model of a merger of a binary black hole (BBH) system. Then in Sec. 5.3, we construct GW echoes using the waveforms computed in Sec. 5.2 and a model of ECO surface reflectivity. In Sec. 5.5, we perform a detectability study to see if GW echoes can be detected with current-generation and future GW detectors in the optimal case where their waveforms are known accurately. Hereinafter we set $c = G = M = 1$.

## 5.2 Computing the gravitational waveform of a particle falling towards a Kerr black hole using the Teukolsky equation

Let us first consider GWs emitted by a particle falling into a Kerr BH.[1] The outgoing gravitational radiation at infinity is encoded in the Newman-Penrose scalar curvature $\psi_4$, which can be decomposed into frequency and angular components in the Boyer-Lindquist coordinates $(t, r, \theta, \phi)$ as

$$\begin{aligned}&\psi_4(t, r, \theta, \phi)\\ &\quad = (r - ia\cos\theta)^{-4} \int_{-\infty}^{+\infty} d\omega \sum_{\ell m} {}_{-2}R_{\ell m\omega}(r)\, {}_{-2}S_{\ell m}(\theta; a\omega) e^{im\phi} e^{-i\omega t}. \quad (5.1)\end{aligned}$$

Here ${}_{-2}S_{\ell m}$ is the spin-weighted spheroidal harmonic with the spin weight $s = -2$ appropriate for $\psi_4$ (see Appendix 4.5 for more details), while ${}_{-2}R_{\ell m\omega}$ is the

[1] Refer to Chapter 4 for the definition and the expression of symbols used here in this chapter.

solution to the radial Teukolsky equation

$$\Delta^2 \frac{d}{dr}\left(\frac{1}{\Delta}\frac{dR_{\ell m\omega}}{dr}\right) - V_{\rm T}(r) R_{\ell m\omega} = -T_{\ell m\omega}(r). \tag{5.2}$$

Note that here we specialized the radial Teukolsky equation to the $s = -2$ case, and hence we drop the subscript for $s$ hereafter when there is no risk for confusion. The source term $T_{\ell m\omega}(r)$ is determined by the mass and the trajectory of the falling test particle, and the full expression of the source term can be found in literature, for example in Ref. [33]. While our perturbative calculation formally should only be valid in the extreme mass-ratio limit, in Ref. [33] we have "calibrated" the source term for a test particle (with mass $\mu \ll M$) such that the gravitational waveforms computed using BH perturbation theory match with those for mergers of comparable mass-ratio BBHs using a surrogate model of numerical relativity NRSur7dq4 [93], which we will be using for subsequent calculations.

We look for solutions to the *sourced* ($T_{\ell m\omega} \neq 0$) radial Teukolsky equation in Eq. (5.2) that are only in-going at the horizon (denoted by the superscript in) and only out-going at infinity (denoted by the superscript up), by imposing that a solution $R^{\rm BH}_{\ell m\omega}(r)$ should behave asymptotically as

$$R^{\rm BH}_{\ell m\omega}(r) = \begin{cases} Z^{\rm in,BH}_{\ell m\omega}\Delta^2 e^{-ipr_*} & \text{as } r \to r_+, \\ Z^{\rm up,BH}_{\ell m\omega} r^3 e^{i\omega r_*} & \text{as } r \to \infty. \end{cases} \tag{5.3}$$

Using the Green's function approach, the wave amplitudes $Z^{\rm up,BH}_{\ell m\omega}, Z^{\rm in,BH}_{\ell m\omega}$ can be computed using convolution integrals of homogeneous solutions (see Chapter 4 for more details) satisfying the aforementioned boundary conditions with the source term $T_{\ell m\omega}$. Explicitly, they are given by

$$Z^{\rm in,BH}_{\ell m\omega} = \frac{B^{\rm trans}_{\rm T}}{2i\omega C^{\rm trans}_{\rm T} B^{\rm inc}_{\rm T}} \int_{r_+}^{\infty} d\bar{r} \frac{R^{\rm up}_{\ell m\omega}(\bar{r}) T_{\ell m\omega}(\bar{r})}{\Delta(\bar{r})^2}, \tag{5.4}$$

$$Z^{\rm up,BH}_{\ell m\omega} = \frac{1}{2i\omega B^{\rm inc}_{\rm T}} \int_{r_+}^{\infty} d\bar{r} \frac{R^{\rm in}_{\ell m\omega}(\bar{r}) T_{\ell m\omega}(\bar{r})}{\Delta(\bar{r})^2}. \tag{5.5}$$

As mentioned in Chapter 3, $\psi_4$ is related to the plus polarization $h_+$ and the cross polarization $h_\times$ of the GW at $r \to \infty$. Mathematically,

$$\psi_4(r \to \infty) = \frac{1}{2}\frac{d^2}{dt^2}\left(h_+ - ih_\times\right). \tag{5.6}$$

Therefore, if an observer is located at a distance $r$, a latitude angle $\Theta$ and an azimuthal angle $\Phi$ with respect to the source, then the GW seen by the observer is given by

$$h_+^{\rm BH} - ih_\times^{\rm BH}|_{(t,r,\Theta,\Phi)} = -\frac{2}{r}\sum_{\ell m}\int_{-\infty}^{+\infty} d\omega \frac{Z^{\rm up,BH}_{\ell m\omega}}{\omega^2}\,{}_{-2}S_{\ell m}(\Theta; a\omega)e^{im\Phi}e^{-i\omega(t-r_*)}. \tag{5.7}$$

Therefore, the wave amplitude $Z^{\rm up,BH}_{\ell m\omega}$ in Eq. (5.5) determines the gravitational waveform seen by observers at infinity.

## 5.3 Constructing gravitational-wave echoes from spinning exotic compact objects

### 5.3.1 Modifications to the boundary conditions

Formally, the Teukolsky equation was derived for Kerr BHs. However, as mentioned in Sec. 5.1, we assume that an exterior ECO spacetime is identical to a Kerr BH spacetime except when very close to the would-be event horizon of the BH. For this reason, we still use the Teukolsky equation to calculate gravitational waves emitted from ECOs. Since GW echoes are mainly sourced by the plunge part (past the light ring) of an in-falling trajectory, which is not significantly affected by the radiation reaction. Hence, we neglect any modification to the trajectory due to the ECO surface. Still, we need to change the boundary condition near the ECO surface at $r = r^{\rm ECO}$ for the radial Teukolsky function $R^{\rm ECO}_{\ell m\omega}(r)$ to a more general form

$$R^{\rm ECO}_{\ell m\omega}(r) = \begin{cases} Z^{\rm in}_{\ell m\omega}\Delta^2 e^{-ipr_*} + Z^{\rm out}_{\ell m\omega}e^{ipr_*} & \text{as } r \to r^{\rm ECO}, \\ Z^{\rm up,ECO}_{\ell m\omega} r^3 e^{i\omega r_*} & \text{as } r \to \infty. \end{cases} \tag{5.8}$$

Note that the form of $R^{\rm ECO}_{\ell m\omega}$ is changed near the ECO surface as we add an outgoing homogeneous solution $e^{ipr_*}$ with the amplitude $Z^{\rm out}_{\ell m\omega}$ (which is absent in

Eq. (5.3)) due to reflections from the ECO surface, while the content of $Z^{\rm in}_{\ell m\omega}$ is modified (compared to Eq. (5.3)) since additional waves propagate toward the ECO upon reflections from the inner side of the Kerr potential barrier near the light ring. Accordingly, the content of $Z^{\rm up,ECO}_{\ell m\omega}$ is also modified compared to $Z^{\rm up,BH}_{\ell m\omega}$ in Eq. (5.3), and that will determine the gravitational waveform from the ECO as observed at infinity.

### 5.3.2 Generation mechanism of gravitational-wave echoes

Schematically the wave amplitude $Z^{\rm up,ECO}_{\ell m\omega}$ should consist of two contributions, namely

$$Z^{\rm up,ECO}_{\ell m\omega} = Z^{\rm up,ringdown}_{\ell m\omega} + Z^{\rm up,echoes}_{\ell m\omega}. \tag{5.9}$$

The first term $Z^{\rm up,ringdown}_{\ell m\omega}$ is the contribution from the ringdown of the ECO due to the plunging particle, and a prescription to compute the second term $Z^{\rm up,echoes}_{\ell m\omega}$ is needed. Fig. 3.2 succinctly illustrates the generation mechanism of GW echoes. The blue arrow pointing to the right in Fig. 3.2 exactly corresponds to the first term $Z^{\rm up,ringdown}_{\ell m\omega}$ in Eq. (5.9). As for the contribution from echoes, from Fig. 3.2 we see that schematically $Z^{\rm up,echoes}_{\ell m\omega}$ can be written as

$$\begin{aligned} Z^{\rm up,echoes}_{\ell m\omega} = &\left(Z^{\rm plunge}_{\ell m\omega}\mathcal{R}^{\rm ECO}_{\ell m\omega}\right)\mathcal{T}^{\rm barrier}_{\ell m\omega} + \left(Z^{\rm plunge}_{\ell m\omega}\mathcal{R}^{\rm ECO}_{\ell m\omega}\mathcal{R}^{\rm barrier}_{\ell m\omega}\mathcal{R}^{\rm ECO}_{\ell m\omega}\right)\mathcal{T}^{\rm barrier}_{\ell m\omega} \\ &+ \left(Z^{\rm plunge}_{\ell m\omega}\mathcal{R}^{\rm ECO}_{\ell m\omega}\mathcal{R}^{\rm barrier}_{\ell m\omega}\mathcal{R}^{\rm ECO}_{\ell m\omega}\mathcal{R}^{\rm barrier}_{\ell m\omega}\mathcal{R}^{\rm ECO}_{\ell m\omega}\right)\mathcal{T}^{\rm barrier}_{\ell m\omega} + \dots \end{aligned}. \tag{5.10}$$

Let us inspect Eq. (5.10) more carefully. Starting from the first term, we see that $\mathcal{T}^{\rm barrier}_{\ell m\omega}$ is some sort of "transmissivity" measure of the Kerr BH potential that relates an out-going wave that goes through the potential barrier and eventually be seen by observers at infinity to the original wave that was incident onto the barrier from the left. As for $\mathcal{R}^{\rm ECO}_{\ell m\omega}$, it is a measure of "reflectivity" or *response* of the ECO surface to an incident wave $Z^{\rm plunge}_{\ell m\omega}$ such that the product $Z^{\rm plunge}_{\ell m\omega}\mathcal{R}^{\rm ECO}_{\ell m\omega}$ gives the wave generated (or "reflected") by the ECO as the result of the incident wave.

Looking at the second term in Eq. (5.10), the structure is identical to the first

term except now the incident wave onto the ECO surface is placed by the product $Z^{\rm plunge}_{\ell m\omega}\mathcal{R}^{\rm ECO}_{\ell m\omega}\mathcal{R}^{\rm barrier}_{\ell m\omega}$, where $\mathcal{R}^{\rm barrier}_{\ell m\omega}$ is some sort of "reflectivity" of the Kerr BH potential that relates an in-going wave that was reflected by the potential barrier to its original wave incident onto the barrier from the left. This in-going wave then becomes the incident wave onto the ECO surface that generates the next echo. It is clear that Eq. (5.10) is just a geometric series with a ratio $\mathcal{R}^{\rm ECO}_{\ell m\omega}\mathcal{R}^{\rm barrier}_{\ell m\omega}$ between successive terms. Therefore, we can write Eq. (5.10) as

$$\begin{aligned} Z^{\rm up,echoes}_{\ell m\omega} =& Z^{\rm plunge}_{\ell m\omega}\mathcal{R}^{\rm ECO}_{\ell m\omega}\mathcal{T}^{\rm barrier}_{\ell m\omega}\left[1+\mathcal{R}^{\rm ECO}_{\ell m\omega}\mathcal{R}^{\rm barrier}_{\ell m\omega}+\left(\mathcal{R}^{\rm ECO}_{\ell m\omega}\mathcal{R}^{\rm barrier}_{\ell m\omega}\right)^2+\dots\right] \\ =& \frac{\mathcal{R}^{\rm ECO}_{\ell m\omega}\mathcal{T}^{\rm barrier}_{\ell m\omega}}{1-\mathcal{R}^{\rm ECO}_{\ell m\omega}\mathcal{R}^{\rm barrier}_{\ell m\omega}} Z^{\rm plunge}_{\ell m\omega} \end{aligned} . \tag{5.11}$$

Now our task is to find a way to compute $Z^{\rm plunge}_{\ell m\omega}$ due to a plunging particle, the reflectivity and transmissivity of the potential barrier $\mathcal{R}^{\rm barrier}_{\ell m\omega}$, $\mathcal{T}^{\rm barrier}_{\ell m\omega}$, respectively, and to model the response of the ECO surface $\mathcal{R}^{\rm ECO}_{\ell m\omega}$.

In Ref. [74], the relation between $Z^{\rm out}_{\ell m\omega}$ and $Z^{\rm in}_{\ell m\omega}$ (c.f. Eq. (5.8)) was determined by considering tidal tensor fields of fiducial observers near the horizon. To summarize the results, we connect $\psi_0$ and $\psi_4$ to the tidal tensors of fiducial observers near the horizon:

$$\mathcal{E} \sim -\frac{\Delta}{4\Sigma}\psi_0 - \frac{\Sigma}{\Delta}\psi_4^*, \tag{5.12}$$

where $^*$ denotes its complex conjugate. Note that it is the in-going piece of $\psi_0$ ($\sim \Delta^{-2}e^{-ipr_*}$) and the out-going piece of $\psi_4$ ($\sim e^{+ipr_*}$) that dominate this expression, with both contributing to $\mathcal{E}$ at the order of $1/\Delta$ since the effect of GWs is heavily blue-shifted for near-horizon observers. Since the in-going piece of $\psi_0$ is externally applied to the ECO, while the out-going piece is generated by the ECO, the ratio of these two terms can then be viewed as a local tidal Love number of the ECO.

By considering tidal distortions of zero-angular-momentum fiducial observers

very close to the horizon, we obtain

$$Z^{\rm out}_{\ell m\omega} = \frac{(-1)^{m+1}}{4}\mathcal{R}^{\rm ECO}_{\ell m\omega}\left(Y^{\rm in}_{\ell -m-\omega}\right)^*, \tag{5.13}$$

where $Y^{\rm in}$ is the in-going piece of $\psi_0$ near the ECO surface (note the subscript for $Y$ is different). Here $\mathcal{R}^{\rm ECO}_{\ell m\omega}$ is the response of the ECO to an external driving. Its modulus, $|\mathcal{R}^{\rm ECO}_{\ell m\omega}|$, corresponds to the energy reflectivity of the ECO surface. Here we have ignored the mixing between different $\ell$-modes, which is a general feature due to the distortion of spacetime geometry by the spin of the ECO.

In literature, one of the Teukolsky-Starobinsky identities is often used to relate the the in-going $\psi_0$ piece with the in-going $\psi_4$ piece, which is

$$Y^{\rm in}_{\ell m\omega} = \sigma_{\ell m\omega} Z^{\rm in}_{\ell m\omega}, \tag{5.14}$$

with $\sigma_{\ell m\omega}$ being the proportionality constant where its expression is shown in Eq. (52) in Ref. [33]. This relation has previously been applied to computing energy and angular momentum carried by GWs into the horizon generated by test particles in non-plunging orbits. However, we need to be careful here because this relation may not work in the presence of source terms, while here we do have a particle plunging into the horizon. In fact, it has been shown in Ref. [34] that the $\psi_0$ solution from a direct calculation differs from that using the Teukolsky-Starobinsky identities as in Eq. (5.14) for a particle plunging towards the horizon of a non-spinning BH. For now, we will still use Eq. (5.14) and leave the improvement of using the actual $\psi_0$ wave as future work.

An important implication of the blatant misuse of the Teukolsky-Starobinsky identities in Eq. (5.14) is that in an numerical calculation of the gravitational waveform of GW echoes, we only need to consider the $\psi_4$ (i.e., $s = -2$) solutions and we do not need to calculate the $\psi_0$ (i.e., $s = 2$) solutions explicitly. To see this, first note that

$$Z_{\ell m\omega} = Z^*_{\ell -m-\omega}, \tag{5.15}$$

for an equatorial, quasi-circular orbit [94] that we consider here. Combining this with Eq. (5.14), we see that

$$\begin{aligned}\left(Y^{\rm in}_{\ell -m -\omega}\right)^* &= \left(\sigma_{\ell -m -\omega} Z^{\rm in}_{\ell -m -\omega}\right)^* \\ &= \sigma^*_{\ell -m -\omega} Z^{\rm in}_{\ell m\omega} \\ &= \sigma_{\ell m\omega} Z^{\rm in}_{\ell m\omega},\end{aligned} \tag{5.16}$$

and therefore $Z^{\rm out}_{\ell m\omega}$ is given by

$$\begin{aligned}Z^{\rm out}_{\ell m\omega} &= \frac{(-1)^{m+1}}{4}\mathcal{R}^{\rm ECO}_{\ell m\omega}\left(Y^{\rm in}_{\ell -m -\omega}\right)^* \\ &= \mathcal{R}^{\rm ECO}_{\ell m\omega}\underbrace{\left[\frac{(-1)^{m+1}}{4}\sigma_{\ell m\omega} Z^{\rm in}_{\ell m\omega}\right]}_{Z^{\rm plunge}_{\ell m\omega}}.\end{aligned} \tag{5.17}$$

Note that the expression enclosed in the square brackets can be identified as $Z^{\rm plunge}_{\ell m\omega}$, where its expression involves $Z^{\rm in}_{\ell m\omega}$ from the $\psi_4$ solution and not $Y^{\rm in}_{\ell m\omega}$ from the $\psi_0$ solution.

Now that we have an expression for $Z^{\rm plunge}_{\ell m\omega}$, we still need to find an expression for the reflectivity $\mathcal{R}^{\rm barrier}_{\ell m\omega}$ and the transmissivity $\mathcal{T}^{\rm barrier}_{\ell m\omega}$ of the potential barrier. They can be computed by considering a wave scattering problem (see Chapter 4 Sec. 4.2.2 and Fig. 4.1b) where an out-going wave is incident on the potential barrier from the left. The ratio of the transmitted wave amplitude to the incident wave amplitude should give us the desired transmissivity, namely

$$\mathcal{T}^{\rm barrier}_{\ell m\omega} = \frac{C^{\rm trans}_{\rm T}}{C^{\rm inc}_{\rm T}}. \tag{5.18}$$

As for the reflectivity, we might expect that it is similarly given by the ratio of the reflected wave amplitude to the incident wave amplitude, namely

$$\mathcal{R}^{\rm barrier}_{\ell m\omega} \stackrel{?}{=} \frac{C^{\rm ref}_{\rm T}}{C^{\rm inc}_{\rm T}}.$$

However, recall from Eq. (5.13) that we need the in-going $\psi_0$ solution in order to compute the out-going $\psi_4$ that is generated by the ECO surface in response. Therefore, we need to multiply the above expression by an addition factor of $\left[\frac{(-1)^{m+1}}{4}\sigma_{\ell m\omega}\right]$ to compute the effective $Z^{\rm plunge}_{\ell m\omega}$ that sources the subsequent echo and we absorb this extra factor into our definition of the reflectivity, namely

$$\mathcal{R}^{\rm barrier}_{\ell m\omega} = \frac{(-1)^{m+1}}{4}\sigma_{\ell m\omega}\frac{C^{\rm ref}_{\rm T}}{C^{\rm inc}_{\rm T}}. \tag{5.19}$$

Finally, the wave amplitude $Z^{\rm up,echoes}_{\ell m\omega}$ as seen by observers at infinity is given by[2]

$$Z^{\rm up,echoes}_{\ell m\omega} = \frac{\mathcal{R}^{\rm ECO}_{\ell m\omega}\mathcal{T}^{\rm barrier}_{\ell m\omega}}{1-\mathcal{R}^{\rm ECO}_{\ell m\omega}\mathcal{R}^{\rm barrier}_{\ell m\omega}}\left[\frac{(-1)^{m+1}}{4}\sigma_{\ell m\omega}Z^{\rm in,ringdown}_{\ell m\omega}\right], \tag{5.20}$$

and all that is left is a model for the response of the surface of an ECO, which is the topic of the next sub-section.

### 5.3.3 Models for the response of the surface of an exotic compact object

We consider two types of reflectivity, namely a generic, parameterized Lorentzian reflectivity and a physically-motivated Boltzmann-type reflectivity [95].

#### 5.3.3.1 Lorentzian reflectivity

In the Lorentzian case, we assume the reflection takes place at a fixed position of $r = r^{\rm ECO}$ (or equivalently in the tortoise coordinate $r_* = r^{\rm ECO}_*$, see Eq. (4.14)) . At that position, the proper distance $\delta$ along the radial direction toward the horizon is given by

$$\delta = \int_{r_+}^{r^{\rm ECO}} \sqrt{g_{rr}}dr \approx \sqrt{\frac{r_+^2 + a^2\cos\theta^2}{r_+\kappa}}\sqrt{r^{\rm ECO}-r_+}, \tag{5.21}$$

[2] Alternatively, we can replace $\mathcal{T}^{\rm barrier}_{\ell m\omega}$ with $\mathcal{J}_{\ell m\omega} \equiv \left[\frac{(-1)^{m+1}}{4}\sigma_{\ell m\omega}\right]\mathcal{T}^{\rm barrier}_{\ell m\omega}$ so that Eq. 5.20 looks more neat. This replacement was done in Ref. [33].

where $g_{\mu\nu}$ is the metric of the ECO (which is identical to a Kerr BH), $\kappa \equiv (r_+ - r_-)/\left[2(r_+^2 + a^2)\right]$ is the surface gravity and we assume that $\delta \ll 1$. For BHs with $a/M$ not too close to unity, this leads to

$$\begin{aligned} r_*^{\rm ECO} &\approx r_+ + \frac{1}{2\kappa}\log\frac{r^{\rm ECO}-r_+}{2} - \frac{r_-}{2\kappa r_+}\log\frac{r_+-r_-}{2} \\ &\approx \frac{1}{\kappa}\log\frac{\delta}{\sqrt{r_+^2 + a^2\cos^2\theta}}. \end{aligned} \tag{5.22}$$

Another way of measuring the closeness to the horizon is via the redshift of zero-angular-momentum observers at a constant $r = r^{\rm ECO}$, with

$$\alpha = \sqrt{\frac{4r_+\kappa}{r_+^2 + a^2\cos^2\theta}}\sqrt{r^{\rm ECO} - r_+}. \tag{5.23}$$

For $a \neq 0$, both $\delta$ and $\alpha$ depend on $\theta$. This can be understood as the deformation of spherical symmetry due to the spin. In Ref. [74], we choose to set the reflection surface at a constant redshift $\alpha$ (i.e., the reflectivity has the same phase for all values of $\theta$ when $\alpha$ is a constant), which leads to mixing between the modes with different $\ell$. Here, for simplicity, we assume that the Lorentzian reflectivity is a constant at $r = r^{\rm ECO}$ (or $r_* = r_*^{\rm ECO}$) and can be written as

$$\mathcal{R}^{\rm L}_{\ell m\omega} = \varepsilon\left(\frac{i\Gamma}{p + i\Gamma}\right)e^{-2ir_*^{\rm ECO}p}. \tag{5.24}$$

Here the quantity $\varepsilon$ parametrizes the amplitude reflectivity of the ECO surface. Note that $\mathcal{R}$ depends on $\omega$ only via $p \equiv \omega - m\Omega_+$, the frequency of oscillations measured by observers co-rotating with the would-be horizon of the Kerr spacetime. The quantity $\Gamma$ characterizes a relaxation rate of the ECO surface, which corresponds to an impulse response function $\sim e^{-\Gamma t}$ in the time domain and imposes a low-pass filtering of waves upon reflection in the frequency domain. For distant observers, GWs with frequencies $|\omega - m\Omega_+| \lesssim \Gamma$ have the highest reflectivity. Note in particular, that peak reflectivity takes place at $\omega \sim 2\Omega_+$ for $m = 2$ and $\omega \sim -2\Omega_+$ for $m = -2$. As argued by Refs. [96, 95], as long as $\varepsilon$ is not too close to unity, the ECO is stable under the Lorentzian reflectivity.

The phase factor $e^{-2ir_*^{\rm ECO}p}$ in $\mathcal{R}^{\rm L}_{\ell m\omega}$ corresponds to a time delay of $-2r_*^{\rm ECO}$. If we consider that the ringdown is generated roughly at $r_* \approx 0$, the term $-2r_*^{\rm ECO}$ provides an estimate of the time delay between the ringdown and the first echo, as well as time delays between successive echoes.

#### 5.3.3.2 Boltzmann reflectivity

Considering wave reflection by a thermal atmosphere, Wang *et al.* [95] and Oshita *et al.* [97] proposed the following Boltzmann reflectivity, given by

$$\mathcal{R}^{\rm B}_{\ell m\omega} = \exp\left(-\frac{|p|}{2T_{\rm H}}\right)\exp\left[-i\frac{p}{\pi T_{\rm H}}\log(\gamma|p|)\right], \tag{5.25}$$

with Hawking temperature

$$T_{\rm H} = \frac{\kappa}{2\pi} = \frac{r_+ - r_-}{4\pi(r_+^2 + a^2)} = \frac{\sqrt{1-a^2}}{4\pi(1+\sqrt{1-a^2})}. \tag{5.26}$$

We may replace $T_{\rm H}$ with a free parameter $T_{\rm QH}$ to generalize the Boltzmann reflectivity,

$$\mathcal{R}^{\rm B}_{\ell m\omega} = \exp\left(-\frac{|p|}{2T_{\rm QH}}\right)\exp\left[-i\frac{p}{\pi T_{\rm QH}}\log(\gamma|p|)\right]. \tag{5.27}$$

We fix the temperature to the Hawking temperature, i.e., $T_{\rm QH} = T_{\rm H}$, until in Sec. 5.5, where we relax this condition to explore the detectability of echoes that arise from a broader class of reflectivity models. Similar to the Lorentzian reflectivity, $\mathcal{R}^{\rm B}_{\ell m\omega}$ depends on $\omega$ via $p \equiv \omega - m\Omega_+$, leading to the peak reflectivity (equal to unity) for modes with zero frequency viewed by observers co-rotating with the horizon, or $\omega \sim m\Omega_+$, and vanishing reflectivity for $|\omega - m\Omega_+| \gg T_{\rm H}$.

Boltzmann reflection does not take place at a fixed point, but for waves oscillating near the quasi-normal mode (QNM) frequency, $\omega \approx \Re[\omega_{\rm QNM}]$. The effective distance traveled by waves at this frequency, in terms of $r_*$, due to the phase factor in Eq. (5.25), is given by

$$2r_*^{\rm ECO,\,eff} = \log(\gamma|{\rm Re}[\omega_{\rm QNM}] - m\Omega_+|)/\pi T_{\rm H}. \tag{5.28}$$

Similar to the Lorentzian case, here $-2r_*^{\rm ECO,\,eff}$ corresponds to the time lag between echoes.

As shown in Ref. [95], the Boltzmann reflectivity leads to a stable ECO. Basically, the BH potential barrier has a reflectivity higher than unity for $\omega < m\Omega_+$, and the ECO simply needs to have a reflectivity that decreases fast enough as $p$ increases from zero.

### 5.4 Features in waveforms of gravitational-wave echoes

Here in this section, we showcase our prescription to compute waveforms of GW echoes using the two reflectivity models, i.e., the Lorentzian and the Boltzmann reflectivity, and discuss some of the features in the waveforms from the two reflectivity models.

In Fig. 5.1, we plot the GR and the echo waveforms for a binary with $q = 1$, using the Lorentzian reflectivity. For Lorentzian reflectivity $\mathcal{R}^{\rm L}$, $\varepsilon$ simply scales the magnitude of the $n$-th echo by $\varepsilon^n$, while $|2r_*^{\rm ECO}|$ shifts the time-domain separation between echoes (effects of $\varepsilon$ and $r^{\rm ECO}$ on the first echo are shown in the top panels of Fig. 5.1). The bandwidth $\Gamma$ of the reflectivity acts as a low-pass filter in the reference frame of the ECO surface, therefore it filters out frequency components with $|\omega - m\Omega_+| \lesssim \Gamma$.

In Fig. 5.2, we plot the GR and the echo waveforms for a binary with $q = 1$, using the Boltzmann reflectivity. The Boltzmann reflectivity $\mathcal{R}^{\rm B}$ only has one free parameter $\gamma$, which simply shifts the separation between echoes (as well as between the first echo and the GR wave) in the time domain by $2r_*^{\rm ECO,\,eff}$, as given by Eq. (5.28).

### 5.5 Detectability of gravitational-wave echoes

In this section, we discuss the detectability of echoes with current and future detectors. To quantify the detectability, one can compute the optimal signal-to-

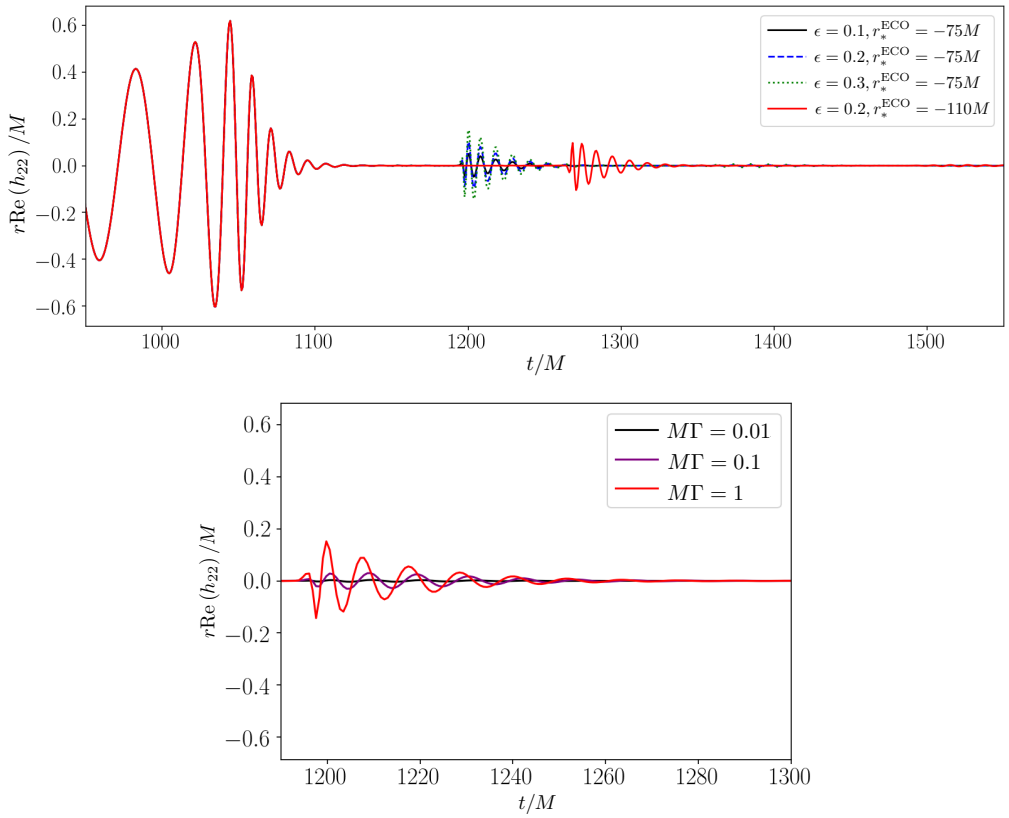


Figure 5.1: Echoes for an equal-mass binary merger ($q = 1$) with the Lorentzian reflectivity. The top panel shows how $\epsilon$ and $r_*^{\rm ECO}/M$ in Lorentzian reflectivity change the magnitude and separation of echoes ($M\Gamma = 0.5$). The lower panel shows how $\Gamma$ impacts the shape of the first echo (with $\varepsilon = 0.2$, $r_*^{\rm ECO}/M = -75$). Fig. reproduced from Ref. [33].

noise ratio (SNR) $\rho_{\rm opt}$, which is defined as [98]

$$\rho_{\rm opt}^2 = 4\int_0^\infty df\ \frac{|\tilde{h}(f)|^2}{S_{\rm n}(f)}, \tag{5.29}$$

where $S_{\rm n}(f)$ is the one-sided noise power spectral density of a detector, and $\tilde{h}(f)$ is the strain measured by a detector which is given by

$$\tilde{h}(f) = F_+\tilde{h}_+(f) + F_\times\tilde{h}_\times(f), \tag{5.30}$$

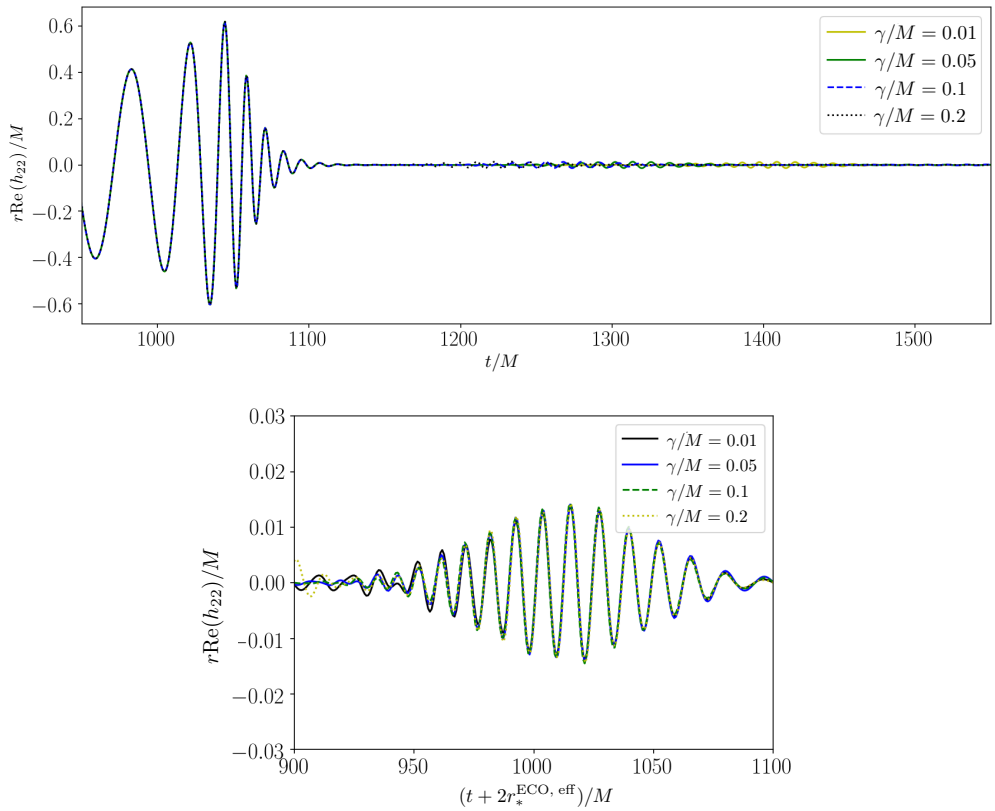


Figure 5.2: Echoes for an equal-mass binary merger ($q = 1$) with the Boltzmann reflectivity. The top panel shows how $\gamma$ in the Boltzmann reflectivity changes the echoes. The bottom panel shows how $\gamma$ impacts the shape of the first echo. Note that the time axis is shifted by $2r_*^{\mathrm{ECO,\,eff}}$, as defined in Eq. (5.28), to align with the first echo. Fig. produced from Ref. [33].

with $F_{+,\times}$ being the detector response to the plus and the cross polarization, respectively.

Following Ref. [98], we define a new quantity $H_{+,\times}(f)$ that factors out the $1/d_{\mathrm{L}}$

dependence on the luminosity distance $d_{\rm L}$ [3] for each polarization, where

$$\tilde{h}_{+,\times}(f) = \frac{1}{d_{\rm L}} H_{+,\times}(f). \tag{5.31}$$

The direction and orientation averaged optimal SNR $\langle \rho^2 \rangle$ is then given by [98]

$$\langle \rho^2 \rangle = \frac{4}{5} \frac{1}{d_{\rm L}^2} \int \frac{d\Omega}{4\pi} \int_0^\infty df \, \frac{|H_+(\Theta, \Phi, f)|^2 + |H_\times(\Theta, \Phi, f)|^2}{S_{\rm n}(f)}, \tag{5.32}$$

where the angle bracket $\langle ... \rangle$ denotes average over the sky location angles of the source with respect to the detector, the polarization angle and the polar angles of the detector with respect to the source (with $d\Omega = \sin\Theta d\Theta d\Phi$). If we only consider the $\ell = |m| = 2$ modes, the averaging over the orientation can also be done analytically. In fact, it is given by [99]

$$\langle \rho^2 \rangle = \frac{16}{25} \frac{1}{d_{\rm L}^2} \int_0^\infty df \, \frac{|H_+(\Theta = 0, \Phi, f)|^2}{S_{\rm n}(f)}. \tag{5.33}$$

Similarly, we can also compute the maximal $\rho_{\rm opt}$ by setting the source to be face-on ($\Theta = 0$) and directly above a detector ($F_{+,\times} = 1$), i.e., both optimally oriented and optimally located.

We compute both the direction-and-orientation averaged, as well as the maximal optimal SNR of the first *five* echoes in Advanced Laser Interferometer Gravitational-Wave Observatory (LIGO) at the design sensitivity [100] and Cosmic Explorer (CE) [28] with both the Lorentzian and Boltzmann reflectivities.

Figs. 5.3 and 5.4 show the SNR and the detectability of echoes in the $\epsilon$–$\Gamma$ parameter space for the Lorentzian reflectivity model assuming the Advanced LIGO and CE at their design sensitivities, respectively. For Advanced LIGO, we see that the echoes obtained using the prescription in this paper are too weak to be detected in the parameter space that we explore here ($0 \leq \epsilon \leq 1$,

[3] To account for the expansion of the Universe, one can simply replace the the coordinate distance $r$ with the luminosity distance $d_{\rm L}$, and replace the total mass $M$ with the redshifted total mass $M(1+z)$ where $z = z(d_{\rm L})$ is the redshift of the source.

$0 \leq \Gamma/\kappa \leq 1$). This implies that if our prescription is correct, we would *not* be able to detect echoes with second-generation terrestrial detectors, and would require next-generation detectors in order to test the existence of ECO via GW echoes. Indeed, Fig. 5.4 indicates that with CE, a much larger fraction of the $\epsilon$–$\Gamma$ parameter space allows detection for echoes from our prescription.

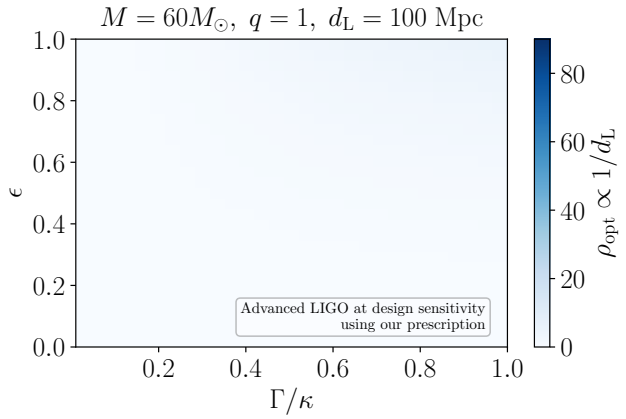


Figure 5.3: SNR and detectability of echoes in the $\epsilon$–$\Gamma$ parameter space for the Lorentzian reflectivity model assuming the Advanced LIGO design sensitivity [100] with $N_{\rm echo} = 5$ at a luminosity distance of $d_{\rm L} = 100$ Mpc. Here we set $r_*^{\rm ECO} = -100M$. This choice of $r_*^{\rm ECO}$ is not expected to affect the detectability as it mostly affects the time delay between echoes. We see that the echoes obtained using the prescription in this paper are generally too weak to be detected.

Fig. 5.5 and 5.6 show the SNR and detectability of echoes in the $T_{\rm QH}$–$\gamma$ parameter space for the Boltzmann reflectivity model assuming the Advanced LIGO and CE at their design sensitivities, respectively. Similar to the Lorentzian reflectivity model, we would not see any echoes from our model with second-generation detectors. Detecting echoes would become more promising with next-generation detectors. Interesting, from the plots we see that the detectability of echoes is generally *independent* of $\gamma$.

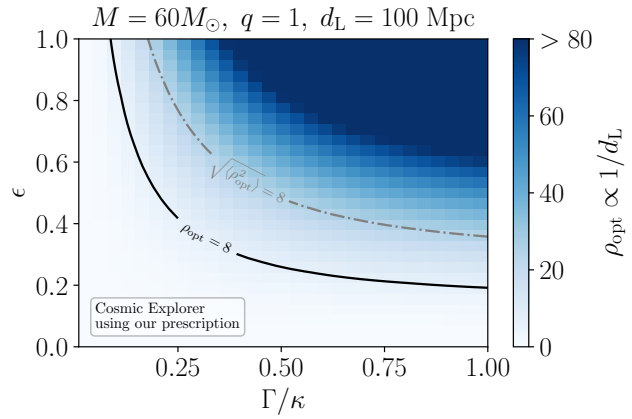


Figure 5.4: Same as Fig. 5.3 but with CE at its design sensitivity [28]. The solid contours correspond to the *maximal SNR* $\rho_{\mathrm{opt}} = 8$ as the detection threshold, while the dash-dotted contours correspond to the location-and-orientation averaged SNR of 8. With CE, the echoes computed using our prescription are now strong enough to be detected.

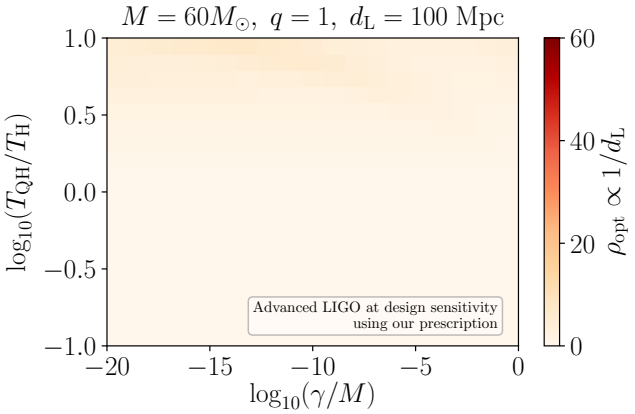


Figure 5.5: SNR and detectability of echoes in the $T_{\mathrm{QH}}$–$\gamma$ parameter space for the Boltzmann reflectivity model assuming the Advanced LIGO design sensitivity [100] with $N_{\mathrm{echo}} = 5$ at a luminosity distance of $d_{\mathrm{L}} = 100$ Mpc. We see that echoes obtained using our prescription are too weak to be detected.

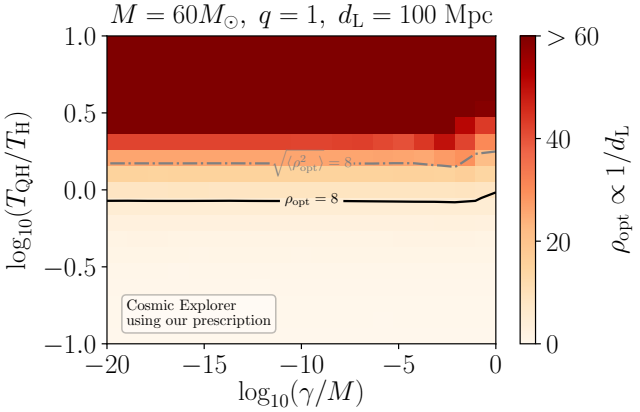


Figure 5.6: Same as Fig. 5.5 but with CE at its design sensitivity [28]. The solid contours correspond to the *maximal optimal SNR* $\rho_{\rm opt} = 8$ as the detection threshold, while the dash-dotted contours correspond to the location-and-orientation averaged SNR of 8. The plot also indicates that the detectability of echoes is generally *independent* of the value of $\gamma$.

## 5.6 Concluding remarks

In this paper, we compute GW echoes from merging compact objects that arise from the waves reflected by the surface of spinning ECOs. The exterior spacetime of a spinning ECO is modeled as a Kerr spacetime except in a small region above the horizon where a reflecting boundary exists. We obtain the echo waveforms by first computing the $\psi_4$ of the GWs that travel toward the horizon of the final BH in the case of BBH mergers, and then computing the subsequent reflection from the ECO surface and the Kerr potential barrier, in the case of ECO. More specifically, we solve the Teukolsky equation for $\psi_4$ sourced by an inspiraling particle that eventually plunges into the horizon of a Kerr BH.

In order to model binaries with comparable masses, which is the most interesting case with existing GW events, we have adopted an approach that modifies the trajectory of the in-falling particle and calibrating the GWs at infinity to match numerical relativity surrogate waveforms, we can obtain the horizon-going GWs that approximate those of comparable-mass mergers.

We propose a prescription of the ECO reflectivity that is better connected to the spacetime geometry near the ECO surface (obtained from a companion paper [74]). More specifically, the reflectivity $\mathcal{R}^{\rm ECO}$ is directly related to the tidal response of the ECO surface to the external curvature perturbations due to incoming GWs. As shown in Sec. 5.5, the echoes obtained in this paper are not expected to be detectable using the second-generation detectors, and we would need the next-generation detectors to test ECOs via GW echoes.

One subtlety in our calculation is about obtaining the reflectivity for $\psi_4$ on the ECO surface. When applying the $\mathcal{R}^{\rm ECO}$ between the in-going and out-going $\psi_4$, the Teukolsky-Starobinsky relation between the in-going $\psi_0$ and the in-going $\psi_4$ has been assumed. Strictly speaking, this relation only applies to homogeneous solutions of the Teukolsky equation where the source term vanishes and may not apply to the situation here. A more direct approach, to be studied in future work, is to compute the in-going $\psi_0$, and then obtain the $\psi_4$ of the echoes by applying reflectivities to the ECO surface.

**Acknowledgements**

Research of B. C. and Y. C. are supported by the Simons Foundation (Award Number 568762), the Brinson Foundation, and the National Science Foundation (Grants PHY–2011968, PHY–2011961 and PHY–1836809). Research of S. X. and Q. W. was done in part during their visits to the California Institute of Technology, which was supported by funds from the Simons Foundation. R. K. L. L. and L. S. acknowledge support of the National Science Foundation and the LIGO Laboratory. LIGO was constructed by the California Institute of Technology and Massachusetts Institute of Technology with funding from the United States National Science Foundation, and operates under cooperative agreement PHY–1764464. Advanced LIGO was built under award PHY–0823459. R. K. L. L. would also like to acknowledge support from the Croucher Foundation. L. S. also acknowledges the support of the Australian Research Council Centre of Excellence for Gravitational Wave Discovery (OzGrav), project number

CE170100004. W.H. is supported by by NSFC (National Natural Science Foundation of China) no. 11773059 The computations presented here were conducted on the Caltech High Performance Cluster partially supported by a grant from the Gordon and Betty Moore Foundation.

*Chapter 6*

# TEMPLATED-BASED GRAVITATIONAL-WAVE ECHOES SEARCH USING BAYESIAN MODEL SELECTION

This chapter contains work from

> R. K. L. Lo, T. G. F. Li, and A. J. Weinstein. "Template-based Gravitational-Wave Echoes Search Using Bayesian Model Selection". In: *Phys. Rev. D* 99.8 (2019), p. 084052. DOI: 10.1103/PhysRevD.99.084052. arXiv: 1811.07431 [gr-qc].
> R. K. L. L performed the analyses and wrote the manuscript.

## 6.1 Introduction

As of this writing, the Laser Interferometer Gravitational-Wave Observatory (LIGO) [1] and Advanced Virgo [2] have successfully detected ten compact binary coalescence events from binary black hole systems [26, 101, 102, 103, 104, 9] and one binary neutron star collision [16]. These discoveries mark the beginning of a new era of gravitational-wave (GW) astronomy and astrophysics, where we can infer and probe the properties and structure of astronomical objects using gravitational waves.

During the inspiral stage of GW emission from the coalescence of a compact binary system, for instance a binary black hole system, the two black holes spiral towards each other with an increasing orbital frequency. Eventually, they coalesce in the merger stage to form one single black hole. The final black hole then relaxes to a Kerr black hole during the ringdown stage.

Cardoso, Franzin and Pani [105] first pointed out that the ringdown part of the GW signal can be used as a probe of the structure of a compact object. A very compact object, not necessarily a black hole, with a light ring will also exhibit a similar ringdown as that of a black hole. Cardoso, Hopper, Macedo,

Palenzuela and Pani [106] further showed that a similar ringdown stage will also be exhibited for different types of *exotic compact objects (ECOs)* with a light ring (or a photon sphere), and there will be a train of echoes in the late-time ringdown stage associated with the photon sphere. Examples of ECOs are theoretical alternatives to black holes, such as gravastars and fuzzballs. A common feature of these alternatives is that there is some kind of structure near the would-be event horizon. The echoes in the late-time ringdown stage are caused by repeated and damped reflections between the effective potential barrier and the reflective structure. Cardoso *et al.* also showed that the time delay between each echo $\Delta t_{\text{echo}}$ can be used to infer the nature of an ECO [106], namely

$$\Delta t_{\text{echo}} \sim -nM \log\left(\frac{l}{M}\right), \tag{6.1}$$

where $M$ is the mass of the ECO, $l \ll M$ is the microscopic correction of the location of the ECO surface from the Schwarzschild radius, and $n$ is an integer of the order of 1 which depends on the nature of the ECO.

Abedi, Dykaar and Afshordi published a paper in December 2016, claiming that they had found tentative evidence of Planck-scale structure near the black hole event horizons at a combined $2.9\sigma$ significance level [107] of GW150914, LVT151012 and GW151226 using the matched filtering technique. However, their analysis methodology, especially the estimation of statistical significance, was questioned [108, 109]. Various teams have also proposed methods to estimate the parameters of the GW echoes [110, 111], and to search for echoes in a morphology-agnostic way [112, 113].

In this paper, we present a template-based search methodology using Bayesian inference to search for echoes of GWs in compact binary coalescence events. The analysis technique in this paper can be used with different GW echoes waveform models to provide robust evidence of the existence of echoes from ECOs by showing consistent results using different models. Detecting an exotic compact object would be a groundbreaking discovery as this would revolutionize our understanding of compact objects, and that this can only be achieved by GW

observations. In parallel to this work, there are efforts to search for GW echoes using Bayesian model selection with templates using the inference package `PyCBC Inference`[114].

This paper is structured as follows. In Sec. 6.2, we first establish the methodology of the search, namely Bayesian model selection and parameter estimation in Sec. 6.2.1, the GW echoes template model in Sec. 6.2.2 and statistical significance estimation in 6.2.3. We then describe ways to evaluate the sensitivity of a search in Sec. 6.2.4, and the combination of Bayesian evidence from multiple GW echoes events in Sec. 6.2.5. In Sec. 6.3, we first describe our implementation in Sec. 6.3.1, and then we present the results of a Bayesian parameter estimation and model selection of the presence of echoes versus their absence that were performed on simulated data with Gaussian noise in Sec. 6.3.3 and Sec. 6.3.4, respectively. Then we evaluate the performance of the search in simulated Gaussian noise and real noise in the first observing run (O1) in Sec. 6.3.5. We demonstrate the idea of combining multiple GW echoes events in Sec. 6.3.6. Finally in Sec. 6.3.7, we show the search results for the three events in O1.

## 6.2 Methods

### 6.2.1 Bayesian model selection and parameter estimation

To search for echoes of GWs from the coalescence of exotic compact objects, we perform Bayesian model selection analyses on confirmed GW events. Here we consider two hypotheses $\mathcal{H}_0$ and $\mathcal{H}_1$, which can also be considered as the null hypothesis and alternative hypothesis in the frequentist language, and they are

$$\mathcal{H}_0 \coloneqq \text{No echoes in the data} \Rightarrow d = n + h_{\text{IMR}},$$
$$\mathcal{H}_1 \coloneqq \text{There are echoes in the data} \Rightarrow d = n + h_{\text{IMRE}},$$

where $d$ denotes the GW data, $n$ denotes the instrumental noise and $h_{\text{IMR}}$, $h_{\text{IMRE}}$ denote the inspiral-merger-ringdown (IMR) GW signal and inspiral-merger-ringdown-echo (IMRE) GW signal, respectively. Note that we *assume there*

*is a GW signal in the data* since we perform the search after the GW signal has been identified, and we are only interested in knowing whether there are echoes in the data or not. When the null hypothesis $\mathcal{H}_0$ is true, that means the data contain a GW signal with IMR. When the alternative hypothesis $\mathcal{H}_1$ is true instead, that means the data contain a GW signal with both echoes and an inspiral-merger-ringdown part.

In the context of GW data analysis, suppose that the strain data $d(t)$ from a detector only consist of noise $n(t)$, which we assume to be Gaussian and stationary (we will relax these assumptions in what follows). The probability that the noise $n(t)$ has a realization $n_0(t)$ (with zero mean) is given by [115]

$$p(n_0) = \mathcal{N} \exp\left[-\frac{1}{2}\int_{-\infty}^{+\infty} df \frac{|\tilde{n_0}(f)|^2}{(1/2)S_n(f)}\right], \tag{6.2}$$

where $\mathcal{N}$ is a normalization constant and $S_n(f)$ is the power spectrum density of noise. We introduce the notion of *noise-weighted inner product*, namely

$$\langle A|B\rangle = 4\Re \int_{f_{\rm low}}^{f_{\rm high}} df \frac{\tilde{A}^*(f)\tilde{B}(f)}{S_n(f)}, \tag{6.3}$$

where $f_{\rm low}$ and $f_{\rm high}$ are the low-frequency cutoff and high-frequency cutoff, respectively. The integration is performed over a finite range because detectors are taking samples at a finite rate, and hence there is a theoretical upper limit on the maximum frequency that one can resolve from the data, and detectors are not sensitive enough below some frequency threshold. Using the inner product, we can rewrite Eq. 6.2 as

$$p(n_0) = \mathcal{N} \exp\left[-\frac{1}{2}\langle n_0|n_0\rangle\right]. \tag{6.4}$$

Now, suppose the strain data $d(t)$ consist of both noise $n_0(t)$ and a GW signal modeled by a template $h(t;\vec{\theta})$, where $\vec{\theta}$ is a set of parameters of the template that describe the signal, that is

$$n_0(t) = d(t) - h(t;\vec{\theta}). \tag{6.5}$$

Then the likelihood $p(d|\vec{\theta}, \mathcal{H}, I)$ for a single detector can be obtained from Eq. 6.2:

$$p(d|\vec{\theta}, \mathcal{H}, I) = \mathcal{N} \exp\left[-\frac{1}{2}\langle d(t) - h(t;\vec{\theta})|d(t) - h(t;\vec{\theta})\rangle\right], \tag{6.6}$$

where $I$ denotes the knowledge known prior to the selection; in this case we knew prior to the model selection that the data contain a GW signal. For the case of multiple detectors (for example, H1, L1 and V1), if we assume that the noise distributions for each detector are all Gaussian and stationary, and more importantly independent of each other, then we have

$$p(d_{\mathrm{H1}}, d_{\mathrm{L1}}, d_{\mathrm{V1}}|\vec{\theta}, \mathcal{H}, I) = \prod_{i\in\{\mathrm{H1,L1,V1}\}} \mathcal{N}_i \exp\left[-\frac{1}{2}\langle d_i(t_i) - h(t_i;\vec{\theta})|d_i(t_i) - h(t_i;\vec{\theta})\rangle\right]. \tag{6.7}$$

With the notion of noise-weighted inner product, we can also define the matched-filtering signal-to-noise ratio (SNR) $\rho$, which tells us how strong a signal is with respect to the noise, as follows:

$$\rho^2 = \frac{\langle d|h\rangle^2}{\langle h|h\rangle}, \tag{6.8}$$

where $d$ denotes the GW data and $h$ is a GW signal template. If we have multiple detectors (for example, H1, L1 and V1), we can define the *network SNR* squared as the sum of the matched filtering SNR squared in each detector

$$\rho^2_{\mathrm{network}} = \sum_{i\in\{\mathrm{H1,L1,V1}\}} \rho_i^2. \tag{6.9}$$

In the optimal case of a template that exactly matches the signal in the data, the matched-filtering SNR is bound by the *optimal SNR*, which is given by

$$\rho^2_{\mathrm{optimal}} = \frac{\langle h|h\rangle^2}{\langle h|h\rangle}, \tag{6.10}$$

and can be used as an indication of how strong a signal is.

In Bayesian model selection, we compute the Bayes factor $\mathcal{B}_0^1$ and odds ratio $O_0^1$, which are defined as

$$\mathcal{B}_0^1 = \frac{p(d|\mathcal{H}_1, I)}{p(d|\mathcal{H}_0, I)}, \tag{6.11}$$

$$O_0^1 = \frac{p(\mathcal{H}_1|d, I)}{p(\mathcal{H}_0|d, I)} = \mathcal{B}_0^1 \times \frac{p(\mathcal{H}_1|I)}{p(\mathcal{H}_0|I)}. \tag{6.12}$$

In the Bayesian language, the odds ratio has the interpretation that when $O_0^1 > 1$, it means that the data favor the hypothesis $\mathcal{H}_1$, and vice versa. For the sake of simplicity, we will drop the superscript and subscript on the Bayes factor $\mathcal{B}$ and odds ratio $O$ from now on when the context is clear. If we assume that each hypothesis is equally likely prior to the model selection, namely

$$p(\mathcal{H}_0\,|I) = p(\mathcal{H}_1\,|I) = \frac{1}{2}, \tag{6.13}$$

then the odds ratio is simply the Bayes factor, that is

$$O = \mathcal{B} = \frac{p(d|\mathcal{H}_1, I)}{p(d|\mathcal{H}_0, I)}. \tag{6.14}$$

It is often more convenient to work in log space, namely we compute the log posterior, log likelihood and log prior. We take the natural logarithm on both sides of Eq. 6.14, and we have

$$\begin{aligned} \ln O &= \ln \mathcal{B} \\ &= \ln p(d|\mathcal{H}_1, I) - \ln p(d|\mathcal{H}_0, I) \\ &= \ln Z_1 - \ln Z_0, \end{aligned} \tag{6.15}$$

where the term $Z_i \equiv p(d|\mathcal{H}_i, I)$, which is known as the *evidence* for the hypothesis $\mathcal{H}_i$, can be estimated by numerically integrating over the template parameter space $\vec{\theta}_i$ of hypothesis $\mathcal{H}_i$ using a sampling algorithm such as parallel-tempering Markov chain Monte Carlo with thermodynamic integration [116, 117, 118, 119]

or nested sampling [120]. In this paper, we will use nested sampling (or more specifically `LALInferenceNest` [121]). Apart from estimating the evidence, we can also obtain a set of posterior samples as byproducts of the nested sampling algorithm, which allow us to perform parameter estimation [1] with little additional computational cost. We can calculate various estimators of parameters as point estimates from the posterior samples, such as the maximum likelihood estimator (MLE), which is

$$\hat{\vec{\theta}}_{i,\mathrm{MLE}} = \arg\max \mathcal{L}(\vec{\theta}_i|d, \mathcal{H}_i, I), \tag{6.16}$$

where $\mathcal{L}(\vec{\theta}_i|d, \mathcal{H}_i, I) = p(d|\vec{\theta}_i, \mathcal{H}_i, I)$ is the likelihood as a function of the parameters $\vec{\theta}_i$. Another estimator is the maximum a posteriori estimator (MAP), which is

$$\hat{\vec{\theta}}_{i,\mathrm{MAP}} = \arg\max p(\vec{\theta}_i|d, \mathcal{H}_i, I), \tag{6.17}$$

where $p(\vec{\theta}_i|d, \mathcal{H}_i, I)$ is the posterior distribution of parameters $\vec{\theta}_i$.

To obtain the evidence for the hypothesis $\mathcal{H}_i$ in the context of GW data analysis, we use GW waveform templates that assume $\mathcal{H}_i$ being true to compute the log likelihood.

#### 6.2.1.1 Occam factor

One must be cautious when performing model selection that the model which fits the data best does not imply that the model gives the highest evidence. A more complicated model, i.e., with more free parameters, is more easily affected by noise in the data than a simpler model, i.e., with less free parameters. This is similar to overfitting in regression. Suppose there are $N$ data points for fitting; one can always use a degree $N-1$ polynomial to fit all points, but very likely the fitted polynomial will not generalize well to new data because it was affected by the noise in the data.

Bayesian analysis embodies the *Occam factor* and penalizes more complicated models automatically. To illustrate this idea, suppose there are two hypotheses,

[1] A detailed discussion of parameter estimation can be found in Ref. [121].

namely $\mathcal{H}_0$ and $\mathcal{H}_1$. Without loss of generality, we assume that $\dim \vec{\theta}_1 > \dim \vec{\theta}_0$, where $\dim \vec{\theta}_i$ denotes the dimension of the parameter vector $\vec{\theta}_i$ that describes the hypothesis $\mathcal{H}_i$. If the posterior distribution has a sharp peak at $\vec{\theta}_i = \vec{\theta}_{i,\mathrm{MAP}}$ with width $\sigma_{i,\mathrm{posterior}}$, then the integral for evidence $Z_i$ can be approximated using Laplace's method. We first write the integral for evaluating the evidence of the hypothesis $\mathcal{H}_i$ into the standard form for Laplace's method

$$Z_i = \int \exp\left\{\ln\left[p(d|\vec{\theta}_i, \mathcal{H}_i, I)p(\vec{\theta}_i|\mathcal{H}_i, I)\right]\right\} d\vec{\theta}_i. \tag{6.18}$$

Let $f(\vec{\theta}_i) \equiv \ln\left[p(d|\vec{\theta}_i, \mathcal{H}_i, I)p(\vec{\theta}_i|\mathcal{H}_i, I)\right]$, and we expand $f(\vec{\theta}_i)$ about the sharp peak $\vec{\theta}_i = \vec{\theta}_{i,\mathrm{MAP}}$, which gives

$$f(\vec{\theta}_i) = f(\vec{\theta}_{i,\mathrm{MAP}}) + \frac{f''(\vec{\theta}_{i,\mathrm{MAP}})}{2}(\vec{\theta}_i - \vec{\theta}_{i,\mathrm{MAP}})^2 + \mathcal{O}(\vec{\theta}_i - \vec{\theta}_{i,\mathrm{MAP}})^3, \tag{6.19}$$

where the first derivative $f'$ vanishes and the second derivative $f''(\vec{\theta}_{i,\mathrm{MAP}}) < 0$ at the local maximum. Substituting this back into Eq. 6.18, we have

$$Z_i \approx \exp f(\vec{\theta}_{i,\mathrm{MAP}}) \int \exp\left[-\frac{|f''(\vec{\theta}_{i,\mathrm{MAP}})|}{2}(\vec{\theta}_i - \vec{\theta}_{i,\mathrm{MAP}})^2\right] d\vec{\theta}_i, \tag{6.20}$$

where the integral becomes a Gaussian integral in the limit that the integration is performed over $(-\infty, \infty)$.

Finally we can approximate the evidence $Z_i$ (up to some constant factors) by

$$Z_i \approx p(d|\vec{\theta}_{i,\mathrm{MAP}}, \mathcal{H}_i, I)p(\vec{\theta}_{i,\mathrm{MAP}}|\mathcal{H}_i, I)\sigma_{i,\mathrm{posterior}}. \tag{6.21}$$

Note that we have assumed that the posterior width $\sigma_{i,\mathrm{posterior}}$ is much smaller than the width of the integration limits such that the integral in Eq. 6.20 can be well approximated by a Gaussian integral. It should also be noted that Eqs. 6.20 and 6.21 *were not used in our analyses*, and they were derived for the purpose of illustrating the Occam factor only.

For a more complicated model, more parameters are needed to describe the observed data. For example, for our hypothesis $\mathcal{H}_1$ (i.e., there are echoes in

the data) we need to introduce extra parameters (discussed in the next section) such as the time delay between each echo $\Delta t_{\rm echo}$ in the model selection analysis. Suppose the prior distribution of parameters $\vec{\theta}_i$ for each hypothesis is uniform over a width $\sigma_{i,\rm prior}$ such that

$$p(\vec{\theta}_i|\mathcal{H}_i, I) = \begin{cases} \dfrac{1}{\sigma_{i,\rm prior}} & \text{within the range,} \\ 0 & \text{otherwise.} \end{cases} \tag{6.22}$$

The ratio $\sigma_{i,\rm posterior}/\sigma_{i,\rm prior}$ hence serves as a penalty to down-weigh the evidence $Z_1$ of the more complicated model $\mathcal{H}_1$ which has a larger prior volume, i.e., $\sigma_{1,\rm prior} > \sigma_{0,\rm prior}$ to account for the uncertainty of the extra parameters. This ratio, sometimes referred to as *Occam factor* [122], allows the analysis to bias the less complicated IMR-only model in a natural way.

### 6.2.2 Phenomenological waveform model of echoes

In this paper, we use the phenomenological waveform model of echoes proposed by Abedi *et al.* in Ref. [107] to search for echoes of GWs. It should be noted that the methodology we propose here is *independent of the GW echoes templates we used*, and different parametrized waveform models can be readily used instead of the model by Abedi *et al.* when more physical models become available in the future [123, 124, 125, 126, 127]. Their model was motivated by the numerical results in Ref. [106]. There are five free parameters in their waveform model, with the phase change between each echo due to the reflection on an ECO surface being $\pi$. The descriptions of these five parameters are tabulated in Table 6.1.

Using the notations in Ref. [107], the echo template $\mathcal{M}_{\rm TE,I}(t)$ in the time domain is given by

$$\begin{aligned} \mathcal{M}_{\rm TE,I}(t) \equiv A \sum_{n=0}^{\infty} (-1)^{n+1} \gamma^n \\ \times \mathcal{M}_{\rm T,I}(t + t_{\rm merger} - t_{\rm echo} - n\Delta t_{\rm echo}, t_0), \end{aligned} \tag{6.23}$$

| Parameter | Description |
|---|---|
| $\Delta t_{\rm echo}$ | The time interval between each echo |
| $t_{\rm echo}$ | The time of arrival of the first echo |
| $t_0$ | The time of truncation of the GW IMR template $\mathcal{M}_{\rm I}(t)$ to produce the echo template $\mathcal{M}_{\rm TE,I}(t)$ |
| $\gamma$ | The damping factor |
| $A$ | The amplitude of the first echo relative to the IMR part of the template |

Table 6.1: The five free parameters and the corresponding descriptions of the phenomenological GW echoes waveform model proposed by Abedi *et al.* [107]. In particular, $\Delta t_{\rm echo}$ is of the most astrophysical interest because it encapsulates the compactness of the exotic compact object that we are observing as shown in Eq. 6.1. Physically $\Delta t_{\rm echo}$ is related to the distance between the effective potential barrier and the reflective surface that GW echoes need to travel. Also, $A$ can tell us the typical strength of the GW echoes emitted from exotic compact objects.

where $t_{\rm merger}$ is the time of merger [2] and $\mathcal{M}_{\rm T,I}(t)$ is a smooth activation of the GW IMR template given by

$$\begin{aligned}\mathcal{M}_{\rm T,I}(t) &\equiv \Theta(t, t_0)\mathcal{M}_{\rm I}(t) \\ &\equiv \frac{1}{2}\left\{1 + \tanh\left[\frac{1}{2}\omega_{\rm I}(t)(t - t_{\rm merger} - t_0)\right]\right\}\mathcal{M}_{\rm I}(t),\end{aligned} \tag{6.24}$$

where $\omega_{\rm I}(t)$ denotes the angular frequency evolution of the IMR waveform as a function of time, and $\mathcal{M}_{\rm I}(t)$ is the IMR waveform. The smooth activation $\Theta(t, t_0)$ essentially selects the ringdown, which is the part of a waveform that one might expect to see in echoes [107]. Note that the time of merger $t_{\rm merger}$ is the only time reference, and therefore we measure all time-related echo parameters $t_0$, $t_{\rm echo}$ and $\Delta t_{\rm echo}$ *with respect to* $t_{merger}$. The top and bottom panels of Fig. 6.1 show a truncated IMR time-domain waveform $\mathcal{M}_{\rm T,I}(t)$ used to generate the echo template and a GW150914-like IMRE time-domain waveform with three echoes, respectively.

[2] Or equivalently time of coalescence, denoted by $t_c$.

In particular, the parameter that represents the time interval between each successive echo $\Delta t_{\rm echo}$ is of the most astrophysical interest because it encapsulates the compactness of the exotic compact object that we are observing as shown in Eq. 6.1. Physically $\Delta t_{\rm echo}$ is related to the distance between the effective potential barrier and the reflective surface that GW echoes need to travel. The relative amplitude $A$ can also tell us the typical strength of the GW echoes emitted from exotic compact objects.

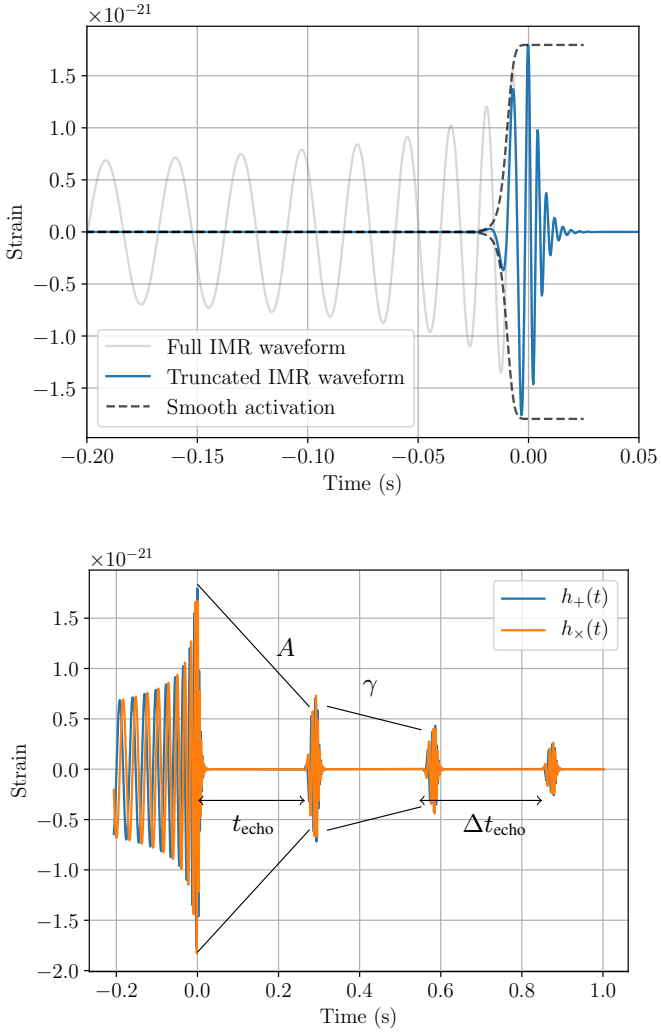


Figure 6.1: A plot of an inspiral-merger-ringdown-echo template generated using the phenomenological waveform model of echoes proposed by Abedi *et al.* [107]. *Top panel*: To generate a template of a GW echo (in blue), we truncate the ringdown part of the IMR part (in gray) of a waveform by applying the smooth activation function $\Theta(t, t_0)$ (in black dashed lines) to get the truncated IMR waveform. *Bottom panel*: A plot of an IMRE template generated using the phenomenological waveform model of echoes proposed by Abedi *et al.* We see that the first echo, which is the truncated IMR template (shown in the top panel) scaled by the parameter $A$, starts at $t_{\rm echo}$ after the merger. Subsequent echoes, which are further scaled down by the parameter $\gamma$ due to the energy loss when the echo reflects off an ECO surface, are separated from each other in time by $\Delta t_{\rm echo}$.

### 6.2.3 Detection statistic and background estimation for statistical significance

In this paper, the log Bayes factor $\ln \mathcal{B}$ [Eqs. 6.11 and 6.15] is the *detection statistic* to decide whether we claim there is an IMRE signal or an IMR signal in data. If the log Bayes factor $\ln \mathcal{B}^1_0$, or equivalently log odds ratio $\ln O^1_0$, is greater than 0, we can conclude, from the Bayesian point of view, that the data favor the alternative hypothesis that the data contain an IMRE signal more than the null hypothesis that the data contain an IMR signal, thus serving the function of distinguishing which hypothesis is more supported by the data.

After we have obtained a detection statistic, a natural question to ask is how statistically significant the detection statistic is. Simply put, how likely is it that the detection is actually caused by an IMRE signal but not due to noise? In the Bayesian school, there are different empirical scales, such as Jeffreys' scale, to interpret the strength of the Bayes factor. However, they are subjective and not universally applicable. Therefore, we are not going to use any of them in this paper.

Calculating the posterior probability of a hypothesis is certainly better than using a subjective scale to determine the strength of the Bayes factor. However, the Bayesian posterior probability fails to tell us the probability that the evidence is simply due to random background noise, since we only consider one set of data. The frequentist approach can answer the following question: given the null hypothesis $\mathcal{H}_0$ is true, what is the probability that the data are going to be *as extreme as or more extreme than* the observed data? The probability that we are looking for is exactly the frequentist $p$-value. We can also interpret this $p$-value as the *false-alarm probability*.

The $p$-value, which we denote as simply $p$, is related to the *null distribution* of

detection statistic $\ln \mathcal{B}$ by

$$p = \Pr(\ln \mathcal{B} \geq \ln \mathcal{B}_{\rm detected} | \mathcal{H}_0) \\ = 1 - \int_{-\infty}^{\ln \mathcal{B}_{\rm detected}} p(\ln \mathcal{B} | \mathcal{H}_0) d \ln \mathcal{B}, \tag{6.25}$$

where $\ln \mathcal{B}_{\rm detected}$ is the detection statistic obtained in an analysis on a segment of data, and $p(\ln \mathcal{B}|\mathcal{H}_0)$ is called the null distribution of $\ln \mathcal{B}$, i.e., the distribution of $\ln \mathcal{B}$ given that $\mathcal{H}_0$ is true.

Hence, from the null distribution, we can compute the detection statistic threshold $\ln \mathcal{B}_{\rm threshold}$ corresponding to a certain statistical significance, e.g., $5\sigma$ and hence we can claim a detection of GW echoes if the detection statistic of a candidate exceeds or is equal to the predetermined threshold.

### 6.2.4 Evaluation of search sensitivity

Apart from getting the statistical significance of a particular candidate event of GW echoes, we are also interested in investigating the sensitivity and accuracy of this search methodology using Bayesian model selection.

#### 6.2.4.1 Sensitive parameter space

To quantify the sensitivity of a search, one can compute the fraction of the parameter space of echo parameters that the search can determine whether the data contain echoes or not, given a threshold on the detection statistic $\ln \mathcal{B}_{\rm threshold}$ and GW detectors operating at specific sensitivities. If a search is sensitive, then it should be able to cover a reasonable fraction of parameter space possible for astrophysical exotic compact objects, which is schematically defined as

$$\{\vec{\theta}_{\rm echoes} = (A, \gamma, t_0, t_{\rm echo}, \Delta t_{\rm echo}) \mid \ln \mathcal{B}(\vec{\theta}_{\rm echo}) \geq \ln \mathcal{B}_{\rm threshold}\}, \tag{6.26}$$

so that the search is able to detect the existence of echoes in the data with echo parameters in the sensitive parameter space.

#### 6.2.4.2 Search efficiency

Another method to quantify the search sensitivity is to compute the probability that the existence of echoes will be detected given a detection statistic threshold, which is also known as the *efficiency* $\zeta$. It is defined as

$$\zeta = \int_{\ln \mathcal{B}_{\rm threshold}}^{\infty} p(\ln \mathcal{B}|\mathcal{H}_1) d \ln \mathcal{B}, \tag{6.27}$$

where $p(\ln \mathcal{B}|\mathcal{H}_1)$ is the *foreground distribution*, i.e., the distribution of $\ln \mathcal{B}$ given that $\mathcal{H}_1$ is true. If a search is sensitive, then it should have a high value of efficiency $\zeta$.

### 6.2.5 Combining Bayesian evidence from a catalog of detection events

Bayesian model selection provides us a natural way to combine evidence of the existence of exotic compact objects from multiple detection events of GW echoes. In the following analysis, we do not assume GW events are described by the same set of echo parameters. Suppose now we have a catalog of $N_{\rm cat}$ independent events so that we have a set of $N_{\rm cat}$ data denoted by $d = \{d_1, d_2, ..., d_{N_{\rm cat}}\}$; the odds ratio for the catalog of sources is given by

$$\begin{aligned} \mathcal{O}_0^1 &= \frac{p(d_1, d_2, ..., d_{N_{\rm cat}}|\mathcal{H}_1, I) p(\mathcal{H}_1|I)}{p(d_1, d_2, ..., d_{N_{\rm cat}}|\mathcal{H}_0, I) p(\mathcal{H}_0|I)} \\ &= {}^{\rm (cat)}\mathcal{B}_0^1 \times \frac{p(\mathcal{H}_1|I)}{p(\mathcal{H}_0|I)}, \end{aligned} \tag{6.28}$$

where

$${}^{\rm (cat)}\mathcal{B}_0^1 = \frac{p(d_1, d_2, ..., d_{N_{\rm cat}}|\mathcal{H}_1, I)}{p(d_1, d_2, ..., d_{N_{\rm cat}}|\mathcal{H}_0, I)} \tag{6.29}$$

is the *catalog Bayes factor*. Since each event is independent, we can write the catalog Bayes factor as

$$
\begin{aligned}
{}^{(\mathrm{cat})}\mathcal{B}^1_0 &= \frac{p(d_1, d_2, ..., d_{N_{\mathrm{cat}}}|\mathcal{H}_1, I)}{p(d_1, d_2, ..., d_{N_{\mathrm{cat}}}|\mathcal{H}_0, I)} \\
&= \prod_{i=1}^{N_{\mathrm{cat}}} \frac{p(d_i|\mathcal{H}_1, I)}{p(d_i|\mathcal{H}_0, I)} \\
&= \prod_{i=1}^{N_{\mathrm{cat}}} {}^{(i)}\mathcal{B}^1_0,
\end{aligned}
\tag{6.30}
$$

where ${}^{(i)}\mathcal{B}^1_0$ is the Bayes factor obtained when performing the Bayesian model selection analysis on the $i$th candidate of GW echoes event candidate. Also, we can define the *catalog log Bayes factor*, which is simply

$$
\ln {}^{(\mathrm{cat})}\mathcal{B}^1_0 = \sum_{i=1}^{N_{\mathrm{cat}}} \ln {}^{(i)}\mathcal{B}^1_0. \tag{6.31}
$$

Hence, by multiplying the Bayes factor or adding the log Bayes factor from a catalog of GW echoes events, we can combine the evidence of the existence of echoes in GW data. Note that if the events share the same value of a parameter, e.g., $\Delta t_{\mathrm{echo}}$, then the analysis is more complicated but still possible to do.

## 6.3 Results

Before performing Bayesian model selection analyses on real events, it is necessary to validate the performance of the search methodology by performing analyses on simulated strain data first, namely strain data with Gaussian noise and an IMRE signal of known parameters.[3] By recovering the injected signal and inferring the parameters correctly, we can validate that the analysis method proposed in this paper will be able to find signals in real strain data. After establishing the validity of the methodology, we can sample the background and foreground distribution of the detection statistic to estimate the statistical significance of a

[3]The signals that were manually added to the data are called injections.

possible GW echoes event, and the search efficiency in simulated Gaussian noise at detectors' design sensitivities and real data in O1 of Advanced LIGO where GW signals were not detected. Finally, we apply the search methodology to search for GW echoes in O1 GW events. The GW strain data in O1 of Advanced LIGO are publicly available from the Gravitational Wave Open Science Center [128, 129].

### 6.3.1 Implementation

In this paper, we make use of the software package `LALSuite` developed by the LIGO and Virgo collaborations [130]. In particular, we extensively used the modules `LALSimulation` for its waveform generation interface and `LALInference` for its stochastic sampler [121]. We implemented the phenomenological waveform model of GW echoes described in Sec. 6.2.2 in `LALSimulation`, and we have used the IMR approximant `IMRPhenomPv2` [131, 132, 133] during the echo waveform generation. We have also modified `LALInference` so that the five extra echo parameters will be sampled by the program.

It should also be noted that in theory there should be infinitely many GW echoes. However, they are damped after each reflection from an ECO surface and more practically we are analyzing a finite segment of GW data, making the detection of all the echoes in an event impossible. Therefore we will only put three echoes in the template during a search, purely due to the limitation of computational power. For the purpose of model selection and statistical significance estimation, the number of echoes in a template does not matter since we are injecting IMR signals into noise in order to estimate the background distribution of the detection statistic. It is true that putting only three echoes in a template will bias the estimation of the amplitude parameter $A$. This can be easily resolved by increasing the number of echoes in a template once we have identified an interesting GW echoes candidate.

### 6.3.2 Details of the validation analysis

We performed our proposed search on a 8-second-long data with an IMRE signal injected into *simulated Gaussian noise* with the Advanced LIGO-Virgo network to validate both the methodology and the implementation. We have chosen the prior distribution of the echo parameters to be uniform over a range (i.e., the *prior range*), and that the echoes will not overlap in time domain. The prior ranges of the parameters used are listed in Table 6.2. The prior range for $A$ was chosen as such because we do not expect the amplitude of echoes to be greater than the amplitude of the inspiral-merger-ringdown part of a signal. However, this is not a stringent requirement and can be easily relaxed. As for the prior range for $\gamma$, it was chosen as such because we expect echoes to be damped after each reflection from an ECO surface. The prior range for $t_0$ was chosen such that we are truncating approximately the ringdown part of a signal. As for the prior ranges for both $t_{\rm echo}$ and $\Delta t_{\rm echo}$, they depend on our knowledge of the position of the surface of an ECO. For the purpose of this work, they were chosen to be wide enough such that their predicted values for all the GW events detected in O1 as calculated in Ref. [107] fall within their corresponding prior ranges, which are sensible.

The IMR parameters of *this particular injected signal*, such as masses and spins, were chosen to be close to the inferred values of GW150914 [134] and the injected echo parameters were chosen *randomly* over the prior range. It should be noted that in this work *we do not assume IMR parameters were known a priori and they were allowed to vary during the validation analysis together with the echo parameters*. This is because the IMR parameters would affect the determination of the echo waveform used and thus the uncertainties in inferring IMR parameters would also propagate to the the search for echoes. This particular injection has a log Bayes factor of 11.5, and a network optimal SNR of 63.8, which will be a realistic value when Advanced LIGO-Virgo detectors reach their design sensitivities.

### 6.3.3 Parameter estimation

As an output of our search methodology, the set of posterior samples allows us to perform the parameter estimation on the simulated data. The search needs to accurately recover the injected IMRE signal if we are to use the proposed search methodology to search for GW echoes in real data. A visualization of the sampled posterior distributions, i.e., a corner plot, that shows the estimated one-dimensional (1D) marginal posterior probability distribution for each parameter and joint posterior probability distribution for each pair of parameters, is shown in Fig. 6.2. We see that the inferred values of the echo parameters are both accurate (close to the injected value) and precise (narrow posterior distribution), especially for the time-related parameters. For example, we see from the 1D histogram of $\Delta t_{\rm echo}$ in Fig. 6.2 that the MAP is very close to the injected value (represented by the vertical blue solid line), and the 90% Bayesian credible interval ([0.2921, 0.2925] s) is much narrower than the prior range ([0.05, 0.5] s), which means that the range is shrunk by about 99.91%.

| Parameter | Prior range |
|---|---|
| $A$ | [0.0,1.0] |
| $\gamma$ | [0.0,1.0] |
| $t_0$ (s) | [−0.1,0.01] |
| $t_{\rm echo}$ (s) | [0.05,0.5] |
| $\Delta t_{\rm echo}$ (s) | [0.05,0.5] |

Table 6.2: The prior range of the echo parameters. The prior distribution of each parameter is *uniform* over the respective prior range. Refer to the main text for the justification for the choice of prior ranges.

As for the amplitude-related parameters $A$ and $\gamma$, the parameter estimation is not as accurate and precise as for the time-related parameters. For instance, we see that the range for $A$ does not shrink as much compared with $\Delta t_{\rm echo}$ (only by about 60%). This is not surprising because the time-related parameters can be inferred using the coherence of the strain with a template, while the amplitude-related parameters can only be inferred using noisy strain data.

By examining the corner plot for recovered IMR parameters (not shown here), we conclude that the parameter estimation of IMR parameters was not significantly affected by the introduction of five extra parameters.

Therefore, from the parameter estimation, we conclude that we have correctly implemented the GW echoes waveform model and modified the sampler, and more importantly the search methodology is able to infer the values of echo parameters in actual analyses on candidate GW echoes events as it has successfully recovered the injected IMRE signal accurately and precisely in this validation analysis.

### 6.3.4 Model selection

#### 6.3.4.1 Statistical significance estimation of a candidate GW echoes event

To estimate the statistical significance of a GW echoes candidate, we sampled the null distribution $p(\ln \mathcal{B}|\mathcal{H}_0)$ of the detection statistic by performing background runs, i.e., data *with an IMR signal injected* (so that the null hypothesis $\mathcal{H}_0$ is true). The IMR parameters of the injection set used to estimate the background distribution were chosen to be representative of what Advanced LIGO and Advanced Virgo would detect, and *were not fixed to be the same as a particular GW event*. We will discuss this choice in Sec. 6.4.1.

The histograms of the sampled null distribution of the *individual log Bayes factor* for simulated Gaussian noise (with 192 samples) and real noise during O1 of Advanced LIGO (with 953 samples)[4] are shown in the left and right panels of Fig. 6.3, respectively. The gray-scale bar in the top panel shows the statistical significance corresponding to the detection statistic. It should be noted that the $p$-value was obtained by extrapolation for the $\gtrsim 3\sigma$ region, as sampling the $> 5\sigma$ region would require roughly $10^7$ samples. For the case of simulated Gaussian noise in the left panel, we see that the null distribution peaks at about $\ln \mathcal{B} \approx -1$, and the tail of the distribution extends only slightly to $\ln \mathcal{B} > 0$. This means

[4]The number of samples for the background distribution in simulated Gaussian noise is less than that for real O1 noise because of the lack of computational resources

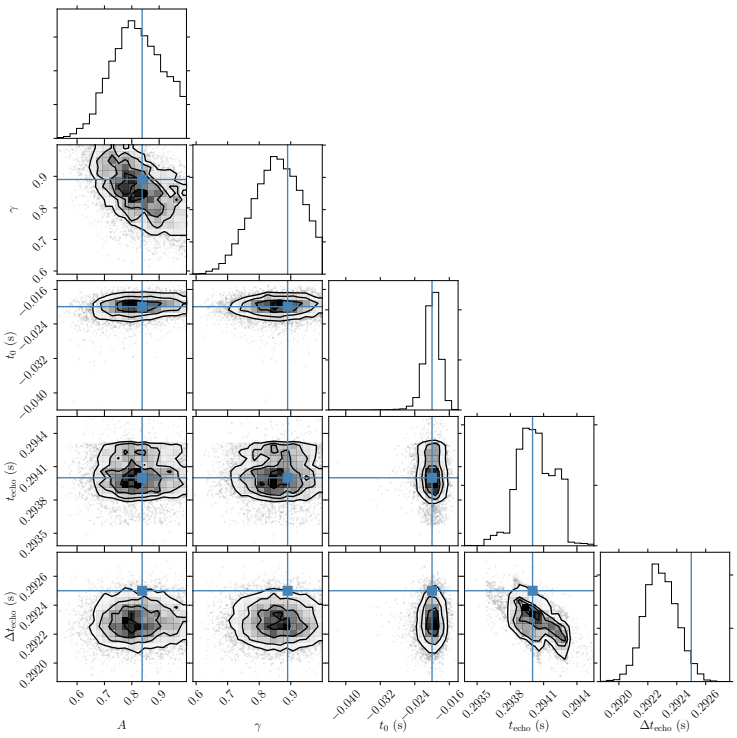


Figure 6.2: A corner plot of the posterior samples from the parameter estimation on simulated data as described in Secs. 6.3.2 and 6.3.3. If we are to use the proposed search methodology to search for GW echoes in real data, then the search needs to accurately recover the injected IMRE signal. The blue solid lines represent the injected values for each parameter. Along the diagonal are histograms of the estimated 1D marginal posterior probability distribution for each parameter. The histograms show that the recovered parameters are both accurate (close to the injected value) and precise (narrow posterior distribution). For example, the 1D marginal posterior probability density of $\Delta t_{\rm echo}$ is very narrow compared to its prior range tabulated in Table 6.2, and the peak of the posterior probability distribution is very close to the injected value. The off-diagonal plots are the two-dimensional histograms of the estimated joint posterior probability distribution of each pair of parameters, which show the correlation between pairs of parameters. We conclude that the search methodology is able to infer the values of the echo parameters in actual analyses on candidate GW echoes events as it has successfully recovered the injected IMRE signal in the validation analysis accurately and precisely.

that it is unlikely for Gaussian noise to mimic GW echoes. For the case of real noise during O1 in the right panel, we see that the distribution also peaks roughly at $\ln \mathcal{B} \approx -1$. However, the noise extends the tail of the distribution more significantly than in the case of Gaussian noise. This means that it is more likely for real detector noises to mimic the effects of GW echoes.

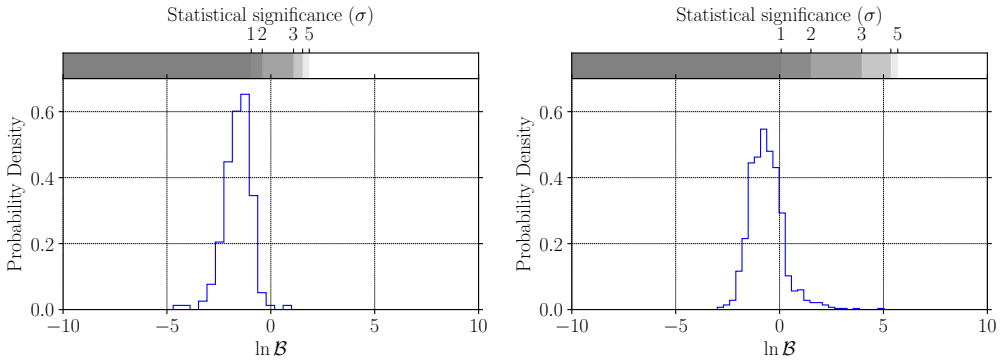


Figure 6.3: To estimate the statistical significance of a potential GW echoes event for simulated Gaussian noise and real noise during O1 of Advanced LIGO, we sampled the null distribution $p(\ln \mathcal{B}|\mathcal{H}_0)$ of the detection statistic by performing background runs, i.e., data with an IMR signal injected. The histograms of null distribution for the case of Gaussian noise with 192 samples and for the case of O1 noise with 953 samples are plotted in the left and right panels, respectively. The gray-scale bar in the top panel shows the statistical significance corresponding to the detection statistic (extrapolating from the $3\sigma$ region to the $5\sigma$ region). *Left panel:* For the case of simulated Gaussian noise, we see that the null distribution peaks at about $\ln \mathcal{B} \approx -1$, and the tail of the distribution extends only slightly towards $\ln \mathcal{B} > 0$. This means that it is unlikely for Gaussian noise to mimic GW echoes. *Right panel:* For the case of real noise during O1, we see that the distribution also peaks roughly at $\ln \mathcal{B} \approx -1$. However, the noise extends the tail of the distribution more significantly than in the case of Gaussian noise. This means that it is likely for real detector noises to mimic the effects of GW echoes.

In particular, we injected an IMRE injection with echo parameters that *Abedi et al. claimed to have found in GW150914* into simulated Gaussian noise with the

Advanced LIGO-Virgo network, and the detection statistic was found to be

$$\ln \mathcal{B}_{\text{detected, Gaussian}} = -0.2576 < 0.$$

This means that in the Bayesian point of view, the data slightly favor the null hypothesis that the data do not contain echoes. We compute the $p$-value and the corresponding statistical significance, given that the noise is Gaussian, as follows:

$$\begin{aligned} p\text{-value} &= 0.01275, \\ \text{statistical significance} &= 2.234\sigma. \end{aligned}$$

This suggests that what was claimed to be found by Abedi et al. in GW150914, even for GW detectors operating at design sensitivities and Gaussian noise, does not have sufficient statistical significance to claim a detection (i.e., $\geq 5\sigma$) in the frequentist approach, and it is also inconclusive whether the data favor the existence of echoes in the data in the Bayesian approach. From the fact that in Fig. 6.3 the null distribution for O1 real noise is more skewed to the right, we can expect that the statistical significance of what Abedi *et al.* [107] had found is small and consistent with noise.

Table 6.3 tabulates the values of the detection statistic $\ln \mathcal{B}$ that correspond to different levels of statistical significance in Gaussian and O1 backgrounds. If we want to make a gold-plated detection of GW echoes, i.e., having statistical significance $\geq 5\sigma$, we can set the detection threshold as

$$\begin{aligned} \ln \mathcal{B}_{\text{threshold, Gaussian}} &= 1.9, \\ \ln \mathcal{B}_{\text{threshold, O1}} &= 5.7, \end{aligned}$$

in the case of Gaussian noise and real O1 noise, respectively, so that any GW echoes detection with a detection statistic greater than or equal to this threshold is a $\geq 5\sigma$ detection of echoes.

| Statistical significance | Detection statistic *(Gaussian noise)* | Detection statistic *(O1 noise)* |
|---|---|---|
| $1\sigma$ | −0.9 | 0.1 |
| $2\sigma$ | −0.4 | 1.5 |
| $3\sigma$ | 1.1 | 4.0 |
| $4\sigma$ | 1.5 | 5.4 |
| $5\sigma$ | 1.9 | 5.7 |

Table 6.3: The values of the detection statistic $\ln \mathcal{B}$ and its corresponding statistical significances in both Gaussian and O1 backgrounds. If we want to make a gold-plated detection of GW echoes, i.e., with a statistical significance $\geq 5\sigma$, we can set the detection statistic threshold as $\ln \mathcal{B}_{\text{threshold, Gaussian}} = 1.9$ in the case of Gaussian noise, and $\ln \mathcal{B}_{\text{threshold, O1}} = 5.7$ so that any GW echoes detection with a detection statistic greater than or equal to this threshold is gold-plated.

### 6.3.5 Search sensitivity, efficiency and accuracy

#### 6.3.5.1 Sensitive parameter space of the search

Given the detection statistic threshold $\ln \mathcal{B}_{\text{threshold}}$, we would like to know what part of the parameter space of echoes we are able to see in the *optimal case*, where the GW detectors are operating at design sensitivities and the instrumental noise is Gaussian. To achieve this, we performed analyses on simulated data injected with an IMRE signal with different values of the echo parameters of interest. In this particular study, the IMR parameters were fixed to be *GW150914-like*. We will be focusing on the two parameters that are of the most astrophysical interest: the time interval between echoes $\Delta t_{\text{echo}}$ and the relative amplitude $A$. The two parameters were varied one at a time.

Figure 6.4 shows plots of the detection statistic $\ln \mathcal{B}$ as a function of $\Delta t_{\text{echo}}$ with the other echo parameters fixed to $(A = 0.6, \gamma = 0.89, t_0 = -0.02\,\text{s}, t_{\text{echo}} = 0.2940\,\text{s})$(left) and as a function of $A$ with other echo parameters fixed to $(\gamma = 0.89, t_0 = -0.02\,\text{s}, t_{\text{echo}} = 0.2940\,\text{s}, \Delta t_{\text{echo}} = 0.2925\,\text{s})$ (right), respectively. The horizontal dashed line in each plot corresponds to the detection statistic threshold of $5\sigma$ significance. Injections with a detection statistic exceeding or equal to the

threshold are marked with a green '`Y`', whereas injections with detection statistic lower than the threshold are marked with a red '`X`'. From the left panel, we see that there is *no trend* for how the detection statistic is distributed with different values of $\Delta t_{\rm echo}$, and that the search is able to detect GW echoes with a range of $\Delta t_{\rm echo}$ (more specifically $[0.05, 0.5]$ s) as expected since different values of $\Delta t_{\rm echo}$ only shift the echoes in time, and whether the search is able to find echoes or not should not depend on their time of occurrence as long as they do not overlap. Therefore, fixing the values of time-related echo parameters when investigating the sensitive parameter space of $A$ is justified. As for the relative amplitude $A$, we see from the right panel that there is a trend that signals with *smaller values of A have smaller values of the detection statistic*, and that the search can only pick up echoes with $A \gtrsim 0.3$ with $\geq 5\sigma$ significance. This is expected because the amplitude of echoes is damped and echoes with small amplitudes are buried in noise. This finding is consistent with that of Westerweck *et al.* that only injections with a strain amplitude $\gtrsim 10^{-22}$ in the echoes part could have the amplitude parameter $A$ recovered accurately [111]. In Ref. [114], a plot similar to the right panel of Fig. 6.4 was also shown [114], but it was unclear in their paper that at what value of their detection statistic (log Bayes factor for signal versus Gaussian noise, which is *different* from what we adopted in this paper) they are claiming a significant detection of echoes, and we will differ the discussion of the differences between two approaches in Sec. 6.4.3.2. It should also be noted that there are injections with echo amplitudes $A \gtrsim 0.1$ that are found by our search, and the number we quoted for the sensitive parameter space for $A$ is based on the loudest echo injection that were missed.

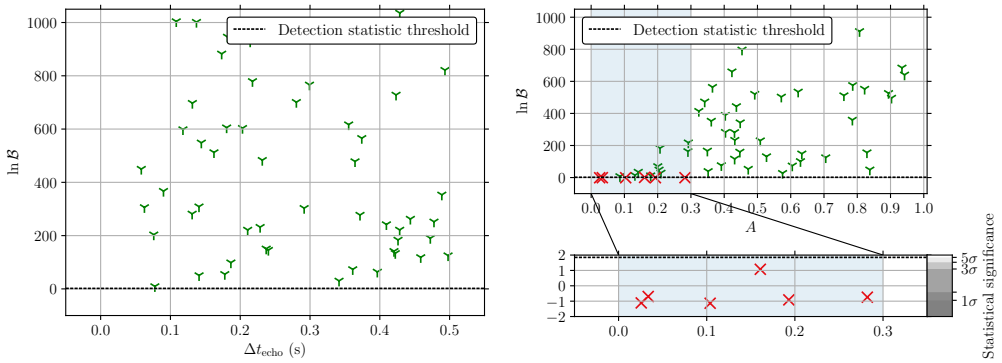


Figure 6.4: To investigate which part of the parameter space of echoes we are able to see in the optimal case, namely the GW detectors are operating at their design sensitivities and the instrumental noise is Gaussian, we performed analyses on simulated data injected with an IMRE signal with different values of the echo parameters of interest. *Left panel*: A plot of the detection statistic $\ln \mathcal{B}$ as a function of $\Delta t_{\rm echo}$, with other echo parameters fixed to ($A = 0.6, \gamma = 0.89, t_0 = -0.02\,{\rm s}, t_{\rm echo} = 0.2940\,{\rm s}$). *Right panel*: A plot of the detection statistic $\ln \mathcal{B}$ as a function of $A$, with the other echo parameters fixed to ($\gamma = 0.89, t_0 = -0.02\,{\rm s}, t_{\rm echo} = 0.2940\,{\rm s}, \Delta t_{\rm echo} = 0.2925\,{\rm s}$). The horizontal dashed line in each plot corresponds to the detection statistic threshold of $5\sigma$ significance. Injections with a detection statistic exceeding or equal to the threshold are marked with a green '`Y`', whereas injections with detection statistic lower than the threshold are marked with a red '`X`'. From the left panel, we see that there is *no trend* for how the detection statistic is distributed with different values of $\Delta t_{\rm echo}$, and that the search is able to detect GW echoes with a range of $\Delta t_{\rm echo}$ (more specifically $[0.05, 0.5]$ s) as expected since different values of $\Delta t_{\rm echo}$ only shift the echoes in time, and whether the search is able to find echoes or not should not depend on their time of occurrence as long as they do not overlap. Therefore, fixing the values of the time-related echo parameters when investigating the sensitive parameter space of $A$ is justified. As for the relative amplitude $A$, we see from the right panel that there is a trend that signals with *smaller values of A have smaller values of the detection statistic*, and that the search can only pick up echoes with $A \gtrsim 0.3$ with $\geq 5\sigma$ significance. This is expected because the amplitude of echoes is damped and echoes with small amplitudes are buried in noise. It should be noted that we found some injections with echo amplitudes $A \gtrsim 0.1$, and the number we quoted for the sensitive parameter space for $A$ is based on the loudest echo injections that were missed.

#### 6.3.5.2 Foreground distribution and search efficiency

To compute the efficiency $\zeta$ of the search as described in Sec. 6.2.4.2, the foreground distribution $p(\ln \mathcal{B}|\mathcal{H}_1)$ of the detection statistic was sampled by performing foreground runs, i.e., analyses on simulated data with IMRE signals injected. The IMR parameters of the injection set used to estimate the foreground distribution were chosen to be representative of what Advanced LIGO and Advanced Virgo would detect, and *were not fixed to be the same as a particular GW event*. We will discuss this choice in Sec. 6.4.1. As for the five echo parameters, their values were drawn randomly from the same distributions described in Table 6.2.

A numerical integration of Eq. 6.27 on the foreground distribution sampled gives the efficiency of the search as

$$\zeta_{\text{Gaussian}} = 0.82,$$
$$\zeta_{\text{O1}} = 0.61.$$

That means, in the frequentist language, that the search has a probability of 0.82 in the case of Gaussian noise and 0.61 in the case of O1 of detecting the existence of echoes *marginalized over a set of IMR and echo parameters* (with echo parameters drawn uniformly from the priors in Table 6.2), given that the data contain GW echoes and that the detection has a $\geq 5\sigma$ significance.

#### 6.3.5.3 Search accuracy

Given the detection statistic threshold $\ln \mathcal{B}_{\text{threshold, Gaussian}} = 1.9$ for the case of simulated Gaussian noise and $\ln \mathcal{B}_{\text{threshold, O1}} = 5.7$ for the case of O1, we make the claim that the data contain echoes only when the detection statistic is greater than or equal to the threshold. To gauge the performance of our proposed search methodology in terms of the ability to classify IMR and IMRE signals, a plot of the receiver operating characteristic (ROC) curve is shown in Fig. 6.5 for both the simulated Gaussian noise case and the O1 noise case. The ROC curve shows

the fraction of IMRE signals that the search has properly identified as IMRE signals (also known as the *true positive rate* for binary classifiers) given the fraction of IMR signals that the search has incorrectly identified as IMRE signals (also known as the *false positive rate*). Equivalently, it can also be interpreted as showing how the efficiency of a search changes with the detection statistic threshold. A more sensitive search will have a higher true positive rate for a given false positive rate. For a random guess, the true positive rate is the same as the false positive rate. Therefore, the ROC curve of a useful search should be to the left of the diagonal ROC curve. From Fig. 6.5, we see that the search in simulated Gaussian noise performs better than the search in O1 noise as expected, and both of the searches perform better than random guessing.

### 6.3.6 Demonstration of combining evidence from multiple GW echoes events

From the investigation of the sensitive parameter space of the search in the optimal case as described in Sec. 6.3.5.1, we see that the GW echoes will need to have a relative strength $A \gtrsim 0.3$ in order to be picked up by our search with $\geq 5\sigma$ significance in the optimal Gaussian noise case. Statistically we can incorporate results from multiple events so that the detection statistic of many weak signals can be added positively to stand out from the combined background, which adds negatively. Instead of combining the posterior distribution of echo parameters, which assumed the echo parameters for each event to be the same, we add the detection statistic log Bayes factor to form the *catalog log Bayes factor*, which is described in Sec. 6.2.5, and this approach only assumes each event to be independent and does not require the parameters of the events to be identical; indeed, it is assumed that they are all different for each event.

Here we demonstrate how combining multiple events can help us to detect weak echoes and make a detection statement about *a collection of events* (i.e., a catalog). Suppose we have ten potential GW echoes events, which is to say we have $N_{\mathrm{cat}} = 10$ events in the catalog. The catalog log Bayes factor is sim-

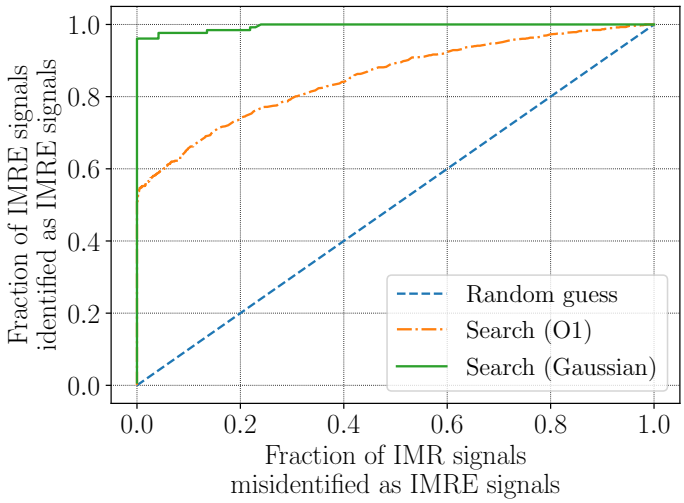


Figure 6.5: To gauge the performance of our proposed search methodology in terms of the ability to classify IMR and IMRE signals, the ROC curves for searches in O1 noise (orange dash-dotted line) and Gaussian simulated noise (green solid line), respectively, are shown. We see that the search in simulated Gaussian noise performs better than the search in O1 noise as expected because the fraction of IMRE signals identified as IMRE signals (with echo parameters drawn uniformly from the priors in Table 6.2) for the simulated Gaussian noise case is higher than that for the O1 noise case for a given fraction of IMR signals misidentified as IMRE signals. Also, both searches in simulated Gaussian noise and O1 noise outperform the random guess (blue dashed line) for the same reason described above.

ply the sum of the log Bayes factors of each individual event according to Eq. 6.31. We sampled the null distribution for the catalog log Bayes factor $p(\ln^{(\mathrm{cat})}\mathcal{B}|\mathcal{H}_0) = p(\sum_{i=1}^{N_{\mathrm{cat}}}\ln{}^{(i)}\mathcal{B}_0^1|\mathcal{H}_0)$ by picking $N_{\mathrm{cat}} = 10$ events from the background distribution and computing the corresponding catalog log Bayes factor. The histograms of the sampled null distribution for the *catalog log Bayes factor* for simulated Gaussian noise and real noise during O1 of Advanced LIGO (both with 10000 samples in the sampled background distributions) are shown in the left and right panels of Fig. 6.6, respectively. The gray-scale bar in the top

panel shows the statistical significance corresponding to the detection statistic. Compared to the histograms for individual log Bayes factors shown in Fig. 6.3, we see that the peak of the null distribution for the catalog log Bayes factor for both the case of Gaussian noise and O1 noise is shifted to be more negative as expected. If we focus on the case of Gaussian noise, and assume that the mean of the log Bayes factor $\langle \ln \mathcal{B} \rangle$ is roughly $-1$, then the mean of the catalog log Bayes factor of the size of $N_{\rm cat} = 10$ should be

$$\langle \ln^{(\rm cat)} \mathcal{B} \rangle \approx N_{\rm cat} \langle \ln \mathcal{B} \rangle = -10,$$

which is indeed the case in the right panel of Fig. 6.6. If we assume, for the sake of demonstration, that we have observed ten GW echoes events similar to what Abedi et al. claimed to have found in GW150914, namely the individual log Bayes factor is about $-0.2576$, then the catalog log Bayes factor will then become roughly

$$\ln^{(\rm cat)} \mathcal{B} \approx N_{\rm cat} \times -0.2576 = -2.576,$$

and thus we can make a statement with $\geq 5\sigma$ significance that there are GW echoes in one or more events in the catalog, but we will not be able to pinpoint which event has echoes.

From this example, we see that by combining the Bayesian evidence from multiple events, we can statistically make a detection statement about whether there are echoes in a collection of potential GW echoes candidates, which may be too weak to be detected individually.

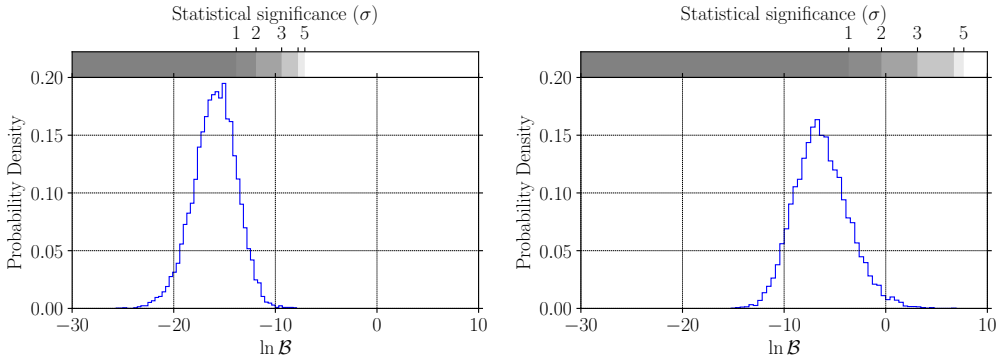


Figure 6.6: To detect GW echoes which may be individually too weak to be detected, we can instead make a detection statement on *a collection of events* (i.e., a catalog). The histograms of the sampled null distribution for the *catalog log Bayes factor* for simulated Gaussian noise and real noise during O1 of Advanced LIGO (both with 10000 samples) with a catalog size $N_{\rm cat} = 10$ are shown in the left and right panels, respectively. The gray-scale bar in the top panel shows the statistical significance corresponding to the detection statistic. Compared to the histograms for individual log Bayes factors shown in Fig. 6.3, we see that the peak of the null distribution for the catalog log Bayes factor for both the case of Gaussian noise and O1 noise is shifted to be more negative as expected. Since weak signals add positively while the background events add negatively in the catalog log Bayes factor, weak GW echoes signals can be detected as a whole, and a statement about whether there are echoes in a collection of potential GW echoes candidates can be made but not about which individual event/events in the catalog has/have echoes.

### 6.3.7 Search results for Advanced LIGO's first observing run data

We applied the search methodology described above to search for GW echoes in Advanced LIGO's O1 data. The prior distribution of the five echo parameters were chosen to be uniform over the respective prior ranges tabulated in Table 6.2. As for the IMR parameters, they were allowed to vary during the analyses and were not fixed to any particular values. For GW150914 and GW151012, we used 8-second-long data with three echoes in the IMRE waveforms for parameter

estimation. As for GW151226, we used 16-second-long data with *ten echoes* in the IMRE waveform. The difference in the length of data used is because the duration (starting from 30 Hz to merger) of the signal for GW151226 is slightly more than 1.5 s [36], while those for GW150914 and GW151012 are roughly less than 0.5 s [36]. This is due to the fact that GW151226 has a lower chirp mass compared to the other two events. Hence, we used a longer data segment for the analysis of GW151226, which enabled us to include more echoes in the IMRE waveforms.

Table 6.4 tabulates the detection statistic and the corresponding statistical significance and $p$-value for the three events (GW150914 [26, 36], GW151012 [36], and GW151226 [101, 36]) in O1. None of the events have a detection statistic greater than the $5\sigma$-detection threshold. Although the detection statistics used in the analyses were different, the ordering of the events by their statistical significance is consistent with that reported by Nielsen *et al.*[114]. For GW150914, the detection statistic is indeed less than the *upper bound* estimated in Sec. 6.3.4.1 for the case of the signal that Abedi et al. claimed to have found in GW150914 [107] in simulated Gaussian noise. In particular, GW151012 has the highest detection statistic among the three, and the value is greater than zero. However, that value is well within the background distribution we showed in the right panel of Fig. 6.3. Figure 6.7 summarizes the O1 search results with a plot of the background distribution of the detection statistic in the case of O1 real noise with the detection statistic of the three events in O1 indicated by vertical dashed lines, which shows that the detection statistic for all the events in O1 are within the background. Therefore, we conclude that no significant evidence was found to support the detection of GW echoes in O1.

Apart from making statistical statements on individual events regarding whether GW echoes are present or not, we can also make a statistical statement about whether GW echoes are present in a collection of events (a catalog) as described in Sec. 6.2.5. The catalog log Bayes factor, which is the sum of the log Bayes

| Event | Detection statistic | $p$-value | Statistical significance ($\sigma$) |
|---|---|---|---|
| GW150914 | $-1.3$ | 0.806 | $< 1$ |
| GW151012 | 0.4 | 0.0873 | 1.4 |
| GW151226 | $-0.2$ | 0.254 | $< 1$ |

Table 6.4: The detection statistic and its corresponding statistical significance and $p$-value for the three events in Advanced LIGO's O1 data. None of the events have a detection statistic greater than the threshold for $5\sigma$ detection. The ordering of the events in their statistical significance is consistent with that reported by Nielsen *et al.*[114].

factors for the three events in O1, was found to be

$$\ln \mathcal{B}^{(\mathrm{cat})}_{\mathrm{O1}} = -1.1.$$

Figure 6.8 shows the sampled background distribution for the catalog log Bayes factor for O1 noise, and the vertical dashed line indicates the catalog log Bayes factor found for the case of O1. We see that the detected value for O1 does not stand out from the background, with a statistical significance $< 1\sigma$. This is expected as the log Bayes factors for individual events lie well within in the background. Hence, we conclude that we also find no statistically significant combined evidence for the existence of GW echoes in O1 data.

## 6.4 Discussions

### 6.4.1 Background and foreground distribution estimation

During background and foreground estimation, the values of the IMR parameters were not fixed to the same as those of a particular GW event but rather were drawn from distributions that are representative of what Advanced LIGO and Advanced Virgo would detect. It is legitimate to do this because in our hypotheses (see Sec. 6.2.1) we did not require the IMR parameters to be known a priori. By allowing the IMR parameters to be different during background and foreground estimation, our sampled foreground distribution can be used to estimate the

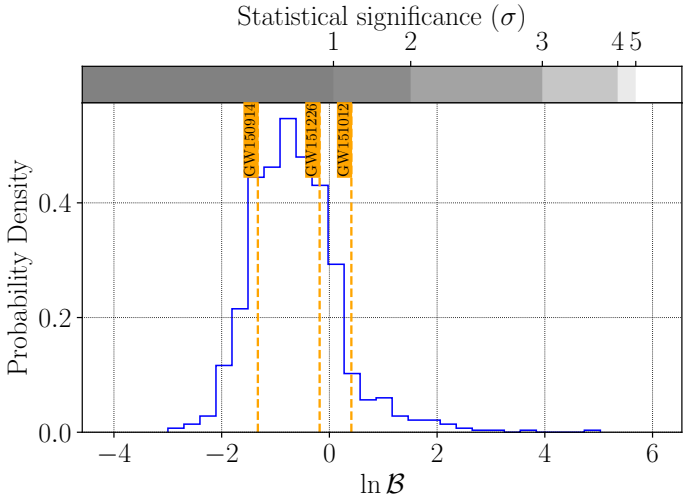


Figure 6.7: The histogram of the sampled null distribution for the *log Bayes factor* $\ln \mathcal{B}$ for Advanced LIGO's O1 data. This is the same plot as in the right panel of Fig. 6.3 with the detected values of the log Bayes factor for the three events in O1 (namely GW150914, GW151012 and GW151226). For GW150914 and GW151226, their detection statistics are less than zero, with a statistical significance less than $1\sigma$. As for GW151012, although the detection statistic for GW151012 is slightly greater than zero, it is still well within the background distribution. In fact, the statistical significance is only about $1.4\sigma$. Therefore, we conclude that no significant evidence was found to support the detection of GW echoes in O1 data.

efficiency of our search to detect GW echoes for a variety of inspiral-merger-ringdown-echo signals. Similarly, our estimated background distribution can be used to estimate the false alarm probability for a variety of inspiral-merger-ringdown signals. Although the background and foreground estimation can also be done specifically for each individual GW event, it will soon become computationally too expensive as we will have more than ten binary black hole mergers in an observing run; for example in the third observing run of Advanced LIGO and Virgo, it was estimated that there will be about $35^{+78}_{-26}$ binary black hole merger events [135]. One can perform a follow-up analysis on interesting

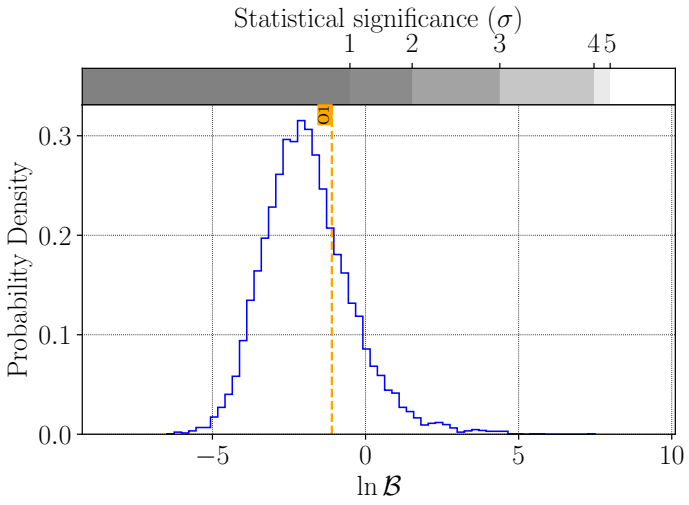


Figure 6.8: The histogram of the sampled null distribution for the *catalog log Bayes factor* $\ln \mathcal{B}^{(\mathrm{cat})}$ for Advanced LIGO's O1 data. This plot is similar to Fig. 6.6 but with a catalog of size $N_{\mathrm{cat}} = 3$. From the figure, we see that the value of the catalog log Bayes factor for O1 is also well within the background, with a statistical significance $< 1\sigma$. Hence, we conclude that we also find no statistically significant combined evidence for the existence of GW echoes in O1 data.

echo triggers found in this search to obtain a more accurate estimate of the false alarm probability and hence statistical significance.

### 6.4.2 Combining evidence from multiple GW echoes events

As described in Sec. 6.2.5, we can combine Bayesian evidence by simply multiplying the Bayes factors from each independent event to give the catalog Bayes factor. Note that when combining evidence, we do not assume GW events are described by the same set of echo parameters, whereas in Abedi *et al.* they assumed that each event has the same values of $\gamma$ and $t_0/\overline{\Delta t_{\mathrm{echo}}}$, where $\overline{\Delta t_{\mathrm{echo}}}$ denotes the average value of $\Delta t_{\mathrm{echo}}$ inferred in the events, which may not be the case in reality [107]. In addition, they combined the GW events by summing up the $\rho^2$'s of each event, without demonstrating that this is a proper way to combine

multiple measurements.

Combining Bayesian evidence from multiple GW echoes events can provide tighter constraints on the existence of GW echoes than a single event. Note that the null distribution for the catalog Bayes factor (and hence catalog log Bayes factor) can be constructed from the null distributions of log Bayes factors in a catalog of events.

### 6.4.3 Comparisons with other proposed search methodologies for GW echoes

#### 6.4.3.1 Model-dependent method proposed by Abedi et al.

As mentioned in the Introduction, Abedi *et al.* proposed a template-based search methodology for echoes using matched filtering. The parameter estimation was achieved by maximizing the square of the SNR $\rho^2$, which is also defined in Eq. 6.8. The set of echo parameters that give the highest value of $\rho^2$ were said to be the inferred values in their analysis. Also, they used $\rho^2$ as the detection statistic of their search. By finding the number of events, in segments of data without gravitational waves, that have a higher or equal value of the detection statistic found in a candidate, the background distribution of their detection statistic can be estimated.

However, the use of $\rho^2$ as the detection statistic is suboptimal because a large short-time instrumental noise fluctuation (also known as a glitch) can easily cause a peak in $\rho^2$, and as a result the search will be trying to overfit the glitch instead of echoes. Also, the addition of five echo parameters when searching for echoes in GW data will often make IMRE templates fit the data better than IMR templates when using $\rho^2$ as the detection statistic as there are more free parameters to be adjusted to fit the noise in the data. The Occam factor (described in Sec. 6.2.1.1) embodied in Bayesian model selection can mitigate the problem described above by penalizing more complicated models (i.e., having more free parameters), making our choice of the log Bayes factor more robust against noise

than $\rho^2$ as chosen by Abedi *et al.* [107].

#### 6.4.3.2 Model-dependent Bayesian model selection approach proposed by Nielsen et al.

Nielsen *et al.* [114] adopted the same Bayesian model selection framework to search for the existence of GW echoes. In their work, they considered two hypotheses — GW strain data consisting of both echoes plus Gaussian noise and data consisting only of Gaussian noise — and they are only looking at the post-merger part of a confirmed GW signal. In comparison to our work, we select between two hypotheses: GW strain data consisting of an inspiral-merger-ringdown-echo signal plus Gaussian noise versus an inspiral-merger-ringdown signal plus Gaussian noise model. Although both works are concerned with whether the data contain echoes, the hypotheses that are tested are not equivalent.

They interpreted their detection statistic (log Bayes factor) in the Bayesian way that when it is greater than zero, the data favor the echo signal plus Gaussian noise hypothesis and when it is less than zero, the data favor the pure Gaussian noise hypothesis. However, it is known and also pointed out by Nielsen *et al.* that the noise in real GW strain data is not strictly Gaussian, and thus the aforementioned interpretation is only approximately true. We can also see from Fig. 6.3 that the background distribution for our detection statistic, the log Bayes factor of IMRE versus IMR, is different for the cases of Gaussian noise and real noise in O1, with a noticeable tail to the right in the case of O1.

When interpreting the O1 results, they stated that a log Bayes factor with a value less than 1 does "not worth more than a bare mention" [114]. The use of a nomenclature to interpret the (log) Bayes factor is suboptimal because the scale to interpret the Bayesian evidence is not universally applicable. As mentioned by Kass *et al.* [136], for forensic evidence to be "conclusive" in court trials, the Bayes factor needs to be at least 10 times larger than what was originally suggested by Jeffreys, which suggests that the scale is not universally applicable to different

situations. A rigorous justification that the scale proposed by Kass *et al.*[136] is appropriate was not given in that paper, and its authors merely mentioned that "From our own experience, these categories seem to furnish appropriate guidelines." When performing the parameter estimation with a Gaussian noise model, the effects due to the non-Gaussianity of the noise can only be properly accounted by sampling the background distribution of the log Bayes factor in real data, which was done in our work as described in Sec. 6.3.4.1.

When generating templates of GW echoes for parameter estimation, Nielsen et al. chose to fix the parameters that govern the inspiral-merger-ringdown part of the waveform such as the component masses and the luminosity distance of the source of the signal. However, these inferred parameters have non-negligible uncertainties. By allowing the IMR parameters to vary during parameter estimation as we do in our work, we can marginalize over these parameters in model selection properly and hence get a more accurate value for the log Bayes factor, instead of replacing the joint posterior distribution, that carries information such as the correlation between parameters, with a product of Dirac delta functions.

#### 6.4.3.3 Model-agnostic method proposed by Tsang et al.

Tsang *et al.* [113] also adopted the Bayesian approach and used the log Bayes factor as the detection statistic. However, their search methodology is morphology agnostic, meaning that no detailed knowledge of the waveform of GW echoes is needed prior to a search. Their method was a modified version of the search pipeline `BayesWave` used for searching GW bursts, which is suitable for searching GW signals that are unmodeled or poorly modeled. This is exactly the current status of the modeling of GW echoes emitted from exotic compact objects, where there is no consensus that a particular waveform model can accurately model echoes. However, it is exactly because their search methodology requires no prior knowledge on the waveform of GW echoes that echoes need to be loud in order to be detected by their search. As in our proposed search methodology, we can make use of the knowledge on the waveform to extract weaker echoes buried

in noise and the estimation of physical parameters of echoes can be done easily.

### 6.5 Conclusions and future work

In this paper, we have demonstrated that our proposed search methodology using Bayesian model selection between the presence of echoes and their absence can identify and estimate the parameters of an IMRE signal buried in both Gaussian noise and real noise in the O1 data of Advanced LIGO. In the validation test, the recovered echo parameters were both close to the true value and had narrow posterior probability distributions. We demonstrated that we can use a Bayesian model selection to test the existence of echoes in simulated data, and report the statistical significance of the detection. By performing many analyses on simulated data with GW echoes injected, we also found that the search was able to identify GW echoes in simulated Gaussian noise about 82% of the time and in O1 real noise about 61% of the time with $\geq 5\sigma$ significance. Applying the search methodology to search for GW echoes in the three O1 events, we found no statistically significant evidence to support the detection of echoes.

In the future, we can repeat the analysis with different parametrized GW echoes waveform models that are more physical to provide more realistic evidence of the existence of echoes from exotic compact objects. When we understand the physics of exotic compact objects better in the sense that we can come up with physical waveform models of the echoes from different types of exotic compact objects, the methodology proposed in this paper can be readily modified to test the nature of exotic compact objects, using subhypotheses of $\mathcal{H}_1$ such as $\mathcal{H}_{\rm Gravastar}$ and $\mathcal{H}_{\rm Fuzzball}$, that is

$$\mathcal{H}_1 = \mathcal{H}_{\rm Gravastar} \vee \mathcal{H}_{\rm Fuzzball} \vee \ldots,$$

so that we can learn even more about the properties and structure of exotic compact objects.

**Acknowledgements**

The authors acknowledge the generous support from the National Science Foundation in the United States. LIGO was constructed by the California Institute of Technology and Massachusetts Institute of Technology with funding from the National Science Foundation and operates under cooperative agreement PHY-0757058. Virgo is funded by the French Centre National de Recherche Scientifique (CNRS), the Italian Istituto Nazionale della Fisica Nucleare (INFN) and the Dutch Nikhef, with contributions by Polish and Hungarian institutes. R.K.L.L. and T.G.F.L. would also like to gratefully acknowledge the support from the Croucher Foundation in Hong Kong. The work described in this paper was partially supported by a grant from the Research Grants Council of the Hong Kong (Project No. CUHK 24304317) and the Direct Grant for Research from the Research Committee of the Chinese University of Hong Kong. The authors acknowledge the use of the IUCAA LDG cluster Sarathi for the computational/numerical work. The authors are also grateful for computational resources provided by the LIGO Laboratory and supported by National Science Foundation Grants PHY-0757058 and PHY-0823459. The authors would like to thank Ajith Parameswaran for reviewing this paper during the LSC internal review. R.K.L.L. would also like to thank Zachary Mark, Rory Smith, Peter T. H. Pang, Ignacio Magana, Alex Nielsen, Ofek Birnholtz and Yanbei Chen for the fruitful conversations with the first author. Figure 6.2 was generated using the Python package `corner.py` [137]. This paper carries LIGO Document Number LIGO-P1800319.

*Chapter 7*

# SEARCHING FOR GRAVITATIONAL-WAVE ECHOES IN BINARY BLACK HOLE EVENTS FROM THE GWTC-1 CATALOG USING TEMPLATE-BASED BAYESIAN MODEL SELECTION APPROACH

This chapter contains work from

> R. K. L. Lo, T. G. F. Li, and A. J. Weinstein. "Searching for gravitational-wave echoes in binary black hole events from the GWTC-1 catalog using template-based Bayesian model selection approach". In: *unpublished* (2019).
> R. K. L. L performed the analyses and wrote the manuscript.

## 7.1 Introduction

Observations of gravitational waves from Advanced Laser Interferometer Gravitational-Wave Observatory (LIGO) [1] and Virgo [2] have proven to have significant impacts on fundamental physics, astrophysics and cosmology. For example, we can constrain the mass of the graviton [102, 20, 138, 22], the number of space-time dimensions [20] or measure the Hubble constant with joint electromagnetic observations in GW170817 [18, 16]. With gravitational waves, we are able to probe directly the strong-field dynamics of gravity, for instead during the merger of two black holes. Cardoso *et al.* [105] suggested that the post-merger part of a gravitational-wave signal can be used to probe the presence of near-horizon structure. Cardoso *et al.* [106] further pointed out that for a class of hypothesized compact objects, namely exotic compact objects (ECOs), will emit repeating gravitational waves due to their near-horizon structures when they merge or when they are formed as a result of the mergers of two 'ordinary' compact objects such as black holes, which are now commonly referred as *gravitational-wave echoes*.

Abedi *et al.* [107] claimed that they have found a combined $2.9\sigma$ evidence of gravitational-wave echoes in the first three binary black hole (BBH) events detected by LIGO [26, 101, 36], while other groups argued that the claimed statistical significance was over-estimated [108, 109, 111, 139, 114]. For a comprehensive review on the physics, the current observational claims and constraints of exotic compact objects, readers can refer to Ref. [140], while we will also review some of the essential physics of ECO in Sec. 7.4.

In this paper, we employ the data analysis method proposed in our earlier paper [139] to search for gravitational-wave echoes in the ten BBH events reported in the GWTC-1 catalog, and we found no statistically significant evidence of echoes in the data. During the preparation of this manuscript, another paper on searching for echoes in BBH events reported in GWTC-1 catalog using different data analysis technique was posted [141]. A paper reporting the search results on all the gravitational-wave (GW) events reported in the GWTC-1 catalog using a morphology-independent technique was also posted [113]. All three of the papers (including ours) also conclude that there is no statistically significant evidence of echoes in the data near the eleven GW events reported in the GWTC-1 catalog [9].

The paper is structured as follows: In Sec. 7.2, we first briefly describe the methodology and setup of the search. In Sec. 7.3, we then report our results on searching for echoes in the ten BBH events from the GWTC-1 catalog, as well as the search efficiency. With that, in Sec. 7.4 we place some limits on the population and physics of ECOs using the results of our search. Finally, in Sec. 7.5 we discuss the systematics of our search and the future prospects of searching for gravitational-wave echoes. In this paper, we adopt the geometrized unit system where $c = G = 1$.

## 7.2 Search description

### 7.2.1 Methodology

In this search, we employ the Bayesian model selection approach where we test the two hypotheses $\mathcal{H}_0$ and $\mathcal{H}_1$, which are defined as

$$\mathcal{H}_0 \coloneqq \text{No echoes in the data} \Rightarrow d = n + h_{\text{IMR}},$$
$$\mathcal{H}_1 \coloneqq \text{There are echoes in the data} \Rightarrow d = n + h_{\text{IMRE}},$$

where $d$ is the GW data, $n$ is the instrumental noise and $h_{\text{IMR}}$, $h_{\text{IMRE}}$ are the inspiral-merger-ringdown (IMR) gravitational-wave signal and inspiral-merger-ringdown-echo (IMRE) gravitational-wave signal, respectively. We compute the log Bayes factor $\ln \mathcal{B}$ as the detection statistic, which is defined as

$$\begin{aligned} \ln \mathcal{B} &= \ln p(d|\mathcal{H}_1, I) - \ln p(d|\mathcal{H}_0, I) \\ &= \ln Z_1 - \ln Z_0, \end{aligned} \tag{7.1}$$

where $I$ denotes the prior knowledge and $Z_i$ is known as the evidence or marginal likelihood of the $i$-th hypothesis, which is given by

$$Z_i = \int p(d|\vec{\theta}_i, \mathcal{H}_i, I) p(\vec{\theta}_i|\mathcal{H}_i, I)\ d\vec{\theta}_i, \tag{7.2}$$

where $p(d|\vec{\theta}_i, \mathcal{H}_i, I)$, is the likelihood function assuming the $i$-th hypothesis is true when viewed as a function of the set of parameters $\vec{\theta}_i$ describing the hypothesis.

In Bayesian statistics, the log Bayes factor has the interpretation that if $\ln \mathcal{B} > 0$, the hypothesis $\mathcal{H}_1$ is favored over the hypothesis $\mathcal{H}_0$ and vice versa. However, we have assumed that the instrumental noise is Gaussian and stationary for the construction of the likelihood function, which are not necessarily true for real data. To circumvent this problem, we sample the *null distribution* $p(\ln \mathcal{B}|\mathcal{H}_0)$, the distribution of the log Bayes factor assuming that $\mathcal{H}_0$ is true, by injecting

IMR waveforms into noise strains, and compute the $p$-value defined as

$$p = \Pr(\ln \mathcal{B} \geq \ln \mathcal{B}_{\rm detected} | \mathcal{H}_0) \tag{7.3}$$

$$= \int_{\ln \mathcal{B}_{\rm detected}}^{\infty} p(\ln \mathcal{B} | \mathcal{H}_0)\ d \ln \mathcal{B}, \tag{7.4}$$

where $\ln \mathcal{B}_{\rm detected}$ is the detection statistic observed in an analysis, and the right-hand-side of Eq. 7.4 is known as the *complementary cumulative distribution function (CCDF)* when viewed as a function of $\ln \mathcal{B}_{\rm detected}$. Note that $p(\ln \mathcal{B}|\mathcal{H}_0)$ is the *marginalized* background distribution of the detection statistic over the parameters $\vec{\theta}$ given by

$$p(\ln \mathcal{B}|\mathcal{H}_0) = \int p \left[ \ln \mathcal{B}(\vec{\theta}) | \mathcal{H}_0 \right] d\vec{\theta}. \tag{7.5}$$

The $p$-value has the interpretation that it is the probability that random noise fluctuation will cause the detection statistic to be as high as or higher than the observed value, which we can use to assign statistical significance to a particular candidate of GW echoes. For more details and discussions on our search methodology, readers can refer to our previous paper [139].

### 7.2.2 Setup

In this search, we use the phenomenological waveform model from Abedi *et al.* [107], which is parametrized by 5 parameters: $A$, $\gamma$, $t_0$, $t_{\rm echo}$, $\Delta t_{\rm echo}$. The amplitude parameter $A$ controls the amplitude of the first echo with respect to the IMR part of the waveform, and the reflectivity parameter $\gamma$ controls the amplitude ratio of each successive echo. The parameter $t_0$ is a nuisance parameter which controls the time of truncation on the IMR template to get the waveform of the ringdown. The parameter $t_{\rm echo}$ is the time difference between the merger $t_{\rm merger}$ and the first echo, which could be different from the time lag between each successive (second and so on) echo, which is denoted as $\Delta t_{\rm echo}$. For a detailed description and an illustration on how these parameters change the echo waveform, reader can again refer to Ref. [139]. We will discuss the effects of waveform systematics to the search in Sec. 7.5.1. It should be noted that

the methodology proposed in [139] is applicable to all parametrized waveform models of echoes.

Table 7.1 tabulates the prior ranges we used in the search. The prior distribution of each parameter is *uniform* over the respective prior range. The prior ranges for $t_{\rm echo}$ and $\Delta t_{\rm echo}$ were chosen such that the values predicted in Ref. [107] that correspond to a reflective surface at a proper distance of a Planck length $l_p$ away from the would-be event horizon of a compact object are included. As for the prior ranges for $A$ and $\gamma$, the prior ranges are wider in the search for the the second observing run (O2) compared to the ranges adopted in the the first observing run (O1) to avoid potential issues with the peak of a posterior distribution railing against the prior range [1].

| Parameter | Prior range (O1) | Prior range (O2) |
|---|---|---|
| $A$ | [0.0,1.0] | [0.0,1.5] |
| $\gamma$ | [0.0,1.0] | [0.0,1.5] |
| $t_0$ (s) | [−0.1,0.01] | [−0.04,0.04] |
| $t_{\rm echo}$ (s) | [0.05,0.5] | [0.05,0.5] |
| $\Delta t_{\rm echo}$ (s) | [0.05,0.5] | [0.05,0.5] |

Table 7.1: The prior range of the echo parameters. The prior distribution of each parameter is *uniform* over the respective prior range. The justification for choosing the prior ranges can be found in the main text.

In this paper, we search over the data near the ten BBH events from the GWTC-1 catalog [9]. Notice that we did not analyze the data near the binary neutron star (BNS) collision GW170817 because we do not have a good waveform model for echoes from binary neutron star mergers. Table 7.4 in Appendix 7.7 tabulates the hyper-parameters such as the starting frequency, segment length and number of echoes in a template we adopted in this search. Some of the results from searching over Advanced LIGO's O1 data were first presented in Ref. [139] and are reported in this paper again for completeness. The gravitational-wave strain

[1] This does not actually happen in our search as shown in Figure 7.3.

data in O1 and O2 of Advanced LIGO and Virgo are publicly available from the Gravitational Wave Open Science Center [128, 142, 129].

## 7.3 Search results

### 7.3.1 Gravitational-wave echoes after the binary black hole coalescences from the GWTC-1 catalog

In this search, we did not find any statistically significant evidence of echoes in the data near the ten BBH events from the GWTC-1 catalog [9]. Table 7.2 tabulates the detection statistic for this echo search, the corresponding $p$-value and the statistical significance of the ten BBH events computed using *only Hanford-Livingston (HL) data*, as well as the detection statistic computed using all Hanford-Livingston-Virgo (HLV) data when available. None of the events has a statistical significance greater than $5\sigma$. In fact, most of the events have a statistical significance $< 1\sigma$. There are only two events with a statistical significance greater than $1\sigma$, namely GW151012 with $1.4\sigma$ and GW170729 with $1.3\sigma$. Interestingly, these two events are actually the two less significant BBH detections reported in the GWTC-1 catalog in terms of their false alarm rate [9]. For the three BBH events in O1, the ordering of the events in their statistical significance is consistent with that reported in Nielsen et al. [114]. The same information is presented in the form of histograms shown in Figure 7.1, where the CCDF of the null distribution of the detection statistic with O1 and O2 noise are plotted, respectively. To achieve a $5\sigma$ detection, the detection statistic would need to be as high as $\approx 5.7$ for O1 and $\approx 5.8$ for O2. Note that the detection statistic calculated using both HLV data for GW170729, GW170809, GW170814 and GW170818 are consistent with that calculated using only HL data, indicating that the addition of Virgo data does not have a significant impact on detection of echoes in this case. Since the estimation of the corresponding null distribution for three-detector log Bayes factor is computational intensive, we did not perform the injection campaigns to estimate the background distribution to report the $p$-value and hence statistical significance with three-detector log Bayes factor.

| Event | Detection statistic (HL only) | $p$-value (HL only) | Statistical significance ($\sigma$) (HL only) | Detection statistic (HLV) |
|---|---|---|---|---|
| GW150914 | −1.3 | 0.806 | $< 1$ | – |
| GW151012 | 0.4 | 0.0873 | 1.4 | – |
| GW151226 | −0.2 | 0.254 | $< 1$ | – |
| GW170104 | −1.2 | 1.00 | $< 1$ | – |
| GW170608 | −1.0 | 0.998 | $< 1$ | – |
| GW170729 | 0.3 | 0.0913 | 1.3 | 0.5 |
| GW170809 | −0.4 | 0.844 | $< 1$ | −0.5 |
| GW170814 | −1.1 | 0.999 | $< 1$ | −1.1 |
| GW170818 | −1.2 | 1.00 | $< 1$ | −1.4 |
| GW170823 | −0.8 | 0.988 | $< 1$ | – |

Table 7.2: The detection statistic and its corresponding statistical significance of *this echo search* for the ten BBH events found during Advanced LIGO and Virgo's O1 and O2 as reported in the GWTC-1 catalog. None of the events has a detection statistic greater than the threshold for $5\sigma$ detection. Most of the events have a statistical significance $< 1\sigma$. There are only two events with a statistical significance greater than $1\sigma$, namely GW151012 with $1.4\sigma$ and GW170729 with $1.3\sigma$. Interestingly, these two events are actually the two less significant BBH detections reported in the GWTC-1 catalog in terms of their false alarm rate [9]. Note that the detection statistic calculated using both HLV data for GW170729, GW170809, GW170814 and GW170818 are consistent with that calculated using only HL data, indicating that the addition of Virgo data does not have a significant impact on detection of echoes in this case.

Apart from making a statistical statement on each individual GW event, we can also combine the log Bayes factor for each event to form a catalog log Bayes factor $\ln \mathcal{B}^{(\mathrm{cat})}$ defined as

$$\ln {}^{(\mathrm{cat})}\mathcal{B} = \sum_{i=1}^{N_{\mathrm{cat}}} \ln {}^{(i)}\mathcal{B}, \tag{7.6}$$

where $\ln {}^{(i)}\mathcal{B}$ is the individual log Bayes factor of the $i$-th event in the catalog of size $N_{\mathrm{cat}}$. The detailed motivation of catalog log Bayes factor can be found

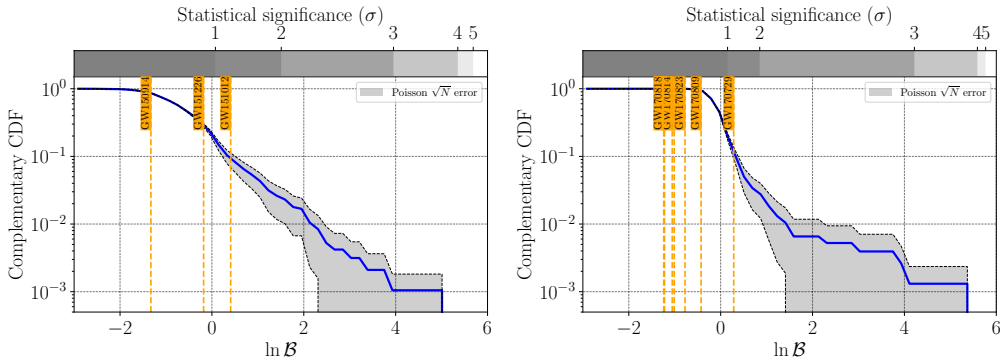


Figure 7.1: The histogram of the sampled complementary cumulative distribution function (CCDF) of the null distribution for the *individual log Bayes factor* $\ln \mathcal{B}$ computed using only HL data for Advanced LIGO's O1 (left panel) and O2 (right panel) data, with a sample size of 953 and 763, respectively. The grey-scale bar on top of each plot indicates the corresponding statistical significance (in $\sigma$) for each value of the detection statistic $\ln \mathcal{B}$. The dashed lines with enclosed area filled with grey color on each plot show the Poisson $\pm\sqrt{N}$ counting error on the number of background injections with detection statistic greater than certain values. Note that we have extrapolated the null distribution for $\gtrsim 3\sigma$ region. This does not affect our null detection claim as none of the events has a detection statistic greater than the corresponding $3\sigma$ value. To have a $5\sigma$ detection, the detection statistic $\ln \mathcal{B}$ would need to be as high as $\approx 5.7$ for O1 and $\approx 5.8$ for O2, respectively.

in Ref. [139]. Figure 7.2 shows the histogram of the sampled null distribution of the catalog log Bayes factor for O1 and O2 using HL data only. The catalog size for O1 and O2 are $N_{\rm cat}^{\rm O1} = 3$ and $N_{\rm cat}^{\rm O2} = 7$, respectively, corresponding to the number of BBH events reported in the GWTC-1 catalog [9]. We see from the plots that the detected value of the catalog log Bayes factor for both O1 and O2 are well within their respective background distribution, with statistical significance $< 1\sigma$ in both cases. Hence, we conclude that we did not find any statistically significant combined evidence for the existence of GW echoes in O1 and O2 data as well.

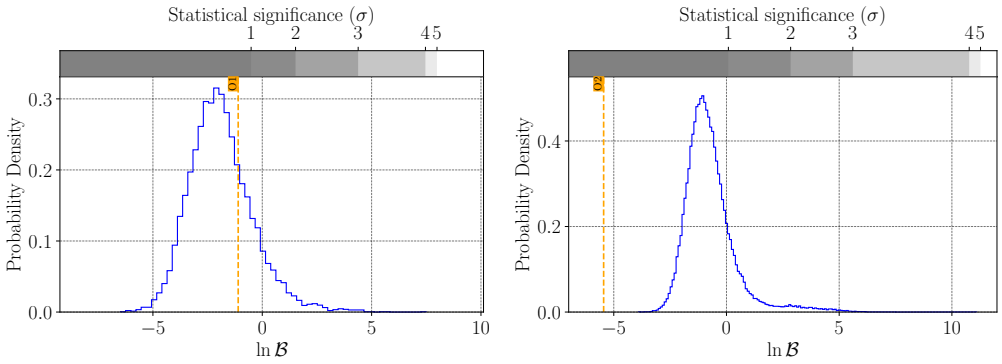


Figure 7.2: The histogram of the sampled null distribution for the *catalog log Bayes factor* $\ln \mathcal{B}^{(\mathrm{cat})}$ for Advanced LIGO's O1 (left panel) and O2 (right panel) data using only HL data. The plot on the left panel has a catalog of size $N_{\mathrm{cat}}^{\mathrm{O1}} = 3$ and the plot on the right panel has a catalog of size $N_{\mathrm{cat}}^{\mathrm{O2}} = 7$, corresponding to the number of BBH events detected in O1 and O2, respectively. From the figures, we see that the detected value of the catalog log Bayes factor for both O1 and O2 are well within the background, with statistical significance $< 1\sigma$. Hence, we conclude that we find no statistically significant combined evidence for the existence of gravitational-wave echoes in O1 and O2 data.

#### 7.3.1.1 Parameter estimation of echo parameters

Figure 7.3 shows violin plots for echo parameters (except for the nuisance parameter $t_0$) estimated from the ten BBH events reported in the GWTC-1 catalog [9]. The parameter estimation is not very informative, which is expected since none of the events has statistically significant evidence for echoes. Visually, the posterior distributions (left-hand-side of a violin) look similar to their corresponding prior distributions (right-hand-side of a violin). However, there is indeed a significant peak in the posterior distribution of $t_{\mathrm{echo}}$ for GW151226. But this alone does not constitute evidence of echoes in GW151226 since there is no repeating echoes seen in GW151226, reflected from the lack of a peak in the posterior distribution of $\Delta t_{\mathrm{echo}}$ for GW151226.

Quantitatively, the 90% Bayesian credible intervals for each parameter (indicated

with orange bars in the plots) are essentially as wide as the prior, meaning that there is not much information gained from parameter estimation. To quantify how much information was gained in parameter estimation from the prior distribution $q(x)$ to the posterior distribution $p(x)$, one can compute the Kullback–Leibler divergence $D_{\mathrm{KL}}$ [143] defined as

$$D_{\mathrm{KL}} = \int_{-\infty}^{\infty} p(x) \ln \left[ \frac{p(x)}{q(x)} \right] dx, \tag{7.7}$$

where we measure the KL divergence in the unit of *nats* that corresponds to the choice of the base $e$ for the logarithm function [2]. To get a sense of the KL divergence, suppose $q(x)$ is a Gaussian distribution with a mean $\mu$ and a standard deviation $2\sigma$, and $p(x)$ is a Gaussian distribution with the same mean $\mu$ but with a standard deviation $\sigma$, the KL divergence is around 0.807 nat. The KL divergence listed on top of each violin in Figure 7.3 shows that most of the posterior distributions are not very informative, in agreement with our visual inspection.

Readers should be very cautious when interpreting the violin plots and trying to look for features in the posterior distributions. Since none of the events has a high statistical significance, the so-called features in the posterior distributions are likely due to noise fluctuation, and the probability of such fluctuation is quantitatively given by the $p$-value.

[2] Another common choice of the base for the logarithm function is 2, and in that case the KL divergence will be in the unit of bits instead.

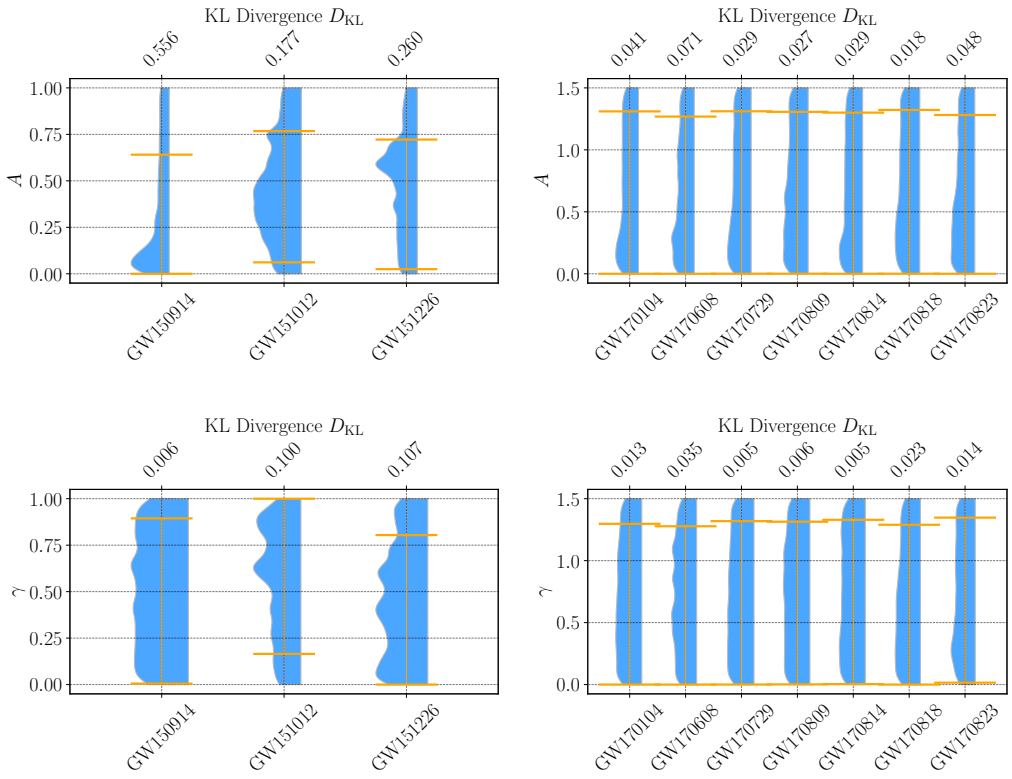


Figure 7.3: Violin plots for various echo parameters (except for the nuisance parameter $t_0$) estimated from the ten BBH events. Each violin consists of two parts: the left-hand-side of the violin shows the *posterior distribution* and the right-hand-side of the violin shows the *prior distribution* of a parameter, respectively. In this case, all the prior distributions are uniform. The orange bars indicate the upper and lower limit of the 90% Bayesian credible interval, respectively. The KL divergence $D_{\rm KL}$ is computed for each parameter inferred from each event to quantify the information gained from the parameter estimation, which is listed on top of each violin. Readers should be very cautious when interpreting the violin plots and trying to look for features in the posterior distributions. Since none of the events has a high statistical significance, the so-called features in the posterior distributions are likely due to noise fluctuation, and the probability of such fluctuation is quantitatively given by the $p$-value.

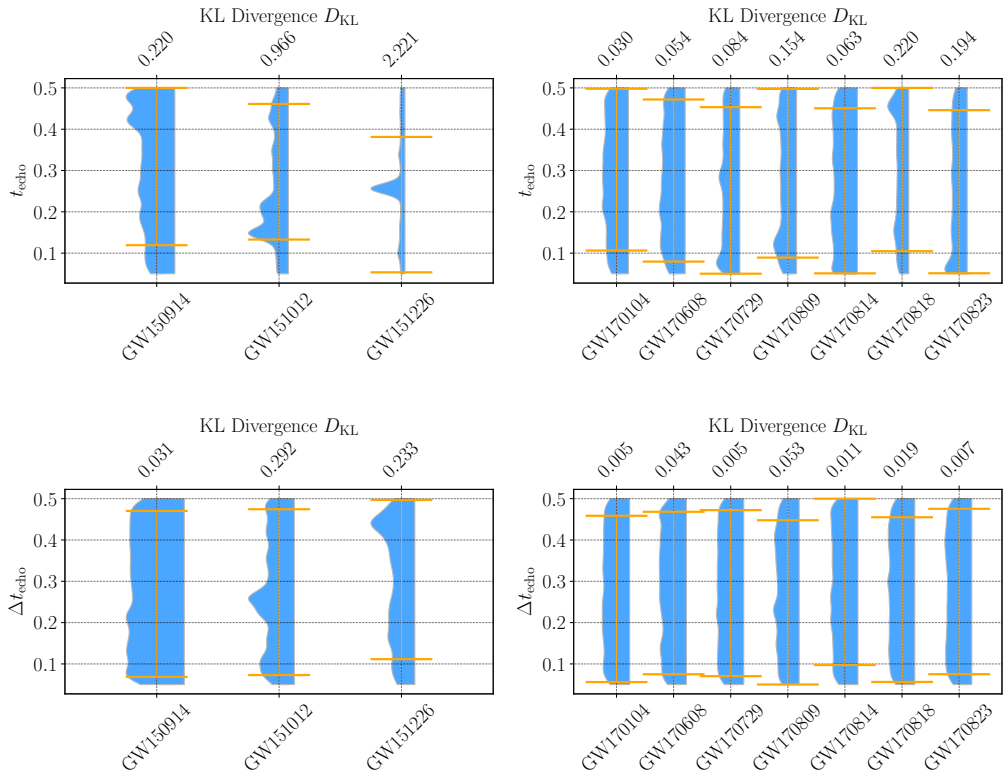


Figure 7.3: Violin plots for various echo parameters (except for the nuisance parameter $t_0$) estimated from the ten BBH events (continued)

### 7.3.2 Search efficiency

To demonstrate the capability of our pipeline for detecting gravitational-wave echoes, quantitatively we can compute the *search efficiency* $\zeta$ defined as

$$\zeta = \int_{\ln \mathcal{B}_{\mathrm{threshold}}}^{\infty} p(\ln \mathcal{B}|\mathcal{H}_1)\, d\ln \mathcal{B}, \tag{7.8}$$

where $p(\ln \mathcal{B}|\mathcal{H}_1)$ is the *marginalized* foreground distribution of the detection statistic over the parameters $\vec{\theta}$ given by

$$p(\ln \mathcal{B}|\mathcal{H}_1) = \int p\left[\ln \mathcal{B}(\vec{\theta})|\mathcal{H}_1\right] d\vec{\theta}. \tag{7.9}$$

Similar to the case for the background distribution $p(\ln \mathcal{B}|\mathcal{H}_0)$, we obtain samples of the foreground distribution $p(\ln \mathcal{B}|\mathcal{H}_1)$ by performing injection campaigns where we inject IMRE signals into noise strains as in real analyses, and then compute the search efficiency integral numerically shown in Eq. 7.8. We obtain the search efficiency with simulated Gaussian noise, real O1 and O2 noise as

$$\begin{aligned}\zeta_{\text{Gaussian}} &= 0.82 \pm 0.03,\\ \zeta_{\text{O1}} &= 0.61 \pm 0.01,\\ \zeta_{\text{O2}} &= 0.59 \pm 0.02.\end{aligned}$$

We see that the search efficiency with real O1 and O2 noise are statistically consistent to each other, and worse than that with simulated Gaussian noise (the ideal case) as expected.

Visually, we can look at receiver operating characteristic (ROC) curves shown in Figure 7.4. A ROC curve is commonly used to gauge the performance of a binary classifier, and here we are classifying a GW signal into either an IMR or IMRE signal. In this particular case, it shows the fraction of IMRE signals that the search correctly identified as IMRE signals as a function of the fraction of IMR signals that the search misidentified as IMRE signals. Essentially, a ROC curve is giving information about the *separation between the background and foreground distribution*. We see from the plot in Figure 7.4 that the search in O1 is slightly more sensitive than the search in O2, and the two are comparable in sensitivity and both are significantly more sensitive than a random guess. The ROC curves are consistent with the quantitative description of the performance of the search with search efficiency $\zeta$.

## 7.4 Limits on population and physics of exotic compact objects from the search

Even with a null detection, we can still extract some information about the population and physics of exotic compact objects, with the caveat that *the echo templates we used in the search accurately model the actual gravitational-wave*

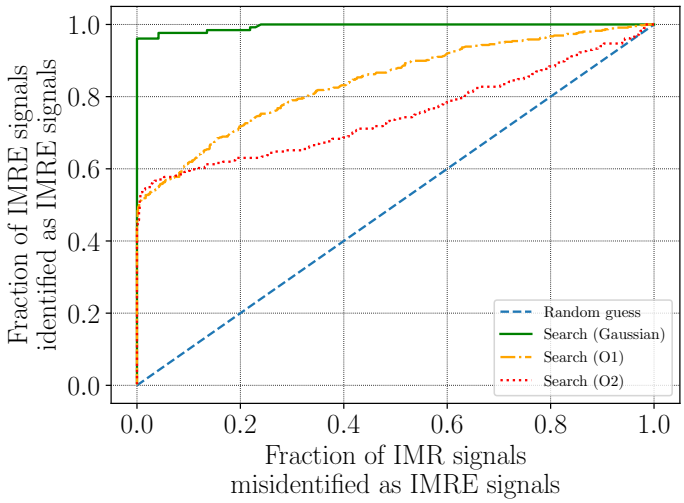


Figure 7.4: The receiver operating characteristic (ROC) curves of the searches with different noise. A ROC curve is commonly used to gauge the performance of a binary classifier, and here we are classifying a GW signal into either an IMR or IMRE signal. In this particular case, it shows the fraction of IMRE signals that the search correctly identified as IMRE signals as a function of the fraction of IMR signals that the search misidentified as IMRE signals. A more sensitive search should have a smaller fraction of IMR signals misidentified as IMRE signals given a fixed fraction of IMRE signals identified as IMRE signals. Essentially, a ROC curve is giving information about the *separation between the background and foreground distribution*. We see from the plot that the search in O1 is slightly more sensitive than the search in O2, and the two are comparable and both are significantly more sensitive than a random guess. The ROC curves are consistent with the quantitative description of the performance of the search with search efficiency $\zeta$.

*signals from exotic compact objects*. We will discuss this issue further in Sec. 7.5.1. With this in mind, the following section serves to *demonstrate* what we can learn from gravitational-wave echoes detections (or the lack thereof) once we have accurate template models of GW echoes.

### 7.4.1 Upper limit on gravitational-wave echoes event rate density

Suppose that the hypothesized exotic compact objects exist, and that they form binary systems and merge just like ordinary compact objects such as black holes[3]; or perhaps an exotic compact object would be formed as the remnant of a binary black hole merger. These scenarios were proposed to emit gravitational-wave echoes. Therefore, we can understand more about the *merger rate of exotic compact objects* or the *formation rate of exotic compact objects* from mergers of ordinary compact objects by measuring the event rate (or the rate density) of gravitational-wave echoes. Since we do not have any confident detection of GW echoes, from this we can infer an upper bound on how frequent GW echoes are emitted and we can place an upper limit on the event rate density. The 90% Bayesian credible interval[4] of the event rate density (for a derivation see Appendix 7.8) [5] is given by $(0, R^{\rm Echoes}_{90\%})$. Assuming a uniform prior, the upper limit $R^{\rm Echoes}_{90\%}$ can be computed as [144, 145]:

$$R^{\rm Echoes}_{90\%} = \frac{-\ln(0.1)}{\langle VT\rangle^{\rm Echoes}_{\rm Sensitive}}, \tag{7.10}$$

where $\langle VT\rangle^{\rm Echoes}_{\rm Sensitive}$ is the sensitive spacetime volume surveyed by our search. The sensitive spacetime volume surveyed by the search for gravitational-wave echoes $\langle VT\rangle^{\rm Echoes}_{\rm Sensitive}$ can be approximated as

$$\langle VT\rangle^{\rm Echoes}_{\rm Sensitive} \approx \frac{N_{\rm recovered}}{N_{\rm injected}} \langle VT\rangle^{\rm BBH}_{\rm Sensitive}, \tag{7.11}$$

where $\langle VT\rangle^{\rm BBH}_{\rm Sensitive}$ is the sensitive spacetime volume for binary black hole events. A detailed justification of this estimate can be found in Appendix 7.9.

[3] If that is the case, then the inspiral phase of the gravitational-wave emission will also imprint information about the exotic compact object binary. Readers can refer to Ref. [140] for details. However, there is an issue with the stability of such a configuration.

[4] For a null detection, Bayesian credible interval and frequentist confidence interval coincide, but they have very different interpretations.

[5] Note that this *does not imply that gravitational-wave echoes exist*. If gravitational-wave echoes do not exist, then its event rate density would be 0 (in any unit), which is indeed smaller than the bound.

From the GWTC-1 catalog [9], we can obtain an estimate of the sensitive spacetime volume for binary black hole events by $\langle VT\rangle^{\rm BBH}_{\rm Sensitive} = \Gamma/R$, where $\Gamma = 10$ is the number of BBH detected in O1 and O2. Choosing the upper limit $R = 101\ {\rm Gpc}^{-3}{\rm yr}^{-1}$ reported in Ref. [9] as a conservative estimate, we have $\langle VT\rangle^{\rm BBH}_{\rm Sensitive} \approx 0.0990\ {\rm Gpc}^{3}{\rm yr}^{1}$. From injection campaigns, we obtained

$$\frac{N_{\rm recovered}}{N_{\rm injected}} \approx 0.489. \tag{7.12}$$

Therefore, we can place an upper limit on the event rate density of gravitational-wave echoes as

$$R^{\rm Echoes}_{90\%} \approx 48\ {\rm Gpc}^{-3}{\rm yr}^{-1}. \tag{7.13}$$

### 7.4.2 Limits on the amplitude of echoes and reflectivity of exotic compact objects

If gravitational-wave echoes are loud enough, they would have been detected by our search. Therefore, the fact that we did not have any detection of echoes means that *if echoes were actually emitted then they are simply not strong enough*. In Ref. [139] we demonstrated that the detectability of echoes mainly depends on the amplitude of GW echoes. Hence, we can place a *joint upper limit* on the amplitude of GW echoes emitted (related to the parameter $A$) and the reflectivity (related to the parameter $\gamma$, where $\gamma \sim \sqrt{\mathcal{R}_{\rm BH}\mathcal{R}_{\rm ECO}}$, with $\mathcal{R}_{\rm BH}$ and $\mathcal{R}_{\rm ECO}$ are the reflectivity of the black hole and that of the surface of exotic compact object, respectively [140]). Using the language of the sensitive parameter space, this is because the search is sensitive to a certain portion of the parameter space and therefore the fact that we did not detect any echoes means that if the exotic compact object is emitting GW echoes, they would not be in the sensitive parameter space. Hence, constraining the amplitude and the reflectivity parameter amounts to finding the sensitive parameter space (at least the $A-\gamma$ subspace), and a null detection can be used to exclude the sensitive parameter space.

Here we only place the upper limit of the amplitude and reflectivity parameter for GW151012, the event with the highest statistical significance for GW echoes

search ($1.4\sigma$). In principle, the analysis can be done for all ten BBH events. However, finding the sensitive parameter space is computationally intensive. Therefore, we picked the GW event with the highest statistical significance for the echo search. Figure 7.5 shows a contour plot of the detection statistic $\ln \mathcal{B}$ in the $A - \gamma$ plane. We have fixed all the other echo parameters (i.e., $t_0$, $t_{\rm echo}$ and $\Delta t_{\rm echo}$) to take the value of the corresponding maximum a posteriori estimator (MAP). In Ref. [139], we have shown that the time-related parameters do not affect the ability of the pipeline to detect echoes, as long as the echoes are not overlapping with each other. Hence, fixing the time-related echo parameters is justified. We see that the sensitive parameter space of $A$ and $\gamma$ parameter is roughly $A \gtrsim 0.7$ *independent* of the value of $\gamma$ [6]. That implies we can rule out echoes with amplitude parameter $A > 0.7$ (with $5\sigma$ significance, since we picked the detection statistic threshold that corresponds to a $5\sigma$ detection), and equivalently if the remnant of GW151012 emits GW echoes, the amplitude parameter $A$ cannot be higher than 0.7, if the true value of the time lag between successive echoes $\Delta t_{\rm echo}$ is *within the prior range* $0.05$ (s) $< \Delta t_{\rm echo} < 0.5$ (s).

### 7.4.3 Limits on the compactness of exotic compact objects

A popular way of modeling an exotic compact object is to think of an ECO as a black hole with a reflective surface near the would-be event horizon at a location of $r_{\rm ECO} = r_{\rm H}\,(1+\epsilon)$ is the coordinate of the would-be event horizon in the Boyer-Lindquist coordinates, where $r_{\rm H} = M\left(1+\sqrt{1-\chi^2_{\rm ECO}}\right)$ and $\chi_{\rm ECO}$ is the dimensionless spin parameter of the ECO. In a *static ECO model*, the ECO surface stays at the same location and the ECO will not expand or contract. In this simplified picture, the light ring and the ECO surface act like a GW cavity, reflecting some GW while transmitting some GW away from the system, which is seen by us as GW echoes. The reflective surface is usually motivated

[6] This is *not* saying that the detection statistic log Bayes factor is independent $\gamma$. On the contrary, one can see the dependence of the detection statistic on the reflectivity parameter $\gamma$ from Figure 7.5. In fact, the statement that the sensitive parameter (sub-)space is independent of $\gamma$ is a gross over-simplification.

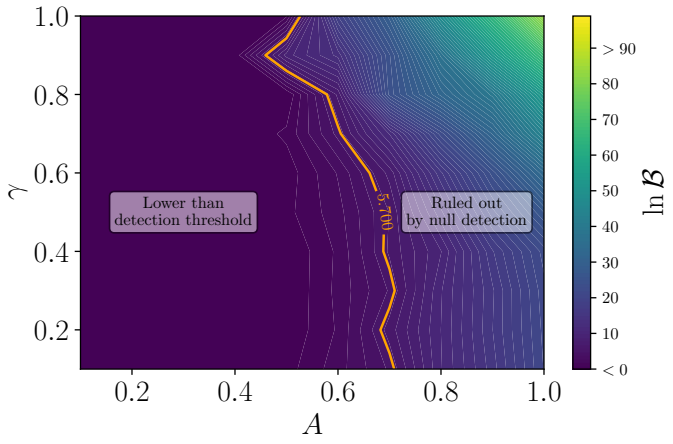


Figure 7.5: A contour plot of the detection statistic $\ln \mathcal{B}$ in the $A - \gamma$ plane for GW151012. The color indicates the value of the detection statistic. A contour line corresponding to the $5\sigma$ detection threshold is drawn to separate the sensitive parameter (sub-)space with the rest of the parameter space. We see that the sensitive parameter space of $A$ and $\gamma$ parameter is roughly $A \gtrsim 0.7$ *independent* of the value of $\gamma$, meaning that we can rule out echoes with amplitude parameter $A > 0.7$ with $5\sigma$ significance.

by considerations of quantum gravity and therefore usually at a proper distance $\Delta \sim l_p$ away from the would-be event horizon, where $l_p$ is the Planck length. Ref. [146] [7] pointed out that echo-emitting ECOs suffer from an instability due to the back-reaction of gravitational waves [146]. As a result, the ECO surface cannot be too close to the would-be event horizon. Nonetheless, we will assume in the following text that the ECO of interest is stable and the surface is static, meaning that gravitational-wave echoes will not induce a prompt collapse of the ECO.

In the limit of $\epsilon \to 0$, for spinning ECOs, the time difference between each

[7] Note that in Ref. [146], they have chosen a different parametrization, where they place the ECO surface at $r_{\rm ECO} = 2M + \epsilon$ instead. Also, readers should be cautious that Ref. [146] uses $\Delta t_{\rm echo}$ to mean both the time lag between the merger and the first echo and the time difference between each successive echo. We make the distinction between the two and use $t_{\rm echo}$ and $\Delta t_{\rm echo}$, respectively.

successive echo $\Delta t_{\rm echo}$ relates to the location of the ECO surface by [140, 107]

$$\Delta t_{\rm echo} \sim -4M \left[1 + \left(1 - \chi^2_{\rm ECO}\right)^{-1/2}\right] \log(\epsilon). \tag{7.14}$$

Note that if we set $\chi_{\rm ECO} = 0$, we get the expression for non-spinning ECOs as

$$\Delta t_{\rm echo} \sim -8M \log(\epsilon). \tag{7.15}$$

Note that $0 < \epsilon < 1/2$ since the $\epsilon = 1/2$ implies that the ECO surface is located at the light ring, which does not give rise to any echo in this simplifying static ECO picture, and $\epsilon = 0$ means that the so-called ECO is actually a black hole and also will not give rise to any echo. In particular, the small parameter $\epsilon$ is related to the proper distance $\Delta$ by [107]

$$\Delta = \frac{2\sqrt{\epsilon}}{\left(1 - \chi^2_{\rm ECO}\right)^{1/4}} r_{\rm H}. \tag{7.16}$$

In the case of non-spinning ECOs, $r_{\rm H} = 2M$ and $\chi_{\rm ECO} = 0$ and we have [107, 146]

$$\Delta = 4\sqrt{\epsilon}M. \tag{7.17}$$

Therefore, we can infer the compactness of an ECO, in terms of $\epsilon$ or $\Delta$, from the parameter $\Delta t_{\rm echo}$.

From Sec. 7.3.1.1, we know that the posterior distributions for $\Delta t_{\rm echo}$ are not informative in a sense that they are more or less the prior distributions we put into the search. However, the prior range we chose for $\Delta t_{\rm echo}$ does not span the entire parameter space [8]. Therefore, we can apply the same logic as in Sec. 7.4.2 that if we assume ECOs truly exist, the fact that the search did not find any echoes means that the echoes emitted must not be inside of the sensitive parameter space. Since in Ref. [139] we showed that the detectability of echoes does not depend

[8] Sadly, if we choose the prior range of a uniform prior distribution to span the entire parameter space of $\Delta t_{\rm echo}$, namely $(0, \infty)$, then the search will not be able to find any echoes because of the infinite prior volume and hence infinitely small Occam factor.

on $\Delta t_{\rm echo}$ much except when echoes are overlapped with each other, this means that the projected sensitive parameter space for $\Delta t_{\rm echo}$ is exactly its prior range. *Suppose that* the true value for the amplitude parameter $A$ is greater than 0.7, and the true value of $\Delta t_{\rm echo}$ is actually greater than 0.5 s, we can use Eq. 7.14 to get an *upper bound* on the small parameter $\epsilon$ and therefore the proper distance $\Delta$ between the event horizon and the ECO surface; similarly if we assume that the true value of $\Delta t_{\rm echo}$ is actually less than 0.05 s, we can get a *lower bound* on $\epsilon$ and hence $\Delta$. Note that the two assumptions are *exclusive*, and therefore the two bounds are not compatible to each other.

Again, in principle the analysis can be done for all ten BBH events. Here we picked GW151012 as an example with the same reason in Sec. 7.4.2. Table 7.3 tabulates what we can say about the compactness (in terms of $\epsilon$ and $\Delta$) of the remnant compact object of GW151012 under different assumptions on the true value of $\Delta t_{\rm echo}$ if the remnant compact object is an ECO. It should be stressed again that in order to obtain the bounds, we assumed that the templates we used accurately modeled the gravitational-wave echoes emitted by an ECO, and that the ECO is static and stable. However, Ref. [146] suggests that the configuration $\epsilon \lesssim 10^{-124}$ is unlikely to be stable and it will promptly collapse to a black hole.

| Assumptions | Bound on $\epsilon$ | Bound on $\Delta$ |
|---|---|---|
| $A \gtrsim 0.7,\ \Delta t_{\rm echo,\,true} > 0.50$ s | $\epsilon \lesssim 10^{-124}$ | $\Delta/l_p \lesssim 10^{-22}$ |
| $A \gtrsim 0.7,\ \Delta t_{\rm echo,\,true} < 0.05$ s | $\epsilon \gtrsim 10^{-12}$ | $\Delta/l_p \gtrsim 10^{34}$ |

Table 7.3: Under different assumptions on the true value of $\Delta t_{\rm echo}$, we can place different bounds on the compactness of the remnant ECO of GW151012 in terms of $\epsilon$ or $\Delta$, if the remnant compact object is an ECO. Note that in order to obtain the bounds, we assumed that the templates we used accurately modeled the gravitational-wave echoes emitted by an ECO, and that the ECO is static and stable. However, Ref. [146] suggests that the configuration $\epsilon \lesssim 10^{-124}$ is unlikely to be stable and it will promptly collapse to a black hole.

## 7.5 Discussion

### 7.5.1 Systematics due to waveform model

The waveform model of gravitational-wave echoes proposed by Abedi *et al.* in Ref. [107], which is also used in our search, is the first attempt to model GW echoes. To construct a template of GW echoes using this model, one simply 'copies' the ringdown part of a IMR template and then 'pastes' the cropped scaled waveform many times with equal time separation. Although this simple recipe may capture some essential features of GW echoes, namely repeating ringdown signals separated by constant time difference, the templates are unlikely to match the phase evolution of real gravitational-wave echoes emitted by exotic compact objects. It is important to maximize the match when one is trying to detect very weak signals in a noisy background in order to maximize the signal-to-noise ratio of the signals.

That being said, the waveform model is still useful for picking up echoes in GW data with echoes projected to the space spanned by the waveform model with *sub-optimal search sensitivity*. With this caveat, readers should carefully interpret the meaning of the parameters in the waveform model since what we observe in a template-based search is the projection of a real signal onto the templates, where the templates might not be faithful in representing the signal.

In fact, Wang *et al.* argued that gravitational-wave echoes might not be separated with a regular time interval [147]. This can be easily seen when one does not assume a static ECO model that the reflective surface moves as energy is being pumped into the object. Indeed, Ref. [146] suggests that in some cases the ECO surface might have to expand *teleologically* in response to the in-falling gravitational radiation to prevent collapse. The authors of Ref. [148] investigated the systematics due to mistakenly assuming a constant $\Delta t_{\rm echo}$ using a search methodology similar to ours proposed in Ref. [139] and they concluded that this will lead to significant bias in parameter estimation. Evidently, allowing each successive pair of echoes to have different $\Delta t_{\rm echo}$ would induce a very large penalty from Occam factor when the number of echoes in a template is large. A

smarter way to deal with this problem, as explored by Ref. [148], is to model the time delay $\Delta t_{\rm echo}$ as a function of some other more tractable parameters, for example the number of echoes already emitted by the object. However, this modeling will also have its own systematics. When the number of echoes $N_{\rm echo}$ in a template is not large, for example in our search, most of the time we only include three echoes in a template, as long as the time scale of the variability of the time delay $\tau_{\rm var} \gg N_{\rm echo}\Delta t_{\rm echo}$, the search will not suffer significant bias from the irregularity of the time delay. It remains unclear as to which is the best solution to account for the possibility of irregular time lag between successive echoes.

To circumvent the systematics due to waveform uncertainties altogether, one can search for gravitational-wave echoes using a morphology-independent method, for instead Ref. [113] and Ref. [112], at the expense of the search sensitivity. However, if gravitational-wave echoes are intrinsically very weak, these morphology-independent searches might not be able to detect these tiny echoes due to insufficient sensitivity.

### 7.5.2 Future searches of gravitational-wave echoes

Efforts were made to model gravitational-wave echoes emitted from exotic compact objects more accurately, for example Refs. [123, 124, 149, 126, 127]. In the future, our search for gravitational-wave echoes will switch to use (perhaps multiple) more physically-motivated waveform models of echoes to provide more robust evidence of the existence (or the non-existent) of gravitational-wave echoes and hence exotic compact objects.

## 7.6 Conclusion

Using the template-based Bayesian model selection approach described in Ref. [139], we find no statistically significant of gravitational-wave echoes in the data near the ten BBH events reported in the GWTC-1 catalog [9]. In particular, the most significant GW event in this echo search, GW151012, only has a significance

of $1.4\sigma$, with most of the GW events having significance $< 1\sigma$ in the echo search. We also find $< 1\sigma$ combined evidence for the existence of gravitational-wave echoes in O1 and O2 data, respectively. With a null detection, we are able to place an upper limit of the 90% Bayesian credible interval on the event rate rate density of echoes, which is found to be 48 $\mathrm{Gpc}^{-3}\mathrm{yr}^{-1}$. For the most significant event in this echo search, GW151012, if we assume that the remnant of the merger is truly an echo-emitting exotic compact object, and the time lag between each successive echo is within 0.05 (s) $< \Delta t_{\mathrm{echo}} <$ 0.5 (s), then the amplitude parameter $A$ of the echoes must be $A < 0.7$. Alternatively, if we instead assume that the amplitude parameter is $A > 0.7$, then we can constrain the compactness in terms of the proper distance $\Delta$ between the ECO surface and the would-be event horizon to be $\Delta/l_p \lesssim 10^{-22}$ if $\Delta t_{\mathrm{echo,\,true}} > 0.50$ (s) or $\Delta/l_p \gtrsim 10^{34}$ if $\Delta t_{\mathrm{echo,\,true}} < 0.05$ (s), where $l_p$ is the Planck length. Readers should be aware of the systematics of these results due to inaccurate waveform model used in this search, and we expect the effects of waveform uncertainties will become less significant when more accurate waveform models of gravitational-wave echoes are available.

**Acknowledgements**

The authors acknowledge the generous support from the National Science Foundation in the United States. LIGO was constructed by the California Institute of Technology and Massachusetts Institute of Technology with funding from the National Science Foundation and operates under cooperative agreement PHY-0757058. Virgo is funded by the French Centre National de Recherche Scientifique (CNRS), the Italian Istituto Nazionale della Fisica Nucleare (INFN) and the Dutch Nikhef, with contributions by Polish and Hungarian institutes. R.K.L.L. and T.G.F.L. would also like to gratefully acknowledge the support from the Croucher Foundation in Hong Kong. The work described in this paper was partially supported by a grant from the Research Grants Council of the Hong Kong (Project No. CUHK 24304317) and the Direct Grant for Re-

search from the Research Committee of the Chinese University of Hong Kong. The authors acknowledge the use of the IUCAA LDG cluster Sarathi for the computational/numerical work. The authors are also grateful for computational resources provided by the LIGO Laboratory and supported by National Science Foundation Grants PHY-0757058 and PHY-0823459. R.K.L.L. would also like to thank Baoyi Chen, Ling Sun, Yiqiu Ma and Yanbei Chen for the fruitful conversations with the first author. This paper carries LIGO Document Number LIGO-P1900057.

## 7.7 Appendix: Starting frequency, segment length and number of echoes in a template adopted in the search

| Event | Starting Frequency (Hz) | Segment Length (s) | Number of echoes in a template |
|---|---|---|---|
| GW150914 | 20 | 8 | 3 |
| GW151012 | 20 | 8 | 3 |
| GW151226 | 20 | 16 | 10 |
| GW170104 | 20 | 8 | 3 |
| GW170608 | 30 | 8 | 3 |
| GW170729 | 20 | 8 | 3 |
| GW170809 | 20 | 8 | 3 |
| GW170814 | 20 | 8 | 3 |
| GW170818 | 16 | 8 | 3 |
| GW170823 | 20 | 8 | 3 |

Table 7.4: Starting frequency, segment length and number of echoes in a template adopted in the search for each event. Notice that nominally the segment length we adopted is 8 s and the number of echoes in a template is fixed to be 3, except for GW151226 where it is a relatively low mass event, implying that the GW signal spends more time in the detector's sensitive frequency band. As a result, we increase the segment length to 16 s and we put 10 echoes in templates used in GW151226.

## 7.8 Appendix: Derivation for upper limit of 90% Bayesian credible interval on event rate density

Assume that the number of gravitational-wave echoes events follows a Poisson distribution, namely the likelihood function $\mathcal{L}$ of observing $k$ events in a time interval $T_{\rm obs}$ is given by

$$\mathcal{L}(k|\bar{N}) = \frac{\bar{N}^k e^{-\bar{N}}}{k!}, \tag{7.18}$$

where $\bar{N}$ is the mean number of events observed in the time interval. With a null detection (i.e., observing 0 event), and assuming a uniform prior on the mean number of events, the posterior probability on the mean number of events

observed is simply

$$p(\bar{N}|k=0) = \mathcal{L}(k=0|\bar{N}) = e^{-\bar{N}}. \tag{7.19}$$

Hence, the 90% Bayesian credible interval on $\bar{N}$ is given by $\left(0, \bar{N}_{90\%}\right)$, where $\bar{N}_{90\%}$ is the upper limit given by solving the equation

$$\int_0^{\bar{N}_{90\%}} e^{-\bar{N}} d\bar{N} = 0.9, \tag{7.20}$$

and we get

$$\bar{N}_{90\%} = -\ln(1-0.9) = -\ln(0.1). \tag{7.21}$$

The upper limit of event rate density is then simply given by

$$R_{90\%} = \frac{\bar{N}_{90\%}}{\langle VT\rangle^{\text{Echoes}}_{\text{Sensitive}}} = \frac{-\ln(0.1)}{\langle VT\rangle^{\text{Echoes}}_{\text{Sensitive}}}. \tag{7.22}$$

## 7.9 Appendix: Derivation for average sensitive spacetime volume for gravitational-wave echoes

In order to estimate the rate density of gravitational-wave echoes, we first need to have an idea on how much spacetime volume our search is able to probe, in terms of the *sensitive spacetime volume* $\langle VT\rangle$, which is defined as

$$\langle VT\rangle = T_{\text{obs}} \int dz d\vec{\theta}\; p(\vec{\theta}|M) p_{\text{det}}(z|\vec{\theta}) \frac{dV_c}{dz}, \tag{7.23}$$

where $T_{\text{obs}}$ is the total observing time, $\vec{\theta}$ is a set of parameters describing the gravitational-wave echoes, $dV_c$ is the differential co-moving volume element between a redshift of $z$ and $z+dz$, $p(\vec{\theta}|M)$ is the probability distribution of $\vec{\theta}$ given an astrophysical model $M$, and $p_{\text{det}}(z|\vec{\theta})$ is the *detection probability* that a search is able to see a signal with parameters $\vec{\theta}$ at a redshift of $z$, respectively. The set of parameters $\vec{\theta}$ can be decomposed into two parts: parameters related to BBH system $\vec{\theta}^{\,\text{BBH}}$ and parameters related to echoes $\vec{\theta}^{\,\text{Echoes}}$. Since we do not know about the astrophysical distribution of echo-related parameters, it is a *simplifying assumption* to assume a uniform probability distribution for these

parameters independent of the BBH parameters. Therefore, we can write the probability distribution $p(\vec{\theta}|M)$ as

$$p(\vec{\theta}|M) = p(\vec{\theta}^{\,\mathrm{BBH}}|M)p(\vec{\theta}^{\,\mathrm{Echoes}}|M). \tag{7.24}$$

If we make a further assumption that the detection probability $p_{\mathrm{det}}(z|\vec{\theta})$ can be factorized into two parts, namely

$$p_{\mathrm{det}}(z|\vec{\theta}) = p_{\mathrm{det}}(z|\vec{\theta}^{\,\mathrm{BBH}})p_{\mathrm{det}}(z|\vec{\theta}^{\,\mathrm{Echoes}}), \tag{7.25}$$

which makes sense because we only perform the echoes search on detected gravitational-wave events. With all the simplifying assumptions, we can write the sensitive spacetime volume as

$$\begin{aligned}&\langle VT\rangle^{\mathrm{Echoes}}_{\mathrm{Sensitive}} = \langle VT\rangle = T_{\mathrm{obs}}\\ &\int dz d\vec{\theta}^{\,\mathrm{BBH}} d\vec{\theta}^{\,\mathrm{Echoes}}\; p(\vec{\theta}^{\,\mathrm{BBH}}|M)p(\vec{\theta}^{\,\mathrm{Echoes}}|M)p_{\mathrm{det}}(z|\vec{\theta}^{\,\mathrm{BBH}})p_{\mathrm{det}}(z|\vec{\theta}^{\,\mathrm{Echoes}})\frac{dV_c}{dz},\end{aligned} \tag{7.26}$$

where we denote the sensitive spacetime volume for BBH as

$$\langle VT\rangle^{\mathrm{BBH}}_{\mathrm{Sensitive}} = T_{\mathrm{obs}}\int dz d\vec{\theta}^{\,\mathrm{BBH}}\; p(\vec{\theta}^{\,\mathrm{BBH}}|M)p_{\mathrm{det}}(z|\vec{\theta}^{\,\mathrm{BBH}})\frac{dV_c}{dz}, \tag{7.27}$$

and the estimated value for $\langle VT\rangle^{\mathrm{BBH}}_{\mathrm{Sensitive}}$ is reported in Refs. [9, 13]. Therefore, Eq. 7.26 can be written as

$$\langle VT\rangle^{\mathrm{Echoes}}_{\mathrm{Sensitive}} = \langle VT\rangle^{\mathrm{BBH}}_{\mathrm{Sensitive}} \times \int d\vec{\theta}^{\,\mathrm{Echoes}} p(\vec{\theta}^{\,\mathrm{Echoes}}|M)p_{\mathrm{det}}(z|\vec{\theta}^{\,\mathrm{Echoes}}). \tag{7.28}$$

The detection probability for echoes $p_{\mathrm{det}}(z|\vec{\theta}^{\,\mathrm{Echoes}})$ can be modeled as an indicator function of the detection statistic $\ln\mathcal{B}$ that

$$p_{\mathrm{det}}(z|\vec{\theta}^{\,\mathrm{Echoes}}) = \begin{cases} 1 & \text{if } \ln\mathcal{B}(\vec{\theta}) \geq \ln\mathcal{B}_{\mathrm{threshold}},\\ 0 & \text{otherwise}\end{cases}. \tag{7.29}$$

With this, we recognize that the second factor in Eq. 7.28 is

$$\int d\vec{\theta}^{\,\text{Echoes}} p(\vec{\theta}^{\,\text{Echoes}}|M) p_{\text{det}}(z|\vec{\theta}^{\,\text{Echoes}}) = \frac{V_{\text{detectable echoes}}}{V_{\text{all echoes}}} \approx \frac{N_{\text{recovered}}}{N_{\text{injected}}}, \tag{7.30}$$

where $V_{\text{all echoes}}$ and $V_{\text{detectable echoes}}$ are the volume of the (five dimensional) parameter space for all echoes and detectable echoes, respectively, and $N_{\text{recovered}}/N_{\text{injected}}$ is the fraction of injections recovered by the search pipeline in an injection campiagn. Hence we arrived at Eq. 7.11 that

$$\langle VT \rangle^{\text{Echoes}}_{\text{Sensitive}} \approx \frac{N_{\text{recovered}}}{N_{\text{injected}}} \langle VT \rangle^{\text{BBH}}_{\text{Sensitive}}.$$

*Chapter 8*

# SEARCHING FOR GRAVITATIONAL-WAVE ECHOES IN BINARY BLACK HOLE EVENTS FROM THE GWTC-2 CATALOG USING TEMPLATE-BASED BAYESIAN MODEL SELECTION APPROACH

This chapter contains work from

> LIGO Scientific, Virgo Collaboration. "Tests of general relativity with binary black holes from the second LIGO-Virgo gravitational-wave transient catalog". In: *Phys. Rev. D* 103.12 (2021), p. 122002. DOI: 10.1103/PhysRevD.103.122002. arXiv: 2010.14529 [gr-qc].
> R. K. L. L performed the analyses featured in this paper that search for echoes from binary black hole events in the second LIGO-Virgo gravitational-wave transient catalog. R. K. L. L was the internal editor/writer for the remnant properties section of the paper.

## 8.1 Introduction

It is hypothesized that there may be compact objects having a light ring and a reflective surface located between the light ring and the would-be event horizon. These compact objects are referred to as exotic compact objects (ECOs), for example gravastars [150] and fuzzballs [151, 152]. When an ECO is formed as the remnant of a compact binary coalescence, a train of repeating pulses known as gravitational-wave (GW) echoes are emitted from the ECO in the late postmerger stage in addition to the usual ringdown we expect from black holes (BHs). The effective potential barrier and the reflective surface act like a cavity trapping the GWs. Unlike BHs, which have a purely in-going boundary condition at the event horizon, the GWs trapped in the cavity will be reflected back and forth between the potential barrier and the surface, emitting pulses of waves towards infinity when some of the waves are transmitted through the potential barrier and escape

[153, 154, 155, 156, 157, 140]. Detecting these GW echoes would be clear evidence of the existence of these proposed ECOs [105, 106, 110], though there are still no full and viable models of ECOs that produce echoes [158, 159, 146, 140, 160].

## 8.2 Search methods

We employ a template-based approach (in Chapter 6; or see Ref. [139]) that uses the model proposed in Ref. [107] to search for GW echoes. The waveform model takes the ringdown part of an IMR waveform and repeats the modulated ringdown waveform according to five additional echo parameters which control the relative amplitude of the echoes, the damping factor between each echo, the start time of ringdown, the time of the first echo with respect to the merger, and the time delay between each echo. We adopt a uniform prior for each of the echo parameters. We used IMRPhenomPv2 [161] as the inspiral-merger-ringdown (IMR) waveform approximant for all the events we analyzed except for GW190521 where NRSur7dq4 [93] was used instead. The pipeline computes the log Bayes factor $\log_{10} \mathcal{B}^{\mathrm{IMRE}}_{\mathrm{IMR}}$ of the data being describable by an inspiral-merger-ringdown-echo (IMRE) waveform versus an IMR waveform, and uses it as the detection statistic to identify the existence of echoes in the data.

## 8.3 Search results

We analyze 31 binary black hole (BBH) signals from GWTC-2 passing our false-alarm rate (FAR) threshold (of $< 10^{-3}$ per year; see Ref. [21]) and report the search results of GW echoes in Table 8.1.[1] No statistically significant evidence of echoes was found in the data; it was reported in [139] that for detector noise fluctuations typical for the first observing run (O1), a detection threshold for $\log_{10} \mathcal{B}^{\mathrm{IMRE}}_{\mathrm{IMR}}$ was found to be roughly 2.48 by empirically constructing the background distribution of the Bayes factor if we require the false-alarm probability to be $\lesssim 3 \times 10^{-7}$. The event GW190915_235702 has the highest $\log_{10} \mathcal{B}^{\mathrm{IMRE}}_{\mathrm{IMR}}$ of

[1] We do not analyze GW190814 because the long data segment and high sampling rate it requires makes the analysis prohibitively expensive.

Table 8.1: Results of search for GW echoes. A positive value of the log Bayes factor $\log_{10} \mathcal{B}^{\rm IMRE}_{\rm IMR}$ indicates a preference for the IMRE model over the IMR model, while a negative value of the log Bayes factor suggests instead a preference for the IMR model over the IMRE model.

| Event | $\log_{10} \mathcal{B}^{\rm IMRE}_{\rm IMR}$ | Event | $\log_{10} \mathcal{B}^{\rm IMRE}_{\rm IMR}$ |
|---|---|---|---|
| GW150914 | −0.57 | GW170809 | −0.22 |
| GW151226 | −0.08 | GW170814 | −0.49 |
| GW170104 | −0.53 | GW170818 | −0.62 |
| GW170608 | −0.44 | GW170823 | −0.34 |
| GW190408_181802 | −0.93 | GW190706_222641 | −0.10 |
| GW190412 | −1.30 | GW190707_093326 | 0.08 |
| GW190421_213856 | −0.11 | GW190708_232457 | −0.87 |
| GW190503_185404 | −0.36 | GW190720_000836 | −0.45 |
| GW190512_180714 | −0.56 | GW190727_060333 | 0.01 |
| GW190513_205428 | −0.03 | GW190728_064510 | 0.01 |
| GW190517_055101 | 0.16 | GW190828_063405 | 0.10 |
| GW190519_153544 | −0.10 | GW190828_065509 | −0.01 |
| GW190521 | −1.82 | GW190910_112807 | −0.22 |
| GW190521_074359 | −0.72 | GW190915_235702 | 0.17 |
| GW190602_175927 | 0.13 | GW190924_021846 | −0.03 |
| GW190630_185205 | 0.08 | | |

merely 0.17, which indicates negligible support for the presence of GW echoes in the data. While we did not present the Bayes factor for GW151012 and GW170729 here as their corresponding FARs are above the threshold, the results are consistent with no significant evidence of echoes being found in the data. The null results for O1 and the second observing run (O2) events are consistent with what was reported in [108, 111, 139, 114, 141, 162]. The posterior distributions of the extra echo parameters mostly recover their corresponding prior distributions, consistent with the fact that we did not detect any echoes in the data.

## 8.4 Conclusion

While we did not explicitly construct a background distribution for the log Bayes factors $\log_{10} \mathcal{B}^{\mathrm{IMRE}}_{\mathrm{IMR}}$ using data from GWTC-2 to compute the exact $p$-values for their statistical significance, it suffices to conclude from the fact that the highest Bayes factor reported here is merely about 1.5 that there was no statistical significant evidence of GW echoes in the postmerger part of the data of the BBH signals reported in GWTC-2.

Even with a null search result for GW echoes as reported here, we can still place limits on properties of the would-be ECOs. For instance, placing a limit on the location of the reflective surface of the ECO as the remnant of a specific GW event, or collectively placing an upper limit on the event rate of the production of an ECO remnant from compact binary coalescence, from the fact that we did not observe echoes in data that are present but are simply too weak to be found. We leave these for future follow-ups.

**Acknowledgements**

The authors gratefully acknowledge the support of the United States National Science Foundation (NSF) for the construction and operation of the LIGO Laboratory and Advanced LIGO as well as the Science and Technology Facilities Council (STFC) of the United Kingdom, the Max-Planck-Society (MPS), and the State of Niedersachsen/Germany for support of the construction of Advanced LIGO and construction and operation of the GEO600 detector. Additional support for Advanced LIGO was provided by the Australian Research Council. The authors gratefully acknowledge the Italian Istituto Nazionale di Fisica Nucleare (INFN), the French Centre National de la Recherche Scientifique (CNRS) and the Netherlands Organization for Scientific Research, for the construction and operation of the Virgo detector and the creation and support of the EGO consortium. The authors also gratefully acknowledge research support from these agencies as well as by the Council of Scientific and Industrial Research of India, the Department of Science and Technology, India, the Science & Engineering Research

Board (SERB), India, the Ministry of Human Resource Development, India, the Spanish Agencia Estatal de Investigación, the Vicepresidència i Conselleria d'Innovació, Recerca i Turisme and the Conselleria d'Educació i Universitat del Govern de les Illes Balears, the Conselleria d'Innovació, Universitats, Ciència i Societat Digital de la Generalitat Valenciana and the CERCA Programme Generalitat de Catalunya, Spain, the National Science Centre of Poland and the Foundation for Polish Science (FNP), the Swiss National Science Foundation (SNSF), the Russian Foundation for Basic Research, the Russian Science Foundation, the European Commission, the European Regional Development Funds (ERDF), the Royal Society, the Scottish Funding Council, the Scottish Universities Physics Alliance, the Hungarian Scientific Research Fund (OTKA), the French Lyon Institute of Origins (LIO), the Belgian Fonds de la Recherche Scientifique (FRS-FNRS), Actions de Recherche Concertées (ARC) and Fonds Wetenschappelijk Onderzoek – Vlaanderen (FWO), Belgium, the Paris Île-de-France Region, the National Research, Development and Innovation Office Hungary (NKFIH), the National Research Foundation of Korea, the Natural Science and Engineering Research Council Canada, Canadian Foundation for Innovation (CFI), the Brazilian Ministry of Science, Technology, Innovations, and Communications, the International Center for Theoretical Physics South American Institute for Fundamental Research (ICTP-SAIFR), the Research Grants Council of Hong Kong, the National Natural Science Foundation of China (NSFC), the Leverhulme Trust, the Research Corporation, the Ministry of Science and Technology (MOST), Taiwan and the Kavli Foundation. The authors gratefully acknowledge the support of the NSF, STFC, INFN and CNRS for provision of computational resources.

*Chapter 9*

# CONCLUDING REMARKS OF PART I

In Part I of the thesis, we first showed the recipes of using the GSN formalism to compute radiation of scalar, electromagnetic and gravitational type from a Kerr BH for the vacuum case in Chapter 4. In particular, this is the first time where the necessary GSN transformations were explicitly shown for the physically relevant cases with spin weight $s = 0, \pm 1, \pm 2$ in literature. Together with the higher-order corrections to the asymptotic solutions to the GSN equation being constructed for all those cases, the GSN formalism was revamped as an efficient approach to perform numerical work in BHPT. An implementation of the GSN formalism written in `julia`, `GeneralizedSasakiNakamura.jl`, is also presented. An important and obvious future work would be to extend the GSN formalism to work also for the non-vacuum/sourced case. Indeed, the work to extend the gravitational case (i.e., $s = \pm 2$) is in progress.

Then in Chapter 5, we presented our prescription to compute waveforms of the speculated GW echoes using BHPT since we model an ECO as a modified Kerr BH. Specifically, we computed some example echo waveforms with two models, the Lorentzian reflectivity model and the Boltzmann reflectivity model, where these models give us the response of the surface of an ECO to an incident GW. A caveat to this work is the misuse of the Teukolsky-Starobinsky identities where the ingoing $\psi_0$ solution was obtained by converting the ingoing $\psi_4$ solution near the ECO surface. However these identities were not true in the non-vacuum case, which is exactly the scenario where we applied those identities. An improvement to this work would be to directly compute the ingoing $\psi_0$ solution sourced by a plunging test particle, which is actually one of the motivations leading to the work in presented Chapter 4.

In addition, in Chapter 5, we performed a study on the detectability of GW

echoes with current and future generation GW detectors and found that it is not likely for us to detect GW echoes with current-generation detectors because the predicted echoes are simply too weak and our current GW detectors are not sensitive enough. That being said, this will not deter us from trying to look for these echoes in our data. In fact, in Chapter 6, we described a Bayesian model selection approach to do just that. Furthermore in Chapter 7, it was used to search for GW echoes in the O1 and O2 data. While we did not find any statistically significant evidence supporting the presence of GW echoes in the data, we showcased what limits we can place with null search results, namely an upper limit on the ECO formation rate density as a remnant of BBH mergers and a bound on the compactness of a BBH merger remnant. Next, in Chapter 8 we extended the analysis to the O3a data. In the future, we plan to extend the echo analysis to the O3b data as well, and possibly using an improved echo waveform model from Chapter 4 and Chapter 5.

# Part II

# Strong Gravitational Lensing of Gravitational Waves

*Chapter 10*

# OVERVIEW OF PART II

In the second part of the thesis, let us focus on another exotic phenomenon of gravitational waves (GWs), though arguably less speculative than what was covered in Part I, namely the strong gravitational lensing (SL) of GWs.

With GWs, it is often said that they travel through the Universe unimpeded, whereas electromagnetic (EM) waves are often obscured by their interactions with intervening matter and thus are not as good as GWs in giving us cleaner signals from their emitters. Actually, GWs are still subject to gravitational interactions as they propagate. For instance, when the deflection due to the gravitational potential from an intervening astronomical object such as a galaxy is significant enough, multiple rays of the same GW can now arrive at our detectors, to be seen as separate arrivals of GWs at different times. This is the same phenomenon, referred to as SL, in the EM spectrum that gives rise to the spectacular arcs seen on deep-field images from the Hubble Space Telescope (HST) [163] and more recently the James Webb Space Telescope (JWST) [164].

While it is commonplace to observe SL of distant objects in the EM world, the same cannot be said of GW. The fundamental reason is in the difference of the nature of sources and datasets: typically for EM, strongly-lensed *persistent* objects can be identified using images (from flux data) with long exposure times manifested as multiple *spatially-resolved* copies of the same source. As for GW, it is more likely to observe *transient* events such as mergers of compact objects as *temporal* data of GW strain with much poorer source localization capability [27]. It is only a matter of time, however, for a binary merger to be sufficiently aligned with a massive foreground object such as a galaxy, to produce multiple GW signals from the same merger. It is up to us the observers to confidently identify these strongly-lensed GWs from a vast dataset.

If confirmed, the potential scientific impacts are plentiful. For example, these lensed GW signals can be used for *testing extra GW polarization modes* since we would have multiple observations of the same source at different times, effectively increasing the number of virtual detectors without having to physically build more detectors. Given the cost of constructing and running a GW interferometer, it is far more cost-effective to invest in using strongly-lensed GW to disentangle the six GW polarization modes that are generally allowed in a metric theory of gravity. To fully disentangle the contents of those six polarization modes from a GW signal without using SL, six GW interferometers will have to be built, which is unlikely given the amount of funding it needs.[1] While the detection of non-tensorial polarizations is enough to show the inadequacy of general relativity (GR) since it only allows for the tensorial modes, measuring also the contents of those non-tensorial modes *allows us to put constraints on and learn much more about alternative theories of gravity in the strong-field regime*.

Strongly-lensed GWs can also be used in cosmography such as determining the Hubble constant $H_0$ with time-delay cosmography [165] or as non-conventional "bright sirens". This is particularly appealing because with EM lensing only, in order to perform time-delay cosmography a time-varying source (that is also EM-bright such as a supernova) and its constant monitoring are needed to measure the time delays between lensed images where the precision of such measurement depends on the cadence of the observations. With GW+EM lensing, the lensed source itself does not have to be EM-bright (such as a binary black hole (BBH) system) as long as we can identify/associate and observe its host galaxy electromagnetically. We can use the superb temporal resolution of GW interferometers to accurately measure the time delays, and use the EM observations to obtain the lens and source redshift measurements. In addition, since GW interferom-

[1] Technically speaking, for GW interferometers, the detector responses for the two "scalar" polarization modes, namely the breathing and the longitudinal modes, are identical. Therefore we only "need" five detectors since we can at best disentangle five out of the six allowed but the argument on the plausibility of securing enough funding to build and run five detectors still holds.

eters measure amplitudes and not intensities, phasing effects from lensing can be used to break some degeneracies. For example, it is possible to break the notorious mass-sheet degeneracy with GW observations [166]. Therefore, *combining both EM and GW lensing observations will lead to a much more accurate determination of* $H_0$.

All these science cases are contingent on the successful identification of strongly-lensed GWs. In Chapter 11, I will describe a Bayesian statistical framework that allows us to differentiate strongly-lensed GWs of the same source from a set of GW events that are coming from different sources by comparing coherence among the signals. The framework is capable of incorporating astrophysical population information on GW sources and gravitational lenses while taking selection effects into account in a statistically consistent manner. The framework also allows us to infer the properties of a lensed source that are free from shifts/biases introduced when one did not take lensing into consideration. The framework is the basis of a `python`-based code `hanabi` that was employed in searching for strongly-lensed GW signals among the detected BBHs in the first half of the third observing run (O3a) as described in Chapter 12 and in the second half of the third observing run (O3b) as described in Chapter 13, respectively. In particular in Chapter 14, I will demonstrate the capability of the framework further and briefly describe SL analyses on two pairs of BBHs found in O3b in which the analyses incorporated the astrophysical information on galaxy-scale lenses from a simulated catalog of strongly-lensed images. The full manuscript describing the details of both the statistical analysis and the simulation is under preparation as of this writing [167].

To establish more confidence in the discovery of a strongly-lensed GW-emitting source, one possible avenue is to find all (and not just *two*) lensed signals/images[2] of the same source and by the same foreground lens. This is because more realistic models of gravitational lenses usually predict more than two images

[2]The term lensed signals and lensed images will be used interchangeably throughout the thesis.

being formed. Among those images, some would be magnified while some could be *de*-magnified compared to the un-lensed signal. This implies that some of the de-magnified signals could become quieter than the background due to instrumentation noise (referred to as being *sub*-threshold signals) and thus potentially be missed by conventional searches for GW signals. In Ref. [168], we presented an approach to perform *targeted* searches of sub-threshold images of strongly-lensed GW signals. In fact, one of the BBH pairs being analyzed in Chapter 14 was found by a targeted sub-threshold search. Finding all lensed images of the same system that could otherwise be buried in the noise floor not only gives us more confidence the identification of strong lensing, but it also permits us to extract more information, such as more time-delay measurements, regarding both the lensed source and the lens responsible, thus leading to better constraints on their properties and applications to cosmography and tests of GR.

However, as the number of detected GW signals $N_{\rm GW}$ increases with longer total observation time, the number of possible strongly-lensed event pairs that we need to consider grows like $N_{\rm GW}(N_{\rm GW}-1)/2$. Of these many candidate pairs, it is likely that only one (to a few) of them are truly lensed. In the idealistic world of unlimited computational resources, in order not to miss the golden pairs, we could have run our best and most complete lensing analyses to each and every possible pair. This approach is clearly impractical. Therefore we need better strategies to both reduce the number of pairs we need to follow up with the full analyses.

In Ref. [169], a work that I conceived and co-mentored two undergraduate students to perform, we demonstrated the use of overlapping sky localization probability maps (skymaps) to filter out pairs that are not lensed as their skymaps should not overlap, and how it could help reduce the number of candidate pairs for subsequent analyses efficiently and rapidly. Alternatively, one can consider the overlap of waveform phases (after accounting for a time shift and a frequency-independent phase shift from lensing) at each detector since GW interferometers best measure phases, and therefore this method has the potential of outperforming

the skymap overlap approach. As of this writing, the manuscript on this new method is under preparation [170].

For future-generation GW detectors (such as LIGO Voyager, Cosmic Explorer (CE) and Einstein Telescope (ET)) that can observe sources much further away compared to the current-generation detectors, the probability of GW signals coming from those sources being strongly-lensed will be substantial (see Fig. 11.3 in Chapter 11). Thanks to their much improved sensitivity, those future-generation GW detectors might allow us to detect unique waveform signature coming from strong lensing and thus give us smoking-gun evidence of lensing [171]. In Chapter 15, I will conclude Part II of my thesis with prospects of SL of GWs in the near term with current-generation detectors and with planned detectors in a more distant future.

*Chapter 11*

# BAYESIAN STATISTICAL FRAMEWORK FOR IDENTIFYING STRONGLY LENSED GRAVITATIONAL-WAVE SIGNALS

This chapter contains work from

> R. K. L. Lo and I. Magana Hernandez. "Bayesian statistical framework for identifying strongly lensed gravitational-wave signals". In: *Phys. Rev. D* 107.12 (2023), p. 123015. DOI: 10.1103/PhysRevD.107.123015. arXiv: 2104.09339 [gr-qc].
> R. K. L. L conceived the project, wrote a `python` implementation of the framework (i.e., `hanabi`), performed the analyses and wrote the manuscript.

## 11.1 Introduction

As gravitational waves propagate through the Universe to the Earth, they can be deflected, or lensed, by intervening matters such as galaxies or galaxy clusters acting as gravitational lenses, just like electromagnetic waves. For visible light coming from a distant background source, in the case of strong lensing where the deflection is sufficiently large, multiple images of the source will be formed that are close to each other, typically separated by only several arcseconds and distorted compared to the unlensed image [172]. For transients, the time variation of the images are correlated and delayed, where the time delays range from days to months [172]. For transient gravitational-wave (GW) signals, such as those emitted from coalescences of compact binary systems, multiple images refer to multiple GW triggers registered at different times by GW detectors.[1] For an in-depth review on strong lensing of explosive transients across the electromagnetic (EM) and the GW spectra, see for example Ref. [173].

[1] We use the term image and signal interchangeably.

To investigate the effects of strong lensing on a GW signal, we first briefly describe how the observed GW strain $h(t)$ depends on some parameters $\boldsymbol{\theta}$ when the signal is not affected by strong lensing.[2] The GW strain observed by a laser-interferometric GW detector is given by

$$h(t - t_c; \boldsymbol{\theta}) = \frac{1}{d_L(z)} \sum_{\text{pol}=+,\times} F_{\text{pol}}(\alpha, \delta, \psi; t_c) h_{\text{pol}}(t - t_c; \boldsymbol{\theta}), \tag{11.1}$$

where the detected GW strain is a projection along the arms of the detector where the response of the detector to the two polarization states of the GW is defined by the detector's beam pattern functions $F_{+,\times}(\alpha, \delta, \psi)$, where $\alpha$ is the right ascension, $\delta$ is the declination, and $\psi$ is the polarization angle of the source, respectively.[3] The luminosity distance to the source $d_L(z)$ is a function of the redshift $z$ and depends explicitly on the cosmology. The time and phase at coalescence of the signal are denoted by $t_c$ and $\phi_c$, respectively. The waveform of the two polarization states $h_+$ and $h_\times$ can be compactly written as

$$h_+(t; \boldsymbol{\theta}) - i h_\times(t; \boldsymbol{\theta}) = \sum_{\ell=2}^{\infty} \sum_{m=-\ell}^{\ell} h_{\ell m}(t; \vartheta) \, {}_{-2}Y_{\ell m}(\iota, \phi_o), \tag{11.2}$$

where $h_{\ell m}$ depends on some intrinsic parameters $\vartheta$ and the source redshift $z$ only, and ${}_{-2}Y_{\ell m}(\iota, \phi_o)$ is the spin-weighted spherical harmonic that depends on the polar angle $\iota$ and the azimuthal angle $\phi_o$ in the source frame.[4,5]

For the case of GWs from quasicircular binary black hole (BBH) mergers, the set of intrinsic parameters $\vartheta = \{\mathcal{M}_c, q, \boldsymbol{\chi}_1, \boldsymbol{\chi}_2\}$ where $\mathcal{M}_c \equiv (m_1 m_2)^{3/5}/(m_1 +$

[2] Here we use $\boldsymbol{\theta}$ as a placeholder to denote any generic set of parameters, which can consist of different parameters in different contexts.

[3] Note that the beam pattern functions $F_{+,\times}$ are usually calculated in a frame where the detector is situated at the origin, where the angles $\alpha$ and $\delta$ are celestial coordinates. Therefore, the beam pattern functions depend implicitly on the time of the event as well.

[4] For nonprecessing binary systems, the angle $\iota$ is also known as the inclination angle, the angle between the line of sight and the orbital angular momentum vector, which is by convention chosen to be along the $z$-axis of the source frame. For generic precessing binary systems, the inclination angle changes over time as the orbital angular momentum vector precesses around the total angular momentum vector.

[5] Note that the phase at coalescence $\phi_c$ does not enter Eq. (11.2) explicitly but through the time-varying azimuthal angle $\phi_o$, with $\phi_c$ as the reference phase.

$m_2)^{1/5}$ is the chirp mass of the binary, $q \equiv m_2/m_1 \leq 1$ is its mass ratio, both in terms of the binary component masses $m_1 \geq m_2$. The vectors $\boldsymbol{\chi}_1$, $\boldsymbol{\chi}_2$ are the dimensionless spin vectors for the binary components. Note that this is just one particular parametrization, and other ways of specifying the intrinsic parameters are also possible; for example, using the total mass of the binary $M_{\rm tot} \equiv m_1 + m_2$ instead of the chirp mass $\mathcal{M}_{\rm c}$. To account for the effect of an expanding universe, one can do so by simply replacing the (source-frame) masses $m_i^{\rm src}$ with the (detector-frame) redshifted masses $m_i^{\rm det} = (1+z)m_i^{\rm src}$. Similarly, we define the redshifted chirp mass as $\mathcal{M}_{\rm c}^{\rm det} = (1+z)\mathcal{M}_{\rm c}^{\rm src}$, while the mass ratio remains unchanged. It should be noted that Eqs. (11.1) and (11.2) hold true regardless of the type of the GW transient source under consideration, and in general the set of intrinsic parameters $\vartheta$ will differ for each kind of source.

Working in the geometric optics limit where the wavelength is much shorter than the lens length scale, for a majority of the time, strongly lensed GW signals from a binary system will have the same morphology with different amplitudes (corresponding to different magnifications) and arrive at different times. A given image has an absolute magnification $\mu$ which can be defined in terms of the true luminosity distance to the source $d_{\rm L}^{\rm src}$ and the apparent luminosity distance $d_{\rm L}$ as

$$d_{\rm L}^{(i)} = \frac{d_{\rm L}^{\rm src}}{\sqrt{\mu^{(i)}}}, \tag{11.3}$$

where the bracketed superscript indexes the images. The lensed images arrive at the (center of the) Earth at different times because of the geometrical time delay, as they follow different null trajectories, and the time delay due the gravitational potential. We define the relative time delay $\Delta t$ between two images as $\Delta t \equiv t_{\rm c}^{(2)} - t_{\rm c}^{(1)}$, where $t_{\rm c}$ is the GW arrival (trigger) time for each image. Here we assume that the time delay $\Delta t$ is large enough so that the lensed images will not overlap with each other and that we can identify them as separate triggers. We refer to the image that arrives first as the first image, and vice versa, such that $\Delta t > 0$. We can also define the relative magnification $\mu_{\rm rel}$, which is simply the

ratio of the two absolute magnifications as

$$\mu_{\rm rel} \equiv \frac{\mu^{(2)}}{\mu^{(1)}}. \tag{11.4}$$

The strong lensing of GW can also induce nontrivial effects on the GW waveform other than a change in the amplitude of the signal and a simple shift in time. In general, the lensed waveform $\tilde{h}_{\rm pol}^{\rm Lensed}(f)$ is related to the unlensed waveform $\tilde{h}_{\rm pol}^{\rm Unlensed}(f)$ by a frequency-dependent amplification factor $F(f)$ as [172, 174]

$$\tilde{h}_{\rm pol}^{\rm Lensed}(f) = F(f)\ \tilde{h}_{\rm pol}^{\rm Unlensed}(f), \tag{11.5}$$

for $f > 0$. The negative frequency components can be obtained via the reality condition $\tilde{h}_{\rm pol}(-f) = \tilde{h}_{\rm pol}^{*}(f)$. In the geometric optics limit, the amplification factor is given by [172, 174]

$$F(f) = \sum_j \sqrt{\mu^{(j)}} \exp(2\pi i f \Delta t^{(j)} - i n^{(j)} \pi/2), \tag{11.6}$$

for $f > 0$ and $n^{(j)} \in \{0, 1, 2\}$ is known as the Morse index of the $j$th image [172].[6] The factor $\sqrt{\mu}$ causes the apparent luminosity distance to differ from the luminosity distance of the source, and the phase factor $\exp(2\pi i f \Delta t)$ causes the aforementioned time delay. The frequency-independent phase shift from $\exp(-in\pi/2)$ is degenerate with a shift in the phase at coalescence when we consider GW signals from nonprecessing binaries with contributions only from the quadrupole $\ell = |m| = 2$ modes [175, 176]. When the geometric optics approximation breaks down and the full wave optics treatment is needed, the expression for the amplification factor can be much more complicated than Eq. (11.6), and encodes more information about the gravitational lens [172, 174].

Previous works have shown that the detection rate for lensed GWs could be, optimistically, $5^{+5}_{-3}\,{\rm yr}^{-1}$ [177] for Advanced LIGO [1] and Advanced Virgo [2]

[6] Unlike Ref. [175], we did not include the $\mathrm{sgn}(f)$ factor explicitly in Eq. (11.6). This is because by imposing the reality condition on $\tilde{h}_{\rm pol}(f)$ to obtain the negative frequency components, adding an additional $\mathrm{sgn}(f)$ will have no effect to the final expression for the waveform.

operating at their design sensitivities, while others predicted more pessimistic rates, ranging from $0.58\,\mathrm{yr}^{-1}$ [178] to $1.20\,\mathrm{yr}^{-1}$ [179] depending on the source population model assumed. The detection rate for lensed GWs can also be constrained from the detection, and more surprisingly the nondetection, of stochastic gravitational-wave background from individually unresolvable binaries [180, 181]. Searches on the first observing run (O1) and the second observing run (O2) data for strongly lensed GW signals were performed [182, 183, 184], and it was concluded that there is no significant evidence that any of the eleven detected GW events during O1 and O2 are lensed, while Ref. [185] suggests that GW170809 and GW170814 could be lensed images of each other due to the similarity of the waveforms for these two events.

It is also possible that strongly lensed GW signals from distant sources are absolutely de-magnified ($\mu < 1$), or relatively demagnified ($\mu_{\mathrm{rel}} < 1$) such that when found by matched-filtering search pipelines (such as `GstLAL` [186, 187] and `PyCBC` [188]) they appeared to be subthreshold triggers, not statistically significant enough to claim detections. If a lensed image is loud enough to be detected individually, then targeted matched-filtering based searches can be performed for each detected GW event and search deeper for its potentially subthreshold lensed image counterparts [168, 189, 183].

An overarching approach in searches for lensed GW signals is the use of Bayesian statistics [190, 182, 189, 184, 183], where a statistic, either called a "Bayes factor" in the usual context of Bayesian hypothesis testing or a ranking score, is calculated. In this paper, we present a Bayesian statistical framework for identifying strongly lensed GW signals that utilizes hierarchical Bayesian modeling. By modeling the data generation processes when the observed GW signals are lensed and not lensed, respectively, we develop a framework that allows us to compute a Bayes factor, and hence a posterior odds, that incorporates astrophysical information directly and accounts for selection effects. We argue that in order to interpret the Bayes factor properly as a ratio of normalized probability densities of the observed data, selection effects cannot be ignored and must be

accounted for in order to normalize the probability densities. The ability to directly incorporate astrophysical information, both on the GW sources as well as the gravitational lenses, serves to better bridge the astrophysical modeling community and the GW data analysis community. In addition, we argue that whether a GW signal is interpreted as lensed or not depends also on the astrophysical models assumed, making the prior astrophysical information an indispensable ingredient of the analysis.

The paper is structured as follows: Section 11.2 presents the hierarchical Bayesian framework for identifying strongly lensed GW signals in a general setting, and the technique to marginalize over the source redshift separately and infer the true source parameters. In Sec. 11.3 and Sec. 11.4 we apply and showcase the statistical framework to analyze strongly lensed GW signals from BBH mergers when we analyze two GW signals jointly and analyze one signal at a time, respectively. Throughout the paper, we assume a flat ΛCDM cosmology with $H_0 = 67.7\ \mathrm{km\,s^{-1}\,Mpc^{-1}}$ and $\Omega_\mathrm{m} = 0.307$ from the Planck 2015 results [191].

## 11.2 Statistical framework

In order to differentiate strongly lensed GW signals from GW signals that are not lensed, we adopt a Bayesian statistical framework where we introduce two models/hypotheses[7] that we want to compare; namely, the lensed hypothesis $\mathcal{H}_\mathrm{L}$ and the not-lensed hypothesis $\mathcal{H}_\mathrm{NL}$.[8] The framework applies for $N \geq 1$, where $N$ is the number of GW events under consideration, unlike much of previous work [190, 182, 189, 184, 183]. In the following we will elaborate on what we mean by the two hypotheses, and model the data generation processes under the two different hypotheses using hierarchical Bayesian modeling.

[7] We will use the word model and hypothesis interchangeably throughout the paper.

[8] The not-lensed hypothesis $\mathcal{H}_\mathrm{NL}$ is often referred as the unlensed hypothesis, denoted by $\mathcal{H}_\mathrm{U}$, in literature.

### 11.2.1 The not-lensed hypothesis $\mathcal{H}_{\rm NL}$

Suppose we have $N$ GW events under consideration, i.e., we have a set of $N$ time series data $\boldsymbol{D} = \{D^{(i)}\}_{i=1}^{i=N}$, where the bracketed superscript indexes the events. The not-lensed hypothesis means that the observed $N$ events are $N$ independent realizations of a population distribution of GW source $p_{\rm src}$, parametrized by some parameters $\boldsymbol{\lambda}$ that control only the shape of the distribution and the total number of sources $N_{\rm src}$ in that population.[9] Note that we have assumed all $N$ of them are of astrophysical origins. Simply put, the $N$ events are just $N$ different systems, with the event-level parameters $\boldsymbol{\theta}^{(i)}$ (such as component masses and spins) describing the $i$th event being randomly drawn from a source population distribution $p_{\rm src}(\boldsymbol{\theta}|\boldsymbol{\lambda})$, where $\boldsymbol{\lambda}$ might be for example the maximum mass of a black hole in that population. These $N$ signals will have different source redshifts $z$ drawn from the distribution $p_z(z^{(i)}|\mathcal{R})$, where $\mathcal{R} = \mathcal{R}(z)$ is the merger rate density that can be a function of the source redshift $z$, and with different extrinsic parameters such as the sky location drawn from the distribution $p_{\rm ext}$. A concise way of expressing this is that $\boldsymbol{\theta}^{(i)} \sim p_{\rm pop}(\boldsymbol{\theta}^{(i)})$ where $p_{\rm pop} = p_{\rm src}(\boldsymbol{\theta}^{(i)}|\boldsymbol{\lambda})p_z(z^{(i)}|\mathcal{R}, \mathcal{H}_{\rm NL})p_{\rm ext}$ is the population-informed prior distribution under the not-lensed hypothesis. The event-level parameters $\boldsymbol{\theta}^{(i)}$ then in turn "generate" the data $D^{(i)}$ that we observed for the $i$th event. Figure 11.1 shows a graphical representation of this data generation process. Although we are not making any inference on the population-level parameters of GW sources and instead we fix them in our analysis (i.e., choosing $\boldsymbol{\lambda}$ and $\mathcal{R}$ a priori), we see that the problem of identifying strongly lensed signals can be naturally framed as a population analysis. Moreover, we can reuse many of the results from rates and population analyses (for example see Refs. [13, 192]).

[9] Note that the source population distribution $p_{\rm src}(\boldsymbol{\theta}|\boldsymbol{\lambda})$ is normalized such that $\mathrm{d}N_{\rm src}/\mathrm{d}\boldsymbol{\theta} = 1/N_{\rm src}\ p_{\rm src}(\boldsymbol{\theta}|\boldsymbol{\lambda})$. Also, $\boldsymbol{\lambda}$ are in general redshift-dependent but for simplicity we ignore the correlations of these parameters with redshift. The framework can be generalized to account for those correlations.

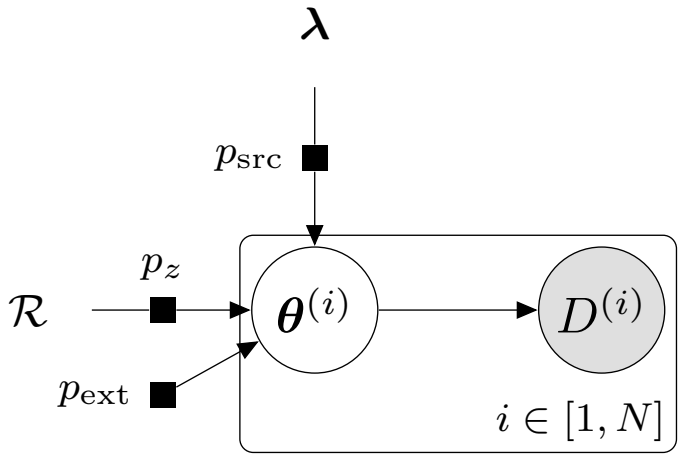


Figure 11.1: Data generation process for the $N$ observed data under the not-lensed hypothesis $\mathcal{H}_{\rm NL}$. Each data $D^{(i)}$ can be described by the event-level parameters $\boldsymbol{\theta}^{(i)}$ which were drawn from the population-informed prior distribution $p_{\rm pop} = p_{\rm src}(\boldsymbol{\theta}^{(i)}|\boldsymbol{\lambda})p_z(z^{(i)}|\mathcal{R}, \mathcal{H}_{\rm NL})p_{\rm ext}$ with $\boldsymbol{\lambda}$ controlling the shape of the source population distribution, $\mathcal{R}$ being the merger rate density, and $p_{\rm ext}$ describing the distribution of the extrinsic parameters except for the redshift.

### 11.2.2 The lensed hypothesis $\mathcal{H}_{\rm L}$

For the lensed hypothesis, suppose we also have the same $N$ events under consideration. However, the lensed hypothesis means that these $N$ events are actually $N$ strongly-lensed images of the same source. Instead of drawing $N$ independent realizations from the population distribution $p_{\rm src}$, now we only have one realization of this source population distribution as the images correspond to the same GW source. In addition to the source population distribution, we will need to introduce the lens population distribution $p_{\rm lens}$, parametrized by some parameters $\boldsymbol{\gamma}$, that describes for example the joint probability distribution of the absolute magnification of lensed images. Furthermore, we partition the event-level parameters $\boldsymbol{\theta}^{(i)}$ into two disjoint sets: common parameters $\boldsymbol{\theta}^{(i)}_{\rm com}$ and independent parameters $\boldsymbol{\theta}^{(i)}_{\rm ind}$. For the common parameters $\boldsymbol{\theta}^{(i)}_{\rm com}$ we expect them to be the

same across the $N$ signals, for example the masses and spins of the source binary system, as the $N$ events correspond to the same source. In addition to the source parameters, we also expect the redshift $z^{(i)}$ of each image to be the same as the source redshift as strong lensing is achromatic, leaving the redshift unchanged. For extrinsic parameters, we can also assume them to be the same except for the (apparent) luminosity distance and the time of arrival. While it is true that strong lensing will deflect a GW signal from its original null trajectory, the typical deflection angle for gravitational lensing due to a galaxy or a galaxy cluster is only of the order of arcseconds and arcminutes, respectively [172, 193], which is much smaller than the typical uncertainty in the source localization of a GW signal. Therefore, it is valid to assume that the $N$ images share the same sky location. We also expect the difference in the polarization angle $\psi$ to be negligible [194]. In summary, the common parameters $\boldsymbol{\theta}^{(i)}_{\rm com}$ are one random draw of the distribution $p_{\rm pop,com} = p_{\rm src}(\boldsymbol{\theta}^{(i)}_{\rm com}|\boldsymbol{\lambda})p_z(z^{(i)}|\mathcal{R},\mathcal{H}_{\rm L})p_{\rm ext}$, where $p_{\rm pop,com}$ is the population-informed prior for the common parameters $\boldsymbol{\theta}_{\rm com}$ under the lensed hypothesis.

As for the independent parameters $\boldsymbol{\theta}^{(i)}_{\rm ind}$, we expect them to be different for each event. For example, the absolute magnification $\mu$ and the arrival time $t_{\rm c}$ of each image would be different. Note that the dimension of the event-level parameters $\boldsymbol{\theta}$ under the lensed hypothesis can be different than that under the not-lensed hypothesis. For example, different lensed images can be classified into three types where each type of an image will have a different phasing effect to the lensed waveform [for example see Eq. (11.6)]. The number of lensed images produced by a gravitational lens can also inform us on the type of lens that produces the images. Here we do not use this information since it is possible (and often the case) that we are only analyzing a subset of lensed images coming from a particular source and lens, either deliberately or simply because we did not observe all of the lensed images. In short, each image will take different values for the independent parameters $\boldsymbol{\theta}^{(i)}_{\rm ind}$ where each of them is a random realization of the distribution $p_{\rm pop,ind} = p_{\rm lens}(\boldsymbol{\theta}^{(i)}_{\rm ind}|\boldsymbol{\gamma})$.

Figure 11.2 shows a graphical representation of this data generation process. Again one should note that we are not making any inference on the population-level parameters of the GW sources and lenses. Instead we consider them as given in our analysis. Next, we will use our knowledge of the data generation processes under the two hypotheses to construct a statistic that would allow us to evaluate whether some GW signals are lensed or not.

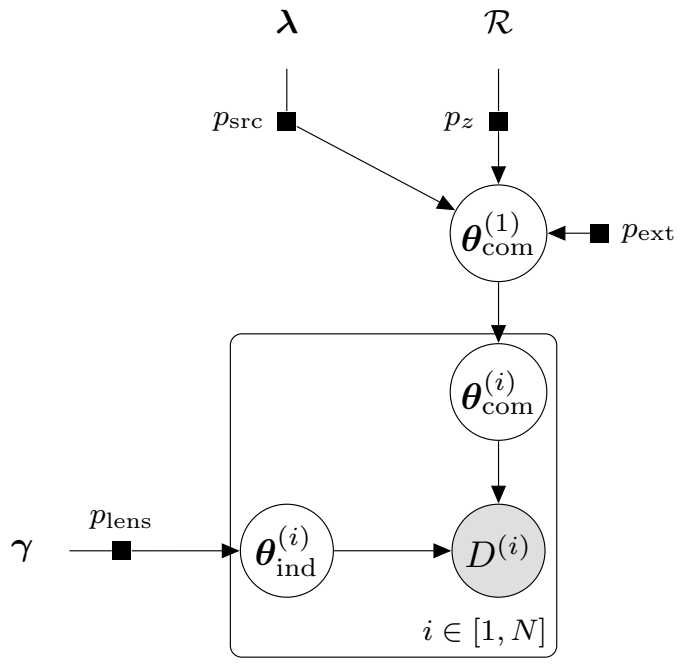


Figure 11.2: Data generation process for the $N$ observed data under the lensed hypothesis $\mathcal{H}_{\rm L}$. Each data $D^{(i)}$ can be described by the event-level parameters $\boldsymbol{\theta}^{(i)}$, which are partitioned into two disjoint sets: $\boldsymbol{\theta}^{(i)}_{\rm com}$ which are assumed to be the same across the $N$ signals and $\boldsymbol{\theta}^{(i)}_{\rm ind}$ which can be different for each signal. Without loss of generality, we assume that $\boldsymbol{\theta}^{(i)}_{\rm com} = \boldsymbol{\theta}^{(1)}_{\rm com}$ in the graph. The common parameters $\boldsymbol{\theta}^{(1)}_{\rm com}$ are one realization of the distribution $p_{\rm pop,com} = p_{\rm src}(\boldsymbol{\theta}^{(i)}_{\rm com}|\boldsymbol{\lambda}) p_z(z^{(i)}|\mathcal{R}, \mathcal{H}_{\rm L}) p_{\rm ext}$, while the independent parameters $\boldsymbol{\theta}^{(i)}_{\rm ind}$ for the $N$ signals are $N$ realizations of the distribution $p_{\rm pop,ind} = p_{\rm lens}(\boldsymbol{\theta}^{(i)}_{\rm ind}|\boldsymbol{\gamma})$.

### 11.2.3 Model comparison

The standard approach to perform a Bayesian model comparison is to compute the posterior odds $O^{\mathcal{H}_\mathrm{L}}_{\mathcal{H}_\mathrm{NL}}$, which is defined as[10]

$$O^{\mathcal{H}_\mathrm{L}}_{\mathcal{H}_\mathrm{NL}} = \frac{p(\mathcal{H}_\mathrm{L}|\boldsymbol{D}, \boldsymbol{\lambda}, \mathcal{R}, \boldsymbol{\gamma})}{p(\mathcal{H}_\mathrm{NL}|\boldsymbol{D}, \boldsymbol{\lambda}, \mathcal{R})}. \tag{11.7}$$

Note that for both models we fix the population-level parameters and the merger rate density, and that they are identical for both the lensed and the not-lensed hypothesis. Therefore we will not write them out explicitly when there is no ambiguity. Using Bayes' theorem, we can easily re-write the posterior odds into a product of two terms, namely the Bayes factor and the prior odds as

$$O^{\mathcal{H}_\mathrm{L}}_{\mathcal{H}_\mathrm{NL}} = \underbrace{\frac{p(\boldsymbol{D}|\mathcal{H}_\mathrm{L})}{p(\boldsymbol{D}|\mathcal{H}_\mathrm{NL})}}_{\text{Bayes factor } \mathcal{B}^{\mathcal{H}_\mathrm{L}}_{\mathcal{H}_\mathrm{NL}}} \times \underbrace{\frac{p(\mathcal{H}_\mathrm{L})}{p(\mathcal{H}_\mathrm{NL})}}_{\text{Prior odds } \mathcal{P}^{\mathcal{H}_\mathrm{L}}_{\mathcal{H}_\mathrm{NL}}} . \tag{11.8}$$

We first focus on getting an expression for evaluating the Bayes factor $\mathcal{B}^{\mathcal{H}_\mathrm{L}}_{\mathcal{H}_\mathrm{NL}}$ from the set of $N$ observed data. And later we will discuss the evaluation of the prior odds $\mathcal{P}^{\mathcal{H}_\mathrm{L}}_{\mathcal{H}_\mathrm{NL}}$.

### 11.2.4 The Bayes factor $\mathcal{B}^{\mathcal{H}_\mathrm{L}}_{\mathcal{H}_\mathrm{NL}}$

The Bayes factor $\mathcal{B}^{\mathcal{H}_\mathrm{L}}_{\mathcal{H}_\mathrm{NL}}$, defined as

$$\mathcal{B}^{\mathcal{H}_\mathrm{L}}_{\mathcal{H}_\mathrm{NL}} = \frac{p(\boldsymbol{D}|\mathcal{H}_\mathrm{L})}{p(\boldsymbol{D}|\mathcal{H}_\mathrm{NL})}, \tag{11.9}$$

is a ratio of the normalized probability densities of observing the data set $\boldsymbol{D}$ assuming the two hypotheses under consideration. In Appendix 11.6 we give the full derivation for the expressions evaluating the normalized probability densities of observing the data set $\boldsymbol{D}$ under each of the hypotheses. Here we will outline the derivation. The core idea is to use the graphs that describe the data generation

[10] We will abuse the notation and use $p$ to denote both probability and probability density when the context is clear.

processes for the two hypotheses in Figs. 11.1 and 11.2 to write down the desired expressions for the probability densities, and that the likelihood functions (which are the probability densities viewed as functions of the event-level parameters) can be factorized under both the hypotheses.

For the not-lensed hypothesis, since the $N$ signals are independent, we have

$$p(\boldsymbol{D}|\mathcal{H}_{\rm NL}) = \prod_{i=1}^{N} p(D^{(i)}|\mathcal{H}_{\rm NL}). \tag{11.10}$$

Combining this with the data generation process described in Fig. 11.1 we have

$$p(\boldsymbol{D}|\mathcal{H}_{\rm NL}) \propto \prod_{i=1}^{N} \int \mathrm{d}\boldsymbol{\theta}^{(i)}\ p(D^{(i)}|\boldsymbol{\theta}^{(i)}, \mathcal{H}_{\rm NL}) p_{\rm pop}(\boldsymbol{\theta}^{(i)}), \tag{11.11}$$

where the expression on the right-hand side is also known as the (unnormalized) marginal likelihood under the not-lensed hypothesis. Note that we need to make sure that the probability density $p(D^{(i)}|\mathcal{H}_{\rm NL})$ is normalized over all observable[11] data, accounting for selection effects [195]. This can be done by evaluating the proper normalization constant $\alpha$, where

$$\alpha = \int_{\text{all obs. data}} \mathrm{d}D^{(i)}\ p(D^{(i)}|\mathcal{H}_{\rm NL}). \tag{11.12}$$

Therefore the expression for the normalized $p(\boldsymbol{D}|\mathcal{H}_{\rm NL})$ is given by

$$p(\boldsymbol{D}|\mathcal{H}_{\rm NL}) = \frac{1}{\alpha^N} \prod_{i=1}^{N} \int \mathrm{d}\boldsymbol{\theta}^{(i)}\ p(D^{(i)}|\boldsymbol{\theta}^{(i)}, \mathcal{H}_{\rm NL}) p_{\rm pop}(\boldsymbol{\theta}^{(i)}). \tag{11.13}$$

As for the lensed hypothesis, unfortunately the probability density $p(\boldsymbol{D}|\mathcal{H}_{\rm L})$ cannot be factorized like Eq. (11.10). However, the likelihood functions can

[11] Here the term *observable data* means that the signals in the data would pass some detection criteria that one imposes, for example the signals would need to have a signal-to-noise ratio above some threshold, such that they would be identified as GW events.

still be factorized if we assume that the noise realizations for the $N$ events are independent and that a signal is deterministic given a set of parameters $\boldsymbol{\theta}$ that describe the waveform. Marginalizing the joint likelihood function with parameters according to Fig. 11.2, we have

$$\begin{aligned} p(\boldsymbol{D}|\mathcal{H}_{\rm L}) \propto \int \mathrm{d}\boldsymbol{\theta}^{(1)}_{\rm com}\, \mathrm{d}\boldsymbol{\theta}^{(1)}_{\rm ind}\, \cdots \mathrm{d}\boldsymbol{\theta}^{(N)}_{\rm ind} \left[\prod_{j=1}^{N} p(D^{(j)}|\boldsymbol{\theta}^{(j)}_{\rm ind}, \boldsymbol{\theta}^{(1)}_{\rm com})\right] \\ \times p_{\rm pop,ind}(\boldsymbol{\theta}^{(1)}_{\rm ind}, ..., \boldsymbol{\theta}^{(N)}_{\rm ind}) p_{\rm pop,com}(\boldsymbol{\theta}^{(1)}_{\rm com}), \end{aligned} \tag{11.14}$$

where the expression on the right-hand side is known as the (unnormalized) marginal likelihood under the lensed hypothesis. Again, we will need to compute the normalized probability density $p(\boldsymbol{D}|\mathcal{H}_{\rm L})$ in order to compute a meaningful Bayes factor, and take selection effects into account. The proper normalization constant $\beta$ in this case, is given by

$$\begin{aligned} \beta \propto \int_{\text{all obs. data set}} \mathrm{d}D^{(1)} \cdots \mathrm{d}D^{(N)} \int \mathrm{d}\boldsymbol{\theta}^{(1)}_{\rm com}\, \mathrm{d}\boldsymbol{\theta}^{(1)}_{\rm ind}\, \cdots \mathrm{d}\boldsymbol{\theta}^{(N)}_{\rm ind} \\ \times \left[\prod_{j=1}^{N} p(D^{(j)}|\boldsymbol{\theta}^{(j)}_{\rm ind}, \boldsymbol{\theta}^{(1)}_{\rm com})\right] \\ \times p_{\rm pop,ind}(\boldsymbol{\theta}^{(1)}_{\rm ind}, ..., \boldsymbol{\theta}^{(N)}_{\rm ind}) p_{\rm pop,com}(\boldsymbol{\theta}^{(1)}_{\rm com}). \end{aligned} \tag{11.15}$$

Therefore, the expression for the normalized $p(\boldsymbol{D}|\mathcal{H}_{\rm L})$ is given by

$$\begin{aligned} p(\boldsymbol{D}|\mathcal{H}_{\rm L}) = \frac{1}{\beta} \int \mathrm{d}\boldsymbol{\theta}^{(1)}_{\rm com}\, \mathrm{d}\boldsymbol{\theta}^{(1)}_{\rm ind}\, \cdots \mathrm{d}\boldsymbol{\theta}^{(N)}_{\rm ind} \\ \times \left[\prod_{j=1}^{N} p(D^{(j)}|\boldsymbol{\theta}^{(j)}_{\rm ind}, \boldsymbol{\theta}^{(1)}_{\rm com})\right] \\ \times p_{\rm pop,ind}(\boldsymbol{\theta}^{(1)}_{\rm ind}, ..., \boldsymbol{\theta}^{(N)}_{\rm ind}) p_{\rm pop,com}(\boldsymbol{\theta}^{(1)}_{\rm com}). \end{aligned} \tag{11.16}$$

Finally, we have the expression that we can use to evaluate the Bayes factor for the lensed hypothesis versus the not-lensed hypothesis, namely

$$\mathcal{B}^{\mathcal{H}_{\rm L}}_{\mathcal{H}_{\rm NL}} = \frac{\alpha(\boldsymbol{\lambda},\mathcal{R})^N}{\beta(\boldsymbol{\lambda},\mathcal{R},\boldsymbol{\gamma})} \times \boxed{\underbrace{\left\{\int \mathrm{d}\boldsymbol{\theta}^{(1)}_{\rm com}\, \mathrm{d}\boldsymbol{\theta}^{(1)}_{\rm ind} \cdots \mathrm{d}\boldsymbol{\theta}^{(N)}_{\rm ind} \left[\prod_{j=1}^{N} p(D^{(j)}|\boldsymbol{\theta}^{(j)}_{\rm ind}, \boldsymbol{\theta}^{(1)}_{\rm com})\right] p_{\rm pop,ind}(\boldsymbol{\theta}^{(1)}_{\rm ind}, ..., \boldsymbol{\theta}^{(N)}_{\rm ind}|\boldsymbol{\gamma}) p_{\rm pop,com}(\boldsymbol{\theta}^{(1)}_{\rm com}|\boldsymbol{\lambda},\mathcal{R})\right\} \left[\prod_{i=1}^{N} \int \mathrm{d}\boldsymbol{\theta}^{(i)}\; p(D^{(i)}|\boldsymbol{\theta}^{(i)},\mathcal{H}_{\rm NL}) p_{\rm pop}(\boldsymbol{\theta}^{(i)}|\boldsymbol{\lambda},\mathcal{R})\right]^{-1}}_{\text{coherence ratio } C}}. \tag{11.17}$$

One can interpret the boxed expression in Eq. (11.17), which is the ratio of unnormalized marginal likelihoods under the two hypotheses, as a measurement of how well the data set $\boldsymbol{D}$ of $N$ signals can be jointly fit by a set of common parameters versus $N$ sets of independent parameters, which we call the coherence ratio $C$ to differentiate it with the Bayes factor. While a negative log-coherence ratio means that the lensed hypothesis, that is setting some of the parameters to be the same across events, fails to fit the $N$ signals jointly, a positive log coherence ratio however does not mean that the $N$ signals are lensed. This is the Occam's razor at play. Assuming that the lensed hypothesis and the not-lensed hypothesis fit the data set $\boldsymbol{D}$ equally well, the lensed hypothesis will be favored by the Bayesian model selection framework because it has fewer free parameters, and hence a smaller prior volume. For GW signals from high-mass BBH mergers, this issue will be more apparent as they produce shorter signals detectable in the interferometers, and we usually make less precise measurements of the masses for these high-mass systems [196]. This is partially alleviated by incorporating the population information that they are rarer compared to lighter systems. It also brings out an important point that the Bayes factor, or generally

any probabilistic statement, that some GW signals are strongly lensed depends on the source population one is considering.

We can think of the factor $\beta(\boldsymbol{\lambda}, \mathcal{R}, \boldsymbol{\gamma})/\alpha(\boldsymbol{\lambda}, \mathcal{R})^N$ in Eq. (11.17) as a population-averaged scale of the coherence ratio accounting for selection effects, which affect the two hypotheses differently. If the coherence ratio is greater than the population typical value for $\beta/\alpha^N$, then the Bayes factor will indicate that the lensed hypothesis is favored by the observed data. In fact, the normalization constant under the not-lensed hypothesis $\alpha$ can be interpreted as the detectable fraction of sources [195]. Similarly, we can interpret the normalization constant under the lensed hypothesis $\beta$ as the fraction of sources that would produce $N$ detectable lensed signals. We expect that the order of magnitude for $\beta$ would be similar to that for $\alpha$. Therefore, essentially selection effects penalize the lensed hypothesis by a factor of roughly $\alpha^{N-1}$, counteracting the Occam's razor.

### 11.2.5 The prior odds $\mathcal{P}^{\mathcal{H}_\mathrm{L}}_{\mathcal{H}_\mathrm{NL}}$

The Bayes factor we derived above in Eq. (11.17) only compares the coherence of the data set with each hypothesis, but not the probability in which each hypothesis would occur. We know empirically, that strong lensing causing at least $N$ images occurs less frequently than observing $N$ independent GW events with each coming from a different source. We can incorporate our knowledge about the rate in the form of prior odds $\mathcal{P}^{\mathcal{H}_\mathrm{L}}_{\mathcal{H}_\mathrm{NL}}$, which is defined as

$$\mathcal{P}^{\mathcal{H}_\mathrm{L}}_{\mathcal{H}_\mathrm{NL}} = \frac{p(\mathcal{H}_\mathrm{L})}{p(\mathcal{H}_\mathrm{NL})}. \tag{11.18}$$

We can then compute the posterior odds $\mathcal{O}^{\mathcal{H}_\mathrm{L}}_{\mathcal{H}_\mathrm{NL}}$ using Eq. (11.8) from the Bayes factor in Eq. (11.17) and the prior odds in Eq. (11.18).

One can assign the prior odds simply as the ratio of the rate of observing $N$ lensed images from a single source over the rate of observing $N$ GW signals coming from $N$ independent sources. Obtaining this will require detailed modeling of GW sources and lenses. In particular these numbers should be computed under the

the chosen source and lens population models for an analysis. However, one can argue that for most of the population models commonly used by the astrophysics community, the prior odds is very small with the current sensitivities of GW detectors, about $\mathcal{P}^{\mathcal{H}_{\rm L}}_{\mathcal{H}_{\rm NL}} \approx 10^{-2} - 10^{-4}$ [177, 178, 179, 180, 181].

### 11.2.6 Marginalization over redshift

With the expression for $p(\boldsymbol{D}|\mathcal{H}_{\rm L})$ under the lensed hypothesis in Eq. (11.16), one can estimate the integral using a stochastic sampling algorithm such as nested sampling [120] by sampling over $\left\{\boldsymbol{\theta}^{(1)}_{\rm com}, \boldsymbol{\theta}^{(1)}_{\rm ind}, \cdots, \boldsymbol{\theta}^{(N)}_{\rm ind}\right\}$ with a prior

$$p_{\rm pop,ind}(\boldsymbol{\theta}^{(1)}_{\rm ind}, ..., \boldsymbol{\theta}^{(N)}_{\rm ind}) p_{\rm pop,com}(\boldsymbol{\theta}^{(1)}_{\rm com})$$

and a *joint* likelihood

$$\prod_{j=1}^{N} p(D^{(j)}|\boldsymbol{\theta}^{(j)}_{\rm ind}, \boldsymbol{\theta}^{(1)}_{\rm com}).$$

However, a direct sampling will be inefficient because of the degeneracy between the absolute magnification and the luminosity distance, and hence the redshift of the source. Under the not-lensed hypothesis, we can infer the source redshift since we can infer the luminosity distance of the source $d^{\rm src}_{\rm L}$, and by assuming a particular cosmology we can compute the redshift $z^{\rm src} = z(d^{\rm src}_{\rm L})$ from the luminosity distance. Under the lensed hypothesis, each image will be, in general, magnified by a different factor. In fact, we can only measure the apparent luminosity distance for each image as in Eq. (11.3). Therefore, we will not be able to infer the absolute magnification for each image and the source redshift at the same time. For example, a signal with a said redshift of $z \approx 0.363$ and an absolute magnification of $\mu = 4$ would have the same apparent luminosity distance of 1 Gpc as a signal with a redshift of $z \approx 0.780$ and an absolute magnification of $\mu = 25$.

In order to explore the degenerate parameter space more efficiently, we can marginalize over the source redshift separately. In fact, the source redshift $z$ stands out from the rest of the parameters. This is because with a given redshift,

one can figure out the prior distribution of the apparent luminosity distance $d_{\rm L}^{(i)}$ given the prior distribution of the absolute magnification $p(\mu^{(i)})$ by

$$\begin{aligned} p(d_{\rm L}^{(i)}) &= p\left(\mu^{(i)} = \left(\frac{d_{\rm L}^{\rm src}(z)}{d_{\rm L}^{(i)}}\right)^2 \middle| z\right) \left|\frac{\partial \mu^{(i)}}{\partial d_{\rm L}^{(i)}}\right| \\ &= \frac{2\mu^{(i)}}{d_{\rm L}^{(i)}} p\left(\mu^{(i)} = \left(\frac{d_{\rm L}^{\rm src}(z)}{d_{\rm L}^{(i)}}\right)^2 \middle| z\right), \end{aligned} \tag{11.19}$$

and similarly for the prior distribution of the redshifted/detector-frame masses given the distribution of source-frame masses and the redshift as

$$\begin{aligned} p(m_{1,2}^{\rm det}) &= p(m_{1,2}^{\rm src} = \frac{m_{1,2}^{\rm det}}{1+z}|z)\left|\frac{\partial m_{1,2}^{\rm src}}{\partial m_{1,2}^{\rm det}}\right| \\ &= \left(\frac{1}{1+z}\right)^2 p(m_{1,2}^{\rm src} = \frac{m_{1,2}^{\rm det}}{1+z}|z). \end{aligned} \tag{11.20}$$

Therefore, we can rewrite Eq. (11.16) as a 1D integral over the redshift as

$$p(\boldsymbol{D}|\mathcal{H}_{\rm L}) \propto \int {\rm d}z\ \mathcal{L}_{\rm marg}(z)\ p_z(z|\mathcal{H}_{\rm L}), \tag{11.21}$$

where $\mathcal{L}_{\rm marg}(z)$ is given by

$$\begin{aligned} \mathcal{L}_{\rm marg}(z) = &\int {\rm d}\boldsymbol{\theta}_{\rm com}^{(1)} \setminus \{z\}\ {\rm d}\boldsymbol{\theta}_{\rm ind}^{(1)}\ \cdots {\rm d}\boldsymbol{\theta}_{\rm ind}^{(N)} \\ &\times \left[\prod_{j=1}^{N} p(D^{(j)}|\boldsymbol{\theta}_{\rm ind}^{(j)}, \boldsymbol{\theta}_{\rm com}^{(1)} \setminus \{z\})\right] \\ &\times p_{\rm pop,ind}(\boldsymbol{\theta}_{\rm ind}^{(1)}, ..., \boldsymbol{\theta}_{\rm ind}^{(N)}) p_{\rm pop,com}(\boldsymbol{\theta}_{\rm com}^{(1)} \setminus \{z\}). \end{aligned} \tag{11.22}$$

The marginalized likelihood $\mathcal{L}_{\rm marg}(z)$, which is a function of $z$ only, can be obtained via the conventional Monte Carlo methods (such as Markov Chain Monte Carlo method and nested sampling) by sampling over redshifted/detector-frame parameters without the redshift. This will alleviate the degeneracy problem, as well as open up the possibility of computing Eq. (11.16) by reusing computations

done with the not-lensed hypothesis assumed, without re-exploring the joint parameter space. It also lends itself to the interpretation of treating the redshift as a hyperparameter of a subpopulation of signals sharing the same intrinsic parameters (and some of the extrinsic parameters).

Given a merger rate density $\mathcal{R}(z) \equiv \mathrm{d}N_{\mathrm{src}}/(\mathrm{d}V_{\mathrm{c}}\mathrm{d}t)$, which is the number density of mergers per comoving volume $V_{\mathrm{c}}$ per unit time $t$ in the source frame, one can compute the probability density of the source redshift $z$ as

$$p(z) \propto \frac{\mathrm{d}V_{\mathrm{c}}}{\mathrm{d}z}\frac{1}{1+z}\mathcal{R}(z). \tag{11.23}$$

Using the product rule, we can write down the prior distribution for the redshift $z$ under the lensed hypothesis as

$$\begin{aligned} p_z(z|\mathcal{H}_{\mathrm{L}}) &= \frac{1}{C}\frac{p(\mathcal{H}_{\mathrm{L}}|z)p(z)}{p(\mathcal{H}_{\mathrm{L}})} \\ &= \frac{1}{C}\frac{\tau(z)p(z)}{p(\mathcal{H}_{\mathrm{L}})}, \end{aligned} \tag{11.24}$$

where $C$ is the normalization constant, and $\tau(z) \equiv p(\mathcal{H}_{\mathrm{L}}|z)$ is the optical depth of strong lensing at redshift $z$. Similarly, under the not-lensed hypothesis, the prior distribution for the redshift $p_z(z|\mathcal{H}_{\mathrm{NL}})$ is given by

$$\begin{aligned} p_z(z|\mathcal{H}_{\mathrm{NL}}) &= \frac{1}{C'}\frac{p(\mathcal{H}_{\mathrm{NL}}|z)p(z)}{p(\mathcal{H}_{\mathrm{NL}})} \\ &= \frac{1}{C'}\frac{[1-\tau(z)]\,p(z)}{p(\mathcal{H}_{\mathrm{NL}})}, \end{aligned} \tag{11.25}$$

where the normalization constant $C'$ is defined accordingly. Figure 11.3 shows the prior distribution of redshift $z$ under the lensed (solid blue line) and not-lensed hypothesis (dashed green line), using the optical depth model in Ref. [182] and a merger rate density tracking the star formation rate in [197, 178]. The peak of the prior distribution under the lensed hypothesis shifts to a higher value of $z \sim 3$ compared to that under the not-lensed hypothesis, which peaks at roughly $z \sim 2$ because of the optical depth (gray dash-dotted line) being higher at higher redshifts.

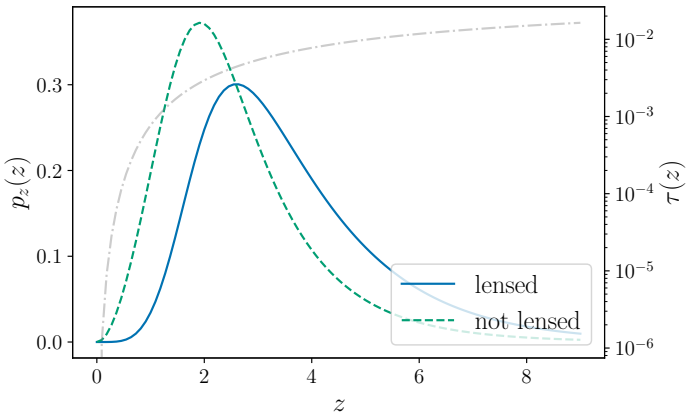


Figure 11.3: The probability densities $p_z(z)$ of the source redshift $z$ under the lensed and not-lensed hypothesis. The gray dotted line shows the optical depth $\tau(z)$. As the optical depth increases with the redshift, the peak of the density $p_z$ under the lensed hypothesis shifts to a higher value of $z \sim 3$ compared to the density under the not-lensed hypothesis.

As a by-product of evaluating Eq. (11.21), we also get a set of posterior samples of $z$, which are distributed according to

$$p(z|\boldsymbol{D}, \mathcal{H}_\mathrm{L}) = \frac{\mathcal{L}_\mathrm{marg}(z) p_z(z|\mathcal{H}_\mathrm{L})}{\int \mathrm{d}z \; \mathcal{L}_\mathrm{marg}(z) \; p_z(z|\mathcal{H}_\mathrm{L})}. \tag{11.26}$$

In the next subsection, we describe how to reconstruct the true (but degenerate) source parameters using Gibbs sampling.

### 11.2.7 Inferring source parameters using Gibbs sampling

Ultimately we want a set of joint posterior samples $\{z, \boldsymbol{\theta}\}$ describing the source of the observed lensed signals. As a by-product of the marginalization over the redshift calculation using nested sampling, we obtain a set of posterior samples of the redshift $z \sim p(z|\boldsymbol{D}, \mathcal{H}_\mathrm{L})$ marginalized over the parameters $\boldsymbol{\theta}$. Using Gibbs sampling, we can obtain the desired joint posterior samples from samples drawn from the conditional probability distributions $p(z|\boldsymbol{D}, \mathcal{H}_\mathrm{L})$ from the

marginalization step and $p(\boldsymbol{\theta}|z, \boldsymbol{D}, \mathcal{H}_{\rm L})$ from the inference step. This is because

$$p(z, \boldsymbol{\theta}|\boldsymbol{D}, \mathcal{H}_{\rm L}) \propto p(\boldsymbol{\theta}|z, \boldsymbol{D}, \mathcal{H}_{\rm L}) p(z|\boldsymbol{D}, \mathcal{H}_{\rm L}). \tag{11.27}$$

Algorithm 1 outlines the (collapsed and blocked) Gibbs sampling algorithm [198] that allows us to reconstruct the joint posterior samples. This variant of Gibbs sampling can be easily parallelized since each iteration is independent. For each set of joint $\{z, \boldsymbol{\theta}\}$ samples, since $\boldsymbol{\theta}$ are redshifted parameters (such as the redshifted component masses) and $z$ is the source redshift, one can compute the true source parameters such as the source masses easily. In Sec. 11.3, we demonstrate the framework and tools we developed with simulated lensed GW signals from BBH mergers.

**Algorithm 1** Gibbs sampling

**procedure** SAMPLE($N_s$)
  $i \leftarrow 1$
  $\boldsymbol{\theta}_{\rm true} \leftarrow [\ ]$
  **while** $i \leq N_s$ **do**
    $z_{\rm drawn} \leftarrow$ a random draw from the samples $z$ from the marginalization step
    compute the ln weight $\ln w_j$ for each of the samples $\boldsymbol{\theta}_j$ from the inference step
    $\boldsymbol{\theta}_{\rm drawn} \leftarrow$ a random draw from $\{\boldsymbol{\theta}_j\}$ with weight $w_j$ using rejection sampling assuming that the true source redshift is $z_{\rm drawn}$
    append $\{z_{\rm drawn}, \boldsymbol{\theta}_{\rm drawn}\}$ to $\boldsymbol{\theta}_{\rm true}$
    $i \leftarrow i + 1$
  **end while**
  return $\boldsymbol{\theta}_{\rm true}$
**end procedure**

## 11.3 Strong lensing of gravitational waves from a binary black hole merger: observing a pair of lensed signals

Now that we have developed the statistical framework in a general setting, here we want to apply the framework to analyze two particular cases and discuss the

technical subtleties involved, namely for the case of strong lensing of a GW signal from a BBH merger with a pair of lensed images (i.e., $N = 2$) observed, and with only one image (i.e., $N = 1$) observed. In this section, we focus on the former case first.

### 11.3.1 Under the not-lensed hypothesis

Suppose we write the event-level parameters for each of the BBH mergers under the not-lensed hypothesis as

$$\boldsymbol{\theta}^{(i)} = \{\underbrace{M_{\rm tot}^{\rm det}, q, \boldsymbol{\chi}_1, \boldsymbol{\chi}_2}_{\text{intrinsic parameters}}, \underbrace{d_{\rm L}, \alpha, \delta, \psi, \iota, \phi_{\rm c}, t_{\rm c}}_{\text{extrinsic parameters}}\}, \tag{11.28}$$

and these are the parameters that are being sampled over during the inference step. As derived in Eq. (11.13) with $N = 2$, under the not-lensed hypothesis we have

$$\begin{aligned} &p(\{D^{(1)}, D^{(2)}\}|\mathcal{H}_{\rm NL}) \\ &= \frac{1}{\alpha^2} p(D^{(1)}|\mathcal{H}_{\rm NL}) p(D^{(2)}|\mathcal{H}_{\rm NL}). \end{aligned} \tag{11.29}$$

Figure 11.4 shows a graphical representation of the data generation process under the not-lensed hypothesis for signals from BBH mergers using the parametrization in Eq. (11.28). Here we use $\boldsymbol{\Phi}$ to denote the set of extrinsic parameters $\{\alpha, \delta, \psi, \iota, \phi_c\}$ that are distributed according to the distribution $p_{\rm ext}$. As for the time of arrival $t_{\rm c}$, we treat it separately and hence it is not shown in Fig. 11.4. From matched-filtering pipelines that scan through all the data looking for GW triggers, we know roughly the time of arrival for each trigger. Let us write $t_{\rm c}^{(1)} = t_1 + \delta t_{\rm c}^{(1)}$ and $t_{\rm c}^{(2)} = t_2 + \delta t_{\rm c}^{(2)}$, where $t_1$ and $t_2$ are the point estimates of the arrival times given by a pipeline for the two triggers, respectively. Instead of sampling over $t_{\rm c}^{(1)}$ and $t_{\rm c}^{(2)}$, we sample over $\delta t_{\rm c}^{(1)}$ and $\delta t_{\rm c}^{(2)}$ with a small prior range (typically $\sim 0.2$ s) and $t_1, t_2$ taken to be known. Mathematically, this means

$$\begin{aligned} &p(t_{\rm c}^{(1)}, t_{\rm c}^{(2)}|\mathcal{H}_{\rm NL}) {\rm d}t_{\rm c}^{(1)} {\rm d}t_{\rm c}^{(2)} \\ &= p(\delta t_{\rm c}^{(1)}, \delta t_{\rm c}^{(2)}|t_1, t_2, \mathcal{H}_{\rm NL}) p(t_1, t_2|\mathcal{H}_{\rm NL}) {\rm d}\delta t_{\rm c}^{(1)} {\rm d}\delta t_{\rm c}^{(2)}. \end{aligned} \tag{11.30}$$

Suppose we order the two events by their times of arrival, i.e., $t_2 > t_1$, and define the time delay $\Delta t \equiv (t_2 - t_1) > 0$. After this transformation, there is an extra factor in the prior that accounts for the probability of having two random events separated by a time delay of $\Delta t$ under the not-lensed hypothesis. If we model the arrival of events by a Poisson process, the prior probability density that any random pair of events having a time delay of $\Delta t$, *given that* there are $N_{\rm obs}$ events during the time interval of $(0, T_{\rm obs}]$, is given by

$$p(\Delta t|\mathcal{H}_{\rm NL}) = \frac{2}{T_{\rm obs}}\left(1 - \frac{\Delta t}{T_{\rm obs}}\right), \tag{11.31}$$

where we give a detailed derivation in Appendix 11.8. This can be considered as the part of the time-delay Bayes factor in Ref. [190] from the not-lensed hypothesis.

Therefore, the full expression for $p(\{D^{(1)}, D^{(2)}\}|\mathcal{H}_{\rm NL})$ now reads

$$\begin{aligned}
&p(\{D^{(1)}, D^{(2)}\}|\mathcal{H}_{\rm NL}) \\
&= \frac{1}{\alpha^2} p(\Delta t|\mathcal{H}_{\rm NL}) \\
&\times \prod_{i=1}^{2} \int \mathrm{d}\{\underbrace{M_{\rm tot}^{\rm det}, q, \boldsymbol{\chi}_1, \boldsymbol{\chi}_2, d_{\rm L}, \alpha, \delta, \psi, \iota, \phi_{\rm c}, \delta t_{\rm c}}_{\boldsymbol{\theta}^{(i)}}\} \\
&\quad p(D^{(i)}|\boldsymbol{\theta}^{(i)}) p_{\rm pop}(\boldsymbol{\theta}^{(i)}|\mathcal{H}_{\rm NL}),
\end{aligned} \tag{11.32}$$

where under the not-lensed hypothesis there is a one-to-one mapping between $d_{\rm L}$ and $z$, and hence one will only need to convert Eq. (11.25) by multiplying the proper Jacobian without the need of a separate marginalization of the source redshift.

### 11.3.2 Under the lensed hypothesis

Under the lensed hypothesis, we write the event-level parameters differently, namely we let the common parameters $\boldsymbol{\theta}_{\rm com}^{(i)} = \{M_{\rm tot}^{\rm det}, q, \boldsymbol{\chi}_1, \boldsymbol{\chi}_2, \alpha, \delta, \psi, \iota, \phi_{\rm c}\}$. As for the independent parameters, we write $\boldsymbol{\theta}_{\rm ind}^{(i)} = \{\delta t_{\rm c}^{(i)}, d_{\rm L}^{(i)}, \Xi^{(i)}\}$, where we

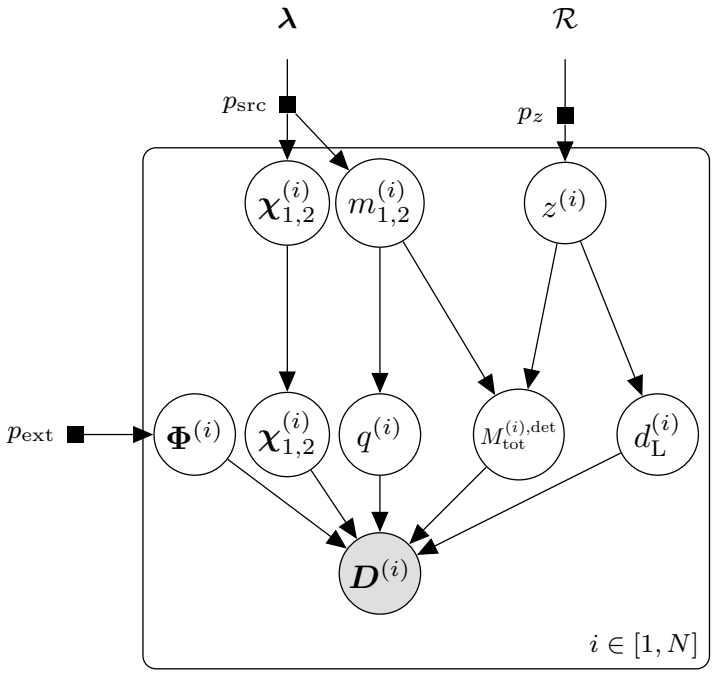


Figure 11.4: Data generation process for the $N$ observed data under the not-lensed hypothesis $\mathcal{H}_{\rm NL}$. This is similar to Fig. 11.1 but with the event-level parameters $\boldsymbol{\theta}^{(i)}$ written out explicitly. Here we use $\boldsymbol{\Phi}$ to denote the set of extrinsic parameters $\{\alpha, \delta, \psi, \iota, \phi_c\}$ that are distributed according to the distribution $p_{\rm ext}$.

perform the same transformation to the time of arrival as in the case under the not-lensed hypothesis, and $\Xi$ denotes the type of an image which can be either {I, II, III}.

Each strongly lensed image can be classified into three types (I, II or III), where each image type corresponds to a Morse index of $\{0, 1, 2\}$, respectively, inducing a different phase shift as shown in Eq. (11.6) to the image because of the interaction of the lensed image with the caustic. One would expect the image that arrives at the Earth first to be of type I since type-I images correspond to local minima of the Fermat time-of-arrival potential. However, the signal that we called the first image in an analysis might not actually be the first image that had arrived the

Earth since, for example, the GW detectors might be offline. Various arguments on the type of images one would see can be made if we know the geometry of the gravitational lens but this is not known prior to the analysis. Therefore, to be lens-model-agnostic we assume that the type of the lensed images in a pair to each follow a discrete uniform distribution and are uncorrelated, namely

$$p_{\rm lens}(\Xi^{(1)}, \Xi^{(2)}) = p_{\rm lens}(\Xi^{(1)}) p_{\rm lens}(\Xi^{(2)}), \tag{11.33}$$

where

$$p_{\rm lens}(\Xi^{(i)}) = \begin{cases} 1/3 & \text{when } \Xi^{(i)} = \text{I} \\ 1/3 & \text{when } \Xi^{(i)} = \text{II} \\ 1/3 & \text{when } \Xi^{(i)} = \text{III} \end{cases} . \tag{11.34}$$

That being said, both the assumptions that the image types are uncorrelated and each follows a uniform distribution are not true. If one adopts a particular lens model and ordering of the images, the appropriate joint distribution that encapsulates the correlation should be used instead.

Figure 11.5 shows a graphical representation of the data generation process under the lensed hypothesis for BBH signals. Similar to Fig. 11.4, we use $\mathbf{\Phi}$ to denote the set of extrinsic parameters $\{\alpha, \delta, \psi, \iota, \phi_{\rm c}\}$ that are distributed according to the distribution $p_{\rm ext}$, and that we treat the time of arrival $t_{\rm c}$ separately. Unlike the not-lensed case, here we assume that $\boldsymbol{\theta}^{(i)}_{\rm com} = \{M^{\rm det}_{\rm tot}, q, \boldsymbol{\chi}_1, \boldsymbol{\chi}_2, \alpha, \delta, \psi, \iota, \phi_{\rm c}\}$ are the same across the signals (hence we dropped the superscript in the graph). Also, even though we sample the apparent luminosity distance for each image, there is no one-to-one mapping between it and the true source redshift since the apparent luminosity distance is also related to the absolute magnification of a lensed image. As discussed in Sec. 11.2.6, we perform the marginalization over the source redshift separately.

For the time of arrival $t^{(i)}_{\rm c}$, we can perform the same transformation as in the case for the not-lensed hypothesis (similar to Eq. (11.30)), and sample $\delta t^{(i)}_{\rm c}$ that has a much smaller range instead. However, instead of having an analytical expression

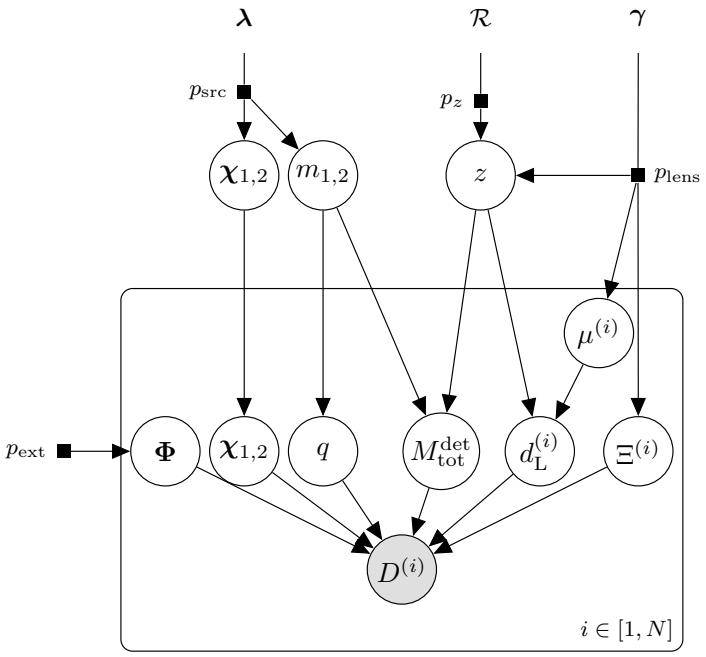


Figure 11.5: Data generation process for the $N$ observed data under the lensed hypothesis $\mathcal{H}_{\rm L}$. This is similar to Fig. 11.2 but with the common parameters $\boldsymbol{\theta}_{\rm com}^{(i)}$ and the independent parameters $\boldsymbol{\theta}_{\rm ind}^{(i)}$ written out explicitly. Again, we use $\boldsymbol{\Phi}$ to denote the set of extrinsic parameters $\{\alpha, \delta, \psi, \iota, \phi_{\rm c}\}$ that are distributed according to the distribution $p_{\rm ext}$.

for the time delay $\Delta t$, there is no analytically tractable expression for the time delay under the lensed hypothesis. That being said, we can obtain it readily from numerical simulations (for example, Ref. [190]). As a result, there is an extra factor of $p(\Delta t|\mathcal{H}_{\rm L})$ in the prior that accounts for the probability of having two lensed images separated by a time delay of $\Delta t$.

Therefore, the full expression for $p(\{D^{(1)}, D^{(2)}\}|\mathcal{H}_{\rm L})$ now reads

$$
\begin{aligned}
&p(\{D^{(1)}, D^{(2)}\}|\mathcal{H}_{\rm L}) \\
&= \frac{1}{\beta} p(\Delta t|\mathcal{H}_{\rm L}) \\
&\times \int {\rm d}z\; p_z(z|\mathcal{H}_{\rm L}) \Bigg[ \int {\rm d}\{\underbrace{M^{\rm det}_{\rm tot}, q, \boldsymbol{\chi}_1, \boldsymbol{\chi}_2, \alpha, \delta, \psi, \iota, \phi_{\rm c}}_{\boldsymbol{\theta}_{\rm com}}\} \\
&\int {\rm d}\{\underbrace{\delta t_{\rm c}^{(1)}, d_{\rm L}^{(1)}, \Xi^{(1)}}_{\boldsymbol{\theta}^{(1)}_{\rm ind}}, \underbrace{\delta t_{\rm c}^{(2)}, d_{\rm L}^{(2)}, \Xi^{(2)}}_{\boldsymbol{\theta}^{(2)}_{\rm ind}}\} p(D^{(1)}|\boldsymbol{\theta}_{\rm com}, \boldsymbol{\theta}^{(i)}_{\rm ind}) \\
&p(D^{(2)}|\boldsymbol{\theta}_{\rm com}, \boldsymbol{\theta}^{(2)}_{\rm ind}) p_{\rm pop,ind}(\boldsymbol{\theta}^{(1)}_{\rm ind}, \boldsymbol{\theta}^{(2)}_{\rm ind}|\mathcal{H}_{\rm L}) p_{\rm pop,com}(\boldsymbol{\theta}_{\rm com}|\mathcal{H}_{\rm L}) \Bigg],
\end{aligned}
\tag{11.35}
$$

where the expression enclosed by the square brackets would be identified as $\mathcal{L}_{\rm marg}(z)$ as discussed in Sec 11.2.6.

### 11.3.3 Demonstration

Here we demonstrate the framework with two examples. In the first example, we injected two GW signals with a redshifted total mass $M^{\rm det}_{\rm tot} = 280 M_\odot$ into simulated data streams. With this example, we show explicitly how the source population model would change the Bayes factor. In the second example, we injected instead two GW signals with a redshifted total mass $M^{\rm det}_{\rm tot} = 60 M_\odot$, which corresponds to typical stellar-mass BBH systems for the LIGO-Virgo detectors. In both examples, we use the waveform approximant `IMRPhenomXPHM` [199], which models both the leading-quadrupole ($\ell = 2$) radiation, as well as some of the nonquadrupole ($\ell > 2$) multipoles. By incorporating the higher-order modes, we show that the image type of each lensed signal can also be inferred. All the results presented here were computed using the software package `hanabi`[12], which is built upon the package `bilby` [200] and `parallel_bilby` [201]. Also, we used the nested sampling algorithm implemented in the package `dynesty` [202] with

[12] `https://github.com/ricokaloklo/hanabi`

the number of live points `nlive` = 2000 and the number of autocorrelation times `nact` = 60 when running the nested sampling algorithm, where the settings are sufficient to give convergent results [203]. More specifically, the results presented in this paper used the aforementioned packages of version `bilby==1.0.2` [204], `parallel_bilby==0.1.5` [205], `dynesty=1.0.1` [206], and `hanabi==0.3.1` [207].

#### 11.3.3.1 Example 1: Two lensed signals from apparent intermediate-mass binary black hole mergers

In this example, we have two lensed GW signals injected into two simulated data streams with Gaussian noise recolored to match the Advanced LIGO (aLIGO) design noise curve [100]. Table 11.1 summarizes some of the waveform parameters for the two signals. The two injected signals, when analyzed on their own, seem to originate from two separate mergers of an intermediate-mass binary black hole system.

To demonstrate how using different source population models would change one's interpretation of the two signals, as well as the numerical value of the Bayes factor using our framework, we first use a log-uniform distribution as the population model for the component masses, namely

$$p_{\rm src}(m_{1,2}^{\rm src}) \propto \begin{cases} 1/m_{1,2}^{\rm src} & \text{for } 5M_\odot \leq m_{1,2}^{\rm src} \leq 300M_\odot \\ 0 & \text{otherwise} \end{cases}. \tag{11.36}$$

For the component spins, we use a distribution that is uniform in the component spin magnitude, and isotropic in the spin orientation.

As for the merger rate density, here we use, for the sake of demonstration, an analytical fit from Ref. [178] that tracks the population synthesis results from Ref. [197] for population-I and population-II stars, namely

$$\mathcal{R}(z) = \frac{6.6 \times 10^3 \ \exp(1.6z)}{30 + \exp(2.1z)}. \tag{11.37}$$

For the absolute magnification, again for the purpose of demonstration, we use a simple power law distribution that is independent of the time delay, namely

$$p_{\rm lens}(\mu^{(1)}, \mu^{(2)}|\Delta t) = p_{\rm lens}(\mu^{(1)}) p_{\rm lens}(\mu^{(2)}), \tag{11.38}$$

with

$$p_{\rm lens}(\mu^{(i)}) \propto \begin{cases} \mu^{-3} & \text{for } \mu \geq 2 \\ 0 & \text{otherwise} \end{cases}, \tag{11.39}$$

where it captures the general $\mu^{-3}$ scaling in the high-magnification regime, as well as the requirement that the absolute magnification has to exceed some threshold in order for multiple lensed images to be formed. However, it does not capture the correlation between the magnifications of the lensed images, and the correlation between the magnification and the time delay. For example, the relative magnification tends to unity if the lensed images are highly magnified [172]. In fact, one can derive a poor-man's prior distribution for the relative magnification, if we assume that the absolute magnification for each of the two images follows Eq. (11.38), with the form

$$p(\mu_{\rm rel}) = \begin{cases} \mu_{\rm rel} & \text{for } \mu_{\rm rel} \leq 1 \\ \mu_{\rm rel}^{-3} & \text{for } \mu_{\rm rel} > 1 \end{cases}, \tag{11.40}$$

where we give a detailed derivation in Appendix 11.9. The poor-man's prior distribution for the relative magnification models the correct power law scaling of $\mu_{\rm rel}^{-3}$ when $\mu_{\rm rel} \geq 1$, but predicts the wrong power law scaling when $\mu_{\rm rel} < 1$.

In addition, we use a simple analytical model for the optical depth [208, 182], which is the probability of strong lensing at a given redshift, with the form

$$\tau(z) = F \left( \frac{d_{\rm c}(z)}{d_{\rm H}} \right)^3, \tag{11.41}$$

where $d_{\rm c}(z)$ is the comoving distance at $z$, and $d_{\rm H}$ is the Hubble distance. The empirical constant $F$ is taken to be 0.0017 here [182]. A more realistic and

detailed model for the merger rate density, the magnification distribution, as well as the optical depth, that impart more astrophysical information to an analysis would certainly help differentiating lensed signals.

With this set of population models, we obtained a log-coherence ratio of $\log_{10} C = 2.7$, and a log-Bayes factor of $\log_{10} \mathcal{B}^{\mathcal{H}_{\rm L}}_{\mathcal{H}_{\rm NL}} = 1.1$ without accounting for the time delay.[13] We see that with this set of population models and the detector sensitivity, the selection effects down-weight the pair by a factor of $\approx 40$. Figure 11.6 shows both the 1D and 2D marginalized posterior distributions for $\left\{M^{\rm src}_{\rm tot}, q, \mu^{(1)}, \mu^{(2)}, \mu_{\rm rel}, z\right\}$ obtained using the algorithm described in Sec. 11.2.7. The orange solid lines show the correct values for each of the parameters if the redshift $z$ is set to 1. The plot shows that our two-step hierarchical procedure described in Sec. 11.2.6 is able to find the correct values describing the signals. From the plot we can also see the various degeneracies between parameters. For example, the degeneracy between the total mass $M^{\rm src}_{\rm tot}$ and the redshift $z$, where the blob in the lower left corner of Fig. 11.6 corresponds to the redshifted total mass that we do measure. Note that we are able to infer the mass ratio $q$ and the relative magnification $\mu_{\rm rel}$ as they are not degenerate with the redshift.

[13]This means that we set $p(\Delta t|\mathcal{H}_{\rm L})/p(\Delta t|\mathcal{H}_{\rm NL}) = 1$ such that the coherence ratios and the Bayes factors reported will *not be boosted* by setting the time-delay of the injected signals to be very consistent with the lensed hypothesis, though incorporating the time delay information would be important in actual analyses.

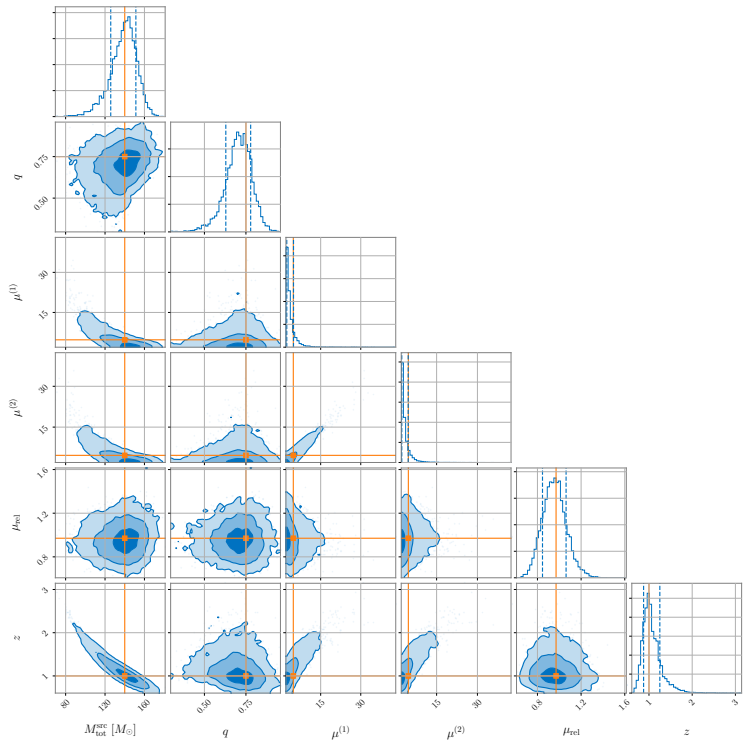

Figure 11.6: The 1D and 2D marginalized posterior distributions of $\left\{M_{\rm tot}^{\rm src}, q, \mu^{(1)}, \mu^{(2)}, \mu_{\rm rel}, z\right\}$ for Example 1 (cf. Sec. 11.3.3.1) obtained using the algorithm described in Sec. 11.2.7. The orange solid lines show the correct values for each of the parameters if the redshift $z$ is set to 1. The plot shows that our two-step hierarchical procedure described in Sec. 11.2.6 is able to find the correct values describing the signals. From the plot we can also see the various degeneracies between parameters. For example, the degeneracy between the total mass $M_{\rm tot}^{\rm src}$ and the redshift $z$, where the blob in the lower left corner corresponds to the redshifted total mass that we do measure. Note that we are able to infer the mass ratio $q$ and the relative magnification $\mu_{\rm rel}$ as they are not degenerate with the redshift.

Table 11.1: Summary of some of the injection parameters for Example 1 in Sec. 11.3.3.1. The two injected signals, when analyzed on their own, seem to originate from two separate mergers of an intermediate-mass binary black hole system. For more detailed definitions of some of the binary parameters, see Ref. [200].

| Parameter | Value |
|---|---|
| Redshifted total mass $M_{\rm tot}^{\rm det}$ | $280M_\odot$ |
| Mass ratio $q$ | 0.75 |
| Redshifted primary mass $m_1^{\rm det}$ | $160M_\odot$ |
| Redshifted secondary mass $m_2^{\rm det}$ | $120M_\odot$ |
| Dimensionless spin magnitude of the primary $\lvert\boldsymbol{\chi}_1\rvert$ | 0.3 |
| Dimensionless spin magnitude of the secondary $\lvert\boldsymbol{\chi}_2\rvert$ | 0.2 |
| Tilt angle between the spin vector of the primary and the orbital angular momentum vector | 0.1 rad |
| Tilt angle between the spin vector of the secondary and the orbital angular momentum vector | 0.2 rad |
| Azimuthal angle between the two spin vectors | 1.1 rad |
| Azimuthal angle of the cone of precession of the orbital angular momentum about the total angular momentum | 2.2 rad |
| Inclination angle between the total angular momentum and the line of sight | 1.04 rad |
| Right ascension $\alpha$ | 0.2 rad |
| Declination $\delta$ | 0.4 rad |
| Polarization angle $\psi$ | 0.6 rad |
| Phase at coalescence $\phi_{\rm c}$ | 0.8 rad |
| Apparent luminosity distance for the first signal $d_{\rm L}^{(1)}$ | 3.11 Gpc |
| Apparent luminosity distance for the second signal $d_{\rm L}^{(2)}$ | 3.15 Gpc |
| Image type of the first signal | I |
| Image type of the second signal | II |

If we instead use a population model that asserts there are no black holes with mass greater than $60M_\odot$, referred as "Model A" in Ref. [13], namely

$$p_{\rm src}(m_1^{\rm src}, m_2^{\rm src}|\alpha, \beta, m_{\rm min}, m_{\rm max}) = \begin{cases} \frac{1-\alpha}{m_{\rm max}^{1-\alpha} - m_{\rm min}^{1-\alpha}} (m_1^{\rm src})^{-\alpha} \frac{1+\beta}{(m_1^{\rm src})^{1+\beta} - m_{\rm min}^{1+\beta}} (m_2^{\rm src})^{\beta} & \text{if } m_{\rm min} \leq m_2^{\rm src} \leq m_1^{\rm src} \leq m_{\rm max} \\ 0 & \text{otherwise} \end{cases}, \tag{11.42}$$

with $\alpha = 1.8$, $\beta = 0$, $m_{\rm min} = 5\ M_\odot$, and $m_{\rm max} = 60\ M_\odot$[14], now both the log-coherence ratio and the log-Bayes factor are infinite, while the log evidence under the lensed hypothesis is finite. This is a "smoking-gun evidence" that the two signals are lensed. This is not surprising because the two signals are impossible under the not-lensed hypothesis with this set of population models. Under the not-lensed hypothesis, we interpret the apparent luminosity distance as the true luminosity distance without any magnification bias, allowing us to infer the redshift directly from the measured luminosity distance. In this case, the redshift that corresponds to the apparent luminosity distance of the first signal is roughly $z \approx 0.53$, meaning that both the primary and secondary mass would be above the $60M_\odot$ maximum. This example, though extreme, clearly shows that the Bayes factor, and hence one's interpretation on the origin, of the signals would be sensitive to the population models that one assumes.

#### 11.3.3.2 Example 2: Two lensed signals from a stellar-mass binary black hole merger

In the second example, we also have two lensed GW signals injected into two simulated data streams with Gaussian noise. However, this time the two signals

[14]Note that the numbers we adopted here are slightly different from the reported values in Ref. [13] because we write the model in the $(m_1^{\rm src}, m_2^{\rm src})$ parametrization here instead of the $(m_1^{\rm src}, q)$ parametrization. The probability density is hence off by a Jacobian of $1/m_1^{\rm src}$, which can be easily accounted for by adjusting the value of $\alpha$.

have a lower redshifted total mass ($M_{\rm tot}^{\rm det} = 60M_\odot$). Table 11.2 summarizes some of the waveform parameters. This example serves to represent typical scenarios for second-generation terrestrial GW detectors such as the two Advanced LIGO detectors [1] and the Advanced Virgo detector [2] observing stellar-mass BBH systems, and demonstrate how would the Bayes factor change with different detector sensitivities. For the population models, we use the same set of models in the last subsection with the "Model A" mass model described in Eq. (11.42).

Table 11.2: Summary of some of the injection parameters for Example 2 in Sec. 11.3.3.2. This example serves to represent typical scenarios for second-generation terrestrial GW detectors observing stellar-mass BBH systems. Parameters for this injection that are not listed explicitly below are identical to that listed in Table 11.1.

| Parameter | Value |
|---|---|
| Redshifted total mass $M_{\rm tot}^{\rm det}$ | $60M_\odot$ |
| Mass ratio $q$ | 0.875 |
| Redshifted primary mass $m_1^{\rm det}$ | $32M_\odot$ |
| Redshifted secondary mass $m_2^{\rm det}$ | $28M_\odot$ |
| Apparent luminosity distance for the first signal $d_{\rm L}^{(1)}$ | 811 Mpc |
| Apparent luminosity distance for the second signal $d_{\rm L}^{(2)}$ | 823 Mpc |

Figure 11.7 shows the marginalized 1D and 2D posterior distributions for $\left\{M_{\rm tot}^{\rm src}, q, \mu^{(1)}, \mu^{(2)}, \mu_{\rm rel}, z\right\}$ we recover when the two lensed signals were injected into data streams with simulated Gaussian noise recolored to match the aLIGO design sensitivity [100]. From the plot we see similar degenerate structures between parameters as in Fig. 11.6. To demonstrate the degeneracies more explicitly, we show the correct source parameters for this two signals if we assume the true source redshift is $z = 0.4$ (solid orange lines), as well as that if the true redshift is instead $z = 1$ (dotted gray lines). Note that both the mass ratio $q$ and the relative magnification $\mu_{\rm rel}$ take the same value when different source redshifts are

assumed. While we are not able to constrain the source parameters individually because of the aforementioned degeneracies, we are capable of providing joint constraints for the source parameters by properly incorporating information from both the detected signals and the astrophysical population models assumed. From Fig. 11.7, we see that it is less likely for the signals to come from a binary system with a total mass of $M_{\rm tot}^{\rm src} = 30M_{\odot}$ at a redshift $z = 1$ under the lensed hypothesis because of the large absolute magnifications required are less probable under the lens model we assumed in the analysis.

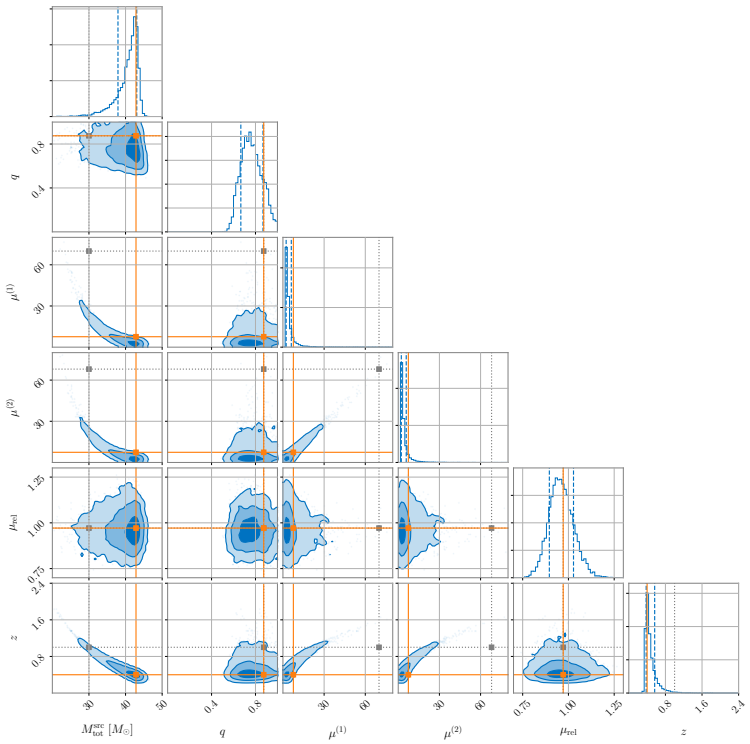

Figure 11.7: The 1D and 2D marginalized posterior distributions of $\left\{M_{\rm tot}^{\rm src}, q, \mu^{(1)}, \mu^{(2)}, \mu_{\rm rel}, z\right\}$ for Example 2 (cf. Sec. 11.3.3.2) obtained using the algorithm described in Sec. 11.2.7. The orange solid lines show the correct values for each of the parameters if the redshift is set to $z = 0.4$, while the gray dotted lines show the correct values for the parameters if the redshift is instead set to $z = 1$. Note that both the mass ratio $q$ and the relative magnification $\mu_{\rm rel}$ take the same value when different source redshifts are assumed. While we are not able to constrain the source parameters individually because of the degeneracies, we are capable of providing joint constraints for the source parameters by properly incorporating information from both the detected signals and the astrophysical population models assumed. We see that it is less likely for the signals to come from a binary system with a total mass of $M_{\rm tot}^{\rm src} = 30\ M_\odot$ at a redshift $z = 1$ under the lensed hypothesis because of the large absolute magnifications required are less probable under the lens model we assumed in the analysis.

For this example, we obtained a log-coherence ratio of $\log_{10} C = 5.2$ and a log-Bayes factor of $\log_{10} \mathcal{B}^{\mathcal{H}_{\rm L}}_{\mathcal{H}_{\rm NL}} = 3.0$ when injecting the signals into simulated Gaussian noise recolored to match the aLIGO design sensitivity [100]. Table 11.3 tabulates the values of $\log_{10} \alpha$, $\log_{10} \beta$, and $\log_{10} \left(\beta/\alpha^2\right)$ for this particular set of population models under different detector sensitivities, computed using `pdetclassifier` [209]. In Appendix 11.7, we give a detailed description on how one can compute these normalization constants, or selection functions, under the lensed and the not-lensed hypothesis. As expected, the values of $\alpha$

| | O1+O2 | O3a | aLIGO design |
|---|---|---|---|
| $\log_{10} \alpha$ | −3.5 | −3.1 | −2.4 |
| $\log_{10} \beta$ | −4.1 | −3.7 | −2.5 |
| $\log_{10} \left(\beta/\alpha^2\right)$ | 2.9 | 2.5 | 2.3 |

Table 11.3: The values of $\log_{10} \alpha(\boldsymbol{\lambda}, \mathcal{R})$, $\log_{10} \beta(\boldsymbol{\lambda}, \mathcal{R}, \boldsymbol{\gamma})$, and $\log_{10} \left[\beta(\boldsymbol{\lambda}, \mathcal{R}, \boldsymbol{\gamma})/\alpha(\boldsymbol{\lambda}, \mathcal{R})^2\right]$ with different detector sensitivities computed using `pdetclassifier` [209] for the population models described in Sec. 11.3.3.2.

and $\beta$ increase as the detector network becomes more sensitive and capable of detecting weaker signals. The difference between the values of $\alpha$ and $\beta$ narrows as the network increases in sensitivity, and that the selection effects penalize the lensed hypothesis to a lesser extent, roughly by a factor of $\sim \alpha$. While we did not perform the same injection test with simulated noise recolored to match the sensitivity during O1+O2 and O3a, we can reasonably expect the log-coherence ratio increases with a more sensitive detector network as we can better measure the waveform parameters to a higher precision. Therefore, the log-coherence ratio, as well as the log-Bayes factor would increase with the detector sensitivity given the same set of lensed signals.

### 11.3.4 Identifying the image types

When we consider only the dominant $\ell = |m| = 2$ modes and a nonprecessing binary system, the phasing effect due to strong lensing reduces to a shift in the observed phase at coalescence (or any reference orbital phase) [175, 176]. For

a GW signal from the merger of a precessing binary system with a significant contribution from higher-order modes, for example when the system is asymmetric in component masses and/or is inclined with respect to our line of sight, we can break the degeneracy between the phasing effect from strong lensing and the orbital phase. This allows us to identify the image type for each of the lensed signals. We demonstrate this by injecting signals with an asymmetric mass ratio $q \approx 0.3$ viewing at an angle of roughly 107 deg between the line of sight and the total angular momentum vector into simulated Gaussian noise at aLIGO design sensitivity using two different waveform models, `IMRPhenomXP` and `IMRPhenomXPHM` [199]. The former approximant, `IMRPhenomXP`, includes only the quadrupole ($\ell = 2$) radiation from a precessing binary system, while the latter approximant, `IMRPhenomXPHM`, includes both the quadrupole radiation and some of the higher multipoles ($\ell > 2$) from the precessing system. In both cases, the first injected lensed GW signal is of type I, while the second injected signal is of type II. Figure 11.8 shows the joint probability mass function of the image type inferred for the first signal $\Xi^{(1)}$ and that for the second signal $\Xi^{(2)}$. We see that when there are measurable contributions from higher modes, we are able to pin-point the type of each lensed image from the phasing effect (left panel of Fig. 11.8), breaking the degeneracy between the phasing effect from strong lensing and the shift in the orbital phase. This is in line with the findings reported in Ref. [171], where one can tell type-II images apart individually for third-generation detectors.

### 11.3.5 Improvement in localizing the source in the sky

Since we expect the lensed GW signals coming from the same source to have approximately identical sky locations, the signals should be better localized when analyzed jointly compared to the case when they are analyzed individually. This is because we gain information about the shared sky location from two data streams instead of just one. We demonstrate this using the inference results from Example 1 in Sec. 11.3.3.1. Figure 11.9 shows the 90% credible regions

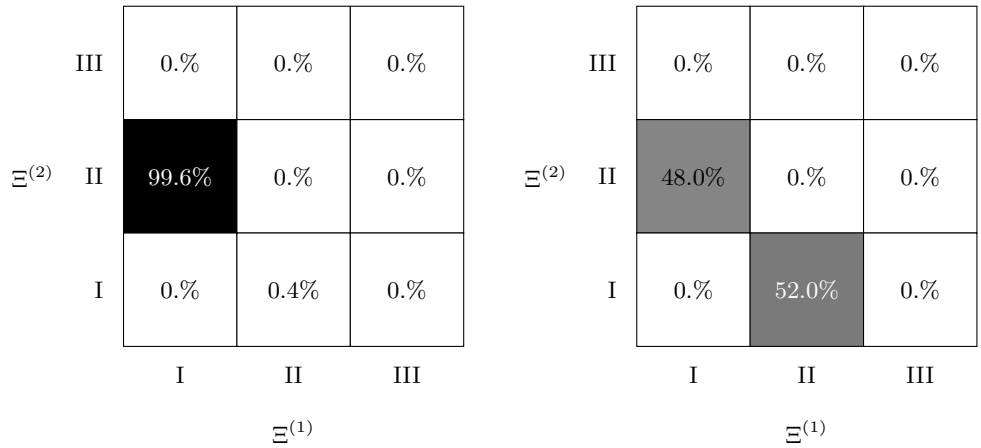


(a) Using `IMRPhenomXPHM` [199] waveform model. It includes some higher modes ($\ell > 2$) other than the quadrupole ($\ell = 2$) radiation.

(b) Using `IMRPhenomXP` [199] waveform model. It only models the quadrupole ($\ell = 2$) radiation.

Figure 11.8: The joint posterior probability mass function of the (discrete) image type for the first signal $\Xi^{(1)}$ and that for the second signal $\Xi^{(2)}$ in an injection test. In the test, we injected a type-I signal into the first data stream, and a type-II signal into the second data stream. We see that when there are measurable contributions from higher modes, we are able to pinpoint the type of each lensed image, breaking the degeneracy between the phasing effect from strong lensing and a shift in the orbital phase. This is in line with the findings in Ref. [171].

of the localization of signals, when analyzed separately (blue and green) and when analyzed jointly (orange). In all cases, the credible regions enclose the true source location (gray crosshair). However, the area of the 90% credible region, a metric for the localization uncertainty, from the joint inference is only 17 $\mathrm{deg}^2$, which is roughly two times smaller than that when localizing the first image only (31 $\mathrm{deg}^2$) and roughly four times smaller than that when localizing the second, fainter, image only (80 $\mathrm{deg}^2$).

Combining the improved sky localization of the source with the joint constraints of the source parameters (such as the redshift), one will be more informed when trying to locate the gravitational lens and the source electromagnetically (see, for

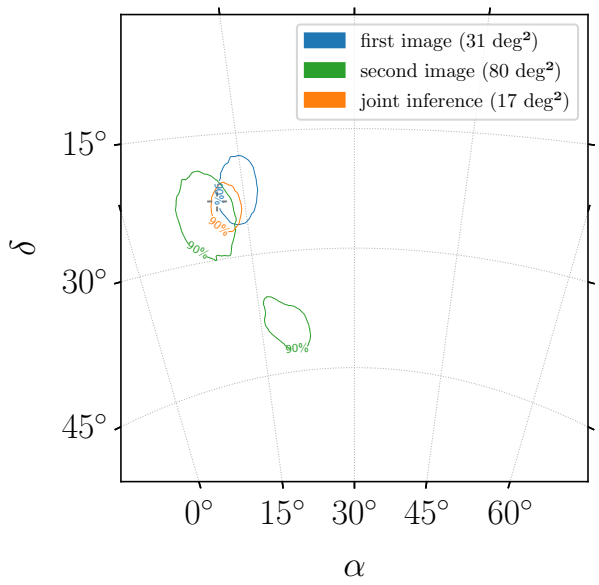


Figure 11.9: The sky localizations when two simulated lensed GW signals are analyzed jointly and when they are analyzed individually. The gray crosshair shows the injected values for the right ascension $\alpha$ and the declination $\delta$. The signals are better localized when analyzed jointly (area of the 90% credible region: 17 deg$^2$) compared to the case when they are analyzed individually (area of the 90% credible region: 31 deg$^2$ for the brighter image, 80 deg$^2$ for the fainter image) as expected [210] since we gain information about the shared sky location from two data streams instead of just one. The improvement in sky localization helps identifying the gravitational lens and the source electromagnetically [210, 211], and hence cross-validating the claim that the GW signals are indeed strongly lensed.

example, Ref. [210, 211]). Indeed, if we were able to identify the massive object responsible for the gravitational lensing and observe lensing of electromagnetic waves as well, that can serve as a cross-validation that the GW signals that were being analyzed are indeed strongly lensed. The lensed source could be by itself electromagnetically bright, for example a binary neutron star system or a

neutron-star-black-hole binary (though it is not expected to see lensed signals coming from these kind of sources with current-generation GW detectors as they have lower merger rates relative to BBH systems). If the lensed source is in a host which emits electromagnetic radiation, such as in a galaxy, one could search for possible foreground lenses (as the electromagnetic signature coming from the host should also be lensed by the same lens) within the joint localization region that would produce lensed GW signals with consistent absolute magnifications and time delays.

## 11.4 Strong lensing of gravitational waves from a binary black hole merger: observing only one lensed signal

The statistical framework can also be applied when only one GW signal (i.e., $N = 1$) is being analyzed at a time. In this case, the expression for the Bayes factor reads

$$\mathcal{B}^{\mathcal{H}_{\rm L}}_{\mathcal{H}_{\rm NL}} = \frac{\alpha(\boldsymbol{\lambda}, \mathcal{R})}{\beta(\boldsymbol{\lambda}, \mathcal{R}, \boldsymbol{\gamma})} \times \frac{\int \mathrm{d}\boldsymbol{\theta}^{(1)}_{\rm com}\, \mathrm{d}\boldsymbol{\theta}^{(1)}_{\rm ind}\; p(D^{(1)}|\boldsymbol{\theta}^{(1)}_{\rm ind}, \boldsymbol{\theta}^{(1)}_{\rm com}) p_{\rm pop,ind}(\boldsymbol{\theta}^{(1)}_{\rm ind}|\boldsymbol{\gamma}) p_{\rm pop,com}(\boldsymbol{\theta}^{(1)}_{\rm com}|\boldsymbol{\lambda}, \mathcal{R})}{\int \mathrm{d}\boldsymbol{\theta}^{(1)}\; p(D^{(1)}|\boldsymbol{\theta}^{(1)}, \mathcal{H}_{\rm NL}) p_{\rm pop}(\boldsymbol{\theta}^{(1)}|\boldsymbol{\lambda}, \mathcal{R})}, \tag{11.43}$$

where the normalization constant $\beta(\boldsymbol{\lambda}, \mathcal{R}, \boldsymbol{\gamma})$ for the case of $N = 1$ is defined accordingly. For BBH systems, the data generation process described in Fig. 11.4 for the not-lensed hypothesis, and that in Fig. 11.5 for the lensed hypothesis, are also applicable here. Compared with the case of $N = 2$ we discussed extensively in Sec. 11.3, the framework is less capable of differentiating a lensed BBH signal in the geometric optics limit from a signal that is not lensed. This is because effectively the framework is leveraging only the inconsistency of the signal with the given population models without the help of Occam's razor and selection effects. However, this will not be the case if gravitational lensing leaves distinctive signatures in the observed waveforms, for example when the geometric

optics approximation breaks down and the full wave optics treatment is needed [172, 174]. The framework can also be easily extended to handle GW lensing from BNS systems (see, for example, Ref. [212]) and NSBH systems.

Here we demonstrate the statistical framework when $N = 1$ with an example where a lensed BBH signal with waveform parameters identical to the first image of Example 1 in Sec. 11.3.3.1 (cf. Table 11.1) injected into simulated Gaussian noise recolored to the aLIGO design noise curve [100]. As we shall see, the framework is less capable of identifying a lensed BBH signal purely from its inconsistency with the population models, unless the models fail to produce such an observed signal (such as Example 1 in Sec. 11.3.3.1 with a source population model asserting that no black hole can have a mass greater than $60M_\odot$). This is very similar to the lensing analysis for GW190521 presented in Ref. [213], and the BNS lensing analysis in Ref. [212].

In this example, we first use the log-uniform distribution in Eq. (11.36) as the population model for the component masses, and use the same models for spin, magnification, optical depth, and merger rate density as in Sec. 11.3.3.1. Figure 11.10 shows the marginalized 1D and 2D posterior distributions of $\left\{M_{\rm tot}^{\rm src}, q, \mu^{(1)}, z\right\}$, again using the Gibbs sampling algorithm described in Sec. 11.2.7. The orange solid lines show the correct values for each of the parameters if the redshift $z$ is set to 1. Similar to the case with $N = 2$ in Fig. 11.6, we observe similar degenerate structures such as that between $M_{\rm tot}^{\rm src}$ and $z$. However, the uncertainty in the joint $M_{\rm tot}^{\rm src} - z$ constraint here when $N = 1$ is greater compared to that in Fig. 11.6. This can be attributed to the less constraining measurements of the redshifted masses when there is only one data stream to infer from, instead of two data streams as in the case for Fig. 11.6.

With this set of population models, we obtained a log-coherence ratio of $\log_{10} C = 0.06$, and a log-Bayes factor of $\log_{10} \mathcal{B}^{\mathcal{H}_{\rm L}}_{\mathcal{H}_{\rm NL}} = 0.08$. The Bayes factor here is not statistically significant and within the statistical uncertainty from using nested sampling. Given the rarity of strong lensing, reflected in the prior odds, the strong

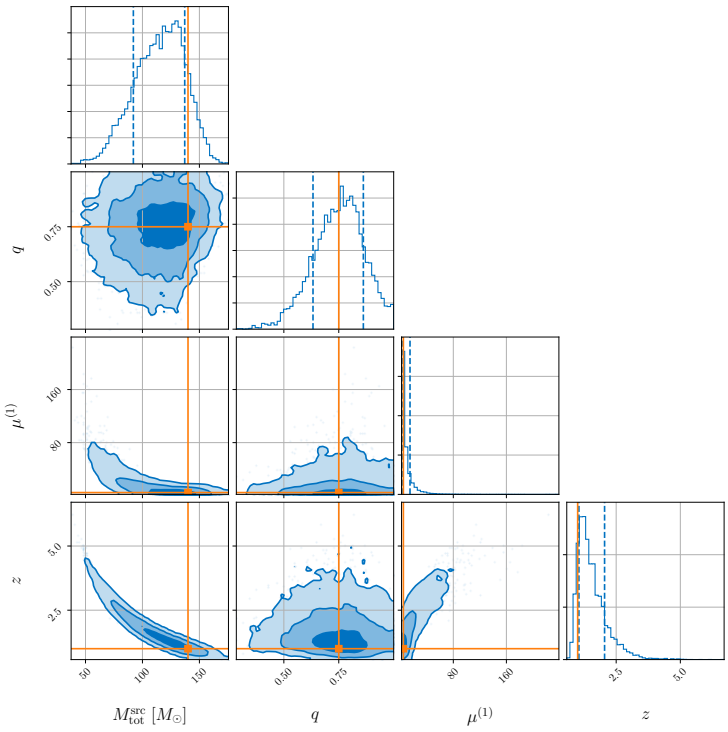


Figure 11.10: The 1D and 2D marginalized posterior distributions of $\{M_{\rm tot}^{\rm src}, q, \mu^{(1)}, z\}$ for the example in Sec. 11.4 obtained using the algorithm described in Sec. 11.2.7. The orange solid lines show the correct values for each of the parameters if the redshift $z$ is set to 1. Similar to the case with $N = 2$ in Fig. 11.6, we observe similar degenerate structures such as that between $M_{\rm tot}^{\rm src}$ and $z$. However, the uncertainty in the joint $M_{\rm tot}^{\rm src} - z$ constraint here when $N = 1$ is greater compared with that in Fig. 11.6. This can be attributed to the less constraining measurements of the redshifted masses when there is only one data stream to infer from, instead of two data streams as in the case for Fig. 11.6.

lensing hypothesis will easily be dismissed with the small posterior odds. While the above example might give a pessimistic impression for identifying strongly lensed BBH signals individually, this does not have to be the case, especially if the signals are of type II, where we might be able to identify them from the distortion to the waveforms due to lensing, for example from the extra Morse

phase [171], or other frequency-dependent wave optics effects.

## 11.5 Conclusions and outlook

In this paper, we present a Bayesian statistical framework for identifying strongly lensed GW signals. By modeling the data generation processes for $N$ observed signals assuming that they are lensed images from the same source and that they are simply $N$ signals from $N$ different sources, respectively, we are able to write down an expression for the Bayes factor which quantifies the ratio of the probability densities of observing the $N$ signals given the two scenarios and the astrophysical models on the properties of the sources and lenses. Selection effects are accounted for naturally as we normalize the probability densities. Combined with the prior odds, we can properly interpret the resultant posterior odds as the ratio of the probability that the $N$ signals are strongly lensed versus not lensed.

In order to compute the marginalization integral for the Bayes factor more efficiently, we present a hierarchical scheme to evaluate the integral over the source redshift separately, breaking down the high-dimensional integral into an integral with a lower dimension and smaller degeneracy among variables that can be computed using Monte Carlo methods such as in Ref. [120], plus a 1D integral over the redshift that can be efficiently evaluated. The true source parameters can be inferred after the hierarchical analysis using a Gibbs sampling algorithm.

We demonstrate the framework with examples when $N = 1$ and $N = 2$, respectively. We show explicitly how changing the assumed astrophysical models can alter one's interpretation on the origin of the observed signals, and sometimes can lead to smoking-gun evidence of strong lensing of GW. For the case of $N = 2$, we also show how one can jointly constrain the total mass and the redshift of the source. Together with the improvement in localizing the source from observing two images, it helps locating the source and the lens electromagnetically [210, 211], and ultimately cross-validating the GW lensing analysis. In some cases where higher multipoles of lensed GW signals are observable, the Morse index, or the type, of the lensed images can be identified.

Currently, one of the key assumptions of the framework is that all $N$ triggers are of astrophysical origins. This might not be the case when we perform a targeted search on subthreshold lensed counterparts [168, 189, 183], especially for a high-mass GW signal. This is because transient noise fluctuations in the detectors, or glitches, can easily mimic these short-duration high-mass signals. In this case, unfortunately, the Occam's razor is working against us as the lensed hypothesis will have a similar goodness-of-fit to the glitches compared to the not lensed hypothesis while having fewer free parameters. The assumption can be relaxed where some of the $N$ triggers are of terrestrial origins. However, this would require a detailed study of the morphology of the glitches and we leave this to future work.

While detecting strongly lensed GW signals are exciting in its own right, it can also be used to improve our understanding on various subjects in fundamental physics, astrophysics and cosmology. For example, observing the strongly lensed GW signals from the same source multiple times effectively boosts the number of "virtual GW detectors", and hence can be used to better constrain the polarization contents of the GW signals and test the general relativity [214]. Strongly lensed GW signals also allow us to probe further to study for example stellar environments at higher redshift through the spin alignment of the lensed binaries [215], and origins of the binaries at high redshift [216, 217]. With the statistical framework presented in this paper, which directly ingests models from the astrophysics community, the GW data analysis community can work closer together with the astrophysical modeling community on finding lensed GWs and extracting more science from them.

**Acknowledgments**

The authors would like to thank Tjonnie G. F. Li, Will Farr, Masamune Oguri, Alan Weinstein, Yanbei Chen, Katerina Chatziioannou, Colm Talbot, and Ken K. Y. Ng for the discussion and the help when preparing this paper. R. K. L. L. acknowledges support from the Croucher Foundation. R. K. L. L also acknowledges

support from NSF Awards No. PHY-1912594, No. PHY-2207758. I. M. H. is supported by the NSF Graduate Research Fellowship Program under Grant No. DGE-17247915. The computations presented here were conducted on the Caltech High Performance Cluster partially supported by a grant from the Gordon and Betty Moore Foundation. I. M. H. also acknowledges support from NSF Awards No. PHY-1607585, No. PHY-1912649, No. PHY-1806990, and No. PHY-2207728. The authors are also grateful for computational resources provided by the LIGO Laboratory and supported by National Science Foundation Grants PHY-0757058 and PHY-0823459. Figs. 11.1, 11.2, 11.4, and 11.5 were generated using `BayesNet`. Figures 11.6, 11.7, and 11.10 were generated using `corner.py` [137]. This is LIGO Document No. P1900058.

## 11.6 Appendix: Full derivation of the probability densities of observing a set of data under various hypotheses

In this section, we give the full derivation for the probability densities of observing a set of data $\boldsymbol{D}$ under the lensed hypothesis $\mathcal{H}_{\rm L}$ and the not-lensed hypothesis $\mathcal{H}_{\rm NL}$, accounting for both the astrophysical information on sources and lenses, and well as selection effects. This would in turn allow us to write down the expression for the (proper) Bayes factor and hence the posterior odds for identifying strongly lensed gravitational-wave signals. The derivations below follow Ref. [195] closely.

### 11.6.1 Under the not-lensed hypothesis $\mathcal{H}_{\rm NL}$

Now let us find the expression for the probability density $p(\boldsymbol{D}|\mathcal{H}_{\rm NL}, \boldsymbol{\lambda}, \mathcal{R})$ under the not-lensed hypothesis $\mathcal{H}_{\rm NL}$. Since each of the observed data in the data set $\boldsymbol{D} = \{D^{(i)}\}_{i=1}^{i=N}$ is simply one random draw from the population distribution $p_{\rm pop}$, we can factorize the probability density into $N$ terms as

$$p(\boldsymbol{D}|\mathcal{H}_{\rm NL}, \boldsymbol{\lambda}, \mathcal{R}) \propto \prod_{i=1}^{N} p(D^{(i)}|\mathcal{H}_{\rm NL}, \boldsymbol{\lambda}, \mathcal{R}). \tag{11.44}$$

Using the marginalization rule, we can write the term $p(D^{(i)}|\mathcal{H}_{\rm NL}, \boldsymbol{\lambda}, \mathcal{R})$ as

$$\begin{aligned} &p(D^{(i)}|\mathcal{H}_{\rm NL}, \boldsymbol{\lambda}, \mathcal{R}) \\ &\propto \int \mathrm{d}\boldsymbol{\theta}^{(i)}\ p(D^{(i)}|\boldsymbol{\theta}^{(i)})\ p_{\rm pop}(\boldsymbol{\theta}^{(i)}|\mathcal{H}_{\rm NL}, \boldsymbol{\lambda}, \mathcal{R}), \end{aligned} \tag{11.45}$$

where this integral can be estimated using nested sampling [120] in a so-called parameter estimation (PE) run. In a PE run, the goal is to obtain a set of posterior samples for $\boldsymbol{\theta}^{(i)}$ that follow the posterior distribution

$$p(\boldsymbol{\theta}^{(i)}|D^{(i)}) = \frac{p(D^{(i)}|\boldsymbol{\theta}^{(i)})p_{\rm PE}(\boldsymbol{\theta}^{(i)})}{Z^{(i)}}, \tag{11.46}$$

where $p_{\rm PE}$ is the sampling prior distribution used in that particular PE run, and $Z^{(i)}$ is the evidence under the particular signal hypothesis in that PE (or equivalently a normalization constant). Note that we can rearrange Eq. (11.45) to get

$$\begin{aligned} &p(D^{(i)}|\mathcal{H}_{\rm NL}, \boldsymbol{\lambda}, \mathcal{R}) \\ &\propto \int \mathrm{d}\boldsymbol{\theta}^{(i)}\ p(D^{(i)}|\boldsymbol{\theta}^{(i)})\ p_{\rm pop}(\boldsymbol{\theta}^{(i)}|\mathcal{H}_{\rm NL}, \boldsymbol{\lambda}, \mathcal{R}) \\ &= \int \mathrm{d}\boldsymbol{\theta}^{(i)}\ p(\boldsymbol{\theta}^{(i)}|D^{(i)})\ Z^{(i)} \frac{p_{\rm pop}(\boldsymbol{\theta}^{(i)}|\mathcal{H}_{\rm NL}, \boldsymbol{\lambda}, \mathcal{R})}{p_{\rm PE}(\boldsymbol{\theta}^{(i)})} \\ &\approx \langle Z^{(i)} \frac{p_{\rm pop}(\boldsymbol{\theta}^{(i)}|\mathcal{H}_{\rm NL}, \boldsymbol{\lambda}, \mathcal{R})}{p_{\rm PE}(\boldsymbol{\theta}^{(i)})} \rangle, \end{aligned} \tag{11.47}$$

where $\langle \cdots \rangle$ denotes an average over posterior samples for $\boldsymbol{\theta}^{(i)}$. This means that we can obtain the unnormalized probability density as

$$p(\boldsymbol{D}|\mathcal{H}_{\rm NL}, \boldsymbol{\lambda}, \mathcal{R}) \propto \prod_{i=1}^{N} Z^{(i)} \langle \frac{p_{\rm pop}(\boldsymbol{\theta}^{(i)}|\mathcal{H}_{\rm NL}, \boldsymbol{\lambda}, \mathcal{R})}{p_{\rm PE}(\boldsymbol{\theta}^{(i)})} \rangle. \tag{11.48}$$

Now, we will need to obtain the normalization constant, denoted as $\tilde{\alpha}$, by requiring that when summed over all observable data sets Eq. (11.44) sums to unity, i.e.,

$$\frac{1}{\tilde{\alpha}} \int_{\text{all obs. data}} \mathrm{d}^N \boldsymbol{D} \prod_{i=1}^{N} p(D^{(i)}|\mathcal{H}_{\rm NL}, \boldsymbol{\lambda}, \mathcal{R}) = 1. \tag{11.49}$$

Since the likelihood function $p(D^{(i)}|\mathcal{H}_{\rm NL}, \boldsymbol{\lambda}, \mathcal{R})$ is independent of each other, we have

$$\begin{aligned}\tilde{\alpha} &= \int_{\text{all obs. data}} \mathrm{d}^N \boldsymbol{D} \prod_{i=1}^{N} p(D^{(i)}|\mathcal{H}_{\rm NL}, \boldsymbol{\lambda}, \mathcal{R}) \\ &= \prod_{i=1}^{N} \underbrace{\int_{\text{all obs. data}} \mathrm{d}D^{(i)}\ p(D^{(i)}|\boldsymbol{\lambda}, \mathcal{R})}_{\text{Selection function } \alpha(\boldsymbol{\lambda},\mathcal{R})} \\ &= \alpha(\boldsymbol{\lambda}, \mathcal{R})^N,\end{aligned} \tag{11.50}$$

where $\alpha(\boldsymbol{\lambda}, \mathcal{R}) \equiv \int_{\text{all obs. data}} \mathrm{d}D^{(i)}\ p(D^{(i)}|\boldsymbol{\lambda}, \mathcal{R})$ is known as the selection function or detectable fraction for the population model parametrized by $\boldsymbol{\lambda}$ with a merger rate density $\mathcal{R}$. We can write the selection function $\alpha(\boldsymbol{\lambda}, \mathcal{R})$ as an integral over all observable data and the event-level parameters $\boldsymbol{\theta}^{(i)}$ as

$$\begin{aligned}\alpha(\boldsymbol{\lambda}, \mathcal{R}) &= \int_{\text{all obs. data}} \mathrm{d}D^{(i)} \\ &\quad \times \int \mathrm{d}\boldsymbol{\theta}^{(i)}\ p(D^{(i)}|\boldsymbol{\theta}^{(i)})\ p_{\rm pop}(\boldsymbol{\theta}^{(i)}|\mathcal{H}_{\rm NL}, \boldsymbol{\lambda}, \mathcal{R}) \\ &= \int \mathrm{d}\boldsymbol{\theta}^{(i)}\ \underbrace{\left(\int_{\text{all obs. data}} \mathrm{d}D^{(i)}\ p(D^{(i)}|\boldsymbol{\theta}^{(i)})\right)}_{\text{detection probability } p_{\rm det}(\boldsymbol{\theta}=\boldsymbol{\theta}^{(i)})} \\ &\quad \times p_{\rm pop}(\boldsymbol{\theta}^{(i)}|\mathcal{H}_{\rm NL}, \boldsymbol{\lambda}, \mathcal{R}) \\ &= \int \mathrm{d}\boldsymbol{\theta}^{(i)}\ p_{\rm det}(\boldsymbol{\theta}^{(i)})\ p_{\rm pop}(\boldsymbol{\theta}^{(i)}|\mathcal{H}_{\rm NL}, \boldsymbol{\lambda}, \mathcal{R}),\end{aligned} \tag{11.51}$$

where $p_{\rm det}(\boldsymbol{\theta})$ is known as the detection probability. The detection probability can be obtained semianalytically, or empirically estimated by performing an injection campaign [218, 219, 13, 192]. In Appendix 11.7.1, we give more details on the numerical computation of the selection function $\alpha$.

To conclude, the full expression of the probability of observing the data set $\boldsymbol{D}$ under the not-lensed hypothesis is given by

$$\begin{aligned} &p(\boldsymbol{D}|\mathcal{H}_{\rm NL}, \boldsymbol{\lambda}, \mathcal{R}) \\ &= \frac{1}{\alpha(\boldsymbol{\lambda}, \mathcal{R})^N} \prod_{i=1}^{N} p(D^{(i)}|\mathcal{H}_{\rm NL}, \boldsymbol{\lambda}, \mathcal{R}). \end{aligned} \tag{11.52}$$

### 11.6.2 Under the lensed hypothesis $\mathcal{H}_{\rm L}$

For the lensed hypothesis $\mathcal{H}_{\rm L}$, we only make *one* random draw from the source population distribution $p_{\rm src}$, and $N$ random draws of the parameters of the lensed images from the lens population distribution $p_{\rm lens}$.

Using the marginalization rule, we write the probability of observing the data set $\boldsymbol{D}$ under this hypothesis as

$$\begin{aligned} &p(\boldsymbol{D}|\mathcal{H}_{\rm L}, \boldsymbol{\lambda}, \mathcal{R}, \boldsymbol{\gamma}) \\ &\propto \int \mathrm{d}\boldsymbol{\theta}^{(1)} \cdots \mathrm{d}\boldsymbol{\theta}^{(N)}\ p(\boldsymbol{\theta}^{(1)}, ..., \boldsymbol{\theta}^{(N)}|\mathcal{H}_{\rm L}, \boldsymbol{\lambda}, \mathcal{R}, \boldsymbol{\gamma}) \\ &\times p(\boldsymbol{D}|\boldsymbol{\theta}^{(1)}, ..., \boldsymbol{\theta}^{(N)}, \mathcal{H}_{\rm L}, \boldsymbol{\lambda}, \mathcal{R}, \boldsymbol{\gamma}). \end{aligned} \tag{11.53}$$

Recall that we partition the event-level parameters $\boldsymbol{\theta}^{(i)}$ into common parameters $\boldsymbol{\theta}_{\rm com}$ and independent parameters $\boldsymbol{\theta}_{\rm ind}$. As a result, we can write the probability density as

$$\begin{aligned} &p(\boldsymbol{D}|\mathcal{H}_{\rm L}, \boldsymbol{\lambda}, \mathcal{R}, \boldsymbol{\gamma}) \\ &\propto \int \mathrm{d}\boldsymbol{\theta}^{(1)}_{\rm com}\ \mathrm{d}\boldsymbol{\theta}^{(1)}_{\rm ind} \cdots \mathrm{d}\boldsymbol{\theta}^{(N)}_{\rm com} \mathrm{d}\boldsymbol{\theta}^{(N)}_{\rm ind}\ p(\boldsymbol{D}|\boldsymbol{\theta}^{(1)}, ..., \boldsymbol{\theta}^{(N)}) \\ &\times p(\boldsymbol{\theta}^{(1)}_{\rm com}, ..., \boldsymbol{\theta}^{(N)}_{\rm com}|\mathcal{H}_{\rm L}, \boldsymbol{\lambda}, \mathcal{R}, \boldsymbol{\gamma}) \\ &\times p(\boldsymbol{\theta}^{(1)}_{\rm ind}, ..., \boldsymbol{\theta}^{(N)}_{\rm ind}|\boldsymbol{\theta}^{(1)}_{\rm com}, ..., \boldsymbol{\theta}^{(N)}_{\rm com}, \mathcal{H}_{\rm L}, \boldsymbol{\lambda}, \mathcal{R}, \boldsymbol{\gamma}). \end{aligned} \tag{11.54}$$

We expect the common parameters to be the same across the $N$ events, and that the independent parameters $\boldsymbol{\theta}_{\rm ind}$ to be distributed according to the same lens population distribution, i.e., $\boldsymbol{\theta}_{\rm ind} \sim p_{\rm pop,ind}(\boldsymbol{\theta}_{\rm ind}|\boldsymbol{\gamma})$. We also assume they are

independent of the common parameters. Therefore, we have

$$\begin{aligned}
&p(\boldsymbol{D}|\mathcal{H}_{\rm L},\boldsymbol{\lambda},\mathcal{R},\boldsymbol{\gamma})\\
&\propto \int \mathrm{d}\boldsymbol{\theta}^{(1)}_{\rm com}\,\mathrm{d}\boldsymbol{\theta}^{(1)}_{\rm ind}\cdots\mathrm{d}\boldsymbol{\theta}^{(N)}_{\rm com}\,\mathrm{d}\boldsymbol{\theta}^{(N)}_{\rm ind}\;p(\boldsymbol{D}|\boldsymbol{\theta}^{(1)},...,\boldsymbol{\theta}^{(N)})\\
&\times p_{\rm pop,ind}(\boldsymbol{\theta}^{(1)}_{\rm ind},...,\boldsymbol{\theta}^{(N)}_{\rm ind}|\boldsymbol{\gamma})p_{\rm pop,com}(\boldsymbol{\theta}^{(1)}_{\rm com}|\boldsymbol{\lambda},\mathcal{R})\\
&\times \delta(\boldsymbol{\theta}^{(2)}_{\rm com}-\boldsymbol{\theta}^{(1)}_{\rm com})\cdots\delta(\boldsymbol{\theta}^{(N)}_{\rm com}-\boldsymbol{\theta}^{(1)}_{\rm com}),
\end{aligned} \tag{11.55}$$

where we impose the $(N-1)$ Dirac-delta distribution to enforce the common parameters to be the same across the $N$ events, reducing the dimension of the integral. Now the expression simplifies to

$$\begin{aligned}
&p(\boldsymbol{D}|\mathcal{H}_{\rm L},\boldsymbol{\lambda},\mathcal{R},\boldsymbol{\gamma})\\
&\propto \int \mathrm{d}\boldsymbol{\theta}^{(1)}_{\rm com}\,\mathrm{d}\boldsymbol{\theta}^{(1)}_{\rm ind}\cdots\mathrm{d}\boldsymbol{\theta}^{(N)}_{\rm ind}\,p(\boldsymbol{D}|\boldsymbol{\theta}^{(1)}_{\rm ind},...,\boldsymbol{\theta}^{(N)}_{\rm ind},\boldsymbol{\theta}^{(1)}_{\rm com})\\
&\times p_{\rm pop,ind}(\boldsymbol{\theta}^{(1)}_{\rm ind},...,\boldsymbol{\theta}^{(N)}_{\rm ind}|\boldsymbol{\gamma})p_{\rm pop,com}(\boldsymbol{\theta}^{(1)}_{\rm com}|\boldsymbol{\lambda},\mathcal{R}).
\end{aligned} \tag{11.56}$$

Note that the joint-likelihood function can still be factorized as

$$\begin{aligned}
&p(\boldsymbol{D}|\boldsymbol{\theta}^{(1)}_{\rm ind},...,\boldsymbol{\theta}^{(N)}_{\rm ind},\boldsymbol{\theta}^{(1)}_{\rm com})\\
&\propto p(D^{(1)}|\boldsymbol{\theta}^{(1)}_{\rm ind},\boldsymbol{\theta}^{(1)}_{\rm com})\cdots p(D^{(N)}|\boldsymbol{\theta}^{(N)}_{\rm ind},\boldsymbol{\theta}^{(1)}_{\rm com}).
\end{aligned} \tag{11.57}$$

Therefore, we have

$$\begin{aligned}
&p(\boldsymbol{D}|\mathcal{H}_{\rm L},\boldsymbol{\lambda},\mathcal{R},\boldsymbol{\gamma})\\
&\propto \int \mathrm{d}\boldsymbol{\theta}^{(1)}_{\rm com}\,\mathrm{d}\boldsymbol{\theta}^{(1)}_{\rm ind}\cdots\mathrm{d}\boldsymbol{\theta}^{(N)}_{\rm ind}\;p(D^{(1)}|\boldsymbol{\theta}^{(1)}_{\rm ind},\boldsymbol{\theta}^{(1)}_{\rm com})\cdots\\
&\times p(D^{(N)}|\boldsymbol{\theta}^{(N)}_{\rm ind},\boldsymbol{\theta}^{(1)}_{\rm com})\\
&\times p_{\rm pop,ind}(\boldsymbol{\theta}^{(1)}_{\rm ind},...,\boldsymbol{\theta}^{(N)}_{\rm ind}|\boldsymbol{\gamma})p_{\rm pop,com}(\boldsymbol{\theta}^{(1)}_{\rm com}|\boldsymbol{\lambda},\mathcal{R}).
\end{aligned} \tag{11.58}$$

To evaluate the evidence integral above, one can use nested sampling [120] to perform a joint-parameter estimation across the $N$ events with the chosen source and lens population distribution, as well as Dirac-delta prior distribution

to enforce the common parameters to be the same across the events. In particular, we choose the likelihood function $\mathcal{L}_{\text{joint-PE}}$ in a joint-PE run as

$$\begin{aligned}\mathcal{L}_{\text{joint-PE}} &= p(D^{(1)}|\boldsymbol{\theta}^{(1)}_{\text{ind}}, \boldsymbol{\theta}^{(1)}_{\text{com}}) \cdots p(D^{(N)}|\boldsymbol{\theta}^{(N)}_{\text{ind}}, \boldsymbol{\theta}^{(1)}_{\text{com}}) \\ &= \prod_{j=1}^{N} p(D^{(j)}|\boldsymbol{\theta}^{(j)}_{\text{ind}}, \boldsymbol{\theta}^{(1)}_{\text{com}}),\end{aligned} \tag{11.59}$$

and with the joint prior distribution $p_{\text{joint-PE}} = p_{\text{joint-PE}}(\boldsymbol{\theta}^{(1)}_{\text{ind}}, ..., \boldsymbol{\theta}^{(N)}_{\text{ind}}, \boldsymbol{\theta}^{(1)}_{\text{com}})$ with parameters $\{\boldsymbol{\theta}^{(1)}_{\text{com}}, \boldsymbol{\theta}^{(1)}_{\text{ind}}, ..., \boldsymbol{\theta}^{(N)}_{\text{ind}}\}$ being sampled over in the joint-PE run.

Still, we will need to find the overall normalization constant $\beta$ by again requiring when summed over all observable data sets that

$$\begin{aligned}1 =& \int_{\text{all obs. data}} \mathrm{d}^N \boldsymbol{D}\ p(\boldsymbol{D}|\mathcal{H}_{\text{L}}, \boldsymbol{\lambda}, \mathcal{R}, \boldsymbol{\gamma}) \\ =& \frac{1}{\beta} \int_{\text{all obs. data}} \mathrm{d}^N \boldsymbol{D} \int \mathrm{d}\boldsymbol{\theta}^{(1)}_{\text{com}}\ \mathrm{d}\boldsymbol{\theta}^{(1)}_{\text{ind}} \cdots \mathrm{d}\boldsymbol{\theta}^{(N)}_{\text{ind}} \\ & \Big[\ p(D^{(1)}|\boldsymbol{\theta}^{(1)}_{\text{ind}}, \boldsymbol{\theta}^{(1)}_{\text{com}}) \cdots p(D^{(N)}|\boldsymbol{\theta}^{(N)}_{\text{ind}}, \boldsymbol{\theta}^{(1)}_{\text{com}}) \\ & \times p_{\text{pop,ind}}(\boldsymbol{\theta}^{(1)}_{\text{ind}}, ..., \boldsymbol{\theta}^{(N)}_{\text{ind}}|\boldsymbol{\gamma}) p_{\text{pop,com}}(\boldsymbol{\theta}^{(1)}_{\text{com}}|\boldsymbol{\lambda}, \mathcal{R})\ \Big] \\ \beta =& \int_{\text{all obs. data}} \mathrm{d}^N \boldsymbol{D} \int \mathrm{d}\boldsymbol{\theta}^{(1)}_{\text{com}}\ \mathrm{d}\boldsymbol{\theta}^{(1)}_{\text{ind}} \cdots \mathrm{d}\boldsymbol{\theta}^{(N)}_{\text{ind}} \\ & p(D^{(1)}|\boldsymbol{\theta}^{(1)}_{\text{ind}}, \boldsymbol{\theta}^{(1)}_{\text{com}}) \cdots p(D^{(N)}|\boldsymbol{\theta}^{(N)}_{\text{ind}}, \boldsymbol{\theta}^{(1)}_{\text{com}}) \\ & \times p_{\text{pop,ind}}(\boldsymbol{\theta}^{(1)}_{\text{ind}}, ..., \boldsymbol{\theta}^{(N)}_{\text{ind}}|\boldsymbol{\gamma}) p_{\text{pop,com}}(\boldsymbol{\theta}^{(1)}_{\text{com}}|\boldsymbol{\lambda}, \mathcal{R}).\end{aligned} \tag{11.60}$$

The normalization constant $\beta = \beta(\boldsymbol{\lambda}, \mathcal{R}, \boldsymbol{\gamma})$ can be viewed as a function of the population models. We can further write this "lensing selection function" as

$$
\begin{aligned}
&\beta(\boldsymbol{\lambda}, \mathcal{R}, \boldsymbol{\gamma}) \\
&= \int_{\text{all obs. data}} \mathrm{d}^N \boldsymbol{D} \int \mathrm{d}\boldsymbol{\theta}^{(1)}_{\text{com}}\, \mathrm{d}\boldsymbol{\theta}^{(1)}_{\text{ind}} \cdots \mathrm{d}\boldsymbol{\theta}^{(N)}_{\text{ind}} \\
&\times p(D^{(1)}|\boldsymbol{\theta}^{(1)}_{\text{ind}}, \boldsymbol{\theta}^{(1)}_{\text{com}}) \cdots p(D^{(N)}|\boldsymbol{\theta}^{(N)}_{\text{ind}}, \boldsymbol{\theta}^{(1)}_{\text{com}}) \\
&\times p_{\text{pop,ind}}(\boldsymbol{\theta}^{(1)}_{\text{ind}}, ..., \boldsymbol{\theta}^{(N)}_{\text{ind}}|\boldsymbol{\gamma}) p_{\text{pop,com}}(\boldsymbol{\theta}^{(1)}_{\text{com}}|\boldsymbol{\lambda}, \mathcal{R}) \\
&= \int \mathrm{d}\boldsymbol{\theta}^{(1)}_{\text{com}}\, \mathrm{d}\boldsymbol{\theta}^{(1)}_{\text{ind}} \cdots \mathrm{d}\boldsymbol{\theta}^{(N)}_{\text{ind}} \\
&\times \underbrace{\left( \int_{\text{all obs. data}} dD^{(1)}\; p(D^{(1)}|\boldsymbol{\theta}^{(1)}_{\text{ind}}, \boldsymbol{\theta}^{(1)}_{\text{com}}) \right)}_{p_{\text{det}}(\boldsymbol{\theta}=\boldsymbol{\theta}^{(1)}_{\text{com}} \cup \boldsymbol{\theta}^{(1)}_{\text{ind}})} \\
&\times \cdots \\
&\times \underbrace{\left( \int_{\text{all obs. data}} \mathrm{d}D^{(N)}\; p(D^{(N)}|\boldsymbol{\theta}^{(N)}_{\text{ind}}, \boldsymbol{\theta}^{(1)}_{\text{com}}) \right)}_{p_{\text{det}}(\boldsymbol{\theta}=\boldsymbol{\theta}^{(1)}_{\text{com}} \cup \boldsymbol{\theta}^{(N)}_{\text{ind}})} . \\
&\times p_{\text{pop,ind}}(\boldsymbol{\theta}^{(1)}_{\text{ind}}, ..., \boldsymbol{\theta}^{(N)}_{\text{ind}}|\boldsymbol{\gamma}) p_{\text{pop,com}}(\boldsymbol{\theta}^{(1)}_{\text{com}}|\boldsymbol{\lambda}, \mathcal{R}). \\
&= \int \mathrm{d}\boldsymbol{\theta}^{(1)}_{\text{com}}\, \mathrm{d}\boldsymbol{\theta}^{(1)}_{\text{ind}} \cdots \mathrm{d}\boldsymbol{\theta}^{(N)}_{\text{ind}} \left[ \prod_{j=1}^{N} p_{\text{det}}(\boldsymbol{\theta} = \boldsymbol{\theta}^{(j)}_{\text{com}} \cup \boldsymbol{\theta}^{(1)}_{\text{ind}}) \right] \\
&\times p_{\text{pop,ind}}(\boldsymbol{\theta}^{(1)}_{\text{ind}}, ..., \boldsymbol{\theta}^{(N)}_{\text{ind}}|\boldsymbol{\gamma}) p_{\text{pop,com}}(\boldsymbol{\theta}^{(1)}_{\text{com}}|\boldsymbol{\lambda}, \mathcal{R}).
\end{aligned}
\tag{11.61}
$$

Therefore, in order to evaluate the lensing selection function $\beta$, we will need to perform a (possibly Monte Carlo) integration, evaluated at the chosen population models. In Appendix 11.7.2, we give more details on the numerical computation of the selection function $\beta$.

In summary, the full expression of the probability of observing the data set $\boldsymbol{D}$ under the lensed hypothesis is

$$
\begin{aligned}
&p(\boldsymbol{D}|\mathcal{H}_{\rm L}, \boldsymbol{\lambda}, \mathcal{R}, \boldsymbol{\gamma}) \\
&= \frac{1}{\beta(\boldsymbol{\lambda}, \mathcal{R}, \boldsymbol{\gamma})} \int \mathrm{d}\boldsymbol{\theta}^{(1)}_{\rm com}\, \mathrm{d}\boldsymbol{\theta}^{(1)}_{\rm ind}\, \cdots \mathrm{d}\boldsymbol{\theta}^{(N)}_{\rm ind} \left[ \prod_{j=1}^{N} p(D^{(j)}|\boldsymbol{\theta}^{(j)}_{\rm ind}, \boldsymbol{\theta}^{(1)}_{\rm com}) \right] \\
&\times p_{\rm pop,ind}(\boldsymbol{\theta}^{(1)}_{\rm ind}, ..., \boldsymbol{\theta}^{(N)}_{\rm ind}|\boldsymbol{\gamma}) p_{\rm pop,com}(\boldsymbol{\theta}^{(1)}_{\rm com}|\boldsymbol{\lambda}, \mathcal{R}).
\end{aligned}
\tag{11.62}
$$

## 11.7 Appendix: Evaluation of selection functions

Here we explain how to numerically compute the selection functions $\alpha$ and $\beta$ under the not-lensed and the lensed hypothesis, respectively. Note that the numerical values are parametrization invariant, and hence we will be using the parametrization that is more convenient in terms of computation. A common technique employed in the evaluation of high-dimensional integral, as in the case here, is Monte Carlo (MC) integration, where we randomly generate points inside the integration region for evaluation. We will be using MC integration extensively here.

### 11.7.1 Under the not-lensed hypothesis

The selection function under the not-lensed hypothesis $\alpha(\boldsymbol{\lambda}, \mathcal{R})$, is given by

$$
\begin{aligned}
\alpha(\boldsymbol{\lambda}, \mathcal{R}) &= \int_{\text{all obs. data}} \mathrm{d}D \int \mathrm{d}\boldsymbol{\theta}\; p(D|\boldsymbol{\theta})\; p_{\rm pop}(\boldsymbol{\theta}|\boldsymbol{\lambda}, \mathcal{R}) \\
&= \int \mathrm{d}\boldsymbol{\theta}\; \underbrace{\left[ \int \mathrm{d}D\; \Theta(\rho - \rho_{\rm th}) p(D|\boldsymbol{\theta}) \right]}_{p_{\rm det}(\boldsymbol{\theta})} p_{\rm pop}(\boldsymbol{\theta}|\boldsymbol{\lambda}, \mathcal{R}) \\
&= \int \mathrm{d}\boldsymbol{\theta}\; p_{\rm det}(\boldsymbol{\theta}) p_{\rm pop}(\boldsymbol{\theta}|\boldsymbol{\lambda}, \mathcal{R}),
\end{aligned}
\tag{11.63}
$$

where we have chosen the network SNR threshold $\rho_{\rm th}$ to be 12 [209], and $\Theta(x)$ denotes the Heaviside step function.

We can evaluate this integral using Monte Carlo integration. If we have $N_{\rm MC}$ samples of $\boldsymbol{\theta}$ drawn from the distribution $p_{\rm pop}(\boldsymbol{\theta}|\boldsymbol{\lambda}, \mathcal{R})$, then we can simply approximate the selection function as

$$\alpha(\boldsymbol{\lambda}, \mathcal{R}) \approx \frac{1}{N_{\rm MC}} \sum_{i=1}^{N_{\rm MC}} p_{\rm det}(\boldsymbol{\theta}_i). \tag{11.64}$$

However, for most of the time, it is not trivial to generate samples from $p_{\rm pop}(\boldsymbol{\theta}|\boldsymbol{\lambda}, \mathcal{R})$. We can generate a set of fiducial samples $\{\boldsymbol{\theta}\}_i$ that instead follow another distribution $q(\boldsymbol{\theta})$ that we can sample easily. This is known as importance sampling (where $q$ should be chosen such that it is nonvanishing wherever $p_{\rm pop}$ is also nonvanishing). The selection function $\alpha$ can be calculated as

$$\alpha(\boldsymbol{\lambda}, \mathcal{R}) \approx \frac{1}{N_{\rm MC}} \sum_{i=1}^{N_{\rm MC}} \left[ p_{\rm det}(\boldsymbol{\theta}_i) \frac{p_{\rm pop}(\boldsymbol{\theta}_i|\boldsymbol{\lambda}, \mathcal{R})}{q(\boldsymbol{\theta}_i)} \right]. \tag{11.65}$$

### 11.7.2 Under the lensed hypothesis

The selection function under the lensed hypothesis $\beta(\boldsymbol{\lambda}, \mathcal{R}, \boldsymbol{\gamma})$ is given by

$$\begin{aligned} &\beta(\boldsymbol{\lambda}, \mathcal{R}, \boldsymbol{\gamma}) \\ &= \int \mathrm{d}\boldsymbol{\theta}^{(1)}_{\rm com}\, \mathrm{d}\boldsymbol{\theta}^{(1)}_{\rm ind} \cdots \mathrm{d}\boldsymbol{\theta}^{(N)}_{\rm ind} \left[ \prod_{j=1}^{N} p_{\rm det}(\boldsymbol{\theta} = \boldsymbol{\theta}^{(j)}_{\rm com} \cup \boldsymbol{\theta}^{(1)}_{\rm ind}) \right] \\ &\times p_{\rm pop,ind}(\boldsymbol{\theta}^{(1)}_{\rm ind}, ..., \boldsymbol{\theta}^{(N)}_{\rm ind}|\boldsymbol{\gamma}) p_{\rm pop,com}(\boldsymbol{\theta}^{(1)}_{\rm com}|\boldsymbol{\lambda}, \mathcal{R}). \end{aligned} \tag{11.66}$$

Here we ignore any kind of observational selection effects, for example due to detector down-time [220] or finite observation period [179]. Suppose we are using the parametrization $\boldsymbol{\theta}_{\rm com} = \{m_1, m_2, \boldsymbol{\chi}_1, \boldsymbol{\chi}_2, \alpha, \delta, \psi, \phi_{\rm c}\}$ and $\boldsymbol{\theta}_{\rm ind} = \left\{\mu^{(1)}, \mu^{(2)}, \Xi^{(1)}, \Xi^{(2)}, z\right\}$. We also ignore the phasing effect due to lensing to the detectability of images [171]. In particular, we can separate the integration over

the source redshift $z$

$$\begin{aligned}
&\beta(\boldsymbol{\lambda}, \mathcal{R}, \boldsymbol{\gamma}) \\
&= \int \mathrm{d}z \; p_{\mathrm{lens}}(z|\mathcal{H}_{\mathrm{L}}, \mathcal{R}) \left\{ \int \mathrm{d}\left\{m_1, m_2, \boldsymbol{\chi}_1, \boldsymbol{\chi}_2, \alpha, \delta, \psi, \phi_{\mathrm{c}}\right\} \right. \\
&\times p_{\mathrm{src}}(m_1, m_2, \boldsymbol{\chi}_1, \boldsymbol{\chi}_2|\boldsymbol{\lambda}) p_{\mathrm{ext}}(\alpha, \delta, \psi, \phi_{\mathrm{c}}) \\
&\left. \times \int \mathrm{d}\left\{\mu^{(1)}, \mu^{(2)}\right\} \; p_{\mathrm{lens}}(\mu^{(1)}, \mu^{(2)}|\boldsymbol{\gamma}) \; \left[p_{\mathrm{det}}(\boldsymbol{\theta}^{(1)}) p_{\mathrm{det}}(\boldsymbol{\theta}^{(2)})\right] \right\},
\end{aligned} \tag{11.67}$$

where the dependence on the image types $\Xi^{(1)}, \Xi^{(2)}$ are trivially integrated over since $\int \mathrm{d}\Xi^{(i)} p_{\mathrm{lens}}(\Xi^{(i)}) = 1$.

Note that the event-level parameters $\boldsymbol{\theta}^{(i)}$ consist of

$$\boldsymbol{\theta}^{(i)} = \left\{m_1, m_2, \boldsymbol{\chi}_1, \boldsymbol{\chi}_2, \alpha, \delta, \psi, \phi_{\mathrm{c}}, \mu^{(i)}, z\right\}.$$

This means that we can evaluate the inner integral enclosed by the curly brackets first using Monte Carlo integration. Again, if we have $N_{\mathrm{MC}}$ samples of $\boldsymbol{\theta}$ drawn from the joint distribution $p_{\mathrm{src}}(m_1, m_2, \boldsymbol{\chi}_1, \boldsymbol{\chi}_2|\boldsymbol{\lambda}) p_{\mathrm{ext}}(\alpha, \delta, \psi, \phi_{\mathrm{c}})$ and $p_{\mathrm{lens}}(\mu^{(i)}|\boldsymbol{\gamma})$ with a given redshift $z$, then we can simply approximate the inner integral $\epsilon(z)$ as

$$\epsilon(z) \approx \frac{1}{N_{\mathrm{MC}}} \sum_{i=1}^{N_{\mathrm{MC}}} \left[\prod_{j=1}^{N} p_{\mathrm{det}}(\boldsymbol{\theta}_i^{(j)}|z)\right]. \tag{11.68}$$

Figure 11.11 shows how $\epsilon(z)$ depends on the redshift $z$. We see that $\epsilon(z)$ decreases as we go higher in $z$. However, the contribution of $\epsilon(z)$ to the $\beta$ selection function integral is weighted by $p_z(z)$ (dotted line) which peaks at $z \sim 3$ for the particular merger-rate density model and lens model we used in the calculation (cf. Sec. 11.3).

We can employ the same Monte Carlo integration technique to evaluate the outer integral over $z$. Suppose we have $N_z$ samples of $z \sim p_z(z)$, then we can approximate the entire $\beta(\boldsymbol{\lambda}, \mathcal{R}, \boldsymbol{\gamma})$ integral as

$$\beta(\boldsymbol{\lambda}, \mathcal{R}, \boldsymbol{\gamma}) \approx \frac{1}{N_z} \sum_{k=1}^{N_z} \frac{1}{N_{\mathrm{MC}}} \sum_{i=1}^{N_{\mathrm{MC}}} \left[\prod_{j=1}^{N} p_{\mathrm{det}}(\boldsymbol{\theta}_i^{(j)}|z_k)\right]. \tag{11.69}$$

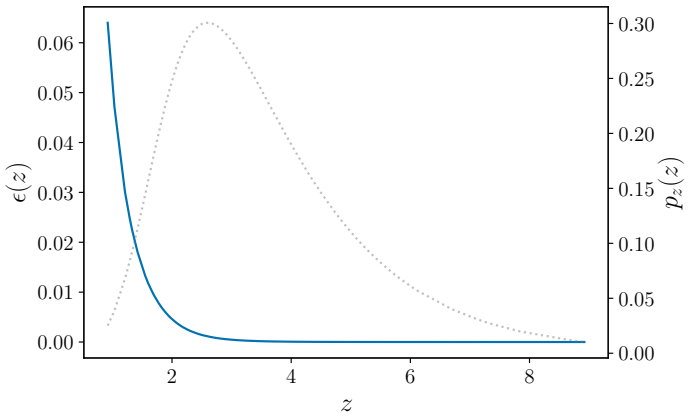


Figure 11.11: The inner integral $\epsilon(z)$ (solid line) as a function of the source redshift $z$ evaluated using Monte Carlo integration. We see that $\epsilon(z)$ decreases as we go further in $z$. However, the contribution of $\epsilon(z)$ to the $\beta$ selection function integral is weighted by $p_z(z)$ (dotted line) which peaks at $z \sim 3$ for the particular merger rate density model and lens model we used in the calculation (cf. Sec. 11.3).

## 11.8 Appendix: Derivation of the arrival time probability density function under the not-lensed hypothesis

Here we give a derivation of the arrival time probability density function under the not-lensed hypothesis we used in the main text, namely

$$p(\Delta t|\mathcal{H}_{\rm NL}) = \frac{2}{T_{\rm obs}}\left(1 - \frac{\Delta t}{T_{\rm obs}}\right). \tag{11.70}$$

Given that we have observed $N_{\rm obs}$ events within the interval $(0, T_{\rm obs}]$, if we assume that the arrival of the events follows a Poisson process with a mean rate $r$, then we can write down the joint probability distribution of the $N_{\rm obs}$ ordered arrival times $t_1, t_2, \ldots, t_{N_{\rm obs}}$ (such that $t_1 < t_2 < \ldots$) conditioned that we have observed $N_{\rm obs}$ events as

$$
\begin{aligned}
& p(t_1, t_2, \ldots, t_{N_{\text{obs}}}, t_1 < t_2 < \cdots < t_{N_{\text{obs}}} | N_{\text{obs}}, r) \\
&= \frac{p(t_1, t_2, \ldots, t_{N_{\text{obs}}}, t_1 < t_2 < \cdots < t_{N_{\text{obs}}}, N_{\text{obs}} | r)}{p(N_{\text{obs}} | r)} \\
&= \frac{r \exp(-r t_1) \ \ldots \ r \exp\left[-r(t_{N_{\text{obs}}} - t_{N_{\text{obs}}-1})\right] \ \exp\left[-r(T_{\text{obs}} - t_{N_{\text{obs}}})\right]}{(r T_{\text{obs}})^{N_{\text{obs}}} \exp(-r T_{\text{obs}}) / N_{\text{obs}}!} \\
&= \frac{N_{\text{obs}}!}{T_{\text{obs}}^{N_{\text{obs}}}},
\end{aligned}
\tag{11.71}
$$

where the second line uses the fact that for a Poisson process one can partition the time interval into many smaller chunks where each chunk still follows the same Poisson process, and that the interarrival time follows an exponential distribution. The factor $\exp\left[-r(T_{\text{obs}} - t_{N_{\text{obs}}})\right]$ is due to the requirement that there is no event between $(t_{N_{\text{obs}}}, T_{\text{obs}}]$. Note that there are exactly $N_{\text{obs}}!$ combinations of unordered arrival times $\left\{t_1, t_2, \ldots, t_{N_{\text{obs}}}\right\}$ that would lead to the same ordered times. Therefore the joint probability distribution of the $N_{\text{obs}}$ unordered arrival times $\left\{t_1, t_2, \ldots, t_{N_{\text{obs}}}\right\}$ is simply

$$
p(t_1, t_2, \ldots, t_{N_{\text{obs}}} | N_{\text{obs}}, r) = \left(\frac{1}{T_{\text{obs}}}\right)^{N_{\text{obs}}}. \tag{11.72}
$$

Note that we are interested in the probability distribution of the time delay between arbitrary two events among these $N_{\text{obs}} \geq 2$ events. If we consider the unordered set of arrival times, without loss of generality we can assume that the arrival times corresponding to the two events are $t_1$ and $t_2$, respectively. The marginalization over $\left\{t_3, t_4, \ldots, t_{N_{\text{obs}}}\right\}$ is trivial since the joint probability density does not depend on $t_i$, and the marginalized density is just

$$
p(t_1, t_2 | N_{\text{obs}}, r) = \left(\frac{1}{T_{\text{obs}}}\right)^2. \tag{11.73}
$$

Note that since $0 < t_1, t_2 \leq T_{\text{obs}}$, this probability distribution is simply two uniform distributions multiplied together, i.e.,

$$
p(t_1 | N_{\text{obs}}, r) = p(t_2 | N_{\text{obs}}, r) = \left(\frac{1}{T_{\text{obs}}}\right). \tag{11.74}
$$

Let us define a new variable $\Delta t = |t_2 - t_1| > 0$. The cumulative distribution function $F(\Delta t) \equiv \Pr(|t_2 - t_1| < \Delta t)$ can be found using simple coordinate geometry by noting that the support of the joint distribution of $p(t_1, t_2|N_{\rm obs}, r)$ forms a square of length $T_{\rm obs}$ (see Fig. 11.12). If we normalize the length by $T_{\rm obs}$, the condition that $\Delta t > 0$ cuts out two triangles of area $(1 - \Delta t/T_{\rm obs})^2/2$ from the unit square. Therefore,

$$\begin{aligned} F(\Delta t) &= \Pr(-\Delta t < t_2 - t_1 < \Delta t) \\ &= 1 - 2\frac{(1 - \Delta t/T_{\rm obs})^2}{2}. \end{aligned} \tag{11.75}$$

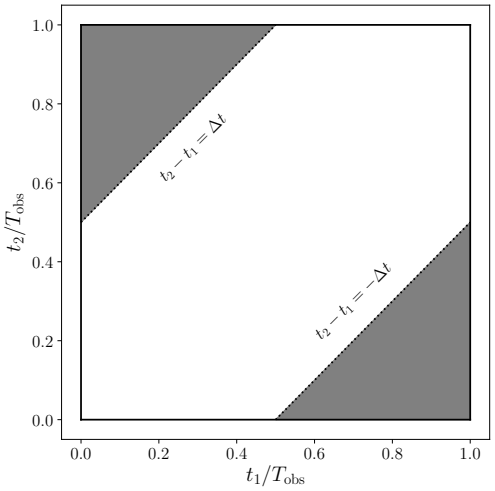


Figure 11.12: A visualization of the integration region over the $t_1/T_{\rm obs} - t_2/T_{\rm obs}$ plane to obtain the distribution $p(\Delta t|\mathcal{H}_{\rm NL})$. The condition that $\Delta t > 0$ carves out two triangles of equal area $(1 - \Delta t/T_{\rm obs})^2/2$ from the unit square. In the figure, we put $\Delta t/T_{\rm obs} = 1/2$ for demonstration.

The desired probability density is a triangular distribution, i.e.,

$$\begin{aligned} p(\Delta t|\mathcal{H}_{\rm NL}) &= \frac{{\rm d}F}{{\rm d}\Delta t} \\ &= \frac{2}{T_{\rm obs}}\left(1 - \frac{\Delta t}{T_{\rm obs}}\right), \end{aligned} \tag{11.76}$$

where the distribution is independent of $r$ and $N_{\rm obs}$. This can be checked against simulations. Figure 11.13 shows two histograms of $\Delta t$ from simulations with $N_{\rm obs} = 10$ and $N_{\rm obs} = 50$, respectively. We can see that the distributions for these two cases are indeed the same, and are well described by Eq. (11.70).

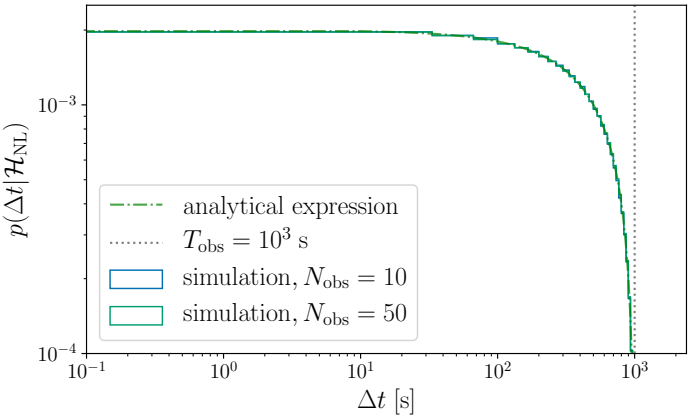


Figure 11.13: The probability density $p(\Delta t|\mathcal{H}_{\rm NL})$ for the time delay $\Delta t$ under the not-lensed hypothesis from an analytical expression (dot-dashed line) and from simulations (blue and green solid lines). For visualization, we set $T_{\rm obs} = 10^3$ s (dotted line) when evaluating the analytical expression and performing the simulations. We see that the distributions are independent of $N_{\rm obs}$ and well-described by the analytical expression in Eq. (11.70).

## 11.9 Appendix: Derivation of the poor-man's prior on the relative magnification

Here we will derive the poor-man's prior on the relative magnification $\mu_{\rm rel} \equiv \mu^{(2)}/\mu^{(1)}$ we used in the main text, namely

$$p(\mu_{\rm rel}) = \begin{cases} \mu_{\rm rel} & \text{for } \mu_{\rm rel} \leq 1 \\ \mu_{\rm rel}^{-3} & \text{for } \mu_{\rm rel} > 1 \end{cases}, \tag{11.77}$$

if we assume that the absolute magnification follows the probability distribution

$$p(\mu) = \begin{cases} 2\mu_{\rm min}^2 \mu^{-3} & \text{for } \mu \geq \mu_{\rm min} \\ 0 & \text{otherwise} \end{cases}, \tag{11.78}$$

where $\mu_{\rm min} > 0$.

Note that the probability distribution of the ratio of two random variables $\mu^{(1)}, \mu^{(2)}$ can be found by evaluating the integral

$$\begin{aligned} &p(\mu_{\rm rel} \equiv \mu^{(2)}/\mu^{(1)}) \\ &= \int_{-\infty}^{+\infty} {\rm d}\mu^{(1)} \; |\mu^{(1)}| \; p(\mu^{(1)}) \; p(\mu^{(2)} = \mu_{\rm rel}\mu^{(1)}). \end{aligned} \tag{11.79}$$

We can divide the integral into two cases; when $\mu_{\rm rel} > 1$ and when $\mu_{\rm rel} \leq 1$. For the former case, the condition that $\mu^{(2)} > \mu_{\rm min}$ is trivially satisfied. Therefore when $\mu_{\rm rel} > 1$, the lower limit of the integral is simply $\mu_{\rm min}$ and the integral is just

$$\begin{aligned} p(\mu_{\rm rel}) &= \int_{\mu_{\rm min}}^{+\infty} {\rm d}\mu^{(1)} \; \mu^{(1)} (2\mu_{\rm min}^2)^2 \left(\mu^{(1)}\right)^{-3} \left(\mu_{\rm rel}\mu^{(1)}\right)^{-3} \\ &= 4\mu_{\rm min}^4 \left[\int_{\mu_{\rm min}}^{+\infty} {\rm d}\mu^{(1)} \; \left(\mu^{(1)}\right)^{-5}\right] \mu_{\rm rel}^{-3} \\ &= \mu_{\rm rel}^{-3}. \end{aligned} \tag{11.80}$$

For the latter case, $\mu^{(1)} \geq \mu_{\rm min}/\mu_{\rm rel}$ for the integral to not vanish. Therefore, the lower limit of the integral becomes $\mu_{\rm min}/\mu_{\rm rel}$ instead, and

$$\begin{aligned} p(\mu_{\rm rel}) &= \int_{\mu_{\rm min}/\mu_{\rm rel}}^{+\infty} {\rm d}\mu^{(1)} \; \mu^{(1)} (2\mu_{\rm min}^2)^2 \left(\mu^{(1)}\right)^{-3} \left(\mu_{\rm rel}\mu^{(1)}\right)^{-3} \\ &= 4\mu_{\rm min}^4 \left[\int_{\mu_{\rm min}/\mu_{\rm rel}}^{+\infty} {\rm d}\mu^{(1)} \; \left(\mu^{(1)}\right)^{-5}\right] \mu_{\rm rel}^{-3} \\ &= 4\mu_{\rm min}^4 \frac{\mu_{\rm rel}^4}{4\mu_{\rm min}^4} \mu_{\rm rel}^{-3} \\ &= \mu_{\rm rel}. \end{aligned} \tag{11.81}$$

Note that this poor-man's prior for $\mu_{\rm rel}$ does not depend on the value of $\mu_{\rm min}$. Again, it can be checked against simulations. Figure 11.14 shows the results of two simulations, assuming that $\mu_{\rm rel} = 2$ and $\mu_{\rm rel} = 10$, respectively. We see that the poor-man's prior for $\mu_{\rm rel}$ is indeed independent of the value of the minimum value of the absolute magnification $\mu_{\rm min}$.

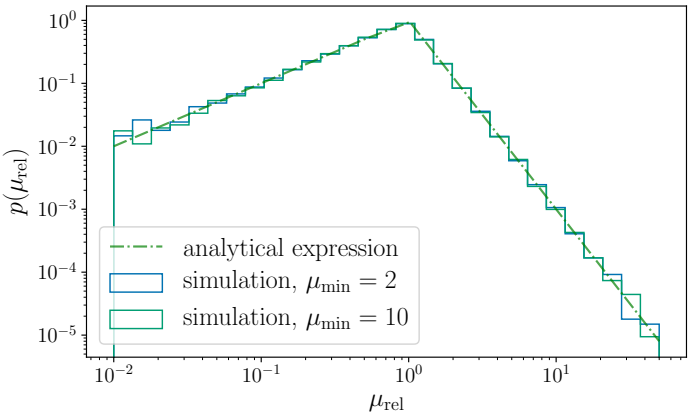


Figure 11.14: The poor-man's prior for the relative magnification. Numerical simulations were performed with different values of $\mu_{\rm min}$ to confirm the analytical expression in Eq. (11.77), and that the distribution (both the shape and normalization) does not depend on the value of $\mu_{\rm min}$.

*Chapter 12*

# SEARCH FOR GRAVITATIONAL-LENSING SIGNATURES IN THE FIRST HALF OF THE THIRD OBSERVING RUN OF THE LIGO-VIRGO NETWORK

This chapter contains work from

> LIGO Scientific, VIRGO Collaboration. "Search for Lensing Signatures in the Gravitational-Wave Observations from the First Half of LIGO–Virgo's Third Observing Run". In: *Astrophys. J.* 923.1 (2021), p. 14. DOI: 10.3847/1538-4357/ac23db. arXiv: 2105.06384 [gr-qc].
> R. K. L. L performed the analyses for identifying strongly lensed binary black hole signals using the code `hanabi` and wrote part of the manuscript.

## 12.1 Introduction

Strong lensing, in addition to magnification, can produce multiple images of a single astrophysical event. These multiple images appear at the gravitational-wave (GW) detectors as repeated events. The images will differ in their arrival time and amplitude [221, 190, 182, 168, 189]. The sky location is the same within the localization accuracy of GW detectors, given that the typical angular separations are of the order of arcseconds. Additionally, lensing can invert or Hilbert transform the image [175, 176], introducing a frequency-independent phase shift. This transformation depends on the image type, set by the lensing time delay at the image position: Type-I, II, and III correspond to a time-delay minimum, saddle point, and maximum, respectively [176]. The multiple-imaged waveforms $\{\tilde{h}_j^L\}$ of a single signal $\tilde{h}$ then satisfy [175, 176]

$$\tilde{h}_j^L(f;\theta,\mu_j,\Delta t_j,\Delta\phi_j) = \sqrt{|\mu_j|}\tilde{h}(f;\theta,\Delta t_j)\exp\left(i\,\mathrm{sign}(f)\Delta\phi_j\right), \tag{12.1}$$

where $\sqrt{|\mu_j|}$ is the lensing magnification experienced by the image $j$ and $\Delta\phi_j = -\pi n_j/2$ is the Morse phase, with index $n_j = 0, 1, 2$ for Type-I, II, and III images. $\tilde{h}(f;\theta,\Delta t_j)$ is the original (unlensed) waveform before lensing, but evaluated as arriving with a time delay $\Delta t_j$. The multi-image hypothesis then states that most parameters measured from the different lensed images of the same event are consistent.

The relative importance of different parameters for the overall consistency under the multi-image hypothesis will vary for different events. For example, the sky localization match will have greater relevance for well-localized, high-signal-to-noise ratio (SNR) events. Similarly, the overlap in measured chirp mass $(1+z)\mathcal{M}_c = (1+z)\,(m_1 m_2)^{3/5}/(m_1+m_2)^{1/5}$, where $z$ is the redshift, will be more significant when the uncertainty in that parameter is lower, although in this case the underlying astrophysical mass distribution will play a key role. The similarities in other parameters such as mass ratios or spins will be more important when they depart from the more common astrophysical expectations. Evidence of strong lensing could also be acquired with a single Type-II (saddle point) image if the induced waveform distortions in the presence of higher modes, precession, or eccentricity are observed [176]. Such evidence is unlikely to be observed without next-generation detectors [171].

Previous studies have searched for multiple images in the GWTC-1 catalog [182, 185, 168, 189, 183, 184] covering events in the first observing run (O1) and the second observing run (O2). The first search for GW lensing signatures in O1 and O2 focused on the posterior overlap of the masses, spins, binary orientation and sky positions [182] and the consistency of time delays with expectations for galaxy lenses, but found no conclusive evidence of lensing. The search did uncover a candidate pair GW170104–GW170814 with a relatively high Bayes factor of $\gtrsim 200$. Still, that study disfavored the candidate due to its long time delay and the low prior probability of lensing. In parallel, Broadhurst, Diego, and Smoot [185] suggested that the candidate pair GW170809–GW170814 could be lensed, but this claim is disfavored by more comprehensive analyses [182, 184].

Both Li et al. [168] and McIsaac et al. [189] performed searches for sub-threshold counterparts to the GWTC-1 events, identifying some marginal candidates but finding no conclusive evidence of lensing. More recently, Dai et al. [183] and Liu, Hernandez, and Creighton [184] searched for lensed GW signals including the analysis of the lensing image type, which can be described through the Morse phases, $\Delta\phi_j$ in Eq. (12.1). These analyses have revisited the pair GW170104–GW170814 and demonstrated that the Morse phase is consistent with the lensed expectation but would require Type-III (time-delay maximum) images, which are rare from an observational standpoint. Dai et al. [183] also pointed out that a sub-threshold trigger, designated by them as GWC170620, is also consistent with coming from the same source. However, the required number and type of images for this lens system make the interpretation unlikely given current astrophysical expectations. Also, two same-day event pairs in the first half of the third observing run (O3a) (on 2019 May 21 and 2019 August 28) have already been considered elsewhere, but were both ruled out due to vanishing localization overlap [193, 213].

In this chapter, we perform a more detailed joint-parameter estimation (PE) analysis for promising pairs in O3a reported by the posterior overlap analysis in Ref. [222], considering all potential correlations in the full parameter space and the image type. This joint analysis provides a more solid determination of the lensing probability for a given GW pair. According to the predictions of the expected lensing time delays and the rate of galaxy and galaxy cluster lensing [223, 178, 183], we expect it to be less likely for counterpart images of the events in O3a to be detected in O1 or O2.[1] Thus, we only search for multiple images within O3a itself.

## 12.2 Methods

Here we follow up on the most significant pairs of events from the posterior-overlap analysis reported in Ref. [222] with a more detailed but more computa-

[1] Relative lensing rates for galaxies and clusters are given in Tab. 1 of Ref. [222].

tionally demanding joint-PE analysis. The benefit of this analysis is that it allows for more stringent constraints on the lensing hypothesis by investigating potential correlations in the full parameter space of binary black hole (BBH) signals, instead of marginalizing over some parameters. Moreover, it also includes a test for the lensing image type by incorporating lensing phase information.

We perform our analysis here using a BILBY-based pipeline, HANABI [224]. Unlike the posterior-overlap analysis, the joint-PE analysis does not start from existing posterior samples. Instead, we start the inference directly using the detector strain data. We follow the same data selection choices (calibration version, available detectors for each event, and noise subtraction procedures) as in the original GWTC-2 analysis [10], with special noise mitigation steps (glitch subtraction and frequency range limitations) taken for some events as listed in Table V of that paper. In this section, we first describe how we quantify the evidence for the strong lensing hypothesis, then detail the pipeline and finally present the results.

### 12.2.1 The coherence ratio and the Bayes factor

There will be three types of outputs for the joint-PE analysis. First, we compute a coherence ratio $\mathcal{C}_{\mathrm{U}}^{\mathrm{L}}$, which is the ratio of the lensed and unlensed evidences, neglecting selection effects and using default priors in the joint-PE inference. We treat this as a ranking statistic, which quantifies how consistent two signals are with the lensed hypothesis. Large coherence ratios indicate that the parameters of the GWs agree with the expectations of multiple lensed events. This occurs, for example, when the masses and sky localization coincide. However, the coherence ratio does not properly account for the possibility that the parameters overlap by chance.

The likelihood that GW parameters overlap by chance sensitively depends on the underlying population of sources and lenses. For example, if there existed formation channels that produced GWs with similar frequency evolutions (as expected of lensing), the likelihood of an unlensed event mimicking lensing would increase substantially. Thus, we introduce a second output, the population-

weighted coherence ratio $\mathcal{C}_{\rm U}^{\rm L}|_{\rm pop}$, which incorporates prior information about the populations of BBHs and lenses. The value of $\mathcal{C}_{\rm U}^{\rm L}|_{\rm pop}$ is subject to the choice of both the BBH and lens models.

Similarly, the probability that two signals agree with the multiple-image hypothesis is altered through selection effects, as some masses and sky orientations are preferentially detected. Thus, we also include the selection effects, which gives us our final output, the Bayes factor $\mathcal{B}_{\rm U}^{\rm L}$. The $\mathcal{B}_{\rm U}^{\rm L}$ quantifies the evidence of the strong lensing hypothesis for a given detector network and population model. For the full derivations and detailed discussion on the difference between the coherence ratio and the Bayes factor, see Ref. [224].

### 12.2.2 The HANABI pipeline

The HANABI pipeline adopts a hierarchical Bayesian framework that models the data generation process under the lensed and the unlensed hypothesis, which is covered extensively in Chapter 11. This pipeline uses the IMRPHENOMXPHM waveform [199], which models the full inspiral–merger–ringdown for generic precessing binaries including both the dominant and some sub-dominant multipole moments.

HANABI differs from the LALINFERENCE-based pipeline in Ref. [184] in the treatment of the Morse phase. Here the lensing phase is directly incorporated in the frequency-domain waveform, accounting for any possible distortion of Type-II images [225, 176, 224]. Moreover, the lensed probability is computed by considering all possible combinations of image types with a discrete uniform prior [224]. For this reason, HANABI only produces one evidence per pair, and not one for each discrete phase difference as the LALINFERENCE-based pipeline. Unlike the LALINFERENCE-based pipeline, HANABI samples the observed masses in a uniform distribution. The mass ranges are different for each event pair, but an overall reweighting is applied later (see below). The rest of the prior choices for the intrinsic parameters are the same as for the LALINFERENCE-based pipeline with the addition of a discrete uniform prior on the Morse phase and isotropic

spin priors.

In addition to computing the joint-PE coherence ratio, HANABI also incorporates prior information about the lens and BBH populations, as well as selection effects. In particular, the BBH population is chosen to follow a POWER LAW + PEAK MODEL in the primary mass following the best-fit parameters in Abbott et al. [10]. Similarly, the secondary mass is fixed to a uniform distribution between the minimum and the primary mass. HANABI also uses an isotropic spin distribution and merger rate history following Model A in Sec. 3 in Ref. [222]. The lens population is modeled by the optical depth described in Hannuksela et al. [182] and a magnification distribution $p(\mu) \propto \mu^{-3}$ for $\mu \geq 2$. HANABI is thus able to output $\mathcal{C}_{\mathrm{U}}^{\mathrm{L}}$, $\mathcal{C}_{\mathrm{U}}^{\mathrm{L}}|_{\mathrm{pop}}$ and $\mathcal{B}_{\mathrm{U}}^{\mathrm{L}}$. However, HANABI does not include any preference for a particular type of image, i.e., HANABI uses a discrete, uniform prior for the Morse phase shift $\Delta\phi_j$.

### 12.3 Results

Within the O3a events, the LALINFERENCE-based pipeline reports 11 pairs with $\log_{10}(\mathcal{C}_{\mathrm{U}}^{\mathrm{L}}) > 4$ as shown in Tab. 3 of Ref. [222], indicating high parameter consistency. We have checked that the results of the LALINFERENCE-based pipeline are qualitatively consistent with those from HANABI. This reinforces our previous argument that the shift in the coalescence phase is a good approximate description of the lensing Morse phase given that in the present catalog most events are dominated by the $\ell = |m| = 2$ multipole moments. However, because of the pair-dependent prior choices of HANABI, we do not present its raw $\mathcal{C}_{\mathrm{U}}^{\mathrm{L}}$ results in Table 12.1.

We then include our prior expectation on the properties of the lensed images (derived from our BBH and lens population priors) and selection effects when computing the population-weighted HANABI coherence ratio and the Bayes factors $\mathcal{B}_{\mathrm{U}}^{\mathrm{L}}$. The results are summarized in Table 12.1. The event pair GW190728_06–GW190930_13, which seemed the most promising from the overlap analysis in Sec. 5.1 of Ref. [222], is disfavored by the HANABI pipeline. After the inclusion

of the population prior and selection effects, none of the event pairs display a preference for the lens hypothesis ($\log_{10} \mathcal{B}^{\rm L}_{\rm U} < 0$).

The population-weighted coherence ratio and the Bayes factor are subject to the BBH and lens model specifications. The population properties are not inferred taking into account the possibility of lensing. This introduces an inevitable bias, but it can be justified *a posteriori* to be a good approximation given the expected low rate of strong lensing. Additionally, the population properties include significant uncertainties in the hyper-parameter estimates and presume a population model. In any case, to quantify this intrinsic uncertainty in the modeling, we consider different choices for the mass distribution and merger rate history. Varying the maximum BBH mass and the redshift evolution of the merger rate using the $R_{\rm min}(z)$ and $R_{\rm max}(z)$ of Model A in Sec. 3 of Ref. [222], we find that the strong lensing hypothesis is always disfavored. While these results are subject to assumptions on prior choices, our results are sufficient to reject the strong lensing hypothesis: Even if other prior choices favored the lensing hypothesis, the evidence would at best be inconclusive.

The impact of selection effects is considerable. Among other reasons, this is because present GW detectors preferentially observe higher mass events [226], making coincidences in observed masses more probable. Along the same lines, given the specific antenna patterns of the current network of detectors, GW events are preferentially seen in specific sky regions with characteristic elongated localization areas [220], which favors the overlap between different events.

We also reanalyze the GW170104–GW170814 event pair in the O2 data previously studied by Dai et al. [183] and Liu, Hernandez, and Creighton [184]. Using the LALInference-based pipeline, Liu, Hernandez, and Creighton [184] found that the coherence ratio, including selection effects associated with the Malmquist bias [227], is $\log_{10}(C^{\rm L}_{\rm U}) \approx 4.3$ for a $\pi/2$ coalescence phase shift. However, when including together population and selection effects with hanabi, we find that the evidence drastically reduces to a Bayes factor of $\log_{10}(\mathcal{B}^{\rm L}_{\rm U}) \approx -2.0$.

In addition to the Bayes factor, it is important to contrast the recovered number of candidate lensed pairs and their properties with astrophysical expectations. In Sec.3.1 of Ref. [222], it was found that the relative rate of GW events with at least two strongly lensed images above the detection threshold is below $\sim 1.3 \times 10^{-3}$ for all considered BBH population models. Thus, the lensing rate estimates significantly disfavor the lensing hypothesis *a priori*; even a moderate Bayes factor would not by itself yet make a compelling case for strong lensing. Additionally, the type of images, arrival times, and magnifications provide additional information on the lensing interpretation's plausibility. For example, a quantification of the time-delay prior can be computed by multiplying the coherence ratio by $\mathcal{R}^{\rm gal}$. However, our final conclusions do not depend on the prior information about the lensing time delays or the prior odds against lensing: the prior lensing knowledge further disfavors the strong lensing hypothesis, but we did not use it to rule out any candidates.

| Event 1 | Event 2 | $\log_{10}(\mathcal{C}_{\rm U}^{\rm L}\vert_{\rm pop})$ HANABI | $\log_{10}(\mathcal{B}_{\rm U}^{\rm L})$ HANABI |
|---|---|---|---|
| GW190412 | GW190708_23 | −6.6 | −9.7 |
| GW190421_21 | GW190910_11 | −0.7 | −3.8 |
| GW190424_18 | GW190727_06 | −0.8 | −3.9 |
| GW190424_18 | GW190910_11 | −0.8 | −3.9 |
| GW190513_20 | GW190630_18 | −2.4 | −5.5 |
| GW190706_22 | GW190719_21 | −0.3 | −3.4 |
| GW190707_09 | GW190930_13 | −9.4 | −12.5 |
| GW190719_21 | GW190915_23 | −0.7 | −3.8 |
| GW190720_00 | GW190728_06 | −6.7 | −9.8 |
| GW190720_00 | GW190930_13 | −9.2 | −12.3 |
| GW190728_06 | GW190930_13 | −8.5 | −11.6 |
| GW190413_05 | GW190424_18 | −1.6 | −4.7 |
| GW190421_21 | GW190731_14 | −0.2 | −3.3 |
| GW190424_18 | GW190521_07 | −2.0 | −5.1 |
| GW190424_18 | GW190803_02 | −1.0 | −4.1 |
| GW190727_06 | GW190910_11 | −1.4 | −4.5 |
| GW190731_14 | GW190803_02 | −0.9 | −4.0 |
| GW190731_14 | GW190910_11 | −1.2 | −4.3 |
| GW190803_02 | GW190910_11 | −0.1 | −3.2 |

Table 12.1: Summary of joint-PE results for event pairs in O3a. We select those events with posterior overlap ranking statistic larger than 50 as reported in Ref. [222]. For each pair of events presented in the first two columns, the third and the fourth columns correspond to the HANABI results for the population-weighted coherence ratio $\mathcal{C}_{\rm U}^{\rm L}\vert_{\rm pop}$ and the Bayes factor $\mathcal{B}_{\rm U}^{\rm L}$. All quantities are given in $\log_{10}$. All high coherence ratio events display a small Bayes factor when including the population priors and selection effects. Table reproduced from Ref. [222].

## 12.4 Conclusion

Although we do not find evidence of strong lensing, future electromagnetic follow-up of the candidates could allow for independent support for the hypothesis if we identified a lensed counterpart galaxy to these events [228, 223, 229, 230, 211, 231, 232, 233]. This identification could take place by matching GW and

electromagnetic image properties when four GW images are available [211]. With two images, the number of hosts could also be constrained [228, 233], but to a lesser degree due to degeneracies with the lens and source alignment and uncertainties introduced by micro/millilensing — although strong lensing by galaxy clusters might allow us to identify a single cluster candidate [223, 229, 230, 231, 232].

**Acknowledgements**

The authors also gratefully acknowledge the support of the Science and Technology Facilities Council (STFC) of the United Kingdom, the Max-Planck-Society (MPS), and the State of Niedersachsen/Germany for support of the construction of Advanced LIGO and construction and operation of the GEO600 detector. Additional support for Advanced LIGO was provided by the Australian Research Council. The authors gratefully acknowledge the Italian Istituto Nazionale di Fisica Nucleare (INFN), the French Centre National de la Recherche Scientifique (CNRS) and the Netherlands Organization for Scientific Research, for the construction and operation of the Virgo detector and the creation and support of the EGO consortium. The authors also gratefully acknowledge research support from these agencies as well as by the Council of Scientific and Industrial Research of India, the Department of Science and Technology, India, the Science & Engineering Research Board (SERB), India, the Ministry of Human Resource Development, India, the Spanish Agencia Estatal de Investigación, the Vicepresidència i Conselleria d'Innovació, Recerca i Turisme and the Conselleria d'Educació i Universitat del Govern de les Illes Balears, the Conselleria d'Innovació, Universitats, Ciència i Societat Digital de la Generalitat Valenciana and the CERCA Programme Generalitat de Catalunya, Spain, the National Science Centre of Poland and the Foundation for Polish Science (FNP), the Swiss National Science Foundation (SNSF), the Russian Foundation for Basic Research, the Russian Science Foundation, the European Commission, the European Regional Development Funds (ERDF), the Royal Society, the Scottish Funding

Council, the Scottish Universities Physics Alliance, the Hungarian Scientific Research Fund (OTKA), the French Lyon Institute of Origins (LIO), the Belgian Fonds de la Recherche Scientifique (FRS-FNRS), Actions de Recherche Concertées (ARC) and Fonds Wetenschappelijk Onderzoek – Vlaanderen (FWO), Belgium, the Paris Île-de-France Region, the National Research, Development and Innovation Office Hungary (NKFIH), the National Research Foundation of Korea, the Natural Science and Engineering Research Council Canada, Canadian Foundation for Innovation (CFI), the Brazilian Ministry of Science, Technology, and Innovations, the International Center for Theoretical Physics South American Institute for Fundamental Research (ICTP-SAIFR), the Research Grants Council of Hong Kong, the National Natural Science Foundation of China (NSFC), the Leverhulme Trust, the Research Corporation, the Ministry of Science and Technology (MOST), Taiwan, the United States Department of Energy, the Kavli Foundation, and the Gordon and Betty Moore Foundation. The authors gratefully acknowledge the support of the NSF, STFC, INFN and CNRS for provision of computational resources.

*Chapter 13*

# SEARCH FOR GRAVITATIONAL-LENSING SIGNATURES IN THE FULL THIRD OBSERVING RUN OF THE LIGO-VIRGO NETWORK

This chapter contains work from

> LIGO Scientific, VIRGO, KAGRA Collaboration. "Search for gravitational-lensing signatures in the full third observing run of the LIGO-Virgo network". *Submitted to Astrophys. J.* arXiv: `2304.08393 [gr-qc]`.
> R. K. L. L performed the analyses for identifying strongly lensed binary black hole signals using the code `hanabi` and wrote part of the manuscript.

## 13.1 Introduction

In this chapter, we search for pairs of gravitational-wave (GW) events consistent with the strong-lensing hypothesis in the third observing run (O3). Some of these pairs will have sufficiently strong amplitudes that can be identified as confident detections (super-threshold) by the search pipelines used in Abbott et al. [10, 11, 12], while others may have not been identified as signals (sub-threshold) because of the relative de-magnification. Our searches will include *both* pairs[1] among super-threshold GW events, as well as pairs among a super-threshold and a sub-threshold GW event.

Similar to the analysis of data for the first half of the third observing run (O3a) in Ref. [222] and Chapter 12, we perform a joint parameter estimation (PE) analysis for the most relevant candidate lensing pairs. We follow up on the pairs that display low false-positive probability in their posterior overlap or machine learning (ML) classification scheme as reported in Ref. [234]. These are pairs

[1] A pair is the minimum association, but higher multiplicities are also possible.

within the whole of O3, but we only consider here those with at least one event in the second half of the third observing run (O3b) since pairs in O3a were studied in Abbott et al. [222].

## 13.2 Methods

Here we use the `hanabi` [224] pipeline, which implements the Bayesian statistical framework described in Chapter 11. It uses the nested sampling algorithm `dynesty` [202], and implement the joint PE with the help of `bilby` [200, 235]. `hanabi` [224] first performs a joint inference on a signal pair by constructing a joint likelihood function that is a product of the likelihood function for each individual event, with a joint prior distribution. The latter is defined for a set of joint parameters that can simultaneously describe both signals if they are truly lensed, for example, the masses and the spins, as well as a set of parameters that are different for each of the signals such as the time of arrival, the apparent luminosity distance, and the Morse phase factor associated to each of the lensed signals. The joint parameter space is explored with the package `hanabi.inference` [224]. The inference result is then reweighted with an astrophysically motivated prior distribution; for example, the astrophysical prior distribution for the redshifted component masses would be dependent on both the population model for the intrinsic binary black hole (BBH) masses and the redshift distribution of the sources. However, the true source redshift cannot be determined from GW observations alone since the true source redshift is degenerate with the magnification from strong lensing. To compute the Bayes factor $\mathcal{B}^{\mathrm{L}}_{\mathrm{U}}$, an indicator of the preference of the lensed hypothesis L over the unlensed hypothesis U, the source redshift which serves as a hyper-parameter for the signal pair must be marginalized over. Selection effects enter as a normalization constant to the marginal data likelihood. This procedure is implemented in `hanabi.hierarchical` with the help of GWPOPULATION [236]. The ratio of unnormalized evidences calculated under the lensed hypothesis and the unlensed hypothesis using this astrophysical prior is referred to as the population-weighted

coherence ratio $C_{\mathrm{U}}^{\mathrm{L}}\big|_{\mathrm{pop}}$, while the ratio of normalized evidences that accounts for both population prior and selection effects is referred to as the Bayes factor $\mathcal{B}_{\mathrm{U}}^{\mathrm{L}}$ in this analysis. We follow our fiducial singular isothermal sphere (SIS) lensing model when computing the magnification prior [222]. This analysis however does not impose any informative prior on the time delay or the image types from the lensing model.

In particular, the analysis presented here uses IMRPhenomXPHM [199] as the waveform model, with an additional Morse phase applied to each of the waveform polarizations in the frequency domain. Other inputs, such as the power spectral density estimates and the calibration envelopes, are chosen to match the analyses done in the GWTC-3 catalog paper [12]. Following the same prescriptions of the other analyses, we fix the BBH population model to the Power-Law + Peak model for the primary masses and the merger rate history to Madau–Dickinson star-formation rate [237] normalized by the median GWTC-3 rate [14].

### 13.3 Results

Our main results are presented in Fig. 13.1, where the left column indicates the event pairs and the horizontal axis their $\mathcal{B}_{\mathrm{U}}^{\mathrm{L}}$. There we can observe that none of the event pairs shows support for the lensing hypothesis, i.e., all $\mathcal{B}_{\mathrm{U}}^{\mathrm{L}} < 1$. The pair with highest $\mathcal{B}_{\mathrm{U}}^{\mathrm{L}}$ is GW190620_030421 – GW200216_220804, for an evidence against lensing of $\sim 1/100$ with the fiducial merger rate density model following the Madau-Dickinson star-formation rate. As a robustness check of how using different merger rate density models would change the results, we repeat the calculations using two more models, namely $R_{\mathrm{min}}(z)$ and $R_{\mathrm{max}}(z)$ from our previous O3a analysis [222] that minimally and maximally bracket many existing population-synthesis results [238, 239, 240, 241]. We see that while the exact values for the Bayes factor change with the use of different merger rate density models, the conclusion remains that there is no support for the lensing hypothesis in any of the event pairs analyzed. To further assess the significance of these pairs we also include a color code to indicate the probability of having an astrophysical

origin $p_{\rm astro}^{\rm pair}$, defined as the product of the highest $p_{\rm astro}$ of each event reported in the GWTC-3 catalog paper [12] by different pipelines. In conclusion, we find no evidence of multiply imaged events.

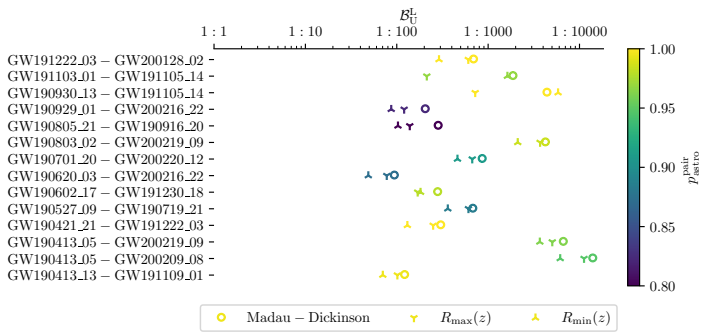


Figure 13.1: Bayes factors $\mathcal{B}^{\rm L}_{\rm U}$ from `hanabi` for the highest-ranked multiple-image candidate pairs. As a check on the robustness of our results, we show the Bayes factors calculated using three different merger rate density models, namely the fiducial model tracking the Madau–Dickinson star-formation rate [237], and also the $R_{\rm min}(z)$ and $R_{\rm max}(z)$ model introduced in Abbott et al. [222]. The color for each marker represents the value of $p_{\rm astro}^{\rm pair}$ for each pair, which is the probability that both of the signals from a pair are of astrophysical origins and not from terrestrial sources.

## 13.4 Conclusion

We have extended the search for lensing signatures to all BBH candidates with a probability of astrophysical origin higher than 0.5 from O3b [12]. Interesting sub-threshold/super-threshold pairs and pairs formed from two super-threshold events with a false-positive probability from either the posterior overlap analysis or the ML classification smaller than $10^{-2}$ as reported in Ref. [234] were further analyzed for their probability of being from a single, strongly lensed source by conducting full joint Bayesian inference analyses that take population priors and selection effects into account. We found no pairs that show significant evidence for strong lensing.

**Acknowledgements**

The authors also gratefully acknowledge the support of the Science and Technology Facilities Council (STFC) of the United Kingdom, the Max-Planck-Society (MPS), and the State of Niedersachsen/Germany for support of the construction of Advanced LIGO and construction and operation of the GEO600 detector. Additional support for Advanced LIGO was provided by the Australian Research Council. The authors gratefully acknowledge the Italian Istituto Nazionale di Fisica Nucleare (INFN), the French Centre National de la Recherche Scientifique (CNRS) and the Netherlands Organization for Scientific Research, for the construction and operation of the Virgo detector and the creation and support of the EGO consortium. The authors also gratefully acknowledge research support from these agencies as well as by the Council of Scientific and Industrial Research of India, the Department of Science and Technology, India, the Science & Engineering Research Board (SERB), India, the Ministry of Human Resource Development, India, the Spanish Agencia Estatal de Investigación, the Vicepresidència i Conselleria d'Innovació, Recerca i Turisme and the Conselleria d'Educació i Universitat del Govern de les Illes Balears, the Conselleria d'Innovació, Universitats, Ciència i Societat Digital de la Generalitat Valenciana and the CERCA Programme Generalitat de Catalunya, Spain, the National Science Centre of Poland and the Foundation for Polish Science (FNP), the Swiss National Science Foundation (SNSF), the Russian Foundation for Basic Research, the Russian Science Foundation, the European Commission, the European Regional Development Funds (ERDF), the Royal Society, the Scottish Funding Council, the Scottish Universities Physics Alliance, the Hungarian Scientific Research Fund (OTKA), the French Lyon Institute of Origins (LIO), the Belgian Fonds de la Recherche Scientifique (FRS-FNRS), Actions de Recherche Concertées (ARC) and Fonds Wetenschappelijk Onderzoek – Vlaanderen (FWO), Belgium, the Paris Île-de-France Region, the National Research, Development and Innovation Office Hungary (NKFIH), the National Research Foundation of Korea, the Natural Science and Engineering Research Council Canada, Canadian

Foundation for Innovation (CFI), the Brazilian Ministry of Science, Technology, and Innovations, the International Center for Theoretical Physics South American Institute for Fundamental Research (ICTP-SAIFR), the Research Grants Council of Hong Kong, the National Natural Science Foundation of China (NSFC), the Leverhulme Trust, the Research Corporation, the Ministry of Science and Technology (MOST), Taiwan, the United States Department of Energy, the Kavli Foundation, and the Gordon and Betty Moore Foundation. The authors gratefully acknowledge the support of the NSF, STFC, INFN and CNRS for provision of computational resources.

*Chapter 14*

# FOLLOW-UP ANALYSES TO THE SEARCH FOR STRONGLY LENSED GRAVITATIONAL-WAVE SIGNALS FROM THE FULL THIRD OBSERVING RUN OF THE LIGO-VIRGO NETWORK

This chapter contains work from

> J. Janquart et al. "Follow-up Analyses to the O3 LIGO-Virgo-KAGRA Lensing Searches". *Submitted to Mon. Not. Roy. Astron. Soc.* arXiv: 2306.03827 [gr-qc].
> R. K. L. L performed the follow-up analyses on the two pairs of binary black hole merger signals highlighted in this paper using the code `hanabi` and wrote part of the manuscript.
>
> R. K. L. Lo. "denmarf: a Python package for density estimation using masked autoregressive flow". *Submitted to J. Open Source Softw.* DOI: 10.48550/arXiv.2305.14379. arXiv: 2305.14379 [astro-ph.IM].

## 14.1 Introduction

In this chapter, we present follow-up analyzes that *could be applied* to assess the significance of possibly lensed gravitational-wave (GW) events and ascertain what information may be extracted about the lens-source system, and apply these analyzes to two candidate event pairs found in the third observing run (O3) and reported in Ref. [234] as demonstrations, even if these signals did not yield a high significance for any of the lensing hypotheses. Applying these additional analyzes does not lead to any additional evidence for lensing in the candidates that have been examined. However, it does provide important insight into potential avenues to deal with high-significance candidates in future observations.

First, we analyze the GW191103–GW191105 pair for strong lensing, which is discarded in Ref. [234] only after the inclusion of both the population priors

and selection effects. Moreover, since some fainter counterparts are likely to be present in a strongly-lensed multiplet, we also follow up on an additional strongly-lensed candidate containing a super-threshold event GW191230_180458 and a weaker "sub-threshold" event LGW200104_184028 found by the sub-threshold targeted search for lensed counterparts [168] and reported in Ref. [234]. This pair was not followed up in Ref. [234] but then was identified for investigation by a new method [242]. We analyze this pair in more details in this work, showing that it is an intriguing pair but is unlikely to be lensed. Although, ultimately, not confirmed as lensed, such events contain features representative of signatures one could find in genuinely lensed events. It is therefore important to see what sort of follow-up analyzes one could do on such events to have a better grasp on their significance, and to extract a maximum of information about the systems.

We stress that whilst the events discussed in this paper may be treated as though they were lensed, they do not display significant evidence for lensing [234]. The goal of this work is to demonstrate the methodologies that can be used to dig deeper in the case of genuinely lensed events and to better assess the importance of candidates. To represent this, we refer to the events as "lensed candidates" in what follows. Additionally, since the events and event pairs analyzed in this work have been selected because they present interesting features, it is often the case that they lead to higher Bayes factors. However, this is generally not enough to claim lensing, and we would also require to have posteriors converging to a given value of the lensing parameters or a high significance compared to a background before considering an event as lensed.

## 14.2 Methods

Following Ref. [234], we use the `hanabi` code [224] to perform joint-parameter estimation (PE) analyzes on the two event pairs to better characterize the properties of their potential sources. The code also calculates Bayes factors $\mathcal{B}^{\mathrm{L}}_{\mathrm{U}}$ for the lensed hypothesis (denoted by a superscript L) versus the unlensed hypothesis (denoted by a superscript U) based on the Bayesian statistical framework

presented in Chapter 11. The Bayes factors computed not only encode the mutual consistency between the GW signals being jointly analyzed but can also encode their consistency with the information from a lens and a source population model [224]. The lens and the source population model affect both the probability of observing a given set of data, in this case $(d_1, d_2)$, under the lensed and the unlensed hypothesis. Specifically, the lens population model informs the joint probability distribution on the magnification, the image type, and the time delay between images, as well as the optical depth for strong lensing, while the source population model informs the distribution of the (true) redshift and the source parameters of a lensed source. This was already done in Ref. [222] and Ref. [234] using the simple singular isothermal sphere (SIS) lens model.

In practice, it is difficult to write down an analytical form for the above-mentioned joint probability distribution from a lens model except for some simple lens models (e.g., the SIS model), and instead one usually resorts to constructing a surrogate that approximates the probability density function, such as the kernel density estimation (KDE) technique [243]. However, it can be computationally expensive to use KDE-based schemes to construct an estimate for the probability density from a catalog of simulated lensed images that contains many (e.g., millions of) samples, which in turn is evaluated over a set of (roughly tens of thousands of) posterior samples.

To understand more the issue of computational cost with using KDE technique, consider a case where we have a set of $D$-dimensional data of size $N$, $(\vec{x}_1, \vec{x}_2, \ldots, \vec{x}_N)$, i.e., $\vec{x}_i$ is a $D$-dimensional vector where $i \in [1, N]$ that follows the probability distribution $f(\vec{x})$ we wish to approximate. The KDE estimator $\hat{f}_{\rm KDE}$ using those input data is given by [243]

$$\hat{f}_{\rm KDE}(\vec{x}) = \frac{1}{N} \sum_{i=1}^{N} K(\vec{x} - \vec{x}_i), \tag{14.1}$$

where $K$ is the kernel function that depends on the distance between the evaluation point $\vec{x}$ and the input data point $\vec{x}_i$. The cost of $M$ such evaluations using Eq. (14.1)

is therefore $O(MND)$. This can be slow if we need to evaluate the KDE of a large data set (i.e., large $N$) many times (i.e., large $M$). In our case, we want to evaluate the probability density, estimated from a large number ($N \sim 10^7$) of simulated lensed astronomical objects, of two lensed images of a background object having certain magnifications over a set of possible ($M \sim 10^5$) values from a joint-PE analysis.

Here we use the probability density surrogate described in Ref. [167] that fits the joint probability density on the magnification and the image type conditioned on the time delay between images from a catalog of mock lens images used in [178] using a normalization-flow-based method (`denmarf` [244]). The underlying strong lensing model adopted in the simulation is a population of galaxy-scale singular isothermal ellipsoid (SIE) lenses with external shear. The lens-redshift-dependent velocity dispersion function is constructed from hybridizing the velocity dispersion measurement for the local Universe derived from the Sloan Digital Sky Survey Data Release 6 [245] with the Illustris simulation result for the velocity dispersion function at higher lens-redshifts [246]. The ellipticity and the external shear follow a Gaussian distribution and a log-normal distribution, respectively, with additional detail found in [178].

The computational advantage of using a normalizing-flow-based approach is that an evaluation of the estimated density is independent of $N$. Suppose $T(\vec{x})$ maps the target distribution $f(\vec{x})$ into the base distribution $u$, usually chosen as a $D$-dimensional standard normal distribution, then the density estimate using normalizing flow (NF) $\hat{f}_{\rm NF}$ is given by

$$\hat{f}_{\rm NF}(\vec{x}) = u(T(\vec{x}))|J_T(\vec{x})|, \tag{14.2}$$

where $|J_T|$ is the Jacobian determinant of the mapping, and note that there is no summation over the $N$ input data. Fig. 14.1 shows the computational cost for $M = 1000$ evaluations of the density estimate from data of size $N$ using KDE and that using NF, respectively. We can see that the evaluation cost using KDE scales with $N$ while that using NF is indeed independent of $N$.

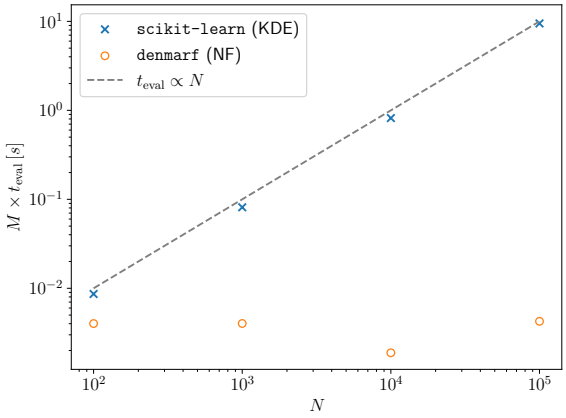


Figure 14.1: Computation cost for $M = 1000$ evaluations of the density estimate from data of size $N$ using KDE with `scikit-learn` [247] and that using NF with `denmarf` [244], respectively. We can see that the evaluation cost using KDE scales with $N$ while that using NF is independent of $N$.

## 14.3 Results

### 14.3.1 GW191103–GW191105

GW191103 and GW191105 were binary black holes (BBHs) detected during the second half of the third observing run (O3b) [12]. In the main LVK analyzes, the standard treatment of the signals revealed nothing out of the ordinary for these events. However, when treating the events as potential lensing candidates, the pair display some intriguing characteristics. For example, there is a notable amount of overlap between some of the reported source parameters, such as the sky location and masses [248]. Moreover, the two events have about two days delay between their merger times which is consistent with galaxy-scale lenses [249, 250]. However, in the LVK lensing search, these events were ultimately discarded once the Bayes factor had been computed [234], meaning that the observed overlap is unlikely to be coming from a lensed BBH and is more likely to be coincidental. Nevertheless, as was stated in the introduction, in the following analyzes we have disregarded this and treated the event as though it were a lensed pair.

Here, we repeat the Bayes factor calculation comparing the probability ratio of the lensed versus the unlensed hypothesis as described in [234] using the more realistic lens population model described in Ref. [178] (see also Ref. [167]) using HANABI [224]. We use the same set of source population models as in Ref. [234], e.g., the POWERLAW + PEAK model for the source masses from the GWTC-3 observations [14] and three models for the merger rate density: Madau-Dickinson [237], $\mathcal{R}_{\rm min}(z)$, and $\mathcal{R}_{\rm max}(z)$. Table 14.1 shows the log-10 Bayes factors computed using the three merger rate density models with the simple SIS lens model reported in Ref. [234] and the SIE + external shear model reported in Ref. [167]. We see that the values calculated using the SIE + external shear model are consistently higher than those using the SIS model, indicating that the pair is more consistent with a more realistic strong lensing model. Still, the $\log_{10}\mathcal{B}^{\rm L}_{\rm U}$ values are negative, and therefore the event pair is most likely unlensed.

| Lens model \ Merger rate density | Madau-Dickinson | $\mathcal{R}_{\rm min}(z)$ | $\mathcal{R}_{\rm max}(z)$ |
|---|---|---|---|
| SIS | −3.27 | −3.21 | −2.33 |
| SIE + external shear | −2.60 | −2.46 | −1.28 |

Table 14.1: $\log_{10}\mathcal{B}^{\rm L}_{\rm U}$ for the GW191103–GW191105 pair from `hanabi` assuming three different merger rate density models and two different lens models. The values computed using the SIS model are reproduced from Ref. [234] for the sake of comparison. We see that the values with the SIE + external shear model are consistently higher than that with the SIS model, indicating a higher compatibility of the pair with a more realistic strong lensing model. However, since the values remain negative, the event is still most likely to be unlensed considering a more realistic lensing population with the most recent population models.

### 14.3.2 GW191230_180458–LGW200104_180425

During the O3 sub-threshold lensing counterpart search, the TESLA pipeline [168] based on the GSTLAL software [186, 251] found roughly 470 triggers which could be potential strong lensing counterparts to the super-threshold events. Of these, two had a false-alarm rate (FAR) lower than 1 in 69 years [234] though none

were found to have support for the lensing hypothesis and all were ultimately discarded. An alternative method for identifying the sub-threshold triggers as possible lensed counterparts to super-threshold events, developed in Goyal et al. [242], uses the BAYESTAR localization skymaps, matched-filter chirp mass estimates and the time delay priors to rank all the super-sub pairs. It identifies the sub-threshold event termed LGW200104_180425[1] as a possible lensed counterpart to the super-threshold GW191230_180458 event. It is the most promising super-sub pair according to this method as it has significant sky and mass overlap, coupled with the magnifications and the time delay matching their expected values from a galaxy-scale lens model (see Goyal et al. [242] for more detail). In the rest of this section, we denote the super-threshold and the sub-threshold events GW191230 and LGW200104, respectively, for brevity.

LGW200104 was detected with both the Laser Interferometer Gravitational-Wave Observatory (LIGO) detectors with an signal-to-noise ratio (SNR) of 6.31 in Hanford and 4.94 in Livingston. The GSTLAL matched-filter estimates on its chirp mass place it at $67.39M_{\odot}$ with the individual component masses being $82.48M_{\odot}$ and $72.71M_{\odot}$. These high component masses combined with the faintness of the signal contribute to a very low $p_{\text{astro}}$ of 0.01 from the usual unlensed super-threshold searches. The event was also found with the SPIIR [252, 253] and cWB [254] pipelines, signifying a significant lack of probability of the event being a genuine detection. Likewise, the FAR found for this event during the super-threshold searches is $4824/\text{yr}$, also favoring a terrestrial origin for the signal [255]. Since the sub-threshold searches have a more focused template bank, they also reduce the FAR for the events when they are in the correct region of the parameter space [189, 168]. Therefore, the FAR for the event decreases to $6.59/\text{yr}$ when it is found with the TESLA pipeline [168], still higher than the threshold used for following-up on sub-threshold events in O3 [234]. In

[1]Here, we follow the usual naming convention, adding an L at the start of the event name to specify it is a sub-threshold candidate. Therefore the name of the sub-threshold trigger is LGWYYMMDD_hhmmss, where YY is the year, MM the month, DD the day, hh the hour, mm the minutes and ss the second in UTC time.

keeping with the analyzes done within this work, whilst we do not claim that the event is both genuine and genuinely lensed, we treat it as though it were. Consequently, we investigate the pair using the lensing identification tools used for super-threshold pairs.

This GW191230-LGW200104 pair was also analyzed by the full joint-PE code HANABI [224] where the joint parameter space of the two events was simultaneous explored by the stochastic sampler DYNESTY [202] with settings identical to those used in [234]. In particular, Fig. 14.2 shows the posterior probability mass function for the possible image types of the GW191230-LGW200104 pair. We see that the image type configurations for the two events that have non-zero support have the difference in the Morse phase factor $\Delta n$ either 0 (i.e., the I-I, II-II and III-III configuration) or 0.5 (i.e., the II-I and III-II configuration).

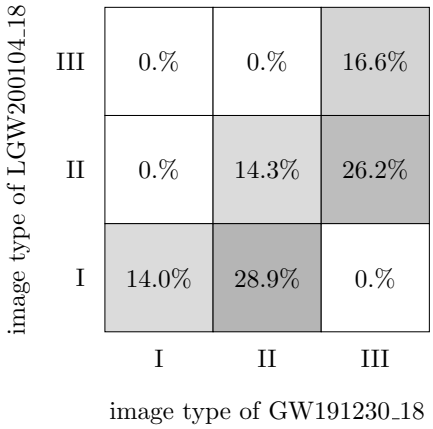


Figure 14.2: Posterior probability mass function for the image type of GW191230 and the image type of LGW200104 from `hanabi`. It is more likely for the difference in Morse factor $\Delta n$ to be $\Delta n = 0.5$ (i.e., the II-I and III-II configuration) than to be $\Delta n = 0$ (i.e., the I-I, II-II and III-III configuration).

We also performed the Bayes factor calculation comparing the probability ratio of the lensed versus the unlensed hypothesis for this pair in the same fashion that we did for the GW191103–GW191105 pair as in Sec. 14.3.1. Again, we use the same set of source population models as in Ref. [234], e.g., the POWERLAW

| Lens model \ Merger rate density | Madau-Dickinson | $\mathcal{R}_{\rm min}(z)$ | $\mathcal{R}_{\rm max}(z)$ |
|---|---|---|---|
| SIS | −0.76 | −0.35 | −0.57 |
| SIE + external shear | 0.14 | 0.57 | 0.30 |

Table 14.2: $\log_{10}\mathcal{B}^{\rm L}_{\rm U}$ for the GW191230 and LGW200104 pair from HANABI assuming three different merger rate density models and two different lens models. We see that the values with the SIE + external shear model are all positive (but only mildly) and consistently higher than that with the SIS model which are all negative, indicating a higher compatibility of the pair with a more realistic strong lensing model. Note that the calculations assumed that both GW events are astrophysical of origin. These values are not sufficient to claim the event pair to be lensed as we would require a positive $\log_{10}$ posterior odds, and the observed Bayes factors are not high enough to balance the low prior odds for strong lensing.

+ PEAK model for the source masses from the GWTC-3 observations [14] and three models for the merger rate density: Madau-Dickinson [237], $\mathcal{R}_{\rm min}(z)$, and $\mathcal{R}_{\rm max}(z)$. Table 14.2 shows the $\log_{10}$ Bayes factors computed using the three merger rate density models with the simple SIS lens model [234] and the SIE + external shear model [167]. We see that the values calculated using the SIE + external shear model are positive but only mildly ($< 1$), and they are also consistently higher than the values computed using the SIS model (which are all negative), indicating that the pair is more consistent with a more realistic strong lensing model. It should be noted that the calculations assumed that both GW events are astrophysical of origin and the second is treated as a super-threshold event.

Despite some of the evidence for this event aligning relatively well with the expectations for a strongly lensed event, there remain several key arguments against a claim of strong lensing for this pair. The first is that whilst it is the case that the event has the highest currently observed Bayes factor, it is insufficient to yield a positive log posterior odds considering that the $\log_{10}$ prior odds is between $-2$ and $-4$ [177, 178, 179, 180, 181, 249]. The second argument is

the nature of the trigger itself. There is no clear evidence that the sub-threshold event is a genuine GW detection.

In the end, although the event pair is unlikely to be lensed, the analyses performed on this event pair serve as a powerful demonstration of the necessity for searching for such sub-threshold counterparts and the kinds of information that they may yield.

## 14.4 Conclusion

In this work, we have analyzed candidates found to be interesting by the LIGO-Virgo-KAGRA lensing searches in the full O3 data [234] as though they were genuinely strongly-lensed.

The GW191103–GW191105 pair we considered here was flagged in Ref. [234] as interesting because of its relatively high coherence ratio and the consistency of the relative amplitudes and time separation with the expectations for the relative magnification and time delay of galaxy lenses. We demonstrate that by including a more realistic SIE model in our analysis, a negative log Bayes factor is obtained disfavoring the lensing hypothesis for this pair.

A new ranking scheme for the sub-threshold counterparts of detected super-threshold events found a new interesting candidate pair: the GW191230_180458 super-threshold and the LGW200104_180425 sub-threshold events. As was done for the other event pairs reported in Ref. [234], we analyzed this pair using the standard and follow-up tools. Analysis with the joint PE showed that upon the inclusion of a galaxy-lens model, the coherence ratio was higher than for the GW191103–GW191105 pair. The computation of the proper Bayes factor with an SIS model leads to negative log Bayes factor, disfavoring the lensing hypothesis. On the other hand, the inclusion of an SIE lens model leads to a marginally positive log Bayes factor. However, it is not high enough to compensate for the prior odds, and therefore the posterior odds is disfavoring the lensing hypothesis.

Though the events investigated do not display strong evidence of being lensed, the

analyses done here demonstrate possible follow-up strategies for future observing runs in order to assess the significance of any lensing candidate event.

**Acknowledgements**

The authors thank Aditya Vijaykumar for the useful discussion, providing some scripts to generate plots, and carefully re-reading the manuscript. The authors thank Christopher Berry for useful discussions on $p_{\rm astro}$.

The authors are grateful for computational resources provided by the LIGO laboratory and Cardiff University and supported by the National Science Foundation Grants PHY-0757058 and PHY-0823459, and the STFC grant ST/I006285/1, respectively. The authors are also grateful to the Inter-University Center for Astronomy & Astrophysics (IUCAA), Pune, India for additional computational resources.

This material is based upon work supported by NSF's LIGO Laboratory which is a major facility fully funded by the National Science Foundation. The authors also gratefully acknowledge the support of the Science and Technology Facilities Council (STFC) of the United Kingdom, the Max-Planck-Society (MPS), and the State of Niedersachsen/Germany for support of the construction of Advanced LIGO and construction and operation of the GEO 600 detector. Additional support for Advanced LIGO was provided by the Australian Research Council. The authors gratefully acknowledge the Italian Istituto Nazionale di Fisica Nucleare (INFN), the French Centre National de la Recherche Scientifique (CNRS) and the Netherlands Organization for Scientific Research (NWO), for the construction and operation of the Virgo detector and the creation and support of the EGO consortium. The authors also gratefully acknowledge research support from these agencies as well as by the Council of Scientific and Industrial Research of India, the Department of Science and Technology, India, the Science & Engineering Research Board (SERB), India, the Ministry of Human Resource Development, India, the Spanish Agencia Estatal de Investigación (AEI), the Spanish Ministerio

de Ciencia e Innovación and Ministerio de Universidades, the Conselleria de Fons Europeus, Universitat i Cultura and the Direcció General de Política Universitaria i Recerca del Govern de les Illes Balears, the Conselleria d'Innovació, Universitats, Ciéncia i Societat Digital de la Generalitat Valenciana and the CERCA Programme Generalitat de Catalunya, Spain, the National Science Centre of Poland and the European Union – European Regional Development Fund; Foundation for Polish Science (FNP), the Swiss National Science Foundation (SNSF), the Russian Foundation for Basic Research, the Russian Science Foundation, the European Commission, the European Social Funds (ESF), the European Regional Development Funds (ERDF), the Royal Society, the Scottish Funding Council, the Scottish Universities Physics Alliance, the Hungarian Scientific Research Fund (OTKA), the French Lyon Institute of Origins (LIO), the Belgian Fonds de la Recherche Scientifique (FRS-FNRS), Actions de Recherche Concerées (ARC) and Fonds Wetenschappelijk Onderzoek – Vlaanderen (FWO), Belgium, the Paris Ile-de-France Region, the National Research, Development and Innovation Office Hungary (NKFIH), the National Research Foundation of Korea, the Natural Science and Engineering Research Council Canada, Canadian Foundation for Innovation (CFI), the Brazilian Ministry of Science, Technology, and Innovations, the International Center for Theoretical Physics South American Institute for Fundamental Research (ICTP-SAIFR), the Research Grants Council of Hong Kong, the National Natural Science Foundation of China (NSFC), the Leverhulme Trust, the Research Corporation, the National Science and Technology Council (NSTC), Taiwan, the United States Department of Energy, and the Kavli Foundation. The authors gratefully acknowledge the support of the NSF, STFC, INFN and CNRS for provision of computational resources. This work was supported by MEXT, JSPS Leading-edge Research Infrastructure Program, JSPS Grant-in-Aid for Specially Promoted Research 26000005, JSPS Grant-inAid for Scientific Research on Innovative Areas 2905: JP17H06358, JP17H06361 and JP17H06364, JSPS Core-to-Core Program A. Advanced Research Networks, JSPS Grantin-Aid for Scientific Research (S) 17H06133 and 20H05639, JSPS Grant-in-Aid

for Transformative Research Areas (A) 20A203: JP20H05854, the joint research program of the Institute for Cosmic Ray Research, University of Tokyo, National Research Foundation (NRF), Computing Infrastructure Project of Global Science experimental Data hub Center (GSDC) at KISTI, Korea Astronomy and Space Science Institute (KASI), and Ministry of Science and ICT (MSIT) in Korea, Academia Sinica (AS), AS Grid Center (ASGC) and the National Science and Technology Council (NSTC) in Taiwan under grants including the Rising Star Program and Science Vanguard Research Program, Advanced Technology Center (ATC) of NAOJ, and Mechanical Engineering Center of KEK.

J. Janquart and C. Van Den Broeck are supported by the research programme of the Netherlands Organisation for Scientific Research (NWO). S.Goyal is supported by the Department of Atomic Energy, Government of India. J.M. Ezquiaga is supported by the European Union's Horizon 2020 research and innovation program under the Marie Sklodowska-Curie grant agreement No. 847523 INTERACTIONS, and by VILLUM FONDEN (grant no. 53101 and 37766).Á. Garrón, D. Keitel, P. Cremonese and S. Husa are supported by the Universitat de les Illes Balears (UIB); the Spanish Ministry of Science and Innovation (MCIN) and the Spanish Agencia Estatal de Investigación (AEI) grants PID2019-106416GB-I00/MCIN/AEI/10.13039/501100011033, RED2022-134204-E, RED2022-134411-T; the MCIN with funding from the European Union NextGenerationEU (PRTR-C17.I1); the FEDER Operational Program 2021–2027 of the Balearic Islands; the Comunitat Autònoma de les Illes Balears through the Direcció General de Política Universitaria i Recerca with funds from the Tourist Stay Tax Law ITS 2017-006 (PRD2018/23, PDR2020/11); the Conselleria de Fons Europeus, Universitat i Cultura del Govern de les Illes Balears; and EU COST Action CA18108. Á. Garrón is supported through SOIB, the Conselleria de Fons Europeus, Universitat i Cultura and the Conselleria de Model Econòmic, Turisme i Treball with funds from the Mecanisme de Recuperació i Resiliència (PRTR, NextGenerationEU). D. Keitel is supported by the Spanish Ministerio de Ciencia, Innovación y Universidades (ref. BEAGAL 18/00148) and cofinanced by UIB. The authors

thank the Supercomputing and Bioinnovation Center (SCBI) of the University of Malaga for their provision of computational resources and technical support (www.scbi.uma.es/site) and thankfully acknowledge the computer resources at Picasso and the technical support provided by Barcelona Supercomputing Center (BSC) through grants No. AECT-2022-1-0024, AECT-2022-2-0028, AECT-2022-3-0024, and AECT-2023-1-0023 from the Red Española de Supercomputación (RES). J. Garcia-Bellido acknowledges support from the Spanish Research Project PID2021-123012NB-C43 [MICINN-FEDER], and the Centro de Excelencia Severo Ochoa Program CEX2020-001007-S at IFT. Prasia P. would like to thank Prof. Sukanta Bose for his support and IUCAA, Pune for providing computational facilities. A. K.Y. Li and R. K. L. Lo are supported by the National Science Foundation Grants PHY-1912594 and PHY-2207758. A. Mishra would like to thank the University Grants Commission (UGC), India, for financial support as a research fellow.

*Chapter 15*

# CONCLUDING REMARKS OF PART II

In Part II of the thesis, we first developed a Bayesian statistical framework that enables us to identify strongly-lensed GWs and at the same time infer their true source properties in a way that are unaffected by strong lensing. The framework also allows us to naturally and consistently impart our assumptions on the population properties of both the GW source and the gravitational lens, which in turn changes the probability that a given set of GW events being the strongly-lensed images of the same source.

This framework forms the basis of a strong lensing analysis code `hanabi` used by the LVK collaboration. Indeed, this code was used by the collaboration to look for possibly strongly-lensed BBHs in the O3a data, where the analysis results from `hanabi` were presented in Chapter 12, and in the entire O3 data with the analysis results presented in Chapter 13, respectively.

While we did not find any statistically significant evidence supporting the claim of having strongly-lensed BBHs in the O3 data, we went ahead and further followed up two interesting candidate BBH pairs in O3 being strongly-lensed in Chapter 14. By treating them as if they are lensed, we demonstrated what consistency checks we could do to further consolidate the strong lensing claim. In particular, in Chapter 14, we incorporated the results of a realistic simulation of many background sources being strongly-lensed by galaxy-scale foreground lenses and re-calculated the Bayes factor for a pair of BBHs being strongly-lensed versus simply being two distinct BBH systems. While the Bayes factors for the two candidate pairs both went up by a small fraction, it is still far from being sufficient for us to confidently claim that they are strongly-lensed BBHs.

In order to exploit the full science of strongly-lensed GW signals, one will need to identify and associate the lensed GW source with the foreground lens responsible for the strong lensing. Instead of only correlating the GW inference result with existing lens catalogs, which is what was done in Ref. [183] and Ref. [248], we can consider extragalactic object catalogs (such as the Sloan Digital Sky Survey (SDSS), and in the future Legacy Survey of Space and Time (LSST)), usually from ground-based telescopes, and perform joint GW+EM modeling of the potential lens system. As a quick proof-of-concept (for an illustration see Figure 15.1), let us for now use the toy SIS model and assume that the candidate object is a galaxy. By combining EM and GW data, we can compute the Einstein radius $\theta_{\rm E}$ of the lens for each sample of the source redshift from the GW inference, with the redshift $z_{\rm lens}$ and the velocity dispersion $\sigma_v$ of the galaxy from those catalogs. The time delay $\Delta t$ between the would-be lensed GWs serves to constrain the possible source position and image positions as an implicit equation. For each of the possible configurations, we can then compute the expected magnification of the would-be lensed GWs and compare them with GW inference result. We can then rule out inconsistent foreground objects from the candidate list. In actual analyses we would need to use a more sophisticated lens model but the concept stays the same. After narrowing down the list to only contain a few targets, we can submit a proposal requesting space telescope time specifically to observe these possible lenses to get much better measurements for the modeling. With the lens responsible for the lensing identified, the detection of gravitationally-lensed GWs can be claimed assertively.

While Part II of this thesis and much of the literature on GW lensing focus on strong lensing, weak lensing in the EM spectrum has been proven equally useful to cosmological measurements. For instance, the weak lensing of photons from the cosmic microwave background was used to map the distribution of (both luminous and dark) matter. As a result, the map allows us to constrain cosmological parameters and the sum of neutrino masses (for example, see Refs. [256, 257, 258]). It would be interesting to further investigate how weak

lensing of GWs would play a role in cosmography and fundamental physics.

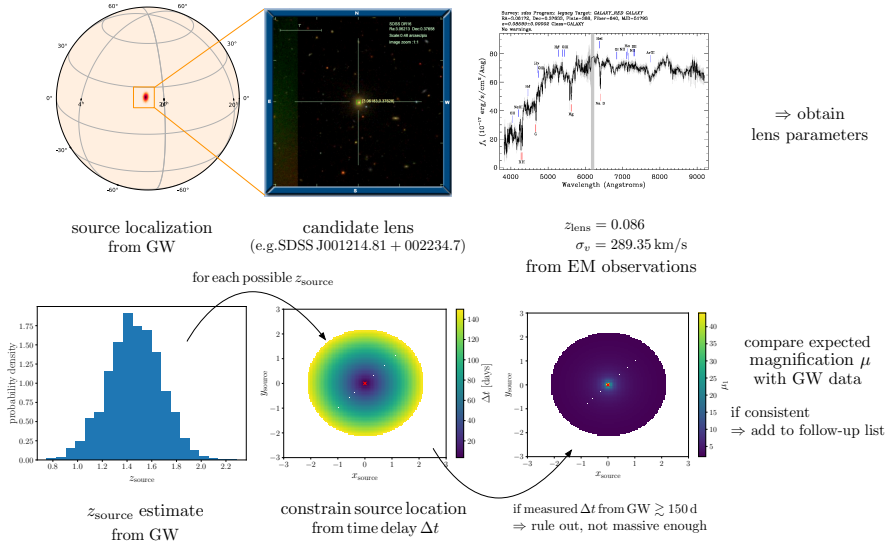


Figure 15.1: Procedures for the proposed joint GW+EM modeling and identification of a lens. The SDSS image (upper middle panel) and spectrum (upper right panel) were taken from SDSS DR16 [259]. The lens equation was solved using `lenstronomy` [260].

# Epilogue

*Chapter 16*

# SUMMARY AND OUTLOOK

In this thesis, I have explored two new arenas of GW physics, namely probing the nature of a merger remnant using the speculative GW echoes when the remnant is an ECO in the first part of the thesis and the strong gravitational lensing of GWs in the second part of the thesis, and have contributed to the two subjects from both data-analysis and theoretical perspectives.

While both searches for ECOs using GW echoes and strong lensing of GWs returned null results, we can still place limits with the null detections and they also serve as good practices should they actually occur. More importantly, many of the tools and the techniques developed in this thesis can also be used in other research topics. For example, the GSN formalism in Chapter 4 was originally motivated by the need of directly computing the in-going gravitational radiation towards a BH due to a plunging particle for the echo waveform calculation described in Chapter 5. The same formalism can also be used to compute excitation factors of various QNMs for Kerr BHs, which will be tremendously useful in the study of gravitational QNMs and their searches in GW data.

Admittedly, the search for the theorized ECOs using GW echoes as their possible waveform signatures are speculative at best and are unlikely to be detectable with current-generation GW detectors even with our own calculations. As for the strong gravitational lensing of gravitational waves, even though it is predicted in GR and hence way less speculative compared to GW echoes, the expected relative rate of observing strongly-lensed GWs to observing un-lensed GWs is very low. All that being said, these are high-reward researches that would have profound impacts if they are seen in data, hence the title of this thesis — they are gravitational-wave exotica.

# BIBLIOGRAPHY

[1] LIGO Scientific Collaboration. "Advanced LIGO". In: *Class. Quant. Grav.* 32 (2015), p. 074001. DOI: 10.1088/0264-9381/32/7/074001. arXiv: 1411.4547 [gr-qc].

[2] VIRGO Collaboration. "Advanced Virgo: a second-generation interferometric gravitational wave detector". In: *Class. Quant. Grav.* 32.2 (2015), p. 024001. DOI: 10.1088/0264-9381/32/2/024001. arXiv: 1408.3978 [gr-qc].

[3] H. Luck et al. "The upgrade of GEO600". In: *J. Phys. Conf. Ser.* 228 (2010). Ed. by Z. Marka and S. Marka, p. 012012. DOI: 10.1088/1742-6596/228/1/012012. arXiv: 1004.0339 [gr-qc].

[4] C. Affeldt et al. "Advanced techniques in GEO 600". In: *Class. Quant. Grav.* 31.22 (2014), p. 224002. DOI: 10.1088/0264-9381/31/22/224002.

[5] K. L. Dooley et al. "GEO 600 and the GEO-HF upgrade program: successes and challenges". In: *Class. Quant. Grav.* 33 (2016), p. 075009. DOI: 10.1088/0264-9381/33/7/075009. arXiv: 1510.00317 [physics.ins-det].

[6] KAGRA Collaboration. "Detector configuration of KAGRA: The Japanese cryogenic gravitational-wave detector". In: *Class. Quant. Grav.* 29 (2012). Ed. by M. Hannam, P. Sutton, S. Hild, et al., p. 124007. DOI: 10.1088/0264-9381/29/12/124007. arXiv: 1111.7185 [gr-qc].

[7] KAGRA Collaboration. "Interferometer design of the KAGRA gravitational wave detector". In: *Phys. Rev. D* 88.4 (2013), p. 043007. DOI: 10.1103/PhysRevD.88.043007. arXiv: 1306.6747 [gr-qc].

[8] KAGRA Collaboration. "Overview of KAGRA: Detector design and construction history". In: *PTEP* 2021.5 (2021), 05A101. DOI: 10.1093/ptep/ptaa125. arXiv: 2005.05574 [physics.ins-det].

[9] LIGO Scientific, Virgo Collaboration. "GWTC-1: A Gravitational-Wave Transient Catalog of Compact Binary Mergers Observed by LIGO and Virgo during the First and Second Observing Runs". In: *Phys. Rev. X*

9.3 (2019), p. 031040. DOI: 10.1103/PhysRevX.9.031040. arXiv: 1811.12907 [astro-ph.HE].

[10] LIGO Scientific, Virgo Collaboration. "GWTC-2: Compact Binary Coalescences Observed by LIGO and Virgo During the First Half of the Third Observing Run". In: *Phys. Rev. X* 11 (2021), p. 021053. DOI: 10.1103/PhysRevX.11.021053. arXiv: 2010.14527 [gr-qc].

[11] LIGO Scientific, VIRGO Collaboration. "GWTC-2.1: Deep Extended Catalog of Compact Binary Coalescences Observed by LIGO and Virgo During the First Half of the Third Observing Run". *Submitted to Phys. Rev. D*. arXiv: 2108.01045 [gr-qc].

[12] LIGO Scientific, VIRGO, KAGRA Collaboration. "GWTC-3: Compact Binary Coalescences Observed by LIGO and Virgo During the Second Part of the Third Observing Run". *Submitted to Phys. Rev. X*. arXiv: 2111.03606 [gr-qc].

[13] LIGO Scientific, Virgo Collaboration. "Binary Black Hole Population Properties Inferred from the First and Second Observing Runs of Advanced LIGO and Advanced Virgo". In: *Astrophys. J. Lett.* 882.2 (2019), p. L24. DOI: 10.3847/2041-8213/ab3800. arXiv: 1811.12940 [astro-ph.HE].

[14] LIGO Scientific, VIRGO, KAGRA Collaboration. "The population of merging compact binaries inferred using gravitational waves through GWTC-3". In: *Phys. Rev. X* 13.1 (2023), p. 011048. DOI: 10.1103/PhysRevX.13.011048. arXiv: 2111.03634 [astro-ph.HE].

[15] LIGO Scientific, Virgo Collaboration. "GW170817: Measurements of neutron star radii and equation of state". In: *Phys. Rev. Lett.* 121.16 (2018), p. 161101. DOI: 10.1103/PhysRevLett.121.161101. arXiv: 1805.11581 [gr-qc].

[16] LIGO Scientific, Virgo Collaboration. "GW170817: Observation of Gravitational Waves from a Binary Neutron Star Inspiral". In: *Phys. Rev. Lett.* 119.16 (2017), p. 161101. DOI: 10.1103/PhysRevLett.119.161101. arXiv: 1710.05832 [gr-qc].

[17] LIGO Scientific, Virgo, Fermi GBM, INTEGRAL, IceCube, AstroSat Cadmium Zinc Telluride Imager Team, IPN, Insight-Hxmt, ANTARES, Swift, AGILE Team, 1M2H Team, Dark Energy Camera GW-EM, DES,

DLT40, GRAWITA, Fermi-LAT, ATCA, ASKAP, Las Cumbres Observatory Group, OzGrav, DWF (Deeper Wider Faster Program), AST3, CAASTRO, VINROUGE, MASTER, J-GEM, GROWTH, JAGWAR, CaltechNRAO, TTU-NRAO, NuSTAR, Pan-STARRS, MAXI Team, TZAC Consortium, KU, Nordic Optical Telescope, ePESSTO, GROND, Texas Tech University, SALT Group, TOROS, BOOTES, MWA, CALET, IKI-GW Follow-up, H.E.S.S., LOFAR, LWA, HAWC, Pierre Auger, ALMA, Euro VLBI Team, Pi of Sky, Chandra Team at McGill University, DFN, ATLAS Telescopes, High Time Resolution Universe Survey, RIMAS, RATIR, SKA South Africa/MeerKAT Collaboration. "Multi-messenger Observations of a Binary Neutron Star Merger". In: *Astrophys. J. Lett.* 848.2 (2017), p. L12. DOI: 10.3847/2041-8213/aa91c9. arXiv: 1710.05833 [astro-ph.HE].

[18] LIGO Scientific, Virgo, 1M2H, Dark Energy Camera GW-E, DES, DLT40, Las Cumbres Observatory, VINROUGE, MASTER Collaboration. "A gravitational-wave standard siren measurement of the Hubble constant". In: *Nature* 551.7678 (2017), pp. 85–88. DOI: 10.1038/nature24471. arXiv: 1710.05835 [astro-ph.CO].

[19] LIGO Scientific, Virgo Collaboration. "Tests of general relativity with GW150914". In: *Phys. Rev. Lett.* 116.22 (2016). [Erratum: Phys.Rev.Lett. 121, 129902 (2018)], p. 221101. DOI: 10.1103/PhysRevLett.116.221101. arXiv: 1602.03841 [gr-qc].

[20] LIGO Scientific, Virgo Collaboration. "Tests of General Relativity with GW170817". In: *Phys. Rev. Lett.* 123.1 (2019), p. 011102. DOI: 10.1103/PhysRevLett.123.011102. arXiv: 1811.00364 [gr-qc].

[21] LIGO Scientific, Virgo Collaboration. "Tests of general relativity with binary black holes from the second LIGO-Virgo gravitational-wave transient catalog". In: *Phys. Rev. D* 103.12 (2021), p. 122002. DOI: 10.1103/PhysRevD.103.122002. arXiv: 2010.14529 [gr-qc].

[22] LIGO Scientific, Virgo Collaboration. "Tests of General Relativity with the Binary Black Hole Signals from the LIGO-Virgo Catalog GWTC-1". In: *Phys. Rev. D* 100.10 (2019), p. 104036. DOI: 10.1103/PhysRevD.100.104036. arXiv: 1903.04467 [gr-qc].

[23] LIGO Scientific, VIRGO, KAGRA Collaboration. “Tests of General Relativity with GWTC-3”. *In press; accepted by Phys. Rev. D*. arXiv: 2112.06861 [gr-qc].

[24] D. Rickles and C. M. DeWitt. *The Role of Gravitation in Physics: Report from the 1957 Chapel Hill Conference*. Feb. 2011.

[25] P. R. Saulson. *Fundamentals of Interferometric Gravitational Wave Detectors*. 2nd. ed. World Scientific, 2017. ISBN: 978-981-314-307-4, 978-981-314-620-4. DOI: 10.1142/10116.

[26] LIGO Scientific, Virgo Collaboration. “Observation of Gravitational Waves from a Binary Black Hole Merger”. In: *Phys. Rev. Lett.* 116.6 (2016), p. 061102. DOI: 10.1103/PhysRevLett.116.061102. arXiv: 1602.03837 [gr-qc].

[27] KAGRA, LIGO Scientific, Virgo, VIRGO Collaboration. “Prospects for observing and localizing gravitational-wave transients with Advanced LIGO, Advanced Virgo and KAGRA”. In: *Living Rev. Rel.* 21.1 (2018), p. 3. DOI: 10.1007/s41114-020-00026-9. arXiv: 1304.0670 [gr-qc].

[28] LIGO Scientific Collaboration. “Exploring the Sensitivity of Next Generation Gravitational Wave Detectors”. In: *Class. Quant. Grav.* 34.4 (2017), p. 044001. DOI: 10.1088/1361-6382/aa51f4. arXiv: 1607.08697 [astro-ph.IM].

[29] D. Reitze et al. “Cosmic Explorer: The U.S. Contribution to Gravitational-Wave Astronomy beyond LIGO”. In: *Bull. Am. Astron. Soc.* 51.7 (2019), p. 035. arXiv: 1907.04833 [astro-ph.IM].

[30] M. Punturo et al. “The third generation of gravitational wave observatories and their science reach”. In: *Class. Quant. Grav.* 27 (2010). Ed. by Z. Marka and S. Marka, p. 084007. DOI: 10.1088/0264-9381/27/8/084007.

[31] LISA Collaboration. “Laser Interferometer Space Antenna”. Feb. 2017. arXiv: 1702.00786 [astro-ph.IM].

[32] S. Kawamura et al. “Current status of space gravitational wave antenna DECIGO and B-DECIGO”. In: *Prog. Theor. Exp. Phys.* 2021.5 (2021), 05A105. DOI: 10.1093/ptep/ptab019. arXiv: 2006.13545 [gr-qc].

[33] S. Xin, B. Chen, R. K. L. Lo, et al. "Gravitational-wave echoes from spinning exotic compact objects: Numerical waveforms from the Teukolsky equation". In: *Phys. Rev. D* 104.10 (2021), p. 104005. DOI: 10.1103/PhysRevD.104.104005. arXiv: 2105.12313 [gr-qc].

[34] M. Srivastava and Y. Chen. "Gravitational radiation close to a black hole horizon: Waveform regularization and the out-going echo". In: *Phys. Rev. D* 104.10 (2021), p. 104006. DOI: 10.1103/PhysRevD.104.104006. arXiv: 2108.01329 [gr-qc].

[35] R. K. L. Lo, M. Srivastava, S. Xin, et al. "Recipes for computing radiation from a Kerr black hole using Generalized Sasaki-Nakamura formalism: II. Inhomogeneous solutions for gravitational radiation". *In prep.*

[36] LIGO Scientific, Virgo Collaboration. "Binary Black Hole Mergers in the first Advanced LIGO Observing Run". In: *Phys. Rev. X* 6.4 (2016). [Erratum: Phys.Rev.X 8, 039903 (2018)], p. 041015. DOI: 10.1103/PhysRevX.6.041015. arXiv: 1606.04856 [gr-qc].

[37] Y. Mino, M. Sasaki, M. Shibata, et al. "Black hole perturbation: Chapter 1". In: *Prog. Theor. Phys. Suppl.* 128 (1997), pp. 1–121. DOI: 10.1143/PTPS.128.1. arXiv: gr-qc/9712057.

[38] M. Sasaki and H. Tagoshi. "Analytic black hole perturbation approach to gravitational radiation". In: *Living Rev. Rel.* 6 (2003), p. 6. DOI: 10.12942/lrr-2003-6. arXiv: gr-qc/0306120.

[39] A. Pound and B. Wardell. "Black Hole Perturbation Theory and Gravitational Self-Force". In: *Handbook of Gravitational Wave Astronomy*. Ed. by C. Bambi, S. Katsanevas, and K. D. Kokkotas. Singapore: Springer Singapore, 2020, pp. 1–119. ISBN: 978-981-15-4702-7. DOI: 10.1007/978-981-15-4702-7_38-1. URL: https://doi.org/10.1007/978-981-15-4702-7_38-1.

[40] H. Nakano and N. Sago. *Gravitational Waves and Perturbation Theory*. Ed. by T. Shiromizu and T. Takayanagi. Research in Theoretical Physics. ISBN: 978-4-254-13531-2. Tokyo, Japan: Asakura Publishing Co., Ltd., 2022. Chap. 4.

[41] S. A. Teukolsky. "Rotating Black Holes: Separable Wave Equations for Gravitational and Electromagnetic Perturbations". In: *Phys. Rev. Lett.* 29 (16 Oct. 1972), pp. 1114–1118. DOI: 10.1103/PhysRevLett.29.1114.

URL: https://link.aps.org/doi/10.1103/PhysRevLett.29.1114.

[42] S. A. Teukolsky. "Perturbations of a rotating black hole. 1. Fundamental equations for gravitational electromagnetic and neutrino field perturbations". In: *Astrophys. J.* 185 (1973), pp. 635–647. DOI: 10.1086/152444.

[43] W. H. Press and S. A. Teukolsky. "Perturbations of a Rotating Black Hole. II. Dynamical Stability of the Kerr Metric". In: *Astrophys. J.* 185 (1973), pp. 649–674. DOI: 10.1086/152445.

[44] S. A. Teukolsky and W. H. Press. "Perturbations of a rotating black hole. III - Interaction of the hole with gravitational and electromagnet ic radiation". In: *Astrophys. J.* 193 (1974), pp. 443–461. DOI: 10.1086/153180.

[45] R. P. Kerr. "Gravitational field of a spinning mass as an example of algebraically special metrics". In: *Phys. Rev. Lett.* 11 (1963), pp. 237–238. DOI: 10.1103/PhysRevLett.11.237.

[46] R. H. Boyer and R. W. Lindquist. "Maximal analytic extension of the Kerr metric". In: *J. Math. Phys.* 8 (1967), p. 265. DOI: 10.1063/1.1705193.

[47] C. W. Misner, K. S. Thorne, and J. A. Wheeler. *Gravitation*. San Francisco: W. H. Freeman, 1973. ISBN: 978-0-7167-0344-0, 978-0-691-17779-3.

[48] S. A. Hughes. "Computing radiation from Kerr black holes: Generalization of the Sasaki-Nakamura equation". In: *Phys. Rev. D* 62 (2000). [Erratum: Phys.Rev.D 67, 089902 (2003)], p. 044029. DOI: 10.1103/PhysRevD.62.044029. arXiv: gr-qc/0002043.

[49] S. Mano, H. Suzuki, and E. Takasugi. "Analytic solutions of the Teukolsky equation and their low frequency expansions". In: *Prog. Theor. Phys.* 95 (1996), pp. 1079–1096. DOI: 10.1143/PTP.95.1079. arXiv: gr-qc/9603020.

[50] R. Fujita and H. Tagoshi. "New numerical methods to evaluate homogeneous solutions of the Teukolsky equation". In: *Prog. Theor. Phys.* 112 (2004), pp. 415–450. DOI: 10.1143/PTP.112.415. arXiv: gr-qc/0410018.

[51] R. Fujita and H. Tagoshi. "New Numerical Methods to Evaluate Homogeneous Solutions of the Teukolsky Equation II. Solutions of the Continued Fraction Equation". In: *Prog. Theor. Phys.* 113 (2005), pp. 1165–1182. DOI: 10.1143/PTP.113.1165. arXiv: 0904.3818 [gr-qc].

[52] M. Sasaki and T. Nakamura. "The regge-wheeler equation with sources for both even and odd parity perturbations of the schwarzschild geometry". In: *Phys. Lett. A* 87.3 (1981), pp. 85–88. ISSN: 0375-9601. DOI: https://doi.org/10.1016/0375-9601(81)90568-5. URL: https://www.sciencedirect.com/science/article/pii/0375960181905685.

[53] M. Sasaki and T. Nakamura. "A class of new perturbation equations for the Kerr geometry". In: *Phys. Lett. A* 89.2 (1982), pp. 68–70. ISSN: 0375-9601. DOI: https://doi.org/10.1016/0375-9601(82)90507-2. URL: https://www.sciencedirect.com/science/article/pii/0375960182905072.

[54] M. Sasaki and T. Nakamura. "Gravitational Radiation from a Kerr Black Hole. I. Formulation and a Method for Numerical Analysis". In: *Prog. Theor. Phys.* 67.6 (June 1982), pp. 1788–1809. ISSN: 0033-068X. DOI: 10.1143/PTP.67.1788. eprint: https://academic.oup.com/ptp/article-pdf/67/6/1788/5332324/67-6-1788.pdf. URL: https://doi.org/10.1143/PTP.67.1788.

[55] W. H. Press, S. A. Teukolsky, W. T. Vetterling, et al. *Numerical Recipes 3rd Edition: The Art of Scientific Computing*. 3rd ed. USA: Cambridge University Press, 2007. ISBN: 0521880688.

[56] J. Bezanson, A. Edelman, S. Karpinski, et al. "Julia: A fresh approach to numerical computing". In: *SIAM Review* 59.1 (2017), pp. 65–98. DOI: 10.1137/141000671. URL: https://epubs.siam.org/doi/10.1137/141000671.

[57] *Black Hole Perturbation Toolkit*. (bhptoolkit.org).

[58] K. Glampedakis, A. D. Johnson, and D. Kennefick. "Darboux transformation in black hole perturbation theory". In: *Phys. Rev. D* 96.2 (2017), p. 024036. DOI: 10.1103/PhysRevD.96.024036. arXiv: 1702.06459 [gr-qc].

[59] A. G. Shah, J. L. Friedman, and T. S. Keidl. "EMRI corrections to the angular velocity and redshift factor of a mass in circular orbit about a Kerr black hole". In: *Phys. Rev. D* 86 (2012), p. 084059. DOI: 10.1103/PhysRevD.86.084059. arXiv: 1207.5595 [gr-qc].

[60] S. E. Gralla, A. P. Porfyriadis, and N. Warburton. "Particle on the Innermost Stable Circular Orbit of a Rapidly Spinning Black Hole". In: *Phys. Rev. D* 92.6 (2015), p. 064029. DOI: 10.1103/PhysRevD.92.064029. arXiv: 1506.08496 [gr-qc].

[61] G. A. Piovano, A. Maselli, and P. Pani. "Extreme mass ratio inspirals with spinning secondary: a detailed study of equatorial circular motion". In: *Phys. Rev. D* 102.2 (2020), p. 024041. DOI: 10.1103/PhysRevD.102.024041. arXiv: 2004.02654 [gr-qc].

[62] C. Rackauckas and Q. Nie. "Differentialequations.jl–a performant and feature-rich ecosystem for solving differential equations in julia". In: *J. Open Res. Softw.* 5.1 (2017), p. 15.

[63] J. Revels, M. Lubin, and T. Papamarkou. "Forward-Mode Automatic Differentiation in Julia". In: *arXiv e-prints*, arXiv:1607.07892 (July 2016), arXiv:1607.07892. DOI: 10.48550/arXiv.1607.07892. arXiv: 1607.07892 [cs.MS].

[64] L. Benet and D. P. Sanders. "TaylorSeries.jl: Taylor expansions in one and several variables in Julia". In: *J. Open Source Softw.* 4.36 (2019), p. 1043. DOI: 10.21105/joss.01043. URL: https://doi.org/10.21105/joss.01043.

[65] L. S. Finn and K. S. Thorne. "Gravitational waves from a compact star in a circular, inspiral orbit, in the equatorial plane of a massive, spinning black hole, as observed by LISA". In: *Phys. Rev. D* 62 (2000), p. 124021. DOI: 10.1103/PhysRevD.62.124021. arXiv: gr-qc/0007074.

[66] J. Verner. "Numerically optimal Runge-Kutta pairs with interpolants". In: *Numer Algorithms* 53.2 (Mar. 2010), pp. 383–396. DOI: 10.1007/s11075-009-9290-3.

[67] B. Wardell, N. Warburton, L. Durkan, et al. *BlackHolePerturbationToolkit/Teukolsky: Teukolsky 0.3.0*. Version 0.3.0. Aug. 2022. DOI: 10.5281/zenodo.7037857. URL: https://doi.org/10.5281/zenodo.7037857.

[68] W.-B. Han and Z. Cao. "Constructing EOB dynamics with numerical energy flux for intermediate-mass-ratio inspirals". In: *Phys. Rev. D* 84 (2011), p. 044014. DOI: 10.1103/PhysRevD.84.044014. arXiv: 1108.0995 [gr-qc].

[69] S. A. Hughes, N. Warburton, G. Khanna, et al. "Adiabatic waveforms for extreme mass-ratio inspirals via multivoice decomposition in time and frequency". In: *Phys. Rev. D* 103.10 (2021). [Erratum: Phys.Rev.D 107, 089901 (2023)], p. 104014. DOI: 10.1103/PhysRevD.103.104014. arXiv: 2102.02713 [gr-qc].

[70] F. J. Agocs and A. H. Barnett. "An adaptive spectral method for oscillatory second-order linear ODEs with frequency-independent cost". In: *arXiv e-prints*, arXiv:2212.06924 (Dec. 2022), arXiv:2212.06924. DOI: 10.48550/arXiv.2212.06924. arXiv: 2212.06924 [math.NA].

[71] E. Poisson. "Gravitational radiation from infall into a black hole: Regularization of the Teukolsky equation". In: *Phys. Rev. D* 55 (1997), pp. 639–649. DOI: 10.1103/PhysRevD.55.639. arXiv: gr-qc/9606078.

[72] M. Campanelli and C. O. Lousto. "Regularization of the Teukolsky equation for rotating black holes". In: *Phys. Rev. D* 56 (1997), pp. 6363–6369. DOI: 10.1103/PhysRevD.56.6363. arXiv: gr-qc/9707017.

[73] S. O'Sullivan and S. A. Hughes. "Strong-field tidal distortions of rotating black holes: Formalism and results for circular, equatorial orbits". In: *Phys. Rev. D* 90.12 (2014). [Erratum: Phys.Rev.D 91, 109901 (2015)], p. 124039. DOI: 10.1103/PhysRevD.91.109901. arXiv: 1407.6983 [gr-qc].

[74] B. Chen, Q. Wang, and Y. Chen. "Tidal response and near-horizon boundary conditions for spinning exotic compact objects". In: *Phys. Rev. D* 103.10 (2021), p. 104054. DOI: 10.1103/PhysRevD.103.104054. arXiv: 2012.10842 [gr-qc].

[75] A. A. Starobinskil and S. M. Churilov. "Amplification of electromagnetic and gravitational waves scattered by a rotating "black hole"". In: *Sov. Phys. JETP* 65.1 (1974), pp. 1–5.

[76] S. Chandrasekhar and S. L. Detweiler. "The quasi-normal modes of the Schwarzschild black hole". In: *Proc. Roy. Soc. Lond. A* 344 (1975), pp. 441–452. DOI: 10.1098/rspa.1975.0112.

[77] K. Glampedakis and N. Andersson. "Quick and dirty methods for studying black hole resonances". In: *Class. Quant. Grav.* 20 (2003), pp. 3441–3464. DOI: 10.1088/0264-9381/20/15/312. arXiv: gr-qc/0304030.

[78] E. W. Leaver. "An Analytic representation for the quasi normal modes of Kerr black holes". In: *Proc. Roy. Soc. Lond. A* 402 (1985), pp. 285–298. DOI: 10.1098/rspa.1985.0119.

[79] E. Berti and V. Cardoso. "Quasinormal ringing of Kerr black holes. I. The Excitation factors". In: *Phys. Rev. D* 74 (2006), p. 104020. DOI: 10.1103/PhysRevD.74.104020. arXiv: gr-qc/0605118.

[80] Z. Zhang, E. Berti, and V. Cardoso. "Quasinormal ringing of Kerr black holes. II. Excitation by particles falling radially with arbitrary energy". In: *Phys. Rev. D* 88 (2013), p. 044018. DOI: 10.1103/PhysRevD.88.044018. arXiv: 1305.4306 [gr-qc].

[81] N. Oshita. "Ease of excitation of black hole ringing: Quantifying the importance of overtones by the excitation factors". In: *Phys. Rev. D* 104.12 (2021), p. 124032. DOI: 10.1103/PhysRevD.104.124032. arXiv: 2109.09757 [gr-qc].

[82] S. A. Hughes. "The Evolution of circular, nonequatorial orbits of Kerr black holes due to gravitational wave emission". In: *Phys. Rev. D* 61.8 (2000). [Erratum: Phys.Rev.D 63, 049902 (2001), Erratum: Phys.Rev.D 65, 069902 (2002), Erratum: Phys.Rev.D 67, 089901 (2003), Erratum: Phys.Rev.D 78, 109902 (2008), Erratum: Phys.Rev.D 90, 109904 (2014)], p. 084004. DOI: 10.1103/PhysRevD.61.084004. arXiv: gr-qc/9910091.

[83] G. B. Cook and M. Zalutskiy. "Gravitational perturbations of the Kerr geometry: High-accuracy study". In: *Phys. Rev. D* 90.12 (2014), p. 124021. DOI: 10.1103/PhysRevD.90.124021. arXiv: 1410.7698 [gr-qc].

[84] J. N. Goldberg, A. J. MacFarlane, E. T. Newman, et al. "Spin s spherical harmonics and edth". In: *J. Math. Phys.* 8 (1967), p. 2155. DOI: 10.1063/1.1705135.

[85] G. B. Arfken, H. J. Weber, and F. E. Harris. "Chapter 7 - Ordinary Differential Equations". In: *Mathematical Methods for Physicists (Seventh Edition)*. Ed. by G. B. Arfken, H. J. Weber, and F. E. Harris. Seventh Edition. Boston: Academic Press, 2013, pp. 329–380. ISBN: 978-0-12-

384654-9. DOI: https://doi.org/10.1016/B978-0-12-384654-9.00007-4. URL: https://www.sciencedirect.com/science/article/pii/B9780123846549000074.

[86] *NIST Digital Library of Mathematical Functions*. https://dlmf.nist.gov/, Release 1.1.9 of 2023-03-15. F. W. J. Olver, A. B. Olde Daalhuis, D. W. Lozier, B. I. Schneider, R. F. Boisvert, C. W. Clark, B. R. Miller, B. V. Saunders, H. S. Cohl, and M. A. McClain, eds. URL: https://dlmf.nist.gov/.

[87] Y. Hatsuda and M. Kimura. "Semi-analytic expressions for quasinormal modes of slowly rotating Kerr black holes". In: *Phys. Rev. D* 102.4 (2020), p. 044032. DOI: 10.1103/PhysRevD.102.044032. arXiv: 2006.15496 [gr-qc].

[88] V. Cardoso, M. Kimura, A. Maselli, et al. "Parametrized black hole quasinormal ringdown: Decoupled equations for nonrotating black holes". In: *Phys. Rev. D* 99.10 (2019), p. 104077. DOI: 10.1103/PhysRevD.99.104077. arXiv: 1901.01265 [gr-qc].

[89] R. McManus, E. Berti, C. F. B. Macedo, et al. "Parametrized black hole quasinormal ringdown. II. Coupled equations and quadratic corrections for nonrotating black holes". In: *Phys. Rev. D* 100.4 (2019), p. 044061. DOI: 10.1103/PhysRevD.100.044061. arXiv: 1906.05155 [gr-qc].

[90] M. Kimura. "Note on the parametrized black hole quasinormal ringdown formalism". In: *Phys. Rev. D* 101.6 (2020), p. 064031. DOI: 10.1103/PhysRevD.101.064031. arXiv: 2001.09613 [gr-qc].

[91] S. R. Dolan. "Scattering and Absorption of Gravitational Plane Waves by Rotating Black Holes". In: *Class. Quant. Grav.* 25 (2008), p. 235002. DOI: 10.1088/0264-9381/25/23/235002. arXiv: 0801.3805 [gr-qc].

[92] S. A. Hughes. "Erratum: Evolution of circular, nonequatorial orbits of Kerr black holes due to gravitational-wave emission [Phys. Rev. D 61, 084004 (2000)]". In: *Phys. Rev. D* 78 (10 Nov. 2008), p. 109902. DOI: 10.1103/PhysRevD.78.109902. URL: https://link.aps.org/doi/10.1103/PhysRevD.78.109902.

[93] V. Varma, S. E. Field, M. A. Scheel, et al. "Surrogate models for precessing binary black hole simulations with unequal masses". In: *Phys. Rev.*

*Research.* 1 (2019), p. 033015. DOI: 10.1103/PhysRevResearch.1.033015. arXiv: 1905.09300 [gr-qc].

[94] E. Maggio, A. Testa, S. Bhagwat, et al. "Analytical model for gravitational-wave echoes from spinning remnants". In: *Phys. Rev. D* 100.6 (2019), p. 064056. DOI: 10.1103/PhysRevD.100.064056. arXiv: 1907.03091 [gr-qc].

[95] Q. Wang, N. Oshita, and N. Afshordi. "Echoes from Quantum Black Holes". In: *Phys. Rev. D* 101.2 (2020), p. 024031. DOI: 10.1103/PhysRevD.101.024031. arXiv: 1905.00446 [gr-qc].

[96] E. Maggio, P. Pani, and V. Ferrari. "Exotic Compact Objects and How to Quench their Ergoregion Instability". In: *Phys. Rev. D* 96.10 (2017), p. 104047. DOI: 10.1103/PhysRevD.96.104047. arXiv: 1703.03696 [gr-qc].

[97] N. Oshita, Q. Wang, and N. Afshordi. "On Reflectivity of Quantum Black Hole Horizons". In: *J. Cosmol. Astropart. Phys.* 04 (2020), p. 016. DOI: 10.1088/1475-7516/2020/04/016. arXiv: 1905.00464 [hep-th].

[98] E. E. Flanagan and S. A. Hughes. "Measuring gravitational waves from binary black hole coalescences: 1. Signal-to-noise for inspiral, merger, and ringdown". In: *Phys. Rev. D* 57 (1998), pp. 4535–4565. DOI: 10.1103/PhysRevD.57.4535. arXiv: gr-qc/9701039.

[99] L. S. Finn and D. F. Chernoff. "Observing binary inspiral in gravitational radiation: One interferometer". In: *Phys. Rev. D* 47 (1993), pp. 2198–2219. DOI: 10.1103/PhysRevD.47.2198. arXiv: gr-qc/9301003.

[100] *Advanced LIGO anticipated sensitivity curves*. https://dcc.ligo.org/LIGO-T1800044/public.

[101] LIGO Scientific, Virgo Collaboration. "GW151226: Observation of Gravitational Waves from a 22-Solar-Mass Binary Black Hole Coalescence". In: *Phys. Rev. Lett.* 116.24 (2016), p. 241103. DOI: 10.1103/PhysRevLett.116.241103. arXiv: 1606.04855 [gr-qc].

[102] LIGO Scientific, VIRGO Collaboration. "GW170104: Observation of a 50-Solar-Mass Binary Black Hole Coalescence at Redshift 0.2". In: *Phys. Rev. Lett.* 118.22 (2017). [Erratum: Phys.Rev.Lett. 121, 129901 (2018)], p. 221101. DOI: 10.1103/PhysRevLett.118.221101. arXiv: 1706.01812 [gr-qc].

[103] LIGO Scientific, Virgo Collaboration. "GW170608: Observation of a 19-solar-mass Binary Black Hole Coalescence". In: *Astrophys. J. Lett.* 851 (2017), p. L35. DOI: 10.3847/2041-8213/aa9f0c. arXiv: 1711.05578 [astro-ph.HE].

[104] LIGO Scientific, Virgo Collaboration. "GW170814: A Three-Detector Observation of Gravitational Waves from a Binary Black Hole Coalescence". In: *Phys. Rev. Lett.* 119.14 (2017), p. 141101. DOI: 10.1103/PhysRevLett.119.141101. arXiv: 1709.09660 [gr-qc].

[105] V. Cardoso, E. Franzin, and P. Pani. "Is the gravitational-wave ringdown a probe of the event horizon?" In: *Phys. Rev. Lett.* 116.17 (2016). [Erratum: Phys.Rev.Lett. 117, 089902 (2016)], p. 171101. DOI: 10.1103/PhysRevLett.116.171101. arXiv: 1602.07309 [gr-qc].

[106] V. Cardoso, S. Hopper, C. F. B. Macedo, et al. "Gravitational-wave signatures of exotic compact objects and of quantum corrections at the horizon scale". In: *Phys. Rev. D* 94.8 (2016), p. 084031. DOI: 10.1103/PhysRevD.94.084031. arXiv: 1608.08637 [gr-qc].

[107] J. Abedi, H. Dykaar, and N. Afshordi. "Echoes from the Abyss: Tentative evidence for Planck-scale structure at black hole horizons". In: *Phys. Rev. D* 96.8 (2017), p. 082004. DOI: 10.1103/PhysRevD.96.082004. arXiv: 1612.00266 [gr-qc].

[108] G. Ashton, O. Birnholtz, M. Cabero, et al. "Comments on: "Echoes from the abyss: Evidence for Planck-scale structure at black hole horizons"". In: *arXiv e-prints* (Dec. 2016). arXiv: 1612.05625 [gr-qc].

[109] J. Abedi, H. Dykaar, and N. Afshordi. "Echoes from the Abyss: The Holiday Edition!" In: (Jan. 2017). arXiv: 1701.03485 [gr-qc].

[110] A. Maselli, S. H. Völkel, and K. D. Kokkotas. "Parameter estimation of gravitational wave echoes from exotic compact objects". In: *Phys. Rev. D* 96.6 (2017), p. 064045. DOI: 10.1103/PhysRevD.96.064045. arXiv: 1708.02217 [gr-qc].

[111] J. Westerweck, A. Nielsen, O. Fischer-Birnholtz, et al. "Low significance of evidence for black hole echoes in gravitational wave data". In: *Phys. Rev. D* 97.12 (2018), p. 124037. DOI: 10.1103/PhysRevD.97.124037. arXiv: 1712.09966 [gr-qc].

[112] R. S. Conklin, B. Holdom, and J. Ren. "Gravitational wave echoes through new windows". In: *Phys. Rev. D* 98.4 (2018), p. 044021. DOI: 10.1103/PhysRevD.98.044021. arXiv: 1712.06517 [gr-qc].

[113] K. W. Tsang, M. Rollier, A. Ghosh, et al. "A morphology-independent data analysis method for detecting and characterizing gravitational wave echoes". In: *Phys. Rev. D* 98.2 (2018), p. 024023. DOI: 10.1103/PhysRevD.98.024023. arXiv: 1804.04877 [gr-qc].

[114] A. B. Nielsen, C. D. Capano, O. Birnholtz, et al. "Parameter estimation and statistical significance of echoes following black hole signals in the first Advanced LIGO observing run". In: *Phys. Rev. D* 99.10 (2019), p. 104012. DOI: 10.1103/PhysRevD.99.104012. arXiv: 1811.04904 [gr-qc].

[115] M. Maggiore. *Gravitational Waves: Volume 1: Theory and Experiments*. Oxford University Press, Oct. 2007. ISBN: 9780198570745.

[116] N. Metropolis and S. Ulam. "The Monte Carlo Method". In: *J. Am. Stat. Assoc.* 44.247 (1949), pp. 335–341. ISSN: 01621459. URL: http://www.jstor.org/stable/2280232.

[117] W. K. Hastings. "Monte Carlo Sampling Methods Using Markov Chains and Their Applications". In: *Biometrika* 57.1 (1970), pp. 97–109. ISSN: 00063444. URL: http://www.jstor.org/stable/2334940.

[118] R. H. Swendsen and J.-S. Wang. "Replica Monte Carlo Simulation of Spin-Glasses". In: *Phys. Rev. Lett.* 57 (21 Nov. 1986), pp. 2607–2609. DOI: 10.1103/PhysRevLett.57.2607. URL: https://link.aps.org/doi/10.1103/PhysRevLett.57.2607.

[119] P. M. Goggans and Y. Chi. "Using Thermodynamic Integration to Calculate the Posterior Probability in Bayesian Model Selection Problems". In: *AIP Conference Proceedings* 707.1 (2004), pp. 59–66. DOI: 10.1063/1.1751356. eprint: http://aip.scitation.org/doi/pdf/10.1063/1.1751356. URL: http://aip.scitation.org/doi/abs/10.1063/1.1751356.

[120] J. Skilling. "Nested Sampling". In: *Bayesian Inference and Maximum Entropy Methods in Science and Engineering: 24th International Workshop on Bayesian Inference and Maximum Entropy Methods in Science and Engineering*. Ed. by R. Fischer, R. Preuss, and U. V. Toussaint. Vol. 735.

American Institute of Physics Conference Series. Nov. 2004, pp. 395–405. DOI: 10.1063/1.1835238.

[121] J. Veitch et al. "Parameter estimation for compact binaries with ground-based gravitational-wave observations using the LALInference software library". In: *Phys. Rev. D* 91.4 (2015), p. 042003. DOI: 10.1103/PhysRevD.91.042003. arXiv: 1409.7215 [gr-qc].

[122] D. J. C. MacKay. *Information Theory, Inference & Learning Algorithms*. New York, NY, USA: Cambridge University Press, 2002. ISBN: 0521642981.

[123] Z. Mark, A. Zimmerman, S. M. Du, et al. "A recipe for echoes from exotic compact objects". In: *Phys. Rev. D* 96.8 (2017), p. 084002. DOI: 10.1103/PhysRevD.96.084002. arXiv: 1706.06155 [gr-qc].

[124] H. Nakano, N. Sago, H. Tagoshi, et al. "Black hole ringdown echoes and howls". In: *Prog. Theor. Exp. Phys.* 2017.7 (2017), 071E01. DOI: 10.1093/ptep/ptx093. arXiv: 1704.07175 [gr-qc].

[125] M. R. Correia and V. Cardoso. "Characterization of echoes: A Dyson-series representation of individual pulses". In: *Phys. Rev. D* 97.8 (2018), p. 084030. DOI: 10.1103/PhysRevD.97.084030. arXiv: 1802.07735 [gr-qc].

[126] Q. Wang and N. Afshordi. "Black hole echology: The observer's manual". In: *Phys. Rev. D* 97.12 (2018), p. 124044. DOI: 10.1103/PhysRevD.97.124044. arXiv: 1803.02845 [gr-qc].

[127] A. Testa and P. Pani. "Analytical template for gravitational-wave echoes: signal characterization and prospects of detection with current and future interferometers". In: *Phys. Rev. D* 98.4 (2018), p. 044018. DOI: 10.1103/PhysRevD.98.044018. arXiv: 1806.04253 [gr-qc].

[128] Gravitational Wave Open Science Center. *The O1 Data Release*. DOI: 10.7935/K57P8W9D. URL: https://doi.org/10.7935/K57P8W9D.

[129] M. Vallisneri, J. Kanner, R. Williams, et al. "The LIGO Open Science Center". In: *J. Phys. Conf. Ser.* 610.1 (2015). Ed. by G. Ciani, J. W. Conklin, and G. Mueller, p. 012021. DOI: 10.1088/1742-6596/610/1/012021. arXiv: 1410.4839 [gr-qc].

[130] LIGO Scientific Collaboration. *LIGO Algorithm Library*. DOI: 10.7935/GT1W-FZ16.

[131] M. Hannam, P. Schmidt, A. Bohé, et al. "Simple Model of Complete Precessing Black-Hole-Binary Gravitational Waveforms". In: *Phys. Rev. Lett.* 113.15 (2014), p. 151101. DOI: 10.1103/PhysRevLett.113.151101. arXiv: 1308.3271 [gr-qc].

[132] S. Husa, S. Khan, M. Hannam, et al. "Frequency-domain gravitational waves from nonprecessing black-hole binaries. I. New numerical waveforms and anatomy of the signal". In: *Phys. Rev. D* 93.4 (2016), p. 044006. DOI: 10.1103/PhysRevD.93.044006. arXiv: 1508.07250 [gr-qc].

[133] S. Khan, S. Husa, M. Hannam, et al. "Frequency-domain gravitational waves from nonprecessing black-hole binaries. II. A phenomenological model for the advanced detector era". In: *Phys. Rev. D* 93.4 (2016), p. 044007. DOI: 10.1103/PhysRevD.93.044007. arXiv: 1508.07253 [gr-qc].

[134] LIGO Scientific, Virgo Collaboration. "Properties of the Binary Black Hole Merger GW150914". In: *Phys. Rev. Lett.* 116.24 (2016), p. 241102. DOI: 10.1103/PhysRevLett.116.241102. arXiv: 1602.03840 [gr-qc].

[135] T. Dent and C. Pankow. "Astrophysical Rates of Gravitational-Wave Compact Binary Sources in O3". OpenLVEM Town Hall Meeting, Amsterdam, Netherlands. 2018. URL: https://dcc.ligo.org/LIGO-G1800370/public.

[136] R. E. Kass and A. E. Raftery. "Bayes Factors". In: *J. Am. Stat. Assoc.* 90.430 (1995), pp. 773–795. DOI: 10.1080/01621459.1995.10476572. eprint: https://www.tandfonline.com/doi/pdf/10.1080/01621459.1995.10476572. URL: https://www.tandfonline.com/doi/abs/10.1080/01621459.1995.10476572.

[137] D. Foreman-Mackey. "corner.py: Scatterplot matrices in Python". In: *J. Open Source Softw.* 24 (2016). DOI: 10.21105/joss.00024. URL: http://dx.doi.org/10.5281/zenodo.45906.

[138] LIGO Scientific, Virgo, Fermi-GBM, INTEGRAL Collaboration. "Gravitational Waves and Gamma-rays from a Binary Neutron Star Merger: GW170817 and GRB 170817A". In: *Astrophys. J. Lett.* 848.2 (2017), p. L13. DOI: 10.3847/2041-8213/aa920c. arXiv: 1710.05834 [astro-ph.HE].

[139] R. K. L. Lo, T. G. F. Li, and A. J. Weinstein. "Template-based Gravitational-Wave Echoes Search Using Bayesian Model Selection". In: *Phys. Rev. D* 99.8 (2019), p. 084052. DOI: 10.1103/PhysRevD.99.084052. arXiv: 1811.07431 [gr-qc].

[140] V. Cardoso and P. Pani. "Testing the nature of dark compact objects: a status report". In: *Living Rev. Rel.* 22.1 (2019), p. 4. DOI: 10.1007/s41114-019-0020-4. arXiv: 1904.05363 [gr-qc].

[141] N. Uchikata, H. Nakano, T. Narikawa, et al. "Searching for black hole echoes from the LIGO-Virgo Catalog GWTC-1". In: *Phys. Rev. D* 100.6 (2019), p. 062006. DOI: 10.1103/PhysRevD.100.062006. arXiv: 1906.00838 [gr-qc].

[142] Gravitational Wave Open Science Center. *The O2 Data Release*. 2019. DOI: 10.7935/CA75-FM95. URL: https://doi.org/10.7935/CA75-FM95.

[143] S. Kullback and R. A. Leibler. "On Information and Sufficiency". In: *Ann. Math. Statist.* 22.1 (Mar. 1951), pp. 79–86. DOI: 10.1214/aoms/1177729694. URL: https://doi.org/10.1214/aoms/1177729694.

[144] J. D. E. Creighton and W. G. Anderson. *Gravitational-wave physics and astronomy: An introduction to theory, experiment and data analysis*. 2011.

[145] LIGO Scientific, Virgo Collaboration. "Upper Limits on the Rates of Binary Neutron Star and Neutron Star–black Hole Mergers From Advanced Ligo's First Observing run". In: *Astrophys. J. Lett.* 832.2 (2016), p. L21. DOI: 10.3847/2041-8205/832/2/L21. arXiv: 1607.07456 [astro-ph.HE].

[146] B. Chen, Y. Chen, Y. Ma, et al. "Instability of Exotic Compact Objects and Its Implications for Gravitational-Wave Echoes". In: *arXiv e-prints* (Feb. 2019). arXiv: 1902.08180 [gr-qc].

[147] Y.-T. Wang, Z.-P. Li, J. Zhang, et al. "Are gravitational wave ringdown echoes always equal-interval?" In: *Eur. Phys. J. C* 78.6 (2018), p. 482. DOI: 10.1140/epjc/s10052-018-5974-y. arXiv: 1802.02003 [gr-qc].

[148] Y.-T. Wang, J. Zhang, S.-Y. Zhou, et al. "On echo intervals in gravitational wave echo analysis". In: *Eur. Phys. J. C* 79.9 (2019), p. 726. DOI: 10.1140/epjc/s10052-019-7234-1. arXiv: 1904.00212 [gr-qc].

[149] S. M. Du and Y. Chen. "Searching for near-horizon quantum structures in the binary black-hole stochastic gravitational-wave background". In: *Phys. Rev. Lett.* 121.5 (2018), p. 051105. DOI: 10.1103/PhysRevLett.121.051105. arXiv: 1803.10947 [gr-qc].

[150] P. O. Mazur and E. Mottola. "Gravitational Condensate Stars: An Alternative to Black Holes". In: *Universe* 9.2 (2023), p. 88. DOI: 10.3390/universe9020088. arXiv: gr-qc/0109035.

[151] O. Lunin and S. D. Mathur. "AdS / CFT duality and the black hole information paradox". In: *Nucl. Phys.* B623 (2002), pp. 342–394. DOI: 10.1016/S0550-3213(01)00620-4. arXiv: hep-th/0109154 [hep-th].

[152] O. Lunin and S. D. Mathur. "Statistical interpretation of Bekenstein entropy for systems with a stretched horizon". In: *Phys. Rev. Lett.* 88 (2002), p. 211303. DOI: 10.1103/PhysRevLett.88.211303. arXiv: hep-th/0202072 [hep-th].

[153] K. Kokkotas. "Pulsating relativistic stars". In: *Les Houches School of Physics: Astrophysical Sources of Gravitational Radiation*. Sept. 1995, pp. 89–102. arXiv: gr-qc/9603024.

[154] K. Tominaga, M. Saijo, and K.-i. Maeda. "Gravitational waves from a test particle scattered by a neutron star: Axial mode case". In: *Phys. Rev. D* 60 (1999), p. 024004. DOI: 10.1103/PhysRevD.60.024004. arXiv: gr-qc/9901040.

[155] V. Ferrari and K. Kokkotas. "Scattering of particles by neutron stars: Time evolutions for axial perturbations". In: *Phys. Rev. D* 62 (2000), p. 107504. DOI: 10.1103/PhysRevD.62.107504. arXiv: gr-qc/0008057.

[156] S. H. Völkel and K. D. Kokkotas. "Ultra Compact Stars: Reconstructing the Perturbation Potential". In: *Class. Quant. Grav.* 34.17 (2017), p. 175015. DOI: 10.1088/1361-6382/aa82de. arXiv: 1704.07517 [gr-qc].

[157] S. H. Völkel and K. D. Kokkotas. "Wormhole Potentials and Throats from Quasi-Normal Modes". In: *Class. Quant. Grav.* 35.10 (2018), p. 105018. DOI: 10.1088/1361-6382/aabce6. arXiv: 1802.08525 [gr-qc].

[158] E. Maggio, V. Cardoso, S. R. Dolan, et al. "Ergoregion instability of exotic compact objects: electromagnetic and gravitational perturbations and the role of absorption". In: *Phys. Rev. D* 99.6 (2019), p. 064007. DOI: 10.1103/PhysRevD.99.064007. arXiv: 1807.08840 [gr-qc].

[159] P. Pani and V. Ferrari. "On gravitational-wave echoes from neutron-star binary coalescences". In: *Class. Quant. Grav.* 35.15 (2018), 15LT01. DOI: 10.1088/1361-6382/aacb8f. arXiv: 1804.01444 [gr-qc].

[160] A. Coates, S. H. Völkel, and K. D. Kokkotas. "Spectral Lines of Quantized, Spinning Black Holes and their Astrophysical Relevance". In: *Phys. Rev. Lett.* 123.17 (2019), p. 171104. DOI: 10.1103/PhysRevLett.123.171104. arXiv: 1909.01254 [gr-qc].

[161] S. Khan, K. Chatziioannou, M. Hannam, et al. "Phenomenological model for the gravitational-wave signal from precessing binary black holes with two-spin effects". In: *Phys. Rev. D* 100.2 (2019), p. 024059. DOI: 10.1103/PhysRevD.100.024059. arXiv: 1809.10113 [gr-qc].

[162] Y.-T. Wang and Y.-S. Piao. "Searching for gravitational wave echoes in GWTC-1 and O3 events". Oct. 2020. arXiv: 2010.07663 [gr-qc].

[163] ESA/Hubble. *Hubble image of Abell S1063*. 2016. URL: https://esahubble.org/images/heic1615a/ (visited on 08/17/2023).

[164] ESA/Hubble/Webb. *Webb spotlights gravitational arcs in 'El Gordo' galaxy cluster (NIRCam image)*. 2023. URL: https://esawebb.org/images/elgordo1/ (visited on 08/17/2023).

[165] S. Refsdal. "On the possibility of determining Hubble's parameter and the masses of galaxies from the gravitational lens effect". In: *Mon. Not. Roy. Astron. Soc.* 128 (1964), p. 307.

[166] P. Cremonese, J. M. Ezquiaga, and V. Salzano. "Breaking the mass-sheet degeneracy with gravitational wave interference in lensed events". In: *Phys. Rev. D* 104.2 (2021), p. 023503. DOI: 10.1103/PhysRevD.104.023503. arXiv: 2104.07055 [astro-ph.CO].

[167] R. K. L. Lo and M. Oguri. "Re-analyzing GWTC-3 catalog for strongly-lensed gravitational waves from binary black hole systems informed by a realistic simulation of lensed background objects by galaxy-scale lenses". *In prep.*

[168] A. K. Y. Li, R. K. L. Lo, S. Sachdev, et al. "Targeted subthreshold search for strongly lensed gravitational-wave events". In: *Phys. Rev. D* 107.12 (2023), p. 123014. DOI: 10.1103/PhysRevD.107.123014. arXiv: 1904.06020 [gr-qc].

[169] H. W. Y. Wong, L. W. L. Chan, I. C. F. Wong, et al. "Using overlap of sky localization probability maps for filtering potentially lensed pairs of gravitational-wave signals". In: *arXiv e-prints* (Dec. 2021). arXiv: 2112.05932 [gr-qc].

[170] J. M. Ezquiaga, W. Hu, and R. K. L. Lo. "Identifying strongly lensed gravitational waves through their phase consistency". In: (*Submitted to Phys. Rev. D*). arXiv: 2308.06616 [astro-ph.CO].

[171] Y. Wang, R. K. L. Lo, A. K. Y. Li, et al. "Identifying Type II Strongly Lensed Gravitational-Wave Images in Third-Generation Gravitational-Wave Detectors". In: *Phys. Rev. D* 103.10 (2021), p. 104055. DOI: 10.1103/PhysRevD.103.104055. arXiv: 2101.08264 [gr-qc].

[172] P. Schneider, J. Ehlers, and E. E. Falco. *Gravitational Lenses*. 1992. DOI: 10.1007/978-3-662-03758-4.

[173] M. Oguri. "Strong gravitational lensing of explosive transients". In: *Rept. Prog. Phys.* 82.12 (2019), p. 126901. DOI: 10.1088/1361-6633/ab4fc5. arXiv: 1907.06830 [astro-ph.CO].

[174] R. Takahashi and T. Nakamura. "Wave effects in gravitational lensing of gravitational waves from chirping binaries". In: *Astrophys. J.* 595 (2003), pp. 1039–1051. DOI: 10.1086/377430. arXiv: astro-ph/0305055.

[175] L. Dai and T. Venumadhav. "On the waveforms of gravitationally lensed gravitational waves". In: *arXiv e-prints* (Feb. 2017). arXiv: 1702.04724 [gr-qc].

[176] J. M. Ezquiaga, D. E. Holz, W. Hu, et al. "Phase effects from strong gravitational lensing of gravitational waves". In: *Phys. Rev. D* 103.6 (2021), p. 064047. DOI: 10.1103/PhysRevD.103.064047. arXiv: 2008.12814 [gr-qc].

[177] K. K. Y. Ng, K. W. K. Wong, T. Broadhurst, et al. "Precise LIGO Lensing Rate Predictions for Binary Black Holes". In: *Phys. Rev. D* 97.2 (2018), p. 023012. DOI: 10.1103/PhysRevD.97.023012. arXiv: 1703.06319 [astro-ph.CO].

[178] M. Oguri. "Effect of gravitational lensing on the distribution of gravitational waves from distant binary black hole mergers". In: *Mon. Not. Roy. Astron. Soc.* 480.3 (2018), pp. 3842–3855. DOI: 10.1093/mnras/sty2145. arXiv: 1807.02584 [astro-ph.CO].

[179] S.-S. Li, S. Mao, Y. Zhao, et al. "Gravitational lensing of gravitational waves: A statistical perspective". In: *Mon. Not. Roy. Astron. Soc.* 476.2 (2018), pp. 2220–2229. DOI: 10.1093/mnras/sty411. arXiv: 1802.05089 [astro-ph.CO].

[180] R. Buscicchio, C. J. Moore, G. Pratten, et al. "Constraining the lensing of binary black holes from their stochastic background". In: *Phys. Rev. Lett.* 125.14 (2020), p. 141102. DOI: 10.1103/PhysRevLett.125.141102. arXiv: 2006.04516 [astro-ph.CO].

[181] S. Mukherjee, T. Broadhurst, J. M. Diego, et al. "Inferring the lensing rate of LIGO-Virgo sources from the stochastic gravitational wave background". In: *Mon. Not. Roy. Astron. Soc.* 501.2 (2021), pp. 2451–2466. DOI: 10.1093/mnras/staa3813. arXiv: 2006.03064 [astro-ph.CO].

[182] O. A. Hannuksela, K. Haris, K. K. Y. Ng, et al. "Search for gravitational lensing signatures in LIGO-Virgo binary black hole events". In: *Astrophys. J. Lett.* 874.1 (2019), p. L2. DOI: 10.3847/2041-8213/ab0c0f. arXiv: 1901.02674 [gr-qc].

[183] L. Dai, B. Zackay, T. Venumadhav, et al. "Search for Lensed Gravitational Waves Including Morse Phase Information: An Intriguing Candidate in O2". In: (July 2020). arXiv: 2007.12709 [astro-ph.HE].

[184] X. Liu, I. M. Hernandez, and J. Creighton. "Identifying strong gravitational-wave lensing during the second observing run of Advanced LIGO and Advanced Virgo". In: *Astrophys. J.* 908.1 (2021), p. 97. DOI: 10.3847/1538-4357/abd7eb. arXiv: 2009.06539 [astro-ph.HE].

[185] T. Broadhurst, J. M. Diego, and G. F. Smoot. "Twin LIGO/Virgo Detections of a Viable Gravitationally-Lensed Black Hole Merger". In: (2019). arXiv: 1901.03190 [astro-ph.CO].

[186] C. Messick et al. “Analysis Framework for the Prompt Discovery of Compact Binary Mergers in Gravitational-wave Data”. In: *Phys. Rev. D* 95.4 (2017), p. 042001. DOI: 10.1103/PhysRevD.95.042001. arXiv: 1604.04324 [astro-ph.IM].

[187] S. Sachdev et al. “The GstLAL Search Analysis Methods for Compact Binary Mergers in Advanced LIGO’s Second and Advanced Virgo’s First Observing Runs”. In: (Jan. 2019). arXiv: 1901.08580 [gr-qc].

[188] S. A. Usman et al. “The PyCBC search for gravitational waves from compact binary coalescence”. In: *Class. Quant. Grav.* 33.21 (2016), p. 215004. DOI: 10.1088/0264-9381/33/21/215004. arXiv: 1508.02357 [gr-qc].

[189] C. McIsaac, D. Keitel, T. Collett, et al. “Search for strongly lensed counterpart images of binary black hole mergers in the first two LIGO observing runs”. In: *Phys. Rev. D* 102.8 (2020), p. 084031. DOI: 10.1103/PhysRevD.102.084031. arXiv: 1912.05389 [gr-qc].

[190] K. Haris, A. K. Mehta, S. Kumar, et al. “Identifying strongly lensed gravitational wave signals from binary black hole mergers”. In: *arXiv e-prints* (July 2018). arXiv: 1807.07062 [gr-qc].

[191] Planck Collaboration. “Planck 2015 results. XIII. Cosmological parameters”. In: *Astron. Astrophys.* 594 (2016), A13. DOI: 10.1051/0004-6361/201525830. arXiv: 1502.01589 [astro-ph.CO].

[192] LIGO Scientific, Virgo Collaboration. “Population Properties of Compact Objects from the Second LIGO-Virgo Gravitational-Wave Transient Catalog”. In: *Astrophys. J. Lett.* 913.1 (2021), p. L7. DOI: 10.3847/2041-8213/abe949. arXiv: 2010.14533 [astro-ph.HE].

[193] L. P. Singer, D. A. Goldstein, and J. S. Bloom. “The Two LIGO/Virgo Binary Black Hole Mergers on 2019 August 28 Were Not Strongly Lensed”. In: (Oct. 2019). arXiv: 1910.03601 [astro-ph.CO].

[194] S. Hou, X.-L. Fan, and Z.-H. Zhu. “Gravitational Lensing of Gravitational Waves: Rotation of Polarization Plane”. In: *Phys. Rev. D* 100.6 (2019), p. 064028. DOI: 10.1103/PhysRevD.100.064028. arXiv: 1907.07486 [gr-qc].

[195] I. Mandel, W. M. Farr, and J. R. Gair. "Extracting distribution parameters from multiple uncertain observations with selection biases". In: *Mon. Not. Roy. Astron. Soc.* 486.1 (2019), pp. 1086–1093. DOI: 10.1093/mnras/stz896. arXiv: 1809.02063 [physics.data-an].

[196] A. Ghosh, W. Del Pozzo, and P. Ajith. "Estimating parameters of binary black holes from gravitational-wave observations of their inspiral, merger and ringdown". In: *Phys. Rev. D* 94.10 (2016), p. 104070. DOI: 10.1103/PhysRevD.94.104070. arXiv: 1505.05607 [gr-qc].

[197] K. Belczynski, T. Ryu, R. Perna, et al. "On the likelihood of detecting gravitational waves from Population III compact object binaries". In: *Mon. Not. Roy. Astron. Soc.* 471.4 (2017), pp. 4702–4721. DOI: 10.1093/mnras/stx1759. arXiv: 1612.01524 [astro-ph.HE].

[198] J. S. Liu. "The Collapsed Gibbs Sampler in Bayesian Computations with Applications to a Gene Regulation Problem". In: *J. Am. Stat. Assoc.* 89.427 (1994), pp. 958–966. ISSN: 01621459. URL: http://www.jstor.org/stable/2290921.

[199] G. Pratten et al. "Computationally efficient models for the dominant and subdominant harmonic modes of precessing binary black holes". In: *Phys. Rev. D* 103.10 (2021), p. 104056. DOI: 10.1103/PhysRevD.103.104056. arXiv: 2004.06503 [gr-qc].

[200] G. Ashton et al. "BILBY: A user-friendly Bayesian inference library for gravitational-wave astronomy". In: *Astrophys. J. Suppl.* 241.2 (2019), p. 27. DOI: 10.3847/1538-4365/ab06fc. arXiv: 1811.02042 [astro-ph.IM].

[201] R. J. E. Smith, G. Ashton, A. Vajpeyi, et al. "Massively parallel Bayesian inference for transient gravitational-wave astronomy". In: *Mon. Not. Roy. Astron. Soc.* 498.3 (2020), pp. 4492–4502. DOI: 10.1093/mnras/staa2483. arXiv: 1909.11873 [gr-qc].

[202] J. S. Speagle. "dynesty: a dynamic nested sampling package for estimating Bayesian posteriors and evidences". In: *Mon. Not. Roy. Astron. Soc.* 493.3 (2020), pp. 3132–3158. DOI: 10.1093/mnras/staa278. arXiv: 1904.02180 [astro-ph.IM].

[203] M. Mateu-Lucena, S. Husa, M. Colleoni, et al. "Parameter estimation with the current generation of phenomenological waveform models applied to the black hole mergers of GWTC-1". In: *Mon. Not. Roy. Astron. Soc.* 517.2 (2022), pp. 2403–2425. DOI: 10.1093/mnras/stac2724. arXiv: 2105.05960 [gr-qc].

[204] *Bilby: A User-Friendly Bayesian Inference Library*. https://git.ligo.org/lscsoft/bilby/-/tree/1.0.2. Version v1.0.2. Sept. 2020. URL: https://git.ligo.org/lscsoft/bilby/-/tree/1.0.2.

[205] *parallel_bilby: A python package to run gravitational wave inference analyses on multiple cores of a machine using their message passing interface*. https://git.ligo.org/lscsoft/parallel_bilby/-/tree/0.1.5. Version v0.1.5. Sept. 2020. URL: https://git.ligo.org/lscsoft/parallel_bilby/-/tree/0.1.5.

[206] J. Speagle, K. Barbary, G. Ashton, et al. *joshspeagle/dynesty: Version 1.0*. https://doi.org/10.5281/zenodo.3461261. Version v1.0.0. Sept. 2019. DOI: 10.5281/zenodo.3461261. URL: https://doi.org/10.5281/zenodo.3461261.

[207] *hanabi: Hierarchical bayesian ANAlysis on lensed GW signals using BIlby*. https://github.com/ricokaloklo/hanabi/tree/0.3.1. Version v0.3.1. Mar. 2021. URL: https://github.com/ricokaloklo/hanabi/tree/0.3.1.

[208] E. L. Turner, J. P. Ostriker, and I. Gott J. R. "The statistics of gravitational lenses : the distributions of image angular separations and lens redshifts." In: *Astrophys. J.* 284 (Sept. 1984), pp. 1–22. DOI: 10.1086/162379.

[209] D. Gerosa, G. Pratten, and A. Vecchio. "Gravitational-wave selection effects using neural-network classifiers". In: *Phys. Rev. D* 102.10 (2020), p. 103020. DOI: 10.1103/PhysRevD.102.103020. arXiv: 2007.06585 [astro-ph.HE].

[210] N. Seto. "Strong gravitational lensing and localization of merging massive black hole binaries with LISA". In: *Phys. Rev. D* 69 (2004), p. 022002. DOI: 10.1103/PhysRevD.69.022002. arXiv: astro-ph/0305605.

[211] O. A. Hannuksela, T. E. Collett, M. Çalışkan, et al. "Localizing merging black holes with sub-arcsecond precision using gravitational-wave lensing". In: *Mon. Not. Roy. Astron. Soc.* 498.3 (2020), pp. 3395–3402. DOI: 10.1093/mnras/staa2577. arXiv: 2004.13811 [astro-ph.HE].

[212] P. T. H. Pang, O. A. Hannuksela, T. Dietrich, et al. "Lensed or not lensed: Determining lensing magnifications for binary neutron star mergers from a single detection". In: *Mon. Not. R. Astron. Soc.* (Feb. 2020). DOI: 10.1093/mnras/staa1430. arXiv: 2002.04893 [astro-ph.HE].

[213] LIGO Scientific, Virgo Collaboration. "Properties and Astrophysical Implications of the 150 $M_\odot$ Binary Black Hole Merger GW190521". In: *Astrophys. J. Lett.* 900.1 (2020), p. L13. DOI: 10.3847/2041-8213/aba493. arXiv: 2009.01190 [astro-ph.HE].

[214] S. Goyal, K. Haris, A. K. Mehta, et al. "Testing the nature of gravitational-wave polarizations using strongly lensed signals". In: *Phys. Rev. D* 103.2 (2021), p. 024038. DOI: 10.1103/PhysRevD.103.024038. arXiv: 2008.07060 [gr-qc].

[215] S. Stevenson, C. P. L. Berry, and I. Mandel. "Hierarchical analysis of gravitational-wave measurements of binary black hole spin–orbit misalignments". In: *Mon. Not. Roy. Astron. Soc.* 471.3 (2017), pp. 2801–2811. DOI: 10.1093/mnras/stx1764. arXiv: 1703.06873 [astro-ph.HE].

[216] T. Nakamura et al. "Pre-DECIGO can get the smoking gun to decide the astrophysical or cosmological origin of GW150914-like binary black holes". In: *Prog. Theor. Exp. Phys.* 2016.9 (2016), 093E01. DOI: 10.1093/ptep/ptw127. arXiv: 1607.00897 [astro-ph.HE].

[217] S. M. Koushiappas and A. Loeb. "Maximum redshift of gravitational wave merger events". In: *Phys. Rev. Lett.* 119.22 (2017), p. 221104. DOI: 10.1103/PhysRevLett.119.221104. arXiv: 1708.07380 [astro-ph.CO].

[218] V. Tiwari. "Estimation of the Sensitive Volume for Gravitational-wave Source Populations Using Weighted Monte Carlo Integration". In: *Class. Quant. Grav.* 35.14 (2018), p. 145009. DOI: 10.1088/1361-6382/aac89d. arXiv: 1712.00482 [astro-ph.HE].

[219] W. M. Farr. "Accuracy Requirements for Empirically-Measured Selection Functions". In: *Research Notes of the AAS* 3.5 (2019), p. 66. DOI: 10.3847/2515-5172/ab1d5f. arXiv: 1904.10879 [astro-ph.IM].

[220] H.-Y. Chen, R. Essick, S. Vitale, et al. "Observational Selection Effects with Ground-based Gravitational Wave Detectors". In: *Astrophys. J.* 835.1 (2017), p. 31. DOI: 10.3847/1538-4357/835/1/31. arXiv: 1608.00164 [astro-ph.HE].

[221] Y. Wang, A. Stebbins, and E. L. Turner. "Gravitational lensing of gravitational waves from merging neutron star binaries". In: *Phys. Rev. Lett.* 77 (1996), pp. 2875–2878. DOI: 10.1103/PhysRevLett.77.2875. arXiv: astro-ph/9605140.

[222] LIGO Scientific, VIRGO Collaboration. "Search for Lensing Signatures in the Gravitational-Wave Observations from the First Half of LIGO–Virgo's Third Observing Run". In: *Astrophys. J.* 923.1 (2021), p. 14. DOI: 10.3847/1538-4357/ac23db. arXiv: 2105.06384 [gr-qc].

[223] G. P. Smith, M. Jauzac, J. Veitch, et al. "What if LIGO's gravitational wave detections are strongly lensed by massive galaxy clusters?" In: *Mon. Not. Roy. Astron. Soc.* 475.3 (2018), pp. 3823–3828. DOI: 10.1093/mnras/sty031. arXiv: 1707.03412 [astro-ph.HE].

[224] R. K. L. Lo and I. Magana Hernandez. "Bayesian statistical framework for identifying strongly lensed gravitational-wave signals". In: *Phys. Rev. D* 107.12 (2023), p. 123015. DOI: 10.1103/PhysRevD.107.123015. arXiv: 2104.09339 [gr-qc].

[225] L. Dai, T. Venumadhav, and K. Sigurdson. "Effect of lensing magnification on the apparent distribution of black hole mergers". In: *Phys. Rev. D* 95.4 (2017), p. 044011. DOI: 10.1103/PhysRevD.95.044011. arXiv: 1605.09398 [astro-ph.CO].

[226] M. Fishbach and D. E. Holz. "Where Are LIGO's Big Black Holes?" In: *Astrophys. J. Lett.* 851.2 (2017), p. L25. DOI: 10.3847/2041-8213/aa9bf6. arXiv: 1709.08584 [astro-ph.HE].

[227] K. G. Malmquist. "On some relations in stellar statistics". In: *Meddelanden fran Lunds Astronomiska Observatorium Serie I* 100 (Mar. 1922), pp. 1–52.

[228] M. Sereno, P. Jetzer, A. Sesana, et al. "Cosmography with strong lensing of LISA gravitational wave sources". In: *Mon. Not. Roy. Astron. Soc.* 415 (2011), p. 2773. DOI: 10.1111/j.1365-2966.2011.18895.x. arXiv: 1104.1977 [astro-ph.CO].

[229] G. Smith et al. "Strong-lensing of Gravitational Waves by Galaxy Clusters". In: *IAU Symp.* 338 (2017). Ed. by G. González and R. Hynes, pp. 98–102. DOI: 10.1017/S1743921318003757. arXiv: 1803.07851 [astro-ph.CO].

[230] LSST Collaboration. "Discovery of Strongly-lensed Gravitational Waves - Implications for the LSST Observing Strategy". In: (Feb. 2019). arXiv: 1902.05140 [astro-ph.HE].

[231] A. Robertson, G. P. Smith, R. Massey, et al. "What does strong gravitational lensing? The mass and redshift distribution of high-magnification lenses". In: (Feb. 2020). DOI: 10.1093/mnras/staa1429. arXiv: 2002.01479 [astro-ph.CO].

[232] D. Ryczanowski, G. P. Smith, M. Bianconi, et al. "On building a cluster watch-list for identifying strongly lensed supernovae, gravitational waves and kilonovae". In: *Mon. Not. Roy. Astron. Soc.* 495.2 (2020), pp. 1666–1671. DOI: 10.1093/mnras/staa1274. arXiv: 2005.02296 [astro-ph.GA].

[233] H. Yu, P. Zhang, and F.-Y. Wang. "Strong lensing as a giant telescope to localize the host galaxy of gravitational wave event". In: *Mon. Not. Roy. Astron. Soc.* 497.1 (2020), pp. 204–209. DOI: 10.1093/mnras/staa1952. arXiv: 2007.00828 [astro-ph.CO].

[234] LIGO Scientific, VIRGO, KAGRA Collaboration. "Search for gravitational-lensing signatures in the full third observing run of the LIGO-Virgo network". *Submitted to Astrophys. J.* arXiv: 2304.08393 [gr-qc].

[235] I. M. Romero-Shaw et al. "Bayesian inference for compact binary coalescences with bilby: validation and application to the first LIGO–Virgo gravitational-wave transient catalogue". In: *Mon. Not. Roy. Astron. Soc.* 499.3 (2020), pp. 3295–3319. DOI: 10.1093/mnras/staa2850. arXiv: 2006.00714 [astro-ph.IM].

[236] C. Talbot, R. Smith, E. Thrane, et al. "Parallelized Inference for Gravitational-Wave Astronomy". In: *Phys. Rev. D* 100.4 (2019), p. 043030. DOI: 10.1103/PhysRevD.100.043030. arXiv: 1904.02863 [astro-ph.IM].

[237] P. Madau and M. Dickinson. "Cosmic Star-Formation History". In: *Ann. Rev. Astron. Astrophys.* 52 (Aug. 2014), pp. 415–486. DOI: 10.1146/annurev-astro-081811-125615. arXiv: 1403.0007 [astro-ph.CO].

[238] K. Belczynski, V. Kalogera, F. A. Rasio, et al. "Compact object modeling with the startrack population synthesis code". In: *Astrophys. J. Suppl.* 174 (2008), p. 223. DOI: 10.1086/521026. arXiv: astro-ph/0511811.

[239] K. Belczynski, M. Dominik, T. Bulik, et al. "The effect of metallicity on the detection prospects for gravitational waves". In: *Astrophys. J. Lett.* 715 (2010), p. L138. DOI: 10.1088/2041-8205/715/2/L138. arXiv: 1004.0386 [astro-ph.HE].

[240] M. Dominik, K. Belczynski, C. Fryer, et al. "Double Compact Objects II: Cosmological Merger Rates". In: *Astrophys. J.* 779 (2013), p. 72. DOI: 10.1088/0004-637X/779/1/72. arXiv: 1308.1546 [astro-ph.HE].

[241] J. J. Eldridge, E. R. Stanway, and P. N. Tang. "A consistent estimate for Gravitational Wave and Electromagnetic transient rates". In: *Mon. Not. Roy. Astron. Soc.* 482.1 (2019), pp. 870–880. DOI: 10.1093/mnras/sty2714. arXiv: 1807.07659 [astro-ph.HE].

[242] S. Goyal, S. Kapadia, J.-R. Cudell, et al. "A rapid method for preliminary identification of subthreshold strongly lensed counterparts to superthreshold gravitational-wave events". In: *arXiv e-prints* (June 2023). arXiv: 2306.04397 [gr-qc].

[243] D. W. Scott. *Multivariate Density Estimation: Theory, Practice, and Visualization*. A Wiley-interscience publication. Wiley, 1992. ISBN: 9780471547709. DOI: 10.1002/9780470316849.

[244] R. K. L. Lo. "denmarf: a Python package for density estimation using masked autoregressive flow". *Submitted to J. Open Source Softw.* DOI: 10.48550/arXiv.2305.14379. arXiv: 2305.14379 [astro-ph.IM].

[245] M. Bernardi, F. Shankar, J. B. Hyde, et al. "Galaxy luminosities, stellar masses, sizes, velocity dispersions as a function of morphological type". In: *Mon. Not. Roy. Astron. Soc.* 404 (2010), p. 2087. DOI: 10.1111/j.1365-2966.2010.16425.x. arXiv: 0910.1093 [astro-ph.CO].

[246] P. Torrey, S. Wellons, F. Machado, et al. "An analysis of the evolving comoving number density of galaxies in hydrodynamical simulations". In: *Mon. Not. Roy. Astron. Soc.* 454.3 (Dec. 2015), pp. 2770–2786. DOI: 10.1093/mnras/stv1986. arXiv: 1507.01942 [astro-ph.GA].

[247] F. Pedregosa, G. Varoquaux, A. Gramfort, et al. "Scikit-learn: Machine Learning in Python". In: *J. Mach. Learn. Res.* 12.85 (2011), pp. 2825–2830. URL: http://jmlr.org/papers/v12/pedregosa11a.html.

[248] J. Janquart et al. "Follow-up Analyses to the O3 LIGO-Virgo-KAGRA Lensing Searches". *Submitted to Mon. Not. Roy. Astron. Soc.* arXiv: 2306.03827 [gr-qc].

[249] A. R. A. C. Wierda, E. Wempe, O. A. Hannuksela, et al. "Beyond the Detector Horizon: Forecasting Gravitational-Wave Strong Lensing". In: *Astrophys. J.* 921.2 (2021), p. 154. DOI: 10.3847/1538-4357/ac1bb4. arXiv: 2106.06303 [astro-ph.HE].

[250] A. More and S. More. "Improved statistic to identify strongly lensed gravitational wave events". In: *Mon. Not. Roy. Astron. Soc.* 515.1 (2022), pp. 1044–1051. DOI: 10.1093/mnras/stac1704. arXiv: 2111.03091 [astro-ph.CO].

[251] K. Cannon, S. Caudill, C. Chan, et al. "GstLAL: A software framework for gravitational wave discovery". In: *SoftwareX* 14, 100680 (June 2021), p. 100680. DOI: 10.1016/j.softx.2021.100680. arXiv: 2010.05082 [astro-ph.IM].

[252] J. Luan, S. Hooper, L. Wen, et al. "Towards low-latency real-time detection of gravitational waves from compact binary coalescences in the era of advanced detectors". In: *Phys. Rev. D* 85 (2012), p. 102002. DOI: 10.1103/PhysRevD.85.102002. arXiv: 1108.3174 [gr-qc].

[253] Q. Chu et al. "SPIIR online coherent pipeline to search for gravitational waves from compact binary coalescences". In: *Phys. Rev. D* 105.2 (2022), p. 024023. DOI: 10.1103/PhysRevD.105.024023. arXiv: 2011.06787 [gr-qc].

[254] S. Klimenko et al. "Method for detection and reconstruction of gravitational wave transients with networks of advanced detectors". In: *Phys. Rev.* D93.4 (2016), p. 042004. DOI: 10.1103/PhysRevD.93.042004. arXiv: 1511.05999 [gr-qc].

[255] S. J. Kapadia et al. “A self-consistent method to estimate the rate of compact binary coalescences with a Poisson mixture model”. In: *Class. Quant. Grav.* 37.4 (2020), p. 045007. DOI: 10.1088/1361-6382/ab5f2d. arXiv: 1903.06881 [astro-ph.HE].

[256] Planck Collaboration. “Planck 2018 results. VIII. Gravitational lensing”. In: *Astron. Astrophys.* 641 (2020), A8. DOI: 10.1051/0004-6361/201833886. arXiv: 1807.06210 [astro-ph.CO].

[257] DES, SPT Collaboration. “Joint analysis of Dark Energy Survey Year 3 data and CMB lensing from SPT and Planck. III. Combined cosmological constraints”. In: *Phys. Rev. D* 107.2 (2023), p. 023531. DOI: 10.1103/PhysRevD.107.023531. arXiv: 2206.10824 [astro-ph.CO].

[258] ACT Collaboration. “The Atacama Cosmology Telescope: DR6 Gravitational Lensing Map and Cosmological Parameters”. In: (Apr. 2023). arXiv: 2304.05203 [astro-ph.CO].

[259] SDSS-IV Collaboration. “The 16th Data Release of the Sloan Digital Sky Surveys: First Release from the APOGEE-2 Southern Survey and Full Release of eBOSS Spectra”. In: *Astrophys. J. Suppl.* 249.1 (2020), p. 3. DOI: 10.3847/1538-4365/ab929e. arXiv: 1912.02905 [astro-ph.GA].

[260] S. Birrer and A. Amara. “Lenstronomy: multi-purpose gravitational lens modelling software package”. In: *Phys. Dark Universe* (2018). DOI: 10.1016/j.dark.2018.11.002. arXiv: 1803.09746 [astro-ph.CO].